



Faculty of Engineering,
Built Environment and
Information Technology

Computational Investigation of Swirling Jet Impingement in a Concentrated Solar Tower Receiver

By
Jesse Quick

Submitted in partial fulfilment of the requirements for the degree of

Master of Engineering

Department of Mechanical and Aeronautical Engineering
Faculty of Engineering, Built Environment and Information Technology

University of Pretoria

2021

Supervisor: Prof KJ Craig
Co-supervisor: Prof JP Meyer

ABSTRACT

With growing concern of climate change and environmental pollution the need for better renewable technologies is a necessity. Solar energy shows the most promise in meeting global energy needs and competing with fossil fuels economically. Currently solar power is generated with photovoltaic (PV) panels and stored in batteries. The disadvantages of PV are expensive batteries, limitations on panel efficiencies and electrical grid considerations to balance electricity generation. Concentrated solar power (CSP) is an alternative that addresses PV limitations and shows potential in a hybrid power generation mix, especially because of its thermal storage capabilities and ability to provide process heat directly.

CSP consists of a variety of systems. Of all available CSP technologies, solar power towers (SPT) show potential to reach high temperatures and effectively store thermal energy. For SPT the central receiver shows promise for improvement in effectively capturing heat. Of the many methods available to improve heat transfer, jet impingement with swirl can improve heat transfer for the receiver fluid. Jet impingement heat transfer is well known to enhance local heat transfer because of the local increase in the heat transfer coefficient and Nusselt number. Swirling flows have also shown to enhance heat transfer for internal pipe flow arrangements and other heat transfer applications. The effect of swirl and jet impingement are not often considered cumulatively as in the current study.

For a proposed solar receiver design, a swirling impinging jet is proposed to enhance heat transfer. The flow behaviour is investigated numerically using computational fluid dynamics (CFD). Ansys Fluent is used to model the flow behaviour and to validate the model with available experimental results. From the validation study the Transition Shear-Stress-Transport turbulence model is shown to predict jet impingement the best. A 2D axisymmetric assumption is however shown to not predict the heat transfer well while a costly full 3D transient Large Eddy simulation does. As LES is too expensive for use in a parametric investigation, both 2D and 3D RANS simulations were used as an engineering tool to improve and optimise heat transfer, keeping in mind their shortcomings.

Swirling jet impingement is further investigated for a curved impingement surface. This is the first investigation of its kind where swirl, jet impingement and a curved impingement surface are considered. From the validation study, a CFD model is used to investigate how curvature affects heat transfer. The parameters show that surface curvature has a large effect on heat transfer and it is shown that a potential optimal curvature exists for the unique flow arrangement. A surrogate optimisation model is used from the numerical results to improve the design.

To provide a realistic heat source on the solar receiver, Monte Carlo ray tracing (MCRT) is used to model the heliostat field. The MCRT model can better predict the solar flux distribution on the receiver absorbing surface. The solar flux distribution is an important consideration for the receiver design. The CFD model of the receiver showed that while swirling jet impingement did not increase the outlet temperature of the heat transfer fluid, it did however show potential to reduce the receiver's maximum surface temperature and as well as radiation losses. The thermal enhancements made do however come at the cost of an increased pressure drop.

ACKNOWLEDGEMENTS

I would hereby like to acknowledge the following people:

- My sincere gratitude and appreciation to my supervisor, Prof Ken J Craig, for his technical guidance, invaluable feedback, all the opportunities he has provided me and a fantastic student-supervisor relationship
- My deepest thanks to my co-supervisor, Prof Josua P Meyer, for his financial and technical support in the attainment of this degree.
- My sincere appreciation for the support of my family and friends, with a special thanks to my parents, Ken and Sandra Quick, for their endless support on so many levels. I could never thank you enough.
- My thanks in particular to Mr Marcel Sloomweg and Mr Derwalt Erasmus for their support.
- My thanks to all the other colleagues, academic as well as non-academic staff members of the Clean Energy Research Group in the Department of Mechanical and Aeronautical Engineering, University of Pretoria, for the pleasant and friendly working environment.

This work is based on research supported by the National Research Foundation (NRF) and the University of Pretoria. The financial assistance of the NRF is hereby acknowledged. Opinions expressed and conclusions arrived at are those of the author and are not necessarily to be attributed to the NRF.

PUBLICATIONS

- Craig, K.J., Quick, J., Sootweg, M., Meyer, J.P., Numerical Investigation of Jet Impingement Heat Transfer in Solar Receivers, 14th International Heat Transfer Conference (HEFAT 2019), Wicklow, Ireland, 22-24 July 2019.
- Craig, K.J., Quick, J., Meyer, J.P., Large Eddy Simulation of swirling impinging jets for a solar cavity absorber, 6th Southern African Solar Energy Conference (SASEC 2019), 25 – 27 November 2019, East London, South Africa.
- Quick, J., Craig, K.J., Meyer, J.P., Implementation of a Swirling Impinging Jet for a Solar Cavity Absorber, 6th Southern African Solar Energy Conference (SASEC 2019), 25 – 27 November 2019, East London, South Africa.

CONTENTS

Abstract.....	i
Acknowledgements.....	iii
Publications.....	iv
List of Symbols and Abbreviations.....	ix
Table of Abbreviations	ix
English Letters and Symbols	ix
Greek Symbols.....	x
Subscripts.....	xi
List of Figures.....	xii
List of Tables	xvi
1 Introduction.....	1
1.1 Background.....	1
1.2 Problem statement.....	6
1.3 Objective	6
1.4 Overview of the dissertation	7
2 Literature Review.....	9
2.1 Introduction.....	9
2.2 Concentrated Solar Power.....	9
2.3 Concentrated solar power concentrator types	10
2.4 Solar power tower history	16
2.4.1 The push towards higher operating temperatures	18
2.5 Collector.....	19
2.5.1 Heliostat field.....	20
2.5.2 Collector performance.....	21
2.6 Solar power tower receiver	22
2.6.1 Receiver performance	23
2.6.2 Configuration	25
2.6.3 Receiver heat transfer fluids	26

2.6.4	Heat transfer enhancement for solar receivers	29
2.7	Jet impingement	31
2.7.1	Jet impingement fundamentals.....	32
2.7.2	Jet impingement parameters and non-dimensional coefficients	33
2.7.3	Jet impingement turbulence effects and heat transfer	34
2.7.4	Jet impingement heat transfer enhancement	37
2.8	Swirl flows	39
2.8.1	Basic effects of swirl.....	40
2.8.2	Swirling impinging jets	42
2.9	Influencing solar receiver designs.....	47
2.10	Optical modelling in literature	53
2.11	Thermal modelling in literature	54
2.11.1	Computational fluid dynamics	54
2.11.2	Jet impingement numerical modelling	55
2.12	Optimisation.....	58
2.12.1	Optimisation fundamentals	59
2.12.2	Receiver optimisation	60
2.13	Conclusion	61
3	Numerical validation of swirling Jet impingement	63
3.1	Introduction.....	63
3.2	Validation experiments	63
3.2.1	Aerodynamically generated swirl	63
3.2.2	Geometrically generated swirl	66
3.3	CFD model settings.....	66
3.3.1	Assumptions.....	67
3.3.2	Fluid properties	67
3.3.3	Solution algorithm.....	68
3.4	General boundary conditions	68
3.5	2D axisymmetric swirl	69

3.5.1	Domain parameterisation and grid generation	69
3.5.2	Turbulence Model selection.....	71
3.5.3	Results for various swirl numbers (Case 3.1)	72
3.6	3D RANS Simulations.....	77
3.6.1	Ahmed swirl generator (Case 3.2)	77
3.6.2	Transient analysis (Case 3.3)	83
3.7	Geometric swirl generator (Case 3.4)	85
3.8	Large Eddy Simulation (Case 3.5).....	88
3.8.1	Domain and mesh strategy.....	89
3.8.2	Numerical solution procedure	90
3.9	Conclusion	93
4	Numerical optimisation of concave swirling jet impingement and cone receiver	96
4.1	Introduction.....	96
4.2	Experimental validation case	96
4.3	Fluid properties	97
4.4	Computational setup	97
4.5	Boundary conditions	98
4.6	2D axi-symmetric without swirl (Case 4.1)	99
4.6.1	Swirling impinging jet on concave surface parameter investigation (Case 4.2).....	103
4.7	3D SIJ (Case 4.3)	106
4.8	Optimisation of receiver cone.....	109
4.8.1	2D cone optimisation (Case 4.4).....	109
4.8.2	Results.....	113
4.9	Conclusion	120
5	Swirling jet impingement in a concentrated SOLAR tower RECEIVER for realistic heat source	121
5.1	Introduction.....	121
5.2	Design overview	121
5.3	Optical modelling.....	122

5.3.1	Optical model inputs	123
5.3.2	Optical simulation results.....	126
5.4	Single cone analysis	127
5.4.1	Domain and mesh.....	128
5.4.2	Material properties	131
5.4.3	Boundary conditions	132
5.4.4	Numerical scheme.....	132
5.4.5	Simulation results.....	133
5.5	Multiple cones radiation.....	136
5.5.1	Swirl and no swirl comparison.....	139
5.6	Conclusions.....	144
6	Conclusions and Future work.....	145
6.1	Conclusions.....	145
6.2	Future work and Recommendations	147
	References.....	149
	APPENDIX A: EXPERIMENTAL RESULTS AND FLUID PROPERTIES	A
	APPENDIX B: VERTICAL ROUND JET IMPINGEMENT HEAT TRANSFER ON A FLAT PLATE SENSITIVITY AND MESH ANALYSIS.....	D
	APPENDIX C: VERTICAL ROUND JET IMPINGEMENT HEAT TRANSFER FOR A CONCAVE SURFACE SENSITIVITY AND MESH ANALYSIS	L
	APPENDIX D: SOURCE CODES FOR GEOMETRY AND SIMULATION AUTOMATION ..	T
	APPENDIX E: SOLAR RECEIVER OPTIMISATION.....	Y
	APPENDIX F: HEAT SOURCE IMPLEMENTATION IN FLUENT.....	FFF

LIST OF SYMBOLS AND ABBREVIATIONS

Table of Abbreviations

ANSYS	Engineering simulation and 3-D design software
CFD	Computational fluid dynamics
CSP	Concentrated solar power
DNI	Direct normal irradiance
DNS	Direct numerical simulation
FLUENT	Computational fluid dynamics software for ANSYS
HTF	Heat transfer fluid
JIHT	Jet impingement heat transfer
LCOE	Levelized cost of electricity
LES	Large Eddy simulation
LFC	Linear Fresnel collectors
MCRT	Monte-Carlo ray tracing
PS	Planta Solar
PTC	Parabolic trough collector
PV	Photovoltaic
RANS	Reynolds-averaged Navier-Stokes
SCRAP	Spiky central receiver air pre-heater
SIJ	Swirling impinging jet
SPD	Solar parabolic dish
SPT	Solar power tower
TES	Thermal energy storage

English Letters and Symbols

A

Area

m^2

bar	Pressure	$10^5 Pa$
c_p	Specific heat	J/kgK
D	Concave surface diameter	m
G	Solar irradiance	W/m^2
h	Heat transfer coefficient	W/m^2K
H	Perpendicular height from Nozzle exit to target surface	m
k	Thermal conductivity	$W/m - K$
K	Kelvin	K
L	Length of pipe	m
m	mass	kg
Ma	Mach number	
Nu	Nusselt number	
Pr	Prandtl number	
q	Heat transfer flux	W/m^2
Q	Heat	W
\dot{Q}	Heat transfer rate	W
r	Radius	m
rad	Radians	
Re	Reynolds number	
p	Pressure	Pa
t	Time	$seconds$
T	Temperature	K
u	Velocity	m/s
u_i	Velocity in direction i	m/s
U	Velocity	m/s
ν	Kinematic viscosity	m^2/s
W	Power	W

Greek Symbols

η	Efficiency	
Δ	Increment	
ε	Emissivity	
ρ	Density	kg/m^3

μ	Dynamic viscosity	kg/ms
σ	Stefan Boltzmann constant	$5.67 \times 10^{-8} W/m^2 K^4$
α	Absorbance	
θ_c	Acceptance half angle	$^\circ$ or rad
γ	Reflectance	

Subscripts

Subscripts are used to identify specific properties where a “,” is used this is done to indicate the relation between subscripts.

c	Cooling source
$carnot$	For the Carnot cycle
$collector$	Collector
$cond$	Conduction
$conv$	Convection
DNI	Direct normal irradiance
e	Exit
eff	Effective
el	Electrical
h	Heating source
HTF	Heat transfer fluid
i	Inlet
in	In
j	Jet
$loss$	Losses
$optical$	Optical
rad	Radiation
$receiver$	Receiver
$reflect$	Reflectance
s	Surface
$surr$	Surroundings
th	Thermal
tot	Total/combined
w	Wall

LIST OF FIGURES

Figure 1. Energy-related carbon dioxide emissions (a) by sector (b) by fuel type (EIA, 2018).	1
Figure 2. Energy resources of the world (Ellabban <i>et al.</i> , 2014).	4
Figure 3. World map of long-term averaged direct normal irradiance (The World Bank, 2017).	5
Figure 4. LCOE for renewable energies displaying the mean, minimum and maximum cost in USD/kWh (IRENA, 2018).	6
Figure 5. CSP power plant energy flow diagram.	9
Figure 6. Solar concentrator configurations: parabolic trough concentrator, solar power tower, linear Fresnel reflector and solar parabolic dish (Fuqiang <i>et al.</i> , 2017).	11
Figure 7. One of the 139.9m tall Ivanpah central towers (Dieterich, 2018).	17
Figure 8. (a) Crescent Dunes 110 MW molten salt SPT plant with surround field (SolarReserve, 2015). (b) PS10 10 MW saturated steam SPT plant with polar field configuration (The Highlanders, 2013).	17
Figure 9. (a) The solar-to-thermal efficiency (η_{th}) and thermal-to-electric efficiency (η_{el}) as a function of temperature at different concentration ratios (Ho, 2017). (b) The combined efficiency (η_{tot}) as a function of temperature at different concentration ratios (Ho, 2017).	19
Figure 10. (a) Surround field heliostat configuration. (b) Polar field heliostat configuration. (c) Radial stagger heliostat field arrangement. (d) Cornfield heliostat field arrangement.	20
Figure 11. Schematic of optical loss mechanisms (Falcone, 1986).	21
Figure 12. Schematic of heat loss mechanisms for the SPT receiver (Falcone, 1986).	23
Figure 13. (a) External receiver basic configuration. (b) Cavity receiver basic configuration (Falcone, 1986).	25
Figure 14. Schematic of a bladed tubular receiver design (Ho <i>et al.</i> , 2016).	30
Figure 15. Schematic of the PLVCR-500 volumetric gas receiver (Pritzkow, 1991).	31
Figure 16. Jet impingement schematic and flow regions.	32
Figure 17. Instability in the turbulent free jet and formation of vortices (Zuckerman & Lior, 2006). ..	36
Figure 18. Heat transfer coefficient normalised with the Reynolds number ($Nu/Re^{0.7}$), plotted against the non-dimensional radial distance (r/d) (Craig, Slootweg & Meyer, 2018).	37
Figure 19. Depiction of flow field for (a) weak swirl flows and (b) strong swirl flows extracted from (Gupta <i>et al.</i> , 1984).	40
Figure 20. Comparison of flow regions for non-swirling jet impingement and swirling jets impingement (without vortex breakdown) adapted from Ahmed (2016).	42
Figure 21. External pyramid receiver central receiver schematic proposed by Garbrecht <i>et al.</i> (2013).	48

Figure 22. (a) External pyramid outer surface temperature contour. (b) Net flux absorbed by pyramid contour. (c) HTF streamlines for pyramid (Garbrecht <i>et al.</i> , 2013).....	49
Figure 23. (a) Schematic of SCRAP receiver. (b) Internally finned tube sectional view (Lubkoll <i>et al.</i> , 2015).	49
Figure 24. (a) Geometric model of proposed jet impingement solar dish receiver. (b) Schematic of proposed jet impingement solar dish receiver (Wang <i>et al.</i> , 2015).	50
Figure 25. Local heat transfer Nusselt number over cylindrical surface (Wang <i>et al.</i> 2015).	51
Figure 26. Hexagonal pyramid receiver design (a) secondary concentrator and pyramid with internal flow arrangement (b) pyramid surface temperature and hot spots (Slootweg <i>et al.</i> , 2019).	52
Figure 27. Vertical round jet impingement on a flat surface, experimental test setup schematic from Ahmed <i>et al.</i> (2017). Key: 1. Swirl nozzle, 2. Stainless steel foil (impingement surface), 3. Aluminium assembly to hold copper busbars, 4. Copper busbars, 5. Infrared camera, 6. DC Power supply, 7. Clamp meter to measure current at steel foil, 8. Digital multimeter to measure voltage across steel foil.....	65
Figure 28. Sectional CAD drawing of swirl nozzle and inlet jets (Ahmed <i>et al.</i> , 2016b). (a) Full sectional view (dimensions in <i>mm</i>). (b) Setup for CTA measurements and coordinate system used.	65
Figure 29 Experimental setup of jet impingement with geometric insert.	66
Figure 30. ANSYS 2D axisymmetric computational domain for flat plate swirling jet impingement.	70
Figure 31. Depiction of a coarse mesh, with the applied mesh refinement, of 11 831 cells for the axisymmetric 2D flat plate JIHT.....	71
Figure 32. Nu vs r/d for different turbulence models for a conventional impinging jet.	72
Figure 33. Nu vs r/d for experimental and numerical results for SIJ for $Re = 35\ 000$, $H/d = 1$, $d = 40\text{mm}$ and $S = 0, 0.27, 0.45, 0.77, 1.05$	73
Figure 34. Nu vs r/d for experimental and numerical results for SIJ for $Re = 35\ 000$, $H/d = 2$, $d = 40\text{mm}$ and $S = 0, 0.27, 0.45, 0.77, 1.05$	73
Figure 35. Nu vs r/d for experimental and numerical results for SIJ for $Re = 35\ 000$, $H/d = 4$, $d = 40\text{mm}$ and $S = 0, 0.27, 0.45, 0.77, 1.05$	74
Figure 36. Nu vs r/d for experimental and numerical results for SIJ for $Re = 35\ 000$, $H/d = 6$, $d = 40\text{mm}$ and $S = 0, 0.27, 0.45, 0.77, 1.05$	74
Figure 37. Ahmed aerodynamic swirl generator.....	77
Figure 38. 3D SIJ domain for flat impingement surface based on the work of Ahmed.....	79
Figure 39. 3D SIJ mesh (a) Mesh on flat impingement surface (b) Mesh refinement near impingement surface in axial direction.	79
Figure 40. 3D SIJ velocity magnitude where $H/d = 2$ and $S = 0.77$	81
Figure 41. Nozzle exit axial and tangential velocity profiles for (a) $S = 0$ (b) $S = 0.27$ (c) $S = 0.45$ (d) $S = 0.77$ (e) $S = 1.05$	82

Figure 42. Nusselt number distributions on impingement surface where (a) $S = 0$ (b) $S = 0.27$ (c) $S = 0.45$ (d) $S = 0.77$ (e) $S = 1.05$.	83
Figure 43. Nusselt number distribution on flat surface as a function of time where $Re = 35\ 000$ and $S = 0.77$.	84
Figure 44. Time averaged Nusselt number in the radial direction.	85
Figure 45. Flow domain with geometric swirl generator.	86
Figure 46. Nusselt number in the radial direction validation.	87
Figure 47. Nusselt number distribution on impingement surface due to geometric insert.	87
Figure 48. Velocity magnitude on mid plane and velocity distributions at nozzle exit.	88
Figure 49. LES instantaneous velocity magnitude contours in central plane and on Q-criterion iso-surfaces, and Nusselt number distribution on impingement surface.	92
Figure 50. LES time averaged Nusselt number distribution on impingement surface in the radial direction.	93
Figure 51. PSD of axial velocity at jet centre exit, Kolmogorov constant plotted for reference.	93
Figure 52. Vertical round jet impingement on a concave surface, experimental test setup schematic (Lee <i>et al.</i> , 1999).	97
Figure 53. 2D Axi-symmetric fluid domain and boundary conditions.	100
Figure 54. Coarse mesh of the 2D axisymmetric mesh.	101
Figure 55. Nu vs r/d for experimental and numerical results for concave JIHT for $Re = [11\ 000, 23\ 000, 50\ 000]$, $H/d = 2$, $d = 34\text{mm}$, $d/D = 0.089$, and $L = 10d$.	102
Figure 56. Vertical round jet impingement on a concave surface, velocity magnitude and streamlines. (Case 4.1)	102
Figure 57. Nusselt number distribution in radial direction (a) $H/d = 2, d/D = 0.089$ (b) $H/d = 1, d/D = 0.034$ (c) $H/d = 1, d/D = 0.089$ (d) $H/d = 2, d/D = 0.034$.	105
Figure 58. Flow variables of SIJ on a concave surface where $S = 0.77, H/d = 2, d/D = 0.089$ velocity magnitude, total pressure, swirl velocity, axial velocity and turbulent kinetic energy (Case 4.2).	106
Figure 59. 3D fluid domain for SIJ on a concave surface.	107
Figure 60. Nusselt number distribution of SIJ on a concave surface where $H/d = 2, d/D = 0.089$ (a) $S = 0$ (b) $S = 0.27$ (c) $S = 0.45$ (d) $S = 0.77$ (e) $S = 1.05$.	108
Figure 61. Nusselt number distribution in radial direction where $H/d = 2, d/D = 0.089$.	109
Figure 62. 2D cone parametric domain with indicated design parameters and boundary conditions.	111
Figure 63. 2D axi-symmetric cone mesh of 9000 cells.	113
Figure 64. Flow variables for optimised design of SIJ in a solar receiver cone CP3 (a) Axial velocity (b) Swirl velocity (c) Turbulent kinetic energy.	119
Figure 65. Flow variables for optimised design of SIJ in a solar receiver cone CP3 (a) Velocity magnitude (b) Static temperature (c) Static pressure.	119

Figure 66. Receiver absorbing surface with SIJ cones and the dimensions of the optimised cone design.	122
Figure 67. Optical model geometry (a) Cad geometry (b) Surface mesh of geometry (c) Rays on the receiver surface (d) Solar heat source.	125
Figure 68. SolTrace ray convergence on absorbing surface.	126
Figure 69. Heat flux distribution on absorber surface.....	127
Figure 70. Heat flux distribution on central cone of the receiver.	127
Figure 71. Single central cone CFD domain with solar heat source.	128
Figure 72. Shuttlecock regions for mesh refinement.	129
Figure 73. Coarse mesh depicting the meshing strategy for the SIJ shuttlecock receiver.	131
Figure 74. Velocity magnitude contours for shuttlecock cone on central plane.	134
Figure 75. Total pressure contours for shuttlecock cone on central plane.	134
Figure 76. Static temperature for shuttlecock cone.....	135
Figure 77. Static temperature [K] on shuttlecock cone absorbing surface.....	135
Figure 78. CFD domain for central shuttlecock cones and surrounding air.	137
Figure 79. Static temperature on shuttlecock cone absorbing surface boundary conditions (a) heat source and surrounding cones static temperature (b) Patched static temperature from central cone (c) Side view of static temperature distribution.	138
Figure 80. Radiation heat flux on absorbing surface.	139
Figure 81. Static temperature on shuttlecock cone absorbing surface in the radial direction for different swirl numbers.....	141
Figure 82. Static temperature on shuttlecock cone where $S = 0$	141
Figure 83. Static temperature on shuttlecock cone where $S = 0.3$	142
Figure 84. Static temperature on shuttlecock cone where $S = 1.2$	142
Figure 85. Non-dimensional Nusselt number on impingements surface for different swirl intensities.	143
Figure 86. Non-dimensional circumferentially averaged Nusselt number on impingement surface for different swirl intensities.....	143
Figure 87. Nu contour plots for experimental results for SIJ for $Re = 35\ 000$ and $S = 0, 0.27, 0.45, 0.77, 1.05$ (Ahmed, Al-Abdeli and Guzzom; 2016a).	A
Figure 88. Flow conditions for experimental tests performed (Ahmed, Al-Abdeli and Guzzom; 2016a).	B
Figure 89. Swirl generator flow conditions and swirl number (Ahmed, Al-Abdeli and Guzzom; 2016a).	C
Figure 90. Nu vs r/D for different heights H/d for vertical JIHT.	D
Figure 91. Nu vs r/D for different radial mesh extents for vertical JIHT.	D

Figure 92. Nu vs r/D for different turbulence models for vertical JIHT.	E
Figure 93. Nu vs r/d for experimental and numerical results of vertical jet validation, where numerical refers to the Transition SST turbulence model	E
Figure 94. Nu vs r/D mesh dependency for $S = 0.77, H/d = 2$ where $r/D \leq 2$	G
Figure 95. Nu vs r/D for $S = 0.77, H/d = 2$ over the entire impingement surface.	H
Figure 96. Nu vs r/D mesh dependency for $S = 0, H/d = 2$ where $r/D \leq 2$	H
Figure 97. Nu vs r/D for $S = 0, H/d = 2$ over the entire impingement surface.	I
Figure 98. Average Nusselt number over the impingement surface vs number of cells for $S = 0$ and $S = 0.77; H/d = 2$	J
Figure 99. Maximum Nusselt number over the impingement surface vs number of cells for $S = 0$ and $S = 0.77; H/d = 2$	J
Figure 100. Maximum $y+$ over the impingement surface vs number of cells for $S = 0$ and $S = 0.77; H/d = 2$	K
Figure 101. Vertical round jet impingement on a concave surface, experimental test setup schematic (Lee <i>et al.</i> , 1999).	L
Figure 102. Nu vs r/D for different turbulence models for concave JIHT.	M
Figure 103. Nu vs r/D for different number of mesh cells for concave JIHT.	N
Figure 104. Nu vs r/d for experimental and numerical results for concave JIHT for $Re = [11\ 000, 23\ 000, 50\ 000], H/d = 2, d = 34\text{mm}, d/D = 0.089,$ and $L = 10d$	O
Figure 105. Nusselt number distribution in radial direction $H/d = 4, d/D = 0.089$	P
Figure 106. Nusselt number distribution in radial direction $H/d = 6, d/D = 0.056$	P
Figure 107. Nusselt number distribution in radial direction $H/d = 6, d/D = 0.034$	Q
Figure 108. Nusselt number distribution in radial direction $H/d = 1, d/D = 0.056$	Q
Figure 109. Nusselt number distribution in radial direction $H/d = 4, d/D = 0.034$	R
Figure 110. Nusselt number distribution in radial direction $H/d = 2, d/D = 0.056$	R
Figure 111. Nusselt number distribution in radial direction $H/d = 4, d/D = 0.056$	S

LIST OF TABLES

Table 1. Advantages and disadvantages of renewable energy resources (Ellabban <i>et al.</i> , 2014).	3
Table 2. Characteristics of CSP technologies adapted and updated from Ardekani (2017), Cavallaro (2009), Fuqiang <i>et al.</i> (2017), Islam <i>et al.</i> (2018), Müller-Steinhagen and Trieb (2004), SolarPaces (2018), Ummadisingu and Soni (2011), and Vashishtha (2012).	13
Table 3. Summary of liquid-based receivers (Ho, 2016; Ho & Iverson, 2014).	29
Table 4. Non-dimensional Parameters used for JIHT Investigations (Zuckerman & Lior, 2006).	34

Table 5. Summary of experimental investigations for jet impingement with swirl adapted from Ahmed (2016).....	44
Table 6. Summary of Numerical investigations of jet impingement with swirl adapted from Ahmed (2016).....	45
Table 7. Comparison of CFD turbulence models for jet impingement (Zuckerman & Lior, 2006).	58
Table 8. Fluid properties for the flat plate JIHT validation.	67
Table 9. Summary of simulation numerical controls.....	68
Table 10. Summary of boundary conditions.....	69
Table 11. Domain geometric parameters and descriptions.....	70
Table 12. Swirl intensities, volumetric flow rate and velocity components.	78
Table 13. Summary of modelling approaches.	95
Table 14. Summary of simulations numerical controls.	97
Table 15. Summary of simulations boundary conditions.....	98
Table 16. Material properties for the cone and HTF.....	110
Table 17. Input Parameters used for Concave SIJ Investigations of one Axisymmetric Cone in the Receiver.	110
Table 18. Design point sample space populated with LHS.	112
Table 19. Linear regression coefficients of design inputs to performance outputs.....	114
Table 20. Candidate points parameters.	117
Table 21. Candidate points performance and validation.....	117
Table 22. Computational settings for optical model of PS-10.	123
Table 23. Optical material properties of receiver/absorber for SolTrace simulation.....	125
Table 24. Mesh controls for central cone.....	129
Table 25. Material properties for Shuttlecock domain.....	132
Table 26. Boundary conditions for shuttlecock receiver.	132
Table 27. CFD results for shuttlecock central cone.....	133
Table 28. CFD results for shuttlecock central cone for different swirl numbers.	139
Table 29. Achievement of dissertation objectives	145
Table 30. Mesh independence metric for vertical flat plate JIHT.....	F

1 INTRODUCTION

1.1 Background

Global energy demand is rapidly increasing due to increased population growth and it is expected to double within the next 20 years (EIA, 2018). Currently, most of the population's energy is generated through the burning of fossil fuels (Islam, Huda, Abdullah & Saidur, 2018). It is recognised that the consumption of fossil fuels at an increasing rate, not only diminishes our limited fossil fuel reserves, but also has a detrimental effect on the environment and our health (Panwar, Kaushik & Kothari, 2011). The burning of fossil fuels results in pollution being released into the atmosphere and the release of greenhouse gasses such as carbon dioxide (CO_2). The production of electricity is the primary contributor of CO_2 emissions across all sectors as can be seen in Figure 1 (EIA, 2018; Islam, Shahir, Uddin & Saifullah, 2014). The CO_2 emissions by sector and by fuel type are depicted in Figure 1.

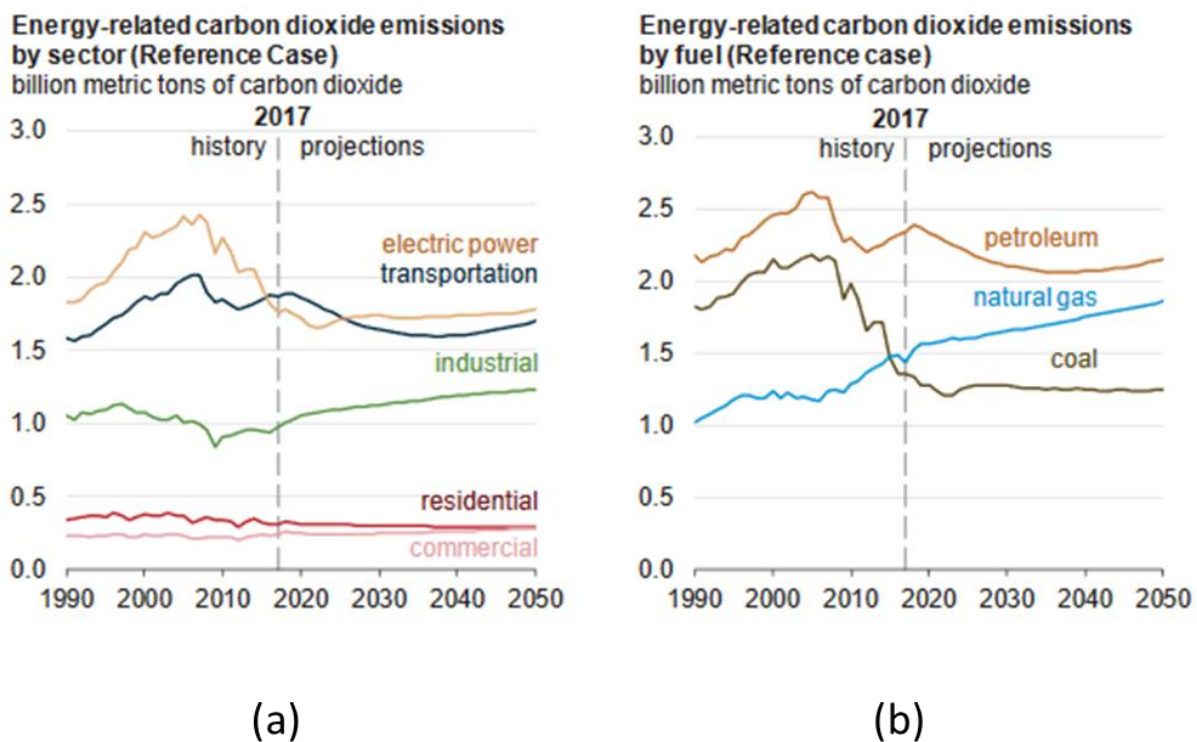


Figure 1. Energy-related carbon dioxide emissions (a) by sector (b) by fuel type (EIA, 2018).

The release of greenhouse gases into the atmosphere is a primary contributor to global warming and climate change. Global warming is considered to be the most prominent environmental concern of our time (Kerzmann, 2010). As can be seen in Figure 1 (a), CO_2 emissions need to be reduced in the electrical power generation sector which can be done but only by breaking our addiction to fossil fuels.

The use of low carbon technologies, predominantly renewable energy technologies, can both meet the future energy demands and reduce greenhouse emissions (Kerzmann, 2010).

In 2011, renewable energy sources supplied only 14% of the total energy demands globally (Panwar *et al.*, 2011). With the current growth estimates, considering legislation and the decline of the levelised cost of electricity (LCOE), it is projected that renewables can account for 64% of total electric power generation by 2050 (EIA, 2018). The predicted improvement of renewable technologies and the reduction of greenhouse gasses can only be achieved if we can innovate and implement more efficient renewable energy technologies. There are multiple types of renewable energy technologies that can be used such as hydropower, geothermal power, wind energy, marine energy, biomass energy, and solar energy.

Biomass is a term used to describe organic material and the storage of the sun's energy within these organic materials through photosynthesis. Biomass energy is the conversion of this stored energy into more useful forms such as heat and electricity (Ellabban, Abu-Rub & Blaabjerg, 2014). The current biomass energy capacity is 109 *GW*, and is expected to grow to a capacity of 270 *GW* by 2030 (IRENA, 2018).

Geothermal energy is the energy generated and stored within the earth's crust as rock, trapped steam, and liquid water (Ellabban *et al.*, 2014). Geothermal energy can be extracted and used to generate electricity, as a heat source or as a combination of both, from a small scale to a utility scale. In 2017, the global geothermal capacity was 12.9 *GW* (IRENA, 2018), where the global potential for geothermal energy is predicted to be 800 *GW* (Ellabban *et al.*, 2014).

Hydropower is power derived from moving water. The movement of water is then converted into electricity using turbines. Typically, hydropower stations use dams to store and generate electricity; however, harnessing wave and tidal energy is becoming more common (EIA, 2018; Ellabban *et al.*, 2014). Marine energy comes from six distinct sources: waves, tidal range, tidal currents, ocean currents, ocean thermal energy conversion, and salinity gradients. The potential for marine energy is estimated to be approximately 7400 *EJ/year*; this exceeds our current and future energy needs (Ellabban *et al.*, 2014).

Wind energy is considered as one of the most important sustainable energy sources due to its abundant supply. Wind energy refers to the conversion of the wind's kinetic energy to electricity, with turbines, or mechanical energy used for pumping (Ellabban *et al.*, 2014). From 2007 to 2017, the electricity capacity of wind energy grew from 91.6 *GW* to 513.5 *GW*. This growth is expected to continue and reach 1759 *GW* by 2030 (IRENA, 2018).

Solar energy generation involves the use of the sun’s energy to provide thermal energy or electricity directly. Solar energy can be classified into two major groups which are solar photovoltaics (PV) and concentrated solar power (CSP) (Stine & Geyer, 2001). Solar PV uses a PV cell which produces electricity directly through the PV effect. The PV panels (arrays of cells) typically produce 50 to 200 *W* of electricity and have efficiencies of 8 – 16% (Ab Kadir, Rafeeu & Adam, 2010). The highest efficiency achieved for PV cells in test facilities are 46% (NREL, 2018). PV technology has experienced enormous growth over its lifetime. In 2007, the global electricity capacity of PV was 8.7 *GW*, and over 10 years the global capacity has increased to 384 *GW* (IRENA, 2018). The limitation for PV technologies is the expense of storing the collected energy in batteries.

CSP technologies produce electricity through a power block where heat is supplied by concentrating sunlight onto a receiver where it is absorbed by the heat transfer fluid (HTF). There are several types of operational CSP plants and developing technologies for CSP. CSP technology has experienced major growth and development in recent years. In 2007 the global installed capacity was 479 *MW* and in 2017 the capacity was 4.9 *GW* (IRENA, 2018). CSP technology is discussed in depth in Chapter 2. For each of the renewable energy sources the advantages and disadvantages are presented in Table 1. This table highlights the differences in the applications of each technology based on the advantages and disadvantages of each technology.

Table 1. Advantages and disadvantages of renewable energy resources (Ellabban *et al.*, 2014).

Energy	Advantages	Disadvantages
Biomass Energy	<ul style="list-style-type: none"> • Conversion to fuels. • Convenient. • Utilisation of waste materials. • Widely distributed and accessible. 	<ul style="list-style-type: none"> • Low energy density. • Not clean. • Costly to produce fuels.
Geothermal energy	<ul style="list-style-type: none"> • Cost effective. • Reliable. • Nearly unlimited supply. • Produces no air or water pollution. • Energy can be stored. 	<ul style="list-style-type: none"> • Initial costs are high. • Operational and maintenance costs are high. • Environmental impact and alterations.
Hydropower energy	<ul style="list-style-type: none"> • Abundant, clean and safe. • Energy can be easily stored. • Low cost to generate electricity. • Most efficient electricity generation (up to 90%). 	<ul style="list-style-type: none"> • May cause flooding. • Can have significant environmental impacts. • Only available where there is a water supply. • The best sites for this technology have already been developed for dams.

Energy	Advantages	Disadvantages
Marine energy	<ul style="list-style-type: none"> • Good for remote island locations. • Captures energy not currently utilised. 	<ul style="list-style-type: none"> • Costly construction. • Negative impacts on marine life. • High spatial requirements.
Wind energy	<ul style="list-style-type: none"> • Produces no water or air pollution. • Relatively inexpensive. • Land around wind farms can still be useful. 	<ul style="list-style-type: none"> • Requires constant and significant wind. • Significant land requirements. • Can have a negative impact on birdlife. • Negative visual impacts on the landscape. • Need for better storage.
Solar energy	<ul style="list-style-type: none"> • Potential infinite supply. • No water or air pollution. • Utility-scale source. • CSP storage. 	<ul style="list-style-type: none"> • Not most cost-effective. • Storage and backup are required. • Reliability dependent on suns availability.

The applications of each renewable energy technology differ based on the requirements for energy generation, but the availability of each technologies needs to be considered. Figure 2 depicts the availability of renewable energy to meet our current energy demands over 3000 times (Ellabban *et al.*, 2014).

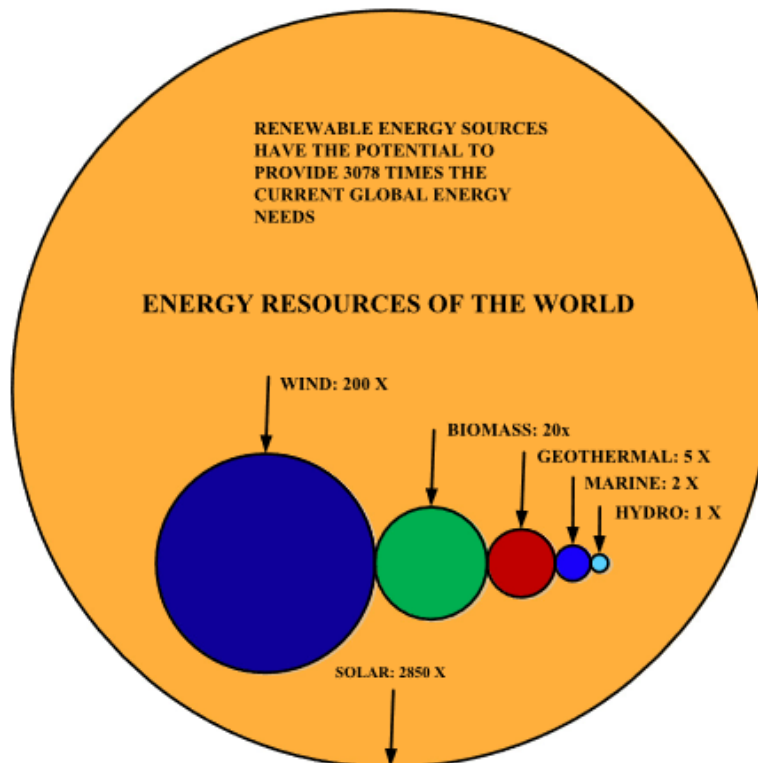


Figure 2. Energy resources of the world (Ellabban *et al.*, 2014).

Solar energy has the most promise with an abundance of available supply. As can be seen in Figure 2, solar energy provides $2850 \times$ our current energy demands (Islam *et al.*, 2018). By using only 2% of the earth's surface, we can meet the current global energy demand by harvesting solar energy. Solar energy does have its disadvantages and can only be used to its full potential in certain areas across the globe. Solar energy does vary over the globe and higher amounts of solar energy are available in certain locations. The available direct normal irradiance (DNI) across the globe is depicted in Figure 3.

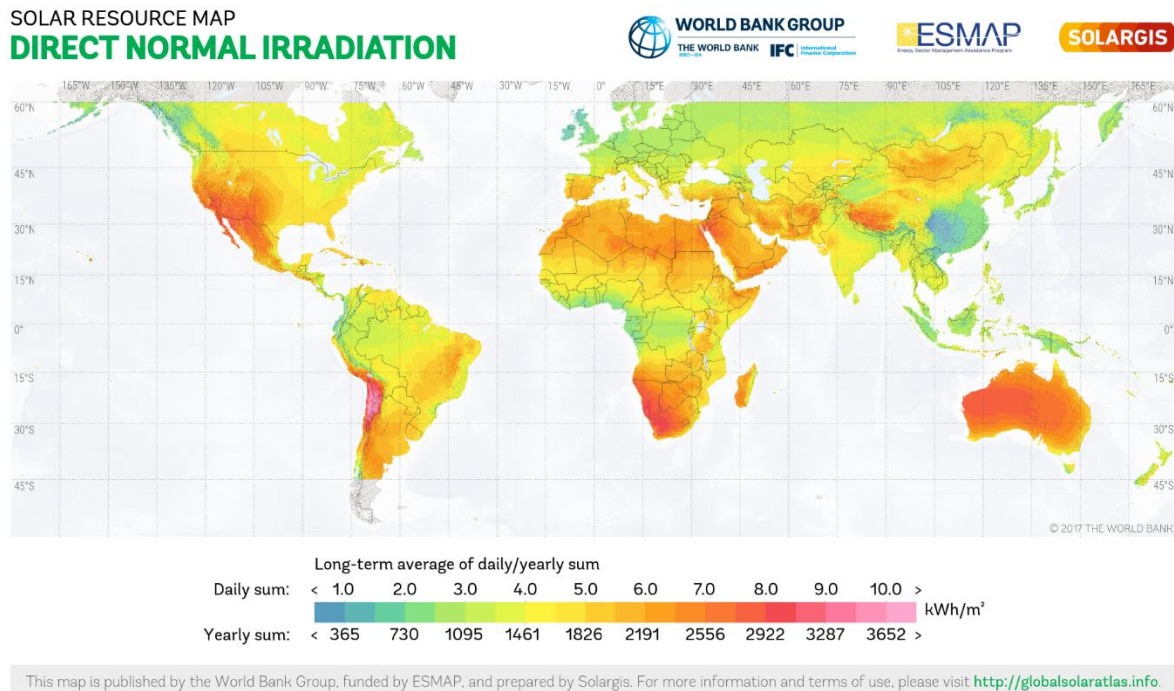


Figure 3. World map of long-term averaged direct normal irradiance (The World Bank, 2017).

PV cells can be used almost everywhere as diffuse sunlight can also be captured and converted by PV cells, and areas with high DNI can use CSP. The LCOE in USD/kWh for renewable energy sources are depicted in Figure 4. The cost range is indicated by the bars, the mean is indicated by the dotted black line, and the fossil fuel cost range is the horizontal grey bar.

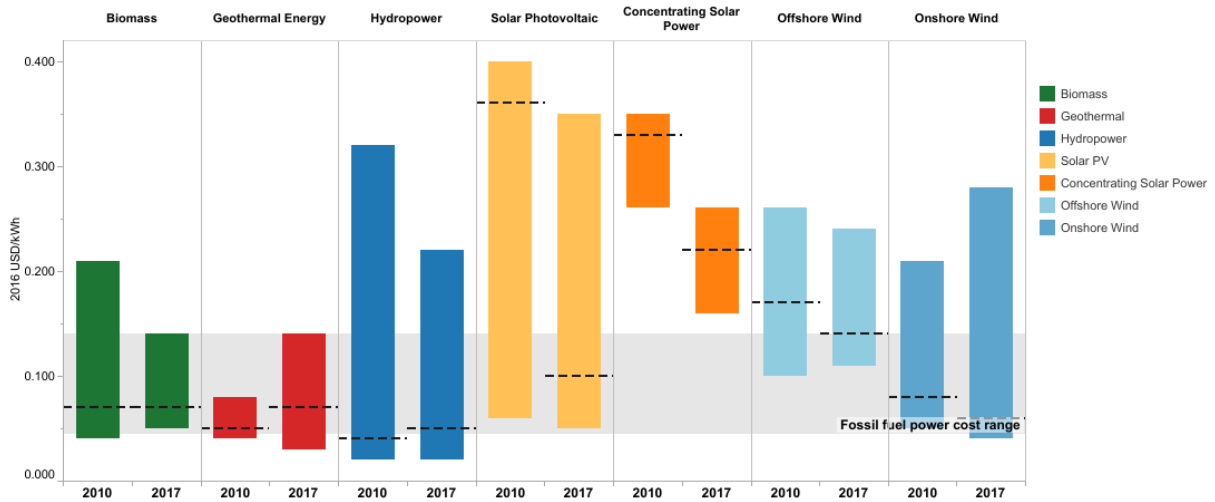


Figure 4. LCOE for renewable energies displaying the mean, minimum and maximum cost in USD/kWh (IRENA, 2018).

Despite the abundance of solar energy supply, CSP is still on average the most expensive energy source as can be seen in Figure 4. The high LCOE of CSP is a major hindrance to commercialisation of the technology despite the distinct advantages of the technology. The LCOE for CSP systems can be lowered by optimising the technology to achieve higher efficiencies or by reducing the cost of the components through mass production (EIA, 2016). Both routes require extensive research to make CSP more economically competitive.

1.2 Problem statement

Current CSP technology is not economically competitive when compared to fossil fuels. In order to lower the LCOE for CSP, the system efficiencies must be improved. Solar power tower (SPT) CSP plants show promise as the technology has substantial room for improvements. The optimisation of the collectors has been extensively researched. However, the optimisation of receiver designs is not as simple because of the complexity involved with accurate thermal modelling. Design and optimisation of novel receivers can improve thermal efficiencies and reduce the LCOE. In order to optimise the receiver, all aspects of realistic operation must be accurately modelled from the collector field to the receiver.

1.3 Objective

The main objectives of this dissertation are:

- to investigate the fundamentals of SPT receivers;
- research methods used for improving receiver efficiencies; and

- to develop a thermal model for a proposed SPT receiver.

This is achieved by formulating the following sub-objective:

- providing a critical analysis of current literature regarding: CSP, SPT, receiver design, SPT receiver modelling, and optimisation methods for CSP receivers.

Based on the literature, further detail on the thermal modelling of a proposed receiver design is presented:

- thermal modelling of the receiver;
- validation of the thermal model;
- investigate the use of swirl with impinging jets for heat transfer enhancements; and
- the use of jet impingement and swirl are investigated with CFD in a realistic application. The CFD model is used to optimise and improve the solar receiver design.

1.4 Overview of the dissertation

Chapter 1 introduces the problem the researcher set out to investigate and provides an overview of the threat of global warming, emphasising the need for improvement of CSP technologies to reduce greenhouse gas emissions. Different renewable energies are discussed and the potential for CSP is highlighted.

Chapter 2 of the report is a literature survey. Literature describing CSP is presented with a focus on SPT systems. The potential for improving SPT technology and the major components of SPT systems is discussed. Multiple receiver types and configurations are presented for SPT systems and a proposed novel receiver design is described. The use of impinging jets and swirl to enhance heat transfer are discussed with literature. Finally, literature on optical modelling, thermal modelling and optimisation methods used for CSP receivers are discussed.

Chapter 3 elaborates on the thermal modelling. Jet impingement heat transfer (JIHT) is discussed in detail and the application of CFD for JIHT is described. CFD is used to simulate JIHT and compare the numerical results to the experimental results. The application of swirl for JIHT is investigated and validated for experimental cases with different modelling complexities.

Chapter 4 conducts CFD simulations on a novel JIHT arrangement for a receiver application. Swirling impinging jets are investigated for concave impingement surfaces. A sensitivity study is conducted for

the proposed receiver absorbing surface. From the sensitivity study an optimisation study is conducted to improve the receivers' design.

Chapter 5 considers a realistic collector field heat flux on the receiver. A realistic heat flux and local radiation effects are considered for the cone absorbing surface model. The effect of swirl for a realistic heat flux is investigated for enhancing heat transfer.

Chapter 6 concludes the dissertation. A summation of the investigation and the results are presented. Conclusions are made for the investigation and recommendations are made for future work.

2 LITERATURE REVIEW

2.1 Introduction

The purpose of this chapter is to present the literature study conducted on CSP systems and jet impingement. The literature study begins by presenting an overview of CSP. Thereafter, the investigation scope is narrowed to SPT systems. JIHT is then discussed for the presented application. Swirl flow phenomena are introduced to the reader for heat transfer enhancement. The literature study section is concluded with numerical modelling methods applicable to the study. A proposed receiver design is described followed by a discussion of the numerical modelling and optimisation methods of SPT receivers from literature.

2.2 Concentrated Solar Power

To address the shortcomings of current solar PV energy systems, CSP shows promise. CSP can provide energy conversion on a utility scale and store the thermal energy efficiently (Ellabban *et al.*, 2014; Islam *et al.*, 2018; Kuravi, Trahan, Goswami, Rahman & Stefanakos, 2013). Energy storage is a major issue, if not the limiting factor, for other renewable technologies. With CSP no intermediate steps are required for an inexpensive reliable energy storage system.

CSP power plants generate electricity using sunlight as the energy source. The CSP plant is made up of various parts that form the solar field, the thermal energy storage (TES) unit, the solar receiver, the power block (where thermal energy is converted to electrical energy), and the backup power system (Kuravi *et al.*, 2013). A depiction of a flow diagram for a CSP power plant is presented in Figure 5.

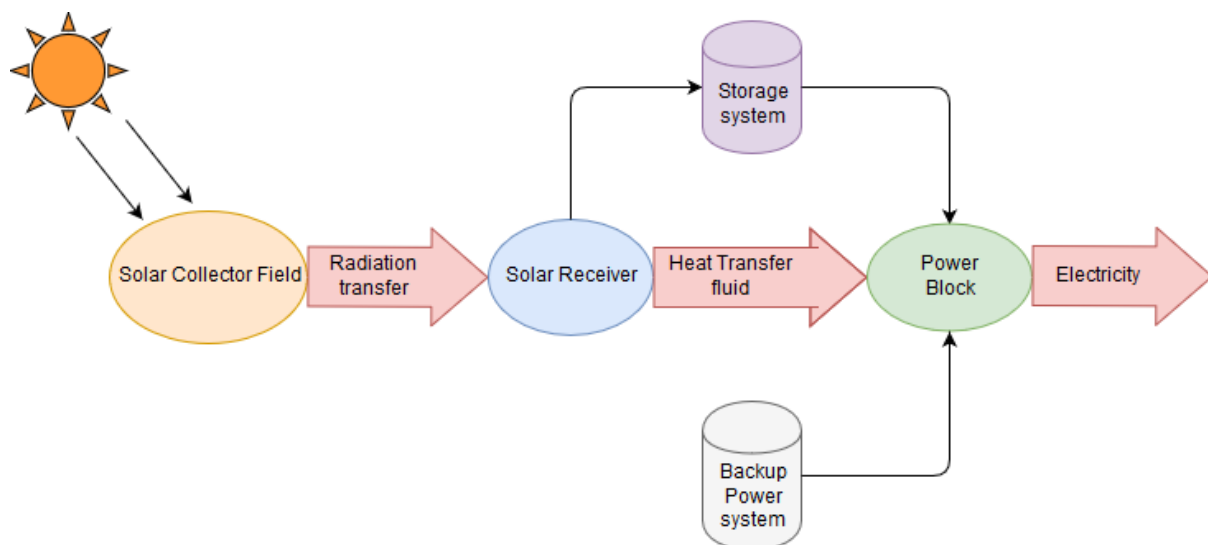


Figure 5. CSP power plant energy flow diagram.

CSP refers to the technologies that use optics to concentrate sunlight (collector) onto the receiver. The receiver can be described as a heat exchanger in which the thermal energy from the incoming concentrated sunlight is transferred into a HTF. The HTF is then commonly used in a power cycle as a heat source to generate electricity and the additional energy can be stored for future use (Stine & Geyer, 2001).

With CSP technologies, higher concentration ratios can be achieved by increasing the operational temperature of HTF. This is beneficial in many industrial applications and improves the thermal efficiency of the technology (Fuqiang, Ziming, Jianyu, Yuan, Yong & Linhua, 2017). Utilising smaller areas can reduce the thermal losses (convective and conductive) of the system and further improve the thermal efficiency. The operational temperature and heat losses are dependent on the type of system used, and it is useful to classify the different CSP technologies.

2.3 Concentrated solar power concentrator types

There are numerous types and configurations for CSP technologies based on the receivers and concentrators. The concentrators can be classified into four main categories based on the focus geometry and receiving technology namely: parabolic trough collector (PTC), SPT, linear Fresnel collectors (LFC), and solar parabolic dish (SPD) concentrators. The configurations for each type are depicted in Figure 6. A summary of the different CSP technologies and their characteristics is presented in Table 2.

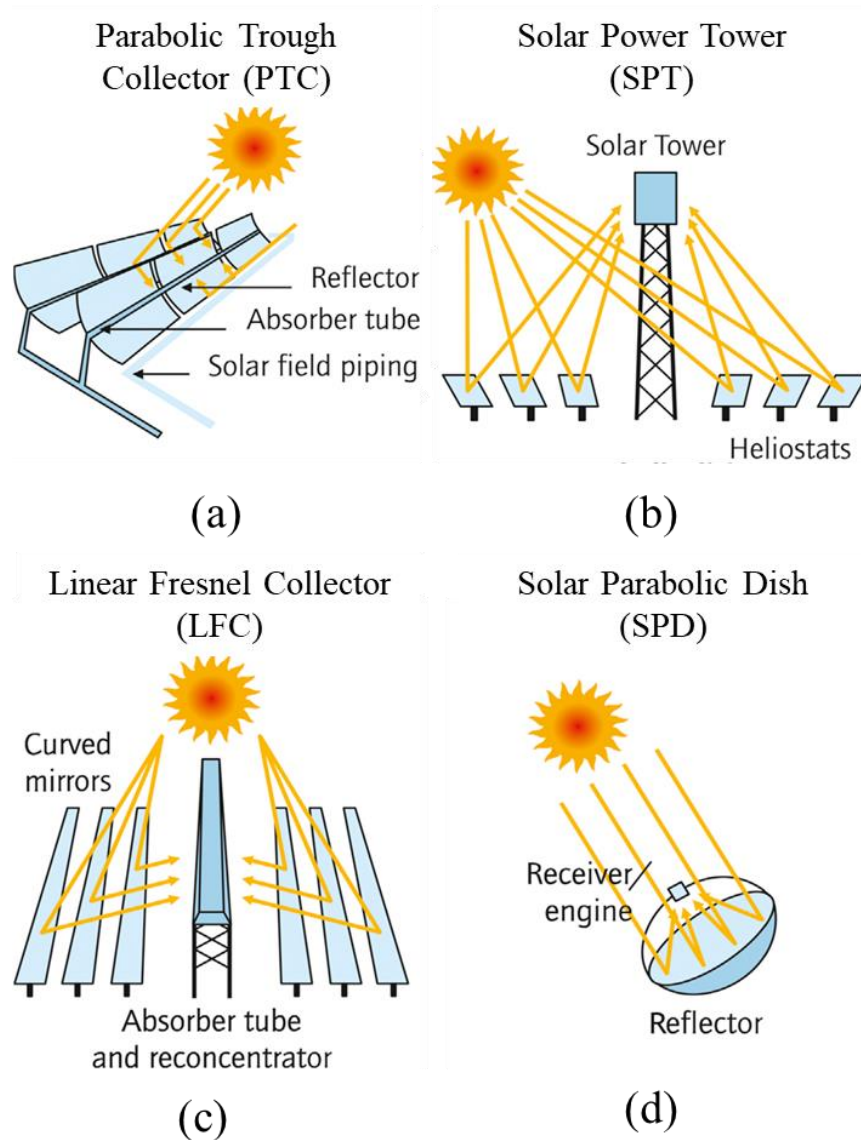


Figure 6. Solar concentrator configurations: parabolic trough concentrator, solar power tower, linear Fresnel reflector and solar parabolic dish (Fuqiang *et al.*, 2017).

The PTC, depicted in Figure 6 (a), is a line-focus concentrator that makes use of large mirrors, in the shape of a parabola, to reflect solar radiation onto a receiver. The receiver is typically a metal absorption tube that is coated to increase absorptivity and reduce heat losses (Islam *et al.*, 2018). A HTF such as molten salt, water or a synthetic oil flows within the metal tube and absorbs the focused radiation heat (Fuqiang *et al.*, 2017).

The SPD concentrator, depicted in Figure 6 (d), is a point-focus technology with two-axis tracking. The concentrator surface is a parabolic highly reflective dish that reflects incoming solar radiation onto a receiver at the focal point (Stine & Geyer, 2001). The parabolic dish surface is usually constructed out

of aluminium or silver with a glass or plastic coating (Islam *et al.*, 2018). The receiver powers an efficient power conversion system such as a Stirling or Brayton engine.

LFCs, depicted in Figure 6 (c), consist of several flat mirrors which reflect solar radiation onto a receiver. LFC is a line-focus technology with single-axis tracking. The receiver is normally a downward facing cavity with absorber tubes inside containing the HTF (Müller-Steinhagen & Trieb, 2004). The HTF absorbs the solar radiation as heat and is used as the heat source for a conventional power cycle (Islam *et al.*, 2018).

SPT technology, depicted in Figure 6 (b), is a point-focus technology. It consists of a central tower with a receiver that is surrounded by a circular or semi-circular array of reflective mirrors that track the sun (heliostats) (Stine & Geyer, 2001). The reflectors are typically mirrors that have two-axis tracking mechanisms. The receiver used will depend on the requirements of the design but is usually made of steels and ceramics that are stable at high temperatures (Sani, Mercatelli, Sansoni, Silverstroni & Sciti, 2012). The receiver is a heat exchanger where the solar radiation is absorbed by the HTF and is used as the heat source of a conventional power cycle (Islam *et al.*, 2018). SPT technology is the primary focus of this research and SPT is discussed in detail in section 2.4.

Table 2. Characteristics of CSP technologies adapted and updated from Ardekani (2017), Cavallaro (2009), Fuqiang *et al.* (2017), Islam *et al.* (2018), Müller-Steinhagen and Trieb (2004), SolarPaces (2018), Ummadisingu and Soni (2011), and Vashishtha (2012).

	PTC	LFC	SPT	SPD
Capacity (MWe)	10-200	10-200	10-150	0.01-0.5
Concentration ratio	25-100	70-80	300-1000	1000-3000
Solar efficiency max	20% (expected)	21% (demonstrated)	20% and 35% (expected)	29% (demonstrated)
Annular solar to electric efficiency (%)	15	8-10	20–35 (concepts)	20–35
Optical efficiency	Medium	Low	Medium	High
Collector concentration	70–80 suns	> 60 suns (depends on secondary reflector)	>1000 suns	>1300 suns
Receiver	Attached to collector, moves with collector, complex design	Fixed absorber, no evacuation, secondary reflector	Fixed external or cavity receiver	Absorber attached to collector and moves with collector
Area required (m^2/MWh)	4-6	6-8	8-12	30-40
Thermal efficiency (%)	30-40	8-10	30-40	30-40
Plant peak efficiency (%)	14-20	~18	23-35	~30
Capital cost (US\$/kW)	3972	-	4000+	12,578
Capital cost (US\$/$m^2$)	424	234	476	-
Operation and Maintenance cost (US\$/kWh)	0.012-0.02	low	0.034	0.21
Basic plant cost (US\$/W)	3.22	-	3.62	2.65
Levelized cost of electricity (US\$/kWh)	0.26–0.37 (no TES) and 0.22–0.34 (with TES)	0.17–0.37 (6 h TES)	0.2–0.29 (6–7.5 h TES) and 0.17–0.24 (12–15 h TES)	-
Land use ($m^2/MWh/year$)	6-8	4-6	8-12	8-12
Specific power (W/m^2)	300	-	300	200

	PTC	LFC	SPT	SPD
Site solar characteristics/solar radiation required	For commercial viability DNI >2000-2800 kWh/m ² /year, however, it can be argued that DNI >1800 kWh/m ² /year is suitable for CSP development (Vishishtha, 2012).			
Land requirements	Large	Medium	Medium	Small
Typical shape of solar plant	Rectangular	Rectangular	Circular or polar semi-circular	Rectangular
Water requirements (m³/MWh)	3 (wet cooling), 0.3 (dry cooling) and 0.4–1.7 (hybrid)	3 (wet cooling) and 0.2 (dry cooling)	2–3 (wet cooling), 0.25 (dry cooling) and 0.3–1 (hybrid)	0.05–0.1 (mirror washing)
Storage with molten salt	Commercially available	Possible, but not proven	Commercially available	Possible, but not proven
Operational temperature of solar field (°C)	290-550, 820 for pressurised gasses	250-390, up to 560 is possible	250-650	800
Annual capacity factor (%)	25–28 (no TES), 29–43 (7 h TES)	22-24	55 (with 10 h storage)	25-28
Grid stability	Medium to high (TES or hybridisation)	Medium (back-up firing possible)	High (large TES)	Low
Power block cycle and fluid conditions	Superheated steam Rankine, steam @380 °C/100 bar	Saturated steam Rankine (steam @ 270 °C/55 bar), superheated steam Rankine (steam @ 380 °C/50 bar)	Superheated steam Rankine, steam @ 540 °C/100–160 bar	Stirling/Brayton
Possible backup/hybrid mode	Yes	Yes	Yes	Yes, limited to specific cases
Storage possibility	Yes, but not for direct steam generation	Yes, but not for direct steam generation	Depends on the plant's configuration	Depends on the plant's configuration
Storage system	indirect 2-tank molten salt at 380 °C ($\Delta T = 100$ °C) or Direct 2-tank molten salt at 550 °C ($\Delta T = 300$ °C) 14h TES	Short-term pressurised steam storage (< 10 min)	Direct 2-tank molten salt at 550 °C ($\Delta T = 300$ °C)	No storage, chemical storage under development

	PTC	LFC	SPT	SPD
Heat Transfer Fluid	Synthetic oil, water/steam (DSG), molten salt (demonstration), air (demonstration)	Water/steam	Water/steam, molten salt, air (demonstration)	Air, hydrogen, helium
Development Status	Most Proven	Demonstration	Mature	Demonstration
Technology development risk	Low	Medium	Medium	Medium
Outlook for improvement	Limited	Significant	Very significant	Through mass production

2.4 Solar power tower history

The first concept of concentrating sunlight that is documented started with Archimedes in 214-212 BC. It was thought of as a defence mechanism to concentrate sunlight onto enemy ships, setting them on fire. The concept of concentrating sunlight onto a target is both simple and brilliant. It took the rest of the world hundreds of years to finally grasp the potential of this idea. Archimedes' idea was later validated by Dr. Ioannis Sakkas who set a Roman galley replica aflame from 165 feet away using bronze shields (Africa, 1975).

The concentration of sunlight is now used in a variety of ways, such as for utility-scale electricity generation. The first mention of a SPT concept was in the 1940's. The original concept was to use flat mirrors to focus sunlight onto a central boiler, placed on a tower. This first boiler system had no tracking and each individual mirror had to be adjusted separately. This idea sparked a path to the development of SPT technologies. The first test SPT was constructed in 1968 by Professor Giovanni Francia. The test plant was able to produce 1 MW of power with superheated steam (Butti & Perlin, 1980). The 1970's oil crisis was only a catalyst for the development of SPT technology leading to an urgent need for alternative energies. As a result, in the 1980's the first experimental plants were constructed.

For commercial SPT systems globally, early central receivers were mainly direct steam generation receiver systems but with the need for storage, newer plants use molten salt as the HTF. In 2018 across the globe there was a gross installed capacity for SPT plants of 618 MW (IRENA, 2018). The first commercial SPT system was the Solar One facility in California, which was operational between 1982-1986. The Solar One plant is a 10 MW plant located in the Mojave Desert (SolarPaces, 2018). The largest plant in the world is the Ivanpah Solar Power Facility, which is also located in the Mojave Desert. The Ivanpah plant generates 377 MW net electricity, using three towers and three surround fields (SolarPaces, 2018). The Ivanpah power plant uses a steam Rankine cycle at 160 bar to produce electricity. The size of the plant spans 3500 acres and the construction of the plant cost approximately $\$1.2\text{ billion USD}$. A photograph of one, of the three, Ivanpah central towers is depicted in Figure 7.



Figure 7. One of the 139.9m tall Ivanpah central towers (Dieterich, 2018).

After the initial development of steam-based receivers, molten salt receivers became popular. Depicted in Figure 8 (a), is the Crescent Dunes molten salt SPT plant. This SPT plant was commissioned in 2016 and it provides 110 MW net generation, powering 75 000 homes in Nevada. The solar field consists of 10 347 tracking heliostats spanning over 1600 acres. The power plant has 1.1 GW of two tank indirect storage capacity that can supply 10 hours of full load demand (SolarPaces, 2018). Figure 8 (b) depicts the Planta Solar (PS) 10 SPT plant of Seville, Spain. The PS10 plant is the first utility scale CSP plant using steam as the HTF, commissioned in 2007. The plant has a net capacity of 11MW with one hour of storage capability. The project was started by Abengoa Solar in 2005, and the heliostat field occupies 55 hectares (SolarPaces, 2018).



(a)



(b)

Figure 8. (a) Crescent Dunes 110 MW molten salt SPT plant with surround field (SolarReserve, 2015). (b) PS10 10 MW saturated steam SPT plant with polar field configuration (The Highlanders, 2013).

The interest in molten salt receiver technology is due to the higher operational temperatures that can be achieved, and molten salt can be used directly as the storage medium. The efficiency of the entire plant is dependent on the concentration ratios achieved and the operational temperature of the receiver.

2.4.1 The push towards higher operating temperatures

Currently, the commercial SPT receivers operate at temperatures between 250 – 650°C. To improve the thermal-to-electric efficiency of the receiver, the operational temperature must be increased. The increase of the operational temperature inadvertently results in higher thermal radiation and convective heat losses (Ho, 2017; Steinfeld & Schubnell, 1993). The thermal-to-electric efficiency (η_{el}) and the solar-to-thermal efficiency (η_{th}) are calculated using equations (1) and (2) respectively.

$$\eta_{el} = 0.7\eta_{carnot} = 0.7\left(1 - \frac{T_c}{T_h}\right) \quad (1)$$

$$\eta_{th} = \alpha - \frac{\varepsilon\sigma T_{receiver}^4 + h(T_{receiver} - T_{surr})}{\eta_{optical}G_{DNI}CR} \quad (2)$$

where η_{carnot} is the Carnot efficiency, T_c is the absolute temperature of the power cycle cooling source in Kelvin (K), T_h is the absolute temperature of the power cycle heating source in Kelvin (K), α is the absorbance of the material, ε is the materials emissivity, σ is the Stefan Boltzmann constant ($\sigma = 5.67 \times 10^{-8} W/m^2K^4$), h is the average heat transfer coefficient over the surface (W/m^2K), $\eta_{optical}$ is the optical efficiency, $T_{receiver}$ is the absolute temperature of the receiver in Kelvin (K), T_{surr} is the absolute temperature of the surroundings in Kelvin (K), CR is the concentration ratio, and G_{DNI} the direct normal incident solar radiation on the receiver(W/m^2). The thermal-to-electric efficiency (η_{el}) and the solar-to-thermal efficiency (η_{th}) are depicted as a function of temperature at different concentration ratios in Figure 9 (a) and Figure 9 (b) respectively.

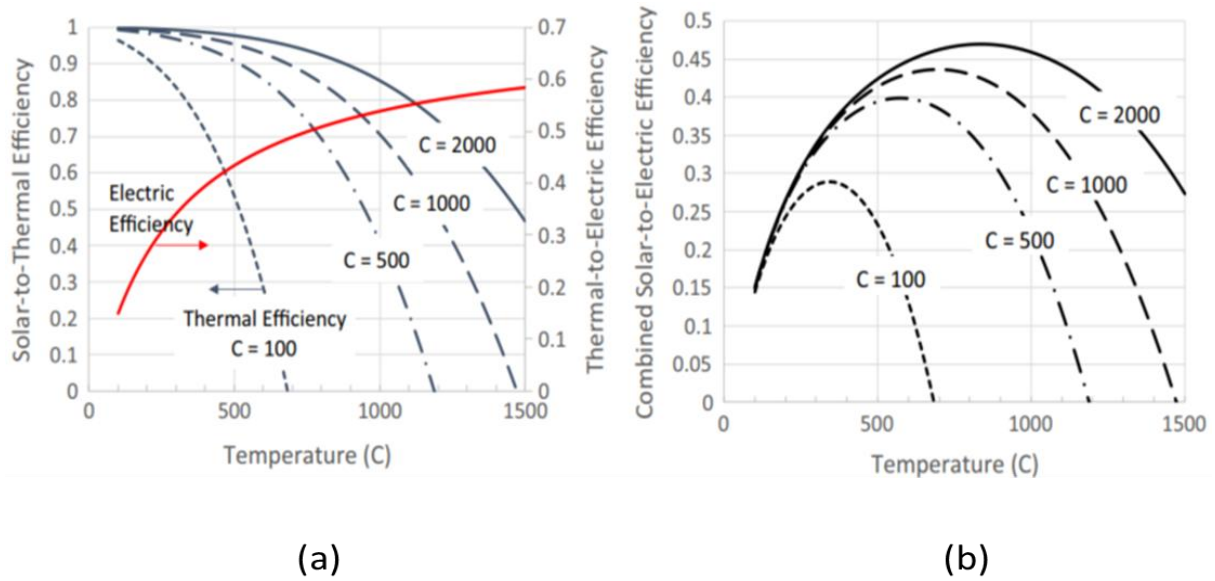


Figure 9. (a) The solar-to-thermal efficiency (η_{th}) and thermal-to-electric efficiency (η_{el}) as a function of temperature at different concentration ratios (Ho, 2017). (b) The combined efficiency (η_{tot}) as a function of temperature at different concentration ratios (Ho, 2017).

As the temperature increases the combined efficiency of the system also increases. However, at a critical temperature, the convective and radiative losses will become more significant, resulting in a decrease in the combined efficiency of the system, depicted in Figure 9 (b). Therefore, for each system an optimal temperature exists (Ho, 2017). The SPT receivers can achieve higher concentration ratios; however, the peak flux is limited based on the HTF. In order to use high temperature central receivers, there is a need to improve materials, HTFs, receiver optimisation and all processes that maximise solar radiation absorptance and minimise thermal losses. Each of the subcomponents can be investigated and optimised but the interaction between these components must first be understood.

2.5 Collector

The collector subsystem consists of all the parts that intercept the solar radiation and reflect the solar radiation onto the central tower's receiver. The collector is made up of the heliostat fields continuously tracking the sun. The heliostat field form the largest capital cost, 30 – 50%, of the SPT system and can significantly influence the performance of the system (Li, Coventry, Bader, Pye & Lipiński, 2016). Up to 40% of total energy losses are attributed to the collector subsystem, therefore the design and layout need to be optimised, to reduce capital costs and improve efficiency (Kreith & Goswami, 2007).

2.5.1 Heliostat field

The heliostat field is the main component of the collector subsystem. The heliostat is the basic tracking reflector that are arranged in an efficient arrangement to collectively form the heliostat field.

The heliostat itself is made up of several major components: the reflector (a mirror module consisting of several smaller mirrors), the supporting structure, and the actuation system (Li *et al.*, 2016). The reflector typically is made up of a silvered glass mirror or a reflective polymer coated metal membrane (Li *et al.*, 2016). Each mirror module usually has a slight concave curvature to improve the focus of the solar radiation and improve the optical efficiency (Behar, Khellaf & Mohammedi, 2013). The mirrors are supported by the beam support that continuously move to track the sun and aim the reflected sunlight at the solar receiver.

The heliostat field configuration and layout are based on a cost and performance trade-off to minimise the cost to annual collection efficiency (Wei, Lu, Lin, Zhang & Ni, 2008). The configurations used are the polar and surround field layouts, the arrangements are how the heliostats are arranged locally within the selected configuration usually radially staggered or in a cornfield arrangement (Falcone, 1986). Both configurations and arrangements are depicted in Figure 10.

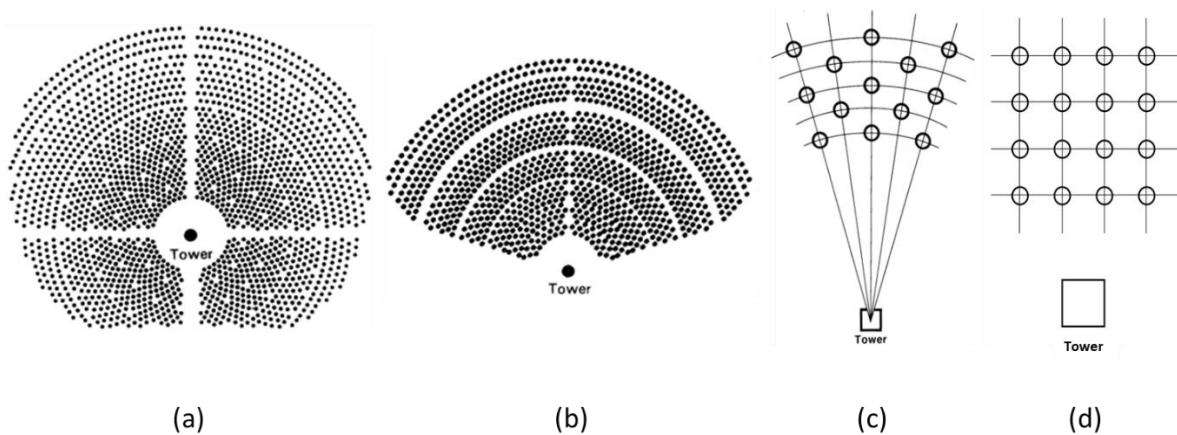


Figure 10. (a) Surround field heliostat configuration. (b) Polar field heliostat configuration. (c) Radial stagger heliostat field arrangement. (d) Cornfield heliostat field arrangement.

In the surround field configuration, the heliostats are placed 360° around a centrally located tower, depicted in Figure 10 (a). The tower is not directly in the centre of the field but is offset to the north or south of the centre, based on the location of the plant. The offset improves the efficiency of the field by reducing the cosine losses (Falcone, 1986). Surround field configurations are used for external receivers.

In a polar configuration, all of the heliostats are located to one side of the power tower, Figure 10 (b). Typically, the polar field heliostats are in a 90° field arrangement. In the polar configuration the heliostats are all situated on the north side or south side of the receiver based on whether the plant is in the northern or southern hemisphere (Falcone, 1986). Polar field configurations are used for cavity receivers due to the limited acceptance angle (Li *et al.*, 2016).

2.5.2 Collector performance

The optical efficiency and the concentration ratio describe the performance of the heliostat field. The optical efficiency is the ratio of net power intercepted by the receiver to the total power intercepted by the heliostat field. The optical efficiency of the plant not accounting for losses can be described by equation (3).

$$\eta_{optical} = \frac{\int_{t_i}^t Q_{receiver} dt}{G_{DNI} A_{collector} \Delta t} \quad (3)$$

where G_{DNI} the direct normal incident solar radiation on the receiver, $A_{collector}$ is the total area of the collector field, $Q_{receiver}$ is the heat flux on the receiver surface (W) and Δt is the difference between the time t and the initial time t_i . The actual optical efficiency accounts for cosine losses, reflective losses, blocking, shadowing, atmospheric transmission, and receiver spillage. The optical loss mechanisms are depicted in Figure 11.

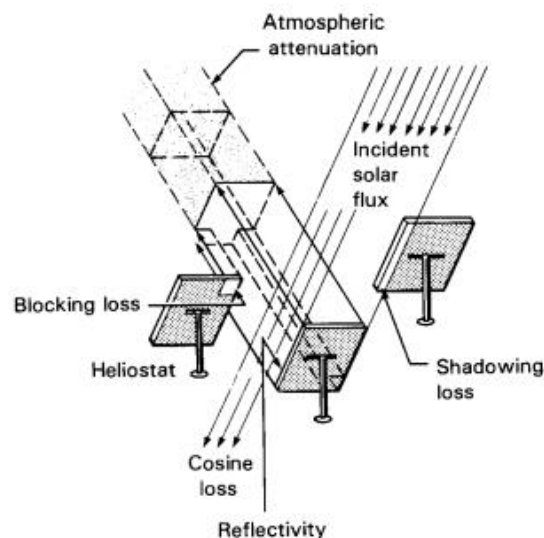


Figure 11. Schematic of optical loss mechanisms (Falcone, 1986).

The net efficiency of the plant includes the optical and thermal efficiencies. The actual optical efficiency is presented in equation (4) described by all the optical loss efficiencies.

$$\eta_{optical} = \eta_{reflection}\eta_{cosine}\eta_{blocking}\eta_{spillage}\eta_{shading}\eta_{atmosphere} \quad (4)$$

The cosine losses are due to the ratio of projected mirror area perpendicular to the solar radiation rays to the total area of the heliostat. Some of the solar radiation that is reflected by the heliostat will be absorbed and scattered by the atmosphere, this is referred to as the atmospheric attenuation loss. The atmospheric attenuation is influenced by the size of the heliostat, the size of the sun, and heliostat surface irregularities which may cause in non-uniform heat flux distributions on the receiver (Chen, Kirbus, Lim, Lim, Chong, Karni, Buck, Pfahl & Bligh, 2004; Li *et al.*, 2016). The portion of solar radiation not intercepted by the receiver is the spillage loss. Blocking losses are due to the sunlight being intercepted by objects between the reflector and receiver. Shadowing losses are due to blocking of incident sunlight not being reflected by the receiver as they do not reach the reflective surface (Falcone, 1986; Li *et al.*, 2016). The optical efficiency of the PS10 is approximately 67.5% which is broken down as 84.4%, 96.6%, 88%, 99.1%, 99.4%, and 95.5% for cosine, shading, reflection, blocking, spillage and atmospheric attenuation efficiencies (Rinaldi, Binotti, Giostri & Manzolini, 2014).

The concentration ratio can be given two common definitions (Baig, Sarmah, Heasman & Mallick, 2013; Calise & Vanoli, 2012). The geometric concentration ratio is the ratio of the receiving aperture area to the ratio of the collector total area. The concentration ratio is the ratio of area averaged radiation on the receiver's aperture compared to the total energy collected DNI on the concentrator's aperture. In practice, the concentration ratios achieved by various technologies and the achievable operational temperatures are presented in Table 2. The concentration ratio and operational temperatures will influence the SPT receiver design.

2.6 Solar power tower receiver

The receiver design and the heliostat field layout are inherently coupled, as the receiver must be designed to accept the highest possible solar flux from the collector. An advantage of SPT technology is the potential to reach higher concentration ratios and achieve greater efficiencies than line focus technologies. However, there is a need to improve the receiver design to reduce thermal losses and optimise the design of the receiver (Ho, 2017; Steinfeld & Schubnell, 1993).

The receiver is the subsystem that intercepts the concentrated solar radiation and transfers the energy into the HTF. The receiver is mounted at the top of the solar tower. The principle components of the receiver are the absorbing surfaces, receiver structure and the HTF. The design of the receiver needs to consider all the principle components.

The performance of the receiver is described in section 2.6.1. The SPT receiver design can be either of external or cavity type, further discussed in section 2.6.2. The HTF and specific receiver designs for gas, solid media and liquid HTF are discussed in sections 2.6.3. Other, more recently developed receivers are further discussed in section 2.9.

2.6.1 Receiver performance

The performance of the receiver depends on the design requirements. The design is usually a trade-off amongst different loss mechanisms. The loss mechanisms experienced by the receiver is depicted in Figure 12.

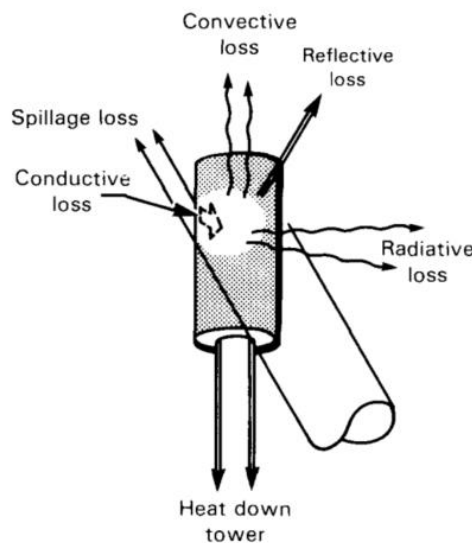


Figure 12. Schematic of heat loss mechanisms for the SPT receiver (Falcone, 1986).

Receiver heat losses

Spillage loss refers to the loss of energy not intercepted by the receiver absorption surface from the heliostat field. Spillage loss is typically due to receiver sizing trade-offs or heliostat aiming errors. Spillage loss is usually low and accounts for up to 5% of the energy reaching the receiver (Falcone, 1986).

Solar radiation reflected from the heliostat field is scattered and reflected by the receiver surface and the energy is lost to the environment as reflective losses. In order to reduce the reflective losses, materials with a high absorptivity are used as the absorbing surface or the surfaces are coated with a high absorptivity paint. Reflective loss is typically only 5% or less (Falcone, 1986).

The conductive heat losses are the heat losses through the insulation and the structural components of the receiver. Conductive heat losses typically are less than 1% for well-insulated receivers (Falcone, 1986). Convective heat loss is the heat lost to the air adjacent to the receiver. The convective heat losses can be natural or forced convection depending on the presence of wind (Falcone, 1986).

Radiative losses are due to the emission of electromagnetic waves from a surface above 0K. These are heat losses by infrared and visible light due to the elevated temperature of the receiver. The radiative losses scale the most with the operational temperature of the receiver and can be the most dominant loss mechanism at high temperatures (Asselineau, 2017; Falcone, 1986; Steinfeld & Schubnell, 1993).

Heat absorbed by heat transfer fluid

Heat absorbed by the HTF is the primary mechanism of heat transfer within the receiver and is due to internal forced convection from the flowing HTF. The HTF is used to drive the power block to generate electricity, therefore, the efficient absorption of heat by the HTF is the driving force behind receiver design along with minimising heat losses. The heat absorbed by the HTF is described by equation (5).

$$\dot{Q}_{HTF} = \dot{m}_{HTF} c_{p,HTF} (T_{e,HTF} - T_{i,HTF}) \quad (5)$$

where \dot{m}_{HTF} is the mass flow rate of the fluid (kg/s), $c_{p,HTF}$ specific heat of the HTF (J/kgK), and T_e and T_i are the exit and inlet temperatures of the HTF respectively (Çengel & Ghajar, 2015).

Thermal efficiency

The thermal efficiency of the receiver is the ratio of useful thermal energy extracted, to input energy the concentrated solar radiation on the receiver. The thermal efficiency of the receiver can be described by equation (6).

$$\eta_{th} = \frac{\dot{Q}_{useful}}{\dot{Q}_{in}} = \frac{\dot{Q}_{in} - \dot{Q}_{losses}}{\dot{Q}_{in}} \quad (6)$$

where \dot{Q}_{losses} describes the thermal losses, which is the sum of the previously mentioned losses, \dot{Q}_{in} is the energy input for the receiver and is described in equation (7).

$$\dot{Q}_{in} = \int_{t_i}^t \int_0^A G_{incident}(t) dA dt \quad (7)$$

where $G_{incident}(t)$ is the incident radiation that varies with time. As the goal is to maximise the efficiency the collector and receiver, both must be optimised. The available \dot{Q}_{in} is dependent on the collector layout and receiver design and often \dot{Q}_{HTF} is considered \dot{Q}_{useful} . Receiver design and configuration affect the losses of the receiver.

2.6.2 Configuration

There is a broad range of receivers to consider. The primary distinction that can be made for the receiver is the configuration of the receiver. The configuration of the receiver is based on the location of the absorbing surface, the distinction can be made between external and cavity receivers. External and cavity receiver schematics are depicted in Figure 13.

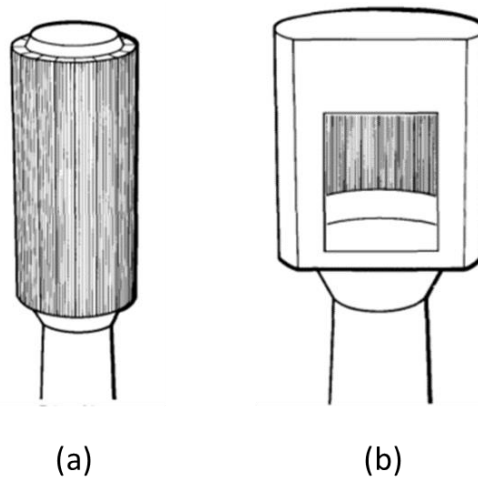


Figure 13. (a) External receiver basic configuration. (b) Cavity receiver basic configuration (Falcone, 1986).

External receivers

External receivers have absorbing surfaces that are exposed to the environment, Figure 13 (a). For external receivers the radiation absorption heat transfer to the working fluid and thermal losses occur over the same surfaces (Li *et al.*, 2016). Typically, external receivers use flat, billboard, or convex surfaces facing towards the heliostat field. For large scale SPT systems a multi-paneled polyhedron

shapes resembling a cylinder form the absorbing surface. Smaller SPT systems use either billboard or a partially cylindrical receiver arrangements (Falcone, 1986).

Cavity receivers

Cavity receivers are receivers where the absorbing surfaces are not directly exposed to the environment but rather the concentrated solar radiation is passed through a limited area referred to as the aperture. After the concentrated solar radiation passes through the aperture it enters a box-like structure, onto the absorbing surface. The box-like shape, housing the absorbing surfaces, is referred to as the cavity. The aperture and geometry of the cavity are designed to minimise thermal losses of the system. The cavity is then insulated to reduce losses and provide protection from the environment (Falcone, 1986). A prototypical design of a cavity receiver is depicted in Figure 13 (b).

Cavity receivers versus external receivers

Radiative losses are higher for external receivers due to higher view factors to the environment. Due to the higher view factor of external receivers, the reflective losses are also higher than cavity receivers. External receivers' operational temperatures are usually limited to below 1000K. External receivers have the practical advantages of lighter supporting structure, simple maintenance, and reduced atmospheric losses due to a lower mean distance of the heliostats to the receiver (Li *et al.*, 2016). For cavity receivers the aperture area is limited, and this results in higher spillage losses. Cavity receivers also require a larger absorbing area than external receivers due to a more non-uniform solar flux on the absorbing surfaces. Cavity receivers do have a high associated cost due to the number of components required compared to external receivers. Cavity receivers have been shown to be 10% more efficient than an external receiver with a polar field configuration (Falcone, 1986). The receiver configuration will dictate the requirements of the HTF. The HTFs available can be described as liquid, gas or solid media.

2.6.3 Receiver heat transfer fluids

There is an abundance of HTFs/mediums that can be used for solar tower receivers with unique properties that are advantageous for heat transfer and practical implementation in the solar industry. Typically, the HTFs/mediums used for central receivers are liquids, gases and solid particles. Considering the heat transfer medium there are trade-offs that must be made for the design.

Liquid-based receivers

Liquid-based receivers use a HTF that is in a liquid form at elevated temperatures. Liquids are used because of higher thermal conductivities compared to gases and the stage capabilities of liquids. Liquid-

based receivers typically use tubes that the solar radiation is focused on, to heat the HTF. The HTF used is usually water, molten salt and liquid metals.

Water and direct steam generation central receivers were the first receivers used and have been commercially proven. These receivers have low exergy losses due to the direct generation of steam without an additional heat exchanger, the limitation is the difficulty of storing the high-pressure steam (Ho, 2017; Kuravi *et al.*, 2013).

Currently molten salt receivers use a solar salt, a eutectoid mixture of ~60% sodium nitrate ($NaNO_3$) and ~40% potassium nitrate (KNO_3). Molten solar salt receivers are limited to operating temperatures of up to 600°C due to corrosion and decomposition of the salt (Bradshaw & Carling, 1987). A drawback of molten salts is that the fluid's freezing temperature is approximately 200°C, and this may lead to issues if the HTF solidifies in the system (Ho, 2017). Due to the limitations of solar salts, other HTFs are being investigated, such as halide salts and carbonate salts. Halide salts, based on chlorides and fluorides, have higher decomposition temperatures up to 800°C and show less corrosion at higher temperatures (Gomez-Vidal & Tirawat, 2016). Fluoride-based halide salts are stable at high temperatures of 850°C and fluoroborate salts are the most economical of the salts (Forsberg, Peterson & Zhao, 2007).

For HTFs that operate at temperatures above 700 °C liquid metals such as liquid sodium, lead bismuth and tin have been investigated. Liquid sodium has a high thermal conductivity which can allow for higher solar fluxes on the receiver and higher thermal stresses (Coventry, Andraka, Pye, Blanco & Fisher, 2015). Lead bismuth has been evaluated as a HTF due to its high boiling temperature of ~1600°C and a heat capacity larger than sodium but lower than solar salt (Benoit, Spreadfico, Gauthier & Flamant, 2016).

For high temperature liquid receivers, nickel-based alloys and ceramics are used for absorbing surfaces. Nickel-based alloys are used in tubular receivers because they maintain strength at temperatures above 700 °C and have high corrosion resistances (Gomez-Vidal & Tirawat, 2016; Vignarooban, Xu, Wang, Molina, Li, Gervasio & Kannan, 2015). Ceramic (silicon carbide) materials exhibit high strength, high thermal conductivity, low thermal expansion, and high solar absorbances. These carbides have melting temperatures of above 2500 °C, making them an attractive material for high temperature receivers (Sani *et al.*, 2012). Tubular designs are the most common where the HTF is contained within tubes and the tubes are heated by the concentrated solar radiation. Other designs are liquid film receivers. Liquid film receivers use gravity-driven flow for the HTF. There are two types of falling film receiver's namely, direct exposure and indirect exposure receivers. With direct exposure receivers, the fluid flows down

an external inclined wall that is illuminated by solar radiation. The issue with direct exposure receivers is the effect of the wind on the falling film resulting in unstable conditions and fouling of the fluid. Demonstrations of direct exposure receivers achieved 80 – 90% thermal efficiencies at temperatures of ~700 °C (Wu, Gobereit, Singer, Amsbeck & Pitz-Paal, 2011). Indirect or internal liquid film receivers reduce wind effects with the fluid flowing on the internal wall of the receiver. Internal liquid film receivers have expected efficiencies of ~80% and have the benefit of operating at low pressures (Wu *et al.*, 2011).

Gas-based receivers

The use of central receivers using gases can be advantageous. Gases can be used for high-temperature applications, as they are a low-cost fluid and the gases used can be relatively inert and environmentally friendly (Benoit *et al.*, 2016). Typically, air or super critical carbon dioxide (CO_2), sCO_2 is used as the HTF and the receivers are constructed from ceramics or metals that can operate at high temperatures. The heated gas can be used as a heat source for a Rankine power cycle or directly be used in a Brayton power cycle. The use of gases do have inherent disadvantages namely the low thermal conductivities of the HTF, the lack of storage capabilities, the higher operational pressures required and flow stability considerations.

Solid medium particle-based receivers

Solid medium absorbers use a solid absorber or solid particles as the HTF. Solid media based-receivers use small particles that flow within the receiver design where they are heated by the concentrated solar radiation. The flow arrangement depends on the receiver design and operating principle, designs for solid media based receivers can be found in (Ho, 2017). The particles can reach high operating temperatures (greater than 1000°C), particles are more stable over a higher temperature range, can be stored directly, and eliminate the need of the heat exchanger in the receiver (as the solid particles are heated directly by the solar radiation) (Martinek & Ma, 2015). The heat exchange between the particles and solar radiation have shown to be extremely efficient (between 60 – 90%) (Ho, 2016). The disadvantages of using solid media is the loss of particles in the receiver, control of particle flows, larger convective losses due to air entrainment, possible blockages in the receiver, an uneven heat transfer over absorbing surfaces creating local hot spots and complexity of construction and operations for such systems (Flamant, Hernandez, Bonet & Traverse, 1980; Lee, Lim, Shin, Sadowski, Abdel-Khalik, Jeter & Al-Ansary, 2015; Wu *et al.*, 2011; Wu, Amsbeck, Buck, Waibel, Langner & Pitz-Paal, 2014,).

Summary

A summary of the liquid-based receiver designs, operating conditions, the advantages, and challenges of the liquid-based technologies are presented in Table 3.

Table 3. Summary of liquid-based receivers (Ho, 2016; Ho & Iverson, 2014).

Receiver design	Outlet temperature/ thermal efficiency	Advantages	Challenges/research needs
Steam receivers	650 °C/80 – 90%	Ability to use features and geometry to increase light trapping; low exergy losses (Ho, 2017; Kuravi <i>et al.</i> , 2013).	High-pressure steam requires thicker tubing and more expensive materials, no direct storage; do not operate above 850K (Benoit <i>et al.</i> , 2016).
Molten salt receivers	800 °C(halide salt, carbonate salt) / To be determined	Ability to achieve high temperatures ~700 °C; relatively low cost (halide); does not require controlled purification and pre-melting procedures (carbonate); storage capabilities.	Salt freezes at ~200 °C; requires trace heating; very expensive (carbonate); highly corrosive in the presence of air or water (halide); requires controlled purification and pre-melting in a vacuum.
Liquid metals receiver	> ~1000 °C (<i>lead – bismuth</i>), 530 – 800°C (<i>liquid sodium</i>) / 90%	High thermal conductivity (liquid sodium); very high boiling point (lead-bismuth); higher heat capacity than sodium but less than solar salt (lead-bismuth).	Reacts violently with water and spontaneously ignites in air above 115 °C (sodium); lower thermal conductivity than sodium (lead-bismuth); costs 10 – 20 times more than solar salt (lead-bismuth) (Coventry <i>et al.</i> , 2015) ; very corrosive (lead-bismuth) (Benoit <i>et al.</i> , 2016); no direct storage.

2.6.4 Heat transfer enhancement for solar receivers

The efficiency of heat transfer is a common design problem for any heat exchanger design. For the specific application in the CSP industry, there is a multitude of methods that can be implemented to enhance the receiver's performance. The methods vary and are too broad of a topic to discuss, therefore, the common methods used and novel and unique methods that have shown promise are discussed.

Based on fundamental heat transfer theory the most common ways of increasing heat transfer are to increase the surface area over which heat transfer occurs or manipulate flow conditions to increase turbulence (Çengel & Ghajar, 2015). The increase of surface area can be achieved by using complex geometry, e.g., using fins to increase surface area. For solar receivers when the surface area is manipulated, it can be done in such a way as to allow for high radiation view factors to adjacent heat transfer surfaces reducing radiation losses to the environment (Garbrecht, Al-Sibai, Kneer & Wiegardt, 2013; Sloopweg, Craig & Meyer, 2019). Other works taking advantage of this principle of improving

receiver performance may be found in works of Asselineau (2018), Garbrecht *et al.* (2013), Lubkoll, Von Backström, Harms and Kröger (2015) and Slootweg *et al.* (2019). Selected receivers are further discussed in section 2.9.

The bladed tubular receiver arrangement is where panels of tubes are arranged in horizontal or vertical layers. The bladed configuration allows for the solar radiation to be reflected and trapped in the cavity receiver (Ho, Ortega, Christian, Yellowhair, Ray, Kelton, Peacock & Andraka, 2016). A bladed receiver tubular arrangement is presented in Figure 14.

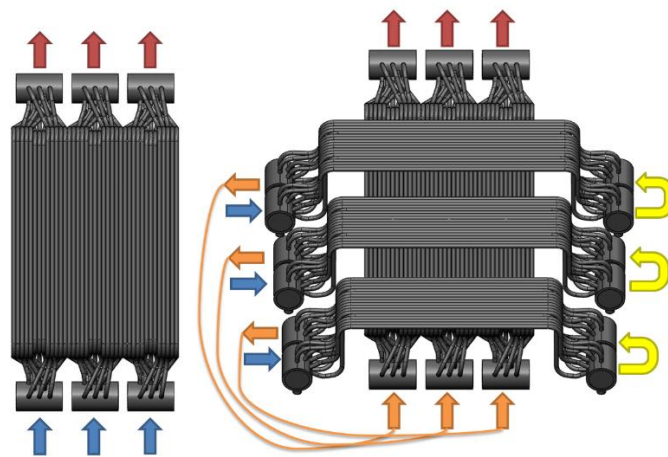


Figure 14. Schematic of a bladed tubular receiver design (Ho *et al.*, 2016).

The heat transfer surface area can be significantly increased for gas receivers using a volumetric receiver. Volumetric receivers consist of a multitude of interlocking porous meshes with specified porosity to absorb heat into the depth of the receiver. The solar radiation is concentrated onto a porous structure, through which the air flows, and is heated by the structure. The volumetric effect causes the temperature of the fluid at the outlet to be higher than the temperature on the absorber side (Ávila-Marín, 2011). The hottest part of the absorber is the aperture, exposed to the environment which may result in higher thermal losses (Ávila-Marín, 2011; Ho, 2017). The disadvantage of using a porous medium is the high-pressure losses due to the flow restrictions. Volumetric receivers are used in a cavity receiver with a quartz glass window when pressurised (Pritzkow, 1991). A depiction of the PLVCR-500 volumetric receiver design is presented in Figure 15.

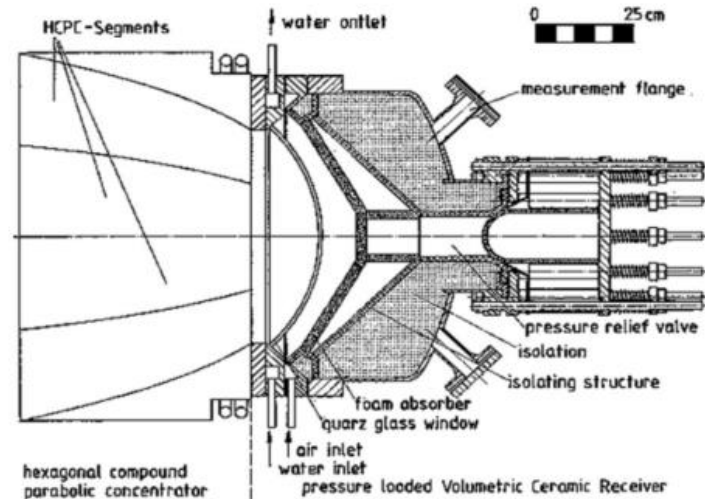


Figure 15. Schematic of the PLVCR-500 volumetric gas receiver (Pritzkow, 1991).

Micro channels are an alternative to increase heat transfer. Microchannel receivers use a channel with a hydraulic diameter of below 1mm . The use of microchannels increase the surface area over which the heat transfer occurs. The microchannels are typically in an enclosed receiver with multiple layers of microchannels. Horizontal quartz tubes are used as the front panel of the receiver to reduce convective and radiative losses (Neber & Lee, 2012). The microchannels can be arranged in arrays of micro channels that can be used as an external receiver surface; this design has the advantage of high thermal efficiencies and the typical advantages of modular designs (Roldán & Fernández-Reche, 2015).

Manipulating the flow of the HTF can result in better heat transfer. By increasing the turbulence in the flow higher heat transfer rates can be achieved, at a high input pressure requirement. The outlet temperature achieved must also be considered, as increasing the flow rate can result in a lower exit temperature for the receiver. Considering only the flow of the HTF, there are additional flow configurations that can increase heat transfer. Jet impingement has promise for high heat flux applications and for CSP receivers (further discussed in section 2.9). Jet impingement has shown to increase heat transfer in a local proximity by 300% when compared to flow in a tube at the same flow conditions (Zuckerman & Lior, 2006). Jet impingement is a complex flow phenomena and is a fundamental part of the proposed receiver design, therefore, a detailed discussion of the flow are given in section 2.7.

2.7 Jet impingement

Jet impingement is an effective and flexible method of energy transfer. Heat transfer applications include electronic cooling, cooling of turbine components and a multitude of industrial applications. Jet impingement is applicable to the receiver as it is used extensively in configurations where intense

cooling is required and for non-uniform heat flux distributions (Wang, Laumert, Xu & Strand, 2015). Jet impingement is investigated for the receiver to improve the heat transfer rate on the absorbing surface. A jet impinging onto an orthogonal plane within the vicinity of the stagnation point produces amongst the highest Nusselt numbers encountered in single face convection (Cooper, Jackson, Launder & Liao, 1993). Heat transfer coefficients of up to three times higher can be achieved compared to conventional confined parallel flow cooling at the same maximum flow rates (Zuckerman & Lior, 2006). The increase in the heat transfer coefficient can be attributed to the much thinner boundary layer, along with spent flow increasing turbulence in the surrounding fluid.

In order to evaluate the performance of the receiver, particular attention must be given to the thermal modelling of the receiver. Due to the complex geometry, turbulent flow and advanced heat transfer mechanisms occurring simultaneously within the receiver, the accuracy of the thermal modelling required cannot be understated. The fundamental theory relating to jet impingement is therefore discussed.

2.7.1 Jet impingement fundamentals

A submerged impinging jet goes through several regimes in its development. A schematic of an impinging jet flow is depicted in Figure 16.

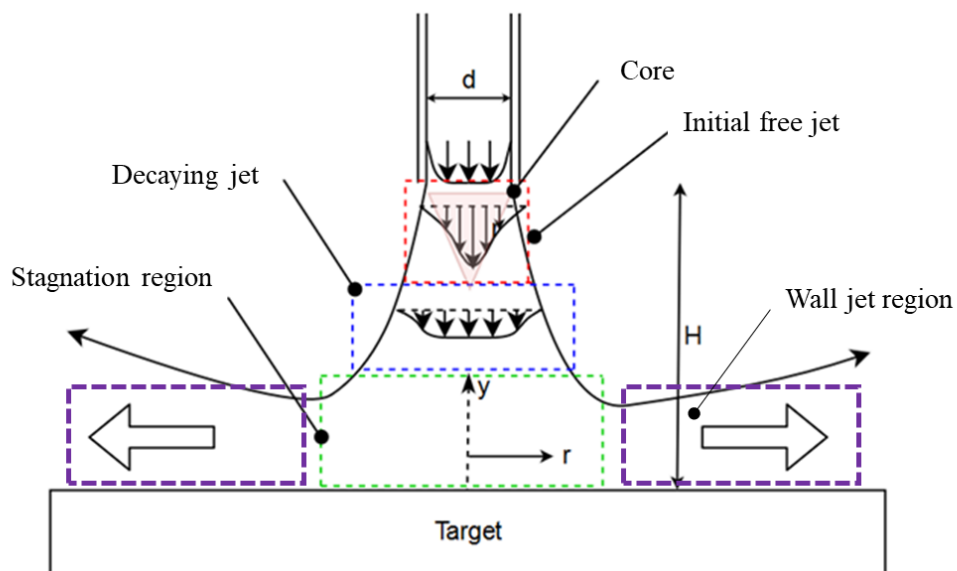


Figure 16. Jet impingement schematic and flow regions.

The jet emerges from a nozzle with a defined velocity, temperature and turbulence characteristics based on the geometry of the nozzle and upstream conditions. After the fluid exits the nozzle as a freely submerged jet, a shear layer develops, and the jet entrains surrounding fluid, thereby increasing the

mass flow (Zuckerman & Lior, 2006). The jet region and its velocity profile widen as the jet entrains surrounding fluid. The internal region forms a core region of higher total pressure. The core region is defined as the axial position where the dynamic pressure reaches 95% of its original pressure, depicted in the red triangle. This initial free-jet region occurs within two diameter lengths and is indicated by the red region in Figure 16.

If the shearing layer expands inwards and reaches the jet axis before reaching the target surface, the jet core starts decaying. The decay region forms between four to eight nozzle diameters downstream of the exit (Zuckerman & Lior, 2006), depicted by the blue region in Figure 16. From here the axial velocity profile magnitude reduces and the velocity profile widens, this resembles a flattened Gaussian profile. In the decay region, the axial velocity varies with axial position. The decay region can be further classified as developing or fully developed based on the velocity profile (Viskanta, 1993).

As the jet approaches the wall, the axial velocity slows, and the flow stagnates, turns and gets accelerated radially outwards. This flow region is called the stagnation region and is depicted in the green region of Figure 16. The flow builds up static pressure in the stagnation region, and this is what turns the flow, resulting in high normal stress in the stagnation region and high shear stresses when the flow accelerates. The resulting flow pattern stretches the vortices (a region in which a fluid revolves around an axis) and increases the turbulence in the flow. The stagnation region extends approximately by 1.2 diameters length above the wall for round jets. This zone can be characterised by the negative normal parallel velocity correlation ($\overline{uv} < 0$) (Maurel & Solliec, 2001).

In the wall-jet region, the flow is in the radial direction parallel to the wall. The wall-jet flow has a minimum thickness of 0.75-3 nozzle diameters and continually thickens in the radial direction. The thickness of the wall jet boundary layer is based on the distance from the wall at which the flow rate drops to 95% from the maximum speed at the radial location. The boundary layer of the flow is formed from the stagnation region and typically doesn't develop to be larger than 1% of the nozzle diameter (Zuckerman & Lior, 2006). As the wall jet develops it further entrains flow, this increases the jet mass flux and reduces the average speed of the flow. For a round jet, mass conservation results in a continual average speed decrease as the flow spreads outwards (Cooper *et al.*, 1993).

2.7.2 Jet impingement parameters and non-dimensional coefficients

The common parameters used for experimental and numerical investigations of jet impingement are described in Zuckerman and Lior (2006). These non-dimensional parameters are used to validate and compare results obtained experimentally and numerically. The primary parameter for evaluating heat

transfer coefficient is the Nusselt number, Nu . This non-dimensionalised parameter as adjusted for jets, is described by equation (8).

$$Nu = \frac{q_w d}{(T_w - T_j)k(T_j)} \quad (8)$$

where q_w is the constant wall heat flux, d is the nozzle diameter, T_w is the static wall temperature, T_j is the jet inlet temperature, and $k(T_j)$ is the thermal conductivity of the fluid at T_j . The heat transfer coefficient can be described by equation (9).

$$h = \frac{q_w}{T_w - T_j} \quad (9)$$

where the heat transfer coefficient for JIHT is described as h . This is not the typical way to describe the heat transfer coefficient but is adopted in practice to compare numerical with experimental results (Ab Kadir *et al.*, 2010; Lee, Chung & Won, 1999; Uddin, 2008; Zuckerman & Lior, 2006).

The other non-dimensional parameters used to describe the JIHT are presented in Table 4. These parameters are typically used to describe the layout of the jet relative to the target and parameters commonly referred to in literature. The dimensions correspond with Figure 16.

Table 4. Non-dimensional Parameters used for JIHT Investigations (Zuckerman & Lior, 2006).

Non-dimensional parameter	Description
H/d	Nozzle height to nozzle diameter ratio
r/d	Radial position from the centre of the jet
y/d	Vertical position measured from the target surface
Tu	Turbulence intensity usually evaluated at the nozzle
Re	Reynolds number
Ma	Mach number based on nozzle exit average velocity
f	Relative nozzle area (total nozzle exit cross sectional area divided by the total target cross sectional area)
A_f	Free area (1 minus the relative nozzle area)

With knowledge of JIHT theory, jet classification and behaviour, and the parameters commonly used to describe the results of jet impingement only the turbulence modelling needs to be further discussed. The numerical modelling focused on turbulent effects for jet impingement is presented in Chapter 3.

2.7.3 Jet impingement turbulence effects and heat transfer

The jet behaviour is correlated to the Reynolds number. The flow can be categorised as follows:

- Laminar flow where $Re < 1000$.
- Transitional flow where $1000 < Re < 3000$.
- Fully developed turbulent where $Re > 3000$.

where the Reynolds number is defined by equation (10).

$$Re = \frac{4Q}{\pi d v} = \frac{\rho U d}{\mu} \quad (10)$$

where d is the diameter of the nozzle, ρ is the density of the fluid, U is the fluid's average velocity, μ is the dynamic viscosity of the fluid and v is the kinematic viscosity of the fluid (Çengel & Ghajar, 2015).

The flow regime will have a large effect on the heat and mass transfer rates. Generally, the relation of Nu to Re is an exponential relationship that exists where $Nu \propto Re^b$, where $b = 0.5$ for low speed flows with a low turbulence jet and $b = 0.85$ for high Re flows and high turbulence wall jet (Zuckerman & Lior, 2006).

The turbulent kinetic energy is a measure of the intensity in the flow. The non-dimensionalised kinetic energy of the flow (Tu) is described by equation (11).

$$Tu = \frac{\sqrt{\overline{u'_j u'_j}}}{\sqrt{\overline{u_i u_i}}} \quad (11)$$

The turbulence of the domain can be further enhanced by altering the upstream flow of the nozzle. The downstream turbulence of the jet is sensitive to both the time averaged and instantaneous fluctuations of the velocity field. Turbulence for the initial jet region is due to the shear flow on the edges. At higher Re numbers the shear layers generate flow instability, this is significant in the transitional flow regime and increasingly so in the turbulent regime. Due to the instability, larger oscillations form downstream and grow to large eddies, portions of the fluid whose flow direction varies from the general flow direction, up to the size of the nozzle diameter (Uddin, 2008). The formation of eddies is depicted in Figure 17.

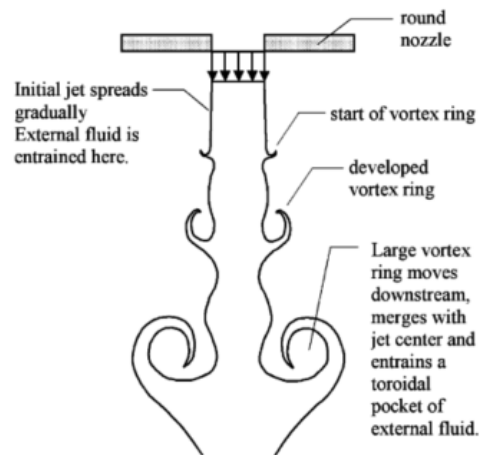


Figure 17. Instability in the turbulent free jet and formation of vortices (Zuckerman & Lior, 2006).

In the decaying jet region, shear layers extend and promote turbulence, generating smaller eddies. The eddies do have a cascading effect and will continue to break down to smaller and smaller eddies. This eventually leads to the fully developed turbulent profile. In the stagnation region, pressure gradients in the flow cause the flow to turn. This turning creates additional normal strains and promote turbulence (Abe & Suga, 2001). The turbulence in the flow is dominated by large scale eddies. Experiments performed by Hoogendoorn (1977) depict the local heat transfer over the stagnation region for pipe and contoured nozzles heat transfer peaked in the centre of the jet for contoured nozzles the Nu peaked at $r/d \approx 0.5$ and had a local minimum at $r = 0$ for the pipe.

The large-scale eddies in the free jet region enhance the heat and mass transfer due to the additional turbulence in the flow. The turbulent fluctuations may produce local flow reversals along the wall and initiate the separation and formation of more vortices. This can describe the formation of the secondary peak of the Nusselt number achieved in jet impingement flows. The Nu is typically plotted against the nondimensional r/d distance, depicted in Figure 18.

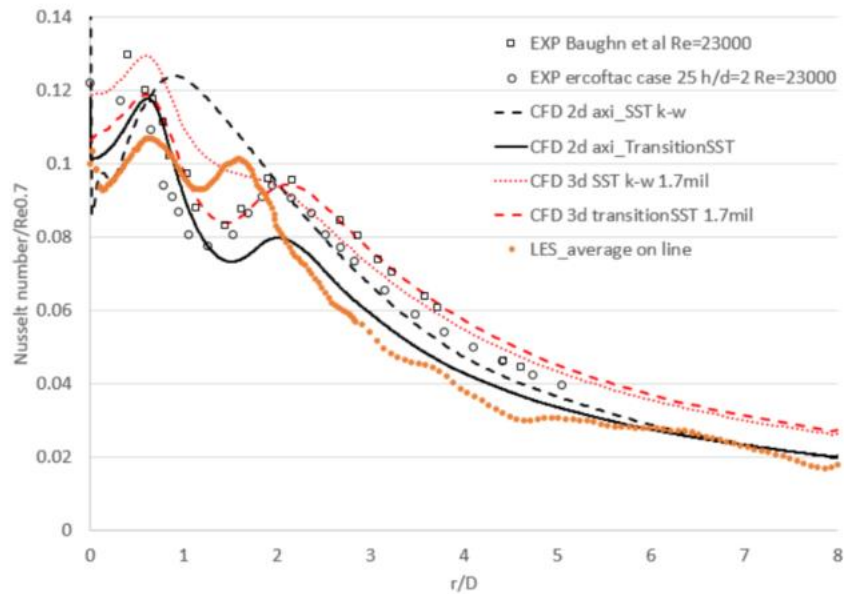


Figure 18. Heat transfer coefficient normalised with the Reynolds number ($Nu/Re^{0.7}$), plotted against the non-dimensional radial distance (r/d) (Craig, Sloomweg & Meyer, 2018).

The formation of this second peak, or the double-hump phenomenon, has been subject to large amounts of investigation and the second peak was likely attributed to the boundary layer transition along the wall (Gardon & Akfirat, 1965). The secondary peak may also be attributed to the large-scale eddies formed along the wall. Some researchers attribute the secondary peak in the flow to the increased shear forces in the wall jet region where time averaged simulations have shown that the shear layer of the upper jet, generates majority of the turbulence (Behnia, Parneix, Shabany & Durbin, 1999). The kinetic energy is the highest at the location where the secondary peak occurs which correlates to the work done by Narayanan, Seyed-Yagoobi and Page (2004).

Not all numerical turbulence models are suited for JIHT due to the complexity of the flow and the turbulent nature. In order to accurately capture the turbulence effect present, various models and schemes have been investigated. An overview of the models available is presented in section 2.11.2.

For the application of JIHT in a CSP receiver, additional methods of enhancing JIHT are discussed with regard to the flow configuration, jet impingement parameters and additional flow manipulation methods.

2.7.4 Jet impingement heat transfer enhancement

To improve the heat transfer for impinging jets, a variety of methods have proven, numerically or experimentally, to be useful strategies. The jet geometry has a significant effect on the heat transfer rates achieved. Experiments conducted by Lee, Song and Jo (2004), show the use of an orifice nozzle can increase the local Nu by up to 65% when $\frac{H}{d} = 2$, where the increase was most significant. A swirl nozzle geometry was investigated by Bilen, Bakirci, Yapici and Yavuz (2002), where at lower $\frac{H}{d}$ distances the Nu distribution was more uniform but with a lower peak value. Additionally, the impinging jet can be pulsed to increase turbulence. When the jet is pulsed the formation of the boundary layer does not develop resulting in higher heat transfer rates. This is counteracted by the loss of energy to the surroundings for a pulsed jet (Seifi, Nazari & Khalaji, 2017). Annular jets have been investigated; annular jets enhanced local heat transfer; however, a local minimum at the target centre was created (Ichimiya, 2003).

The target surface can also be enhanced for heat transfer. For instance, a concave target surface can be used to increase pressure gradients and reduce the boundary layer growth. Surface curvature enforces recirculation and generates more vortices in the flow. The effect of curvature and the nozzle to target distances were investigated by Lee *et al.* (1999). The authors used a digital colour image processing system to measure the temperature over the surface. It was found that Nu increases generally for increasing Re and curvature. The double hump was likely attributed to stagnation point flow effects and transition to turbulent flow. Concave heat transfer increased 20% over flat plate jet impingement for a specific combination of parameters. Additional non-dimensional parameters and Re can be investigated and optimisation can be carried out on the receiver. Additionally, the target surface may make use of ribs or fins, these have shown up to a 30% increase in heat transfer over a flat plate but reduce the heat transfer rates far from the stagnation region and increase pressure losses (Gau & Lee, 1992). A pinned surface (a surface with extruded pins) is proposed for heat transfer enhancement by Yang, Lin, Wang and Hsu (2013). The authors numerically investigated the effects of various parameters for enhancement. It was concluded that the use of pins on the target surface enhanced heat transfer, the pins shape and spacing were additionally optimised to enhance the average Nusselt number by 17.97%.

The effect of multiple parameters such as Re , $\frac{H}{d}$, and $\frac{d}{D}$ were investigated by Zhou, Lin, Bu, Bai and wen (2017). The authors conducted experiments for a round impinging jet on a concave surface for $27000 < Re < 130000$, $3.3 < \frac{H}{d} < 30$ and $0.005 < \frac{d}{D} < 0.03$. For the experiments conducted, the authors concluded that the peak and average Nu increased with increasing Re . However, the stagnation point Nu increased with a decrease in nozzle to surface distances. The curvature effect on the heat transfer may have opposing effects, for a fixed nozzle diameter the average Nu declined with increasing curvature and when the nozzle diameter increased relative to the curvature the average heat transfer was

enhanced. For all experiments, the effect of confinement enhanced the heat transfer rates more than the other enhancement effects. The authors suggest optimisation of the curvature based on the nozzle diameter.

For the application in a solar receiver one of the most promising methods of enhancing heat transfer can be by imparting swirl flow in the impinging jet, as discussed in the next section.

2.8 Swirl flows

Swirling flows result from an application of a spiralling motion in the flow where the tangential velocity component is manipulated (Gupta, Lilley & Syred, 1984). Studies on swirl flows have shown to have large-scale effects on the flow field such as: jet growth, entrainment of fluid, decay of flow regions, stability of the flow field, and flow intensity. These large-scale effects might be advantageous, but literature has had mixed results. The method of swirl generation can be described as geometric or aerodynamically generated swirl. Geometrically generated swirl is when the swirl is imparted into the flow by means of the flow geometry. This can be achieved using geometric inserts or vanes which change the flow direction to increase the tangential velocity component usually at the expense of reducing the axial flow component. Aerodynamically generated swirl is where the swirl is imparted in the flow without manipulating the flow domain's geometry directly. This can be achieved by using axial and tangential inlet jets.

The degree of swirl imparted in the flow is typically characterised as the swirl number, S . The non-dimensional swirl number described by Gupta *et al.* (1984), presented in equation (12).

$$S = \frac{G_{\theta}}{RG_{ax}} \quad (12)$$

where G_{θ} and G_{ax} are the tangential and axial momentum fluxes respectively, R is the jet nozzle radius.

The tangential and axial momentum fluxes can be described by equations (13) and (14):

$$G_{\theta} = \int_0^{\infty} (\rho uw + \rho \overline{u'w'}) r^2 dr \quad (13)$$

$$G_{ax} = \int_0^{\infty} (\rho u^2 + \rho \overline{u'^2} + (P - P_{\infty})) r dr. \quad (14)$$

For an incompressible jet, the axial and momentum fluxes are further simplified (Uddin, Weigand & Younis, 2019) to the following equations:

$$G_{\theta} = \int_0^R r^2 u_{ax} u_{\theta} dr \quad (15)$$

$$G_{ax} = \int_0^R r u_{ax}^2 dr \quad (16)$$

The swirl number equation is further simplified, when the velocity components are held constant at the inlet face. The swirl number can then be described by equation (17).

$$S = \frac{2 u_{\theta}}{3 u_{ax}} \quad (17)$$

This describes the swirl number based on the bulk axial velocity (u_{ax}) and bulk tangential velocity (u_{θ}). The addition of swirl in the flow can result in a wide variety of effects in the flow field which may or may not be advantageous for enhancing heat transfer, the basic effects of swirl are therefore discussed.

2.8.1 Basic effects of swirl

The effects of swirl have been extensively studied for combustor jets, however not directly for jet impingement. From literature the effects of swirl in jets are: an increase the width of the jet, increase the rate of entrainment of the surrounding fluid and increase the rate of decay of the jet (Gupta *et al.*, 1984, Lucca-Negro & O'Doherty, 2001). Basically, increasing flow instabilities and mixing in the fluid. The observed flow behaviour changes for the intensity of the swirl, swirl is usually described as either weak or strong swirl. The flow patterns of weak swirling and strong swirling jets are depicted in Figure 19.

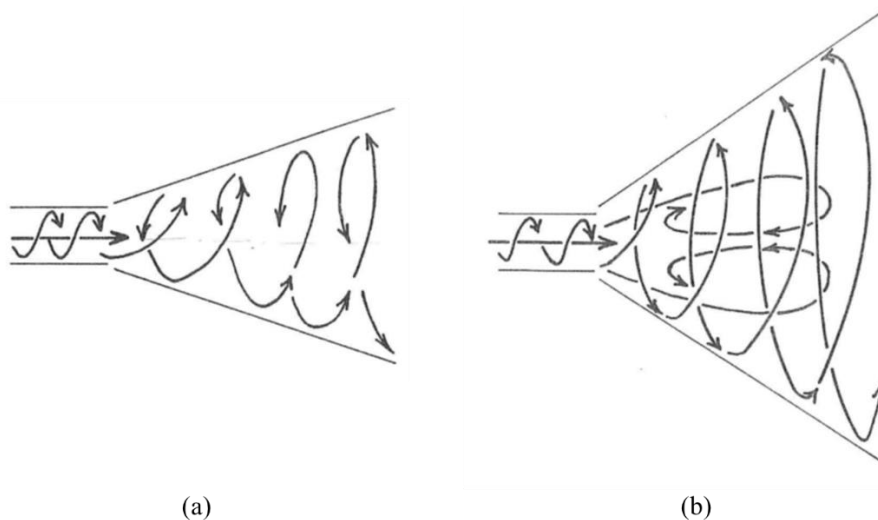


Figure 19. Depiction of flow field for (a) weak swirl flows and (b) strong swirl flows extracted from (Gupta *et al.*, 1984).

In weak swirl flows, where $S \leq 0.4$, swirl has shown to increase the width of the free jet region, the jet growth rate is increased (due to the increase of fluid entrainment) and the decay of the jet increases. For

the weak swirl flows the adverse pressure gradient is not significant enough to cause axial recirculation in the flow. For weak swirling flows the axial velocity distribution has a Gaussian profile at the nozzle exit, with the maximum velocity located on the central axis of the jet. With low swirl flows with high turbulence intensity, regions may spontaneously form where reverse flow is present. For strong swirling flows the velocity maximum location is displaced from the jet's central axis (Chigier & Chervinsky, 1967). In high swirl flows, the flow characteristics may differ significantly from weak swirl flows. High swirl enhances the rates of entrainment and allows for fast mixing at the nozzle exit and near recirculation boundaries (Gupta *et al.*, 1984; Lucca-Negro & O'Doherty, 2001; Martin, Gouldin & Yetter, 1975; Syred & Beér, 1974). This effect results in highly unstable, intense, and usually oscillatory flow increasing the rate of fluid mixing and fluid entrainment.

At high swirl rates, where $S \geq 0.6$, the pressure gradients in the radial and axial direction are much higher than the weak swirl flows particularly near the nozzle exit. The pressure gradients produce a much wider jet spread. If the adverse axial pressure gradient exceeds the forward kinetic forces, then the flow will reverse and form a recirculation zone in the central region of the jet near the nozzle exit (Lucca-Negro & O'Doherty, 2001).

High swirl flows are associated with high shear stresses, turbulent intensity, and large-scale fluctuations in the flow near boundaries and stagnation points. Swirl flows are unstable, oscillatory, and complex making even the gross features such as the shape and size of the recirculation zone difficult to quantify (Chigier & Chervinsky, 1967; Gupta *et al.*, 1984; Gupta & Lilley, 1985). High swirl flows typically result in vortex breakdown where a free stagnation point and recirculation zone are formed in the vortex core that enhances the streamwise vorticity in the local region.

Irrespective of the particularities and swirl generation method used for high swirl flows the recirculation zone "eye" is always present near the nozzle exit resulting in similar streamline flow patterns. The recirculation zone at extremely high swirl rates ($S = 2.2$) has been seen to occupy 75% of the nozzle diameter and recirculates 80% of the initial mass flow rate (Syred & Beér, 1974). Turbulence intensities are extremely high in the recirculation zone, where measurements of the turbulent stress components were measured there exist strong variations in turbulent kinetic energy (up to 300% increase) and non-isotropy (Syred & Beér, 1974). The size and shape of the recirculation zones eye are typically similar. The increase in swirl number has shown to widen the eye but reduce the length of the eye downstream from the nozzle (Chigier & Dvorak, 1975).

From experimental investigations for turbulent jets (Chigier & Chervinsky, 1967; Gupta *et al.*, 1984), it was shown that the increase in swirl level in the flow has pronounced effects on the turbulence structure, such as the: turbulent kinetic energy k , the dissipation rate ε , length scale and the shear

stresses in the flow. The described effects of swirl might enhance heat transfer and therefore are of interest for jet impingement applications.

2.8.2 Swirling impinging jets

Swirl flows exist in a wide range of applications such as vortex amplifiers, cyclone separators, tornadoes, gas turbines, gasoline and petrol engines, and a wide range of industrial combustion systems (Gupta *et al.*, 1984). The investigation of swirl flows in conjunction with jet impingement have been extremely limited particularly for aerodynamically generated swirl flows (Chigier & Chervinsky, 1967; Chigier & Dvorak, 1975).

The effect of swirl for jet impingement has had mixed results for the numerical and experimental investigations. Some authors have shown swirl to enhance heat transfer rates and others have shown a reduction in heat transfer rates. The flow field comparison between jets with and without swirl for impingement is depicted in Figure 20.

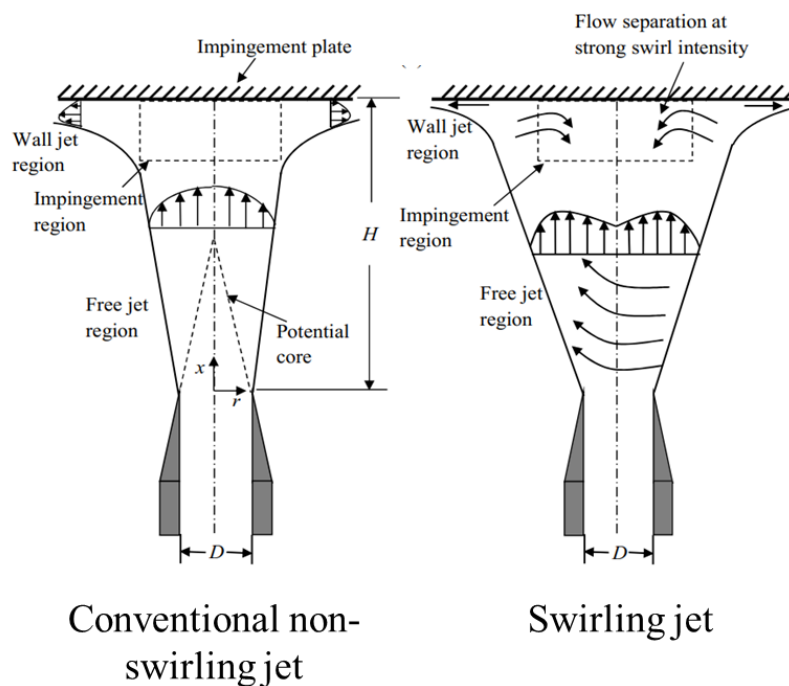


Figure 20. Comparison of flow regions for non-swirling jet impingement and swirling jets impingement (without vortex breakdown) adapted from Ahmed (2016).

Swirl has shown to have a pronounced effect on the jet flow behaviour with the inclusion of the vortex core region developed and the flow separation. The primary characteristics that may be advantageous for jet impingement is the jet spread, increase in turbulence intensity, increase in the turbulent kinetic

energy, and increased flow instability. This can be translated to additional mixing of the fluid due to swirl.

The advantage of swirl has been seen for small nozzle offset distances (Ahmed, Al-Abdeli & Guzzomi, 2016b). As no clear repeatable trends are evident besides the possible potential for improvement, due to many different methods of swirl generation, large ranges of flow parameters considered and the complexities of creating repeatable studies, the precise application must be considered.

The literature study for swirl flows investigated with jet impingement are limited and inconclusive. A tabled summary of the literature review for jet impingement and swirling impinging jets is presented. Table 5 provides a summary of the experimental investigations and Table 6 provides a summary of the numerical investigations.

Table 5. Summary of experimental investigations for jet impingement with swirl adapted from Ahmed (2016).

Study	Re	Swirl Generator	Parameters
Abrantes and Azevedo (2006)	21,000	Aerodynamic.	$ V , u'_i, Nu, \frac{H}{D} = [0.25, 2], S = [0, 0.5]$
Alekseenko, Bilsky, Dulin and Markovich (2007)	8900	Geometric.	$ V , \langle u'_i \rangle, \overline{u'_i u'_i}, \overline{u'_i u'_j}, \frac{H}{D} = 3, S = [0, 1]$
Bilen <i>et al.</i> (2002)	10,000– 40,000	Geometric.	$Nu, \frac{H}{D} = [6, 14], S = [0, 0.89]$
Brown, Persoons and Murray (2010)	8000– 20,000	Geometric.	$Nu, \frac{H}{D} = [0.5, 10], S = [0, 0.67]$
Ianiro and Cardone (2011)	28,000	Geometric.	$Nu, \frac{H}{D} = [2, 10], S = [0, 0.8]$
Kinsella, Donnelly, O'Donovan and Murray (2008)	10,000– 30,000	Geometric.	$Nu, \frac{H}{D} = [0.5, 6], S = NA$
Lee, Won, Kim and Chung (2002)	23000	Geometric.	$Nu, \frac{H}{D} = [2, 10], S = [0, 0.77]$
Nozaki, Igarashi and Hishida (2003)	4000	Geometric.	$ V , \langle u_i \rangle, \overline{u'_i u'_i}, \overline{u'_i u'_j}, r^{0.5}, Nu, \frac{H}{D} = 2, S = [0, 0.43]$
Nuntadusit, Wae-hahyee, Bunyajitradulya and Shakouch (2010)	20,000	Geometric.	$\langle u_i \rangle, Nu, \frac{H}{D} = 2 - 10, S = [0.4, 0.94]$
Ortega-Casanova, Campos and Fernandez-Feria (2011)	7000 – 20000	Geometric.	$\langle u_i \rangle, \frac{H}{D} = 5 - 30, S = NA$
Senda, Inaoka, Toyoda and Sato (2005)	8100	Geometric.	$\langle u_i \rangle, u_i, Nu, \frac{H}{D} = 0 - 6, S = [0, 0.45]$
Wen and Jang (2003)	500– 27,000	Geometric.	$Nu, \frac{H}{D} = [3, 16], S = NA$
Yuan, Chen, Jiang, and Ma (2006)	7500– 28,300	Geometric.	$Nu, H/D = 3, S = NA$
Ahmed (2015)	11600, 24600, 35000	Aerodynamic.	$\langle u_i \rangle, u'_i, Cp, \frac{H}{D} = [1, 2, 4, 6], S = [0, 0.16, 0.27, 0.45, 0.77, 0.83, 1.05]$

Study	Re	Swirl Generator	Parameters
Ahmed (2016)	11600,24600,35000	Aerodynamic.	$\langle u_i \rangle, u_i', Cp, \frac{H}{D} = [1,2,4,6], S = [0 - 1.05]$
Fenot, Dorignac and Lalizel (2015)	23000,28000,33000	Geometric (angular vane helical insert).	$\langle u_i \rangle, u_i, Nu, velocity distribution plots, Nu distribution plots, \frac{H}{D} = 1 - 6, S = [0,0.26]$
Eiamsa-ard (2015)	5000 – 20000	Geometric (multiple twisted tape inserts with baffles and swirl ratios for co/counter swirl).	$Nu, Nu_{avg}, Nu distribution plots, flow visualization, \frac{H}{D} = 1 - 6, y/w = [3 - 6]$
Nuntadusit, Wae-hayee, Bunyajitradulya and Eiamsa-ard (2012a)	20000	Geometric (single tape inserts with twist ratio).	$Temperatur distribution, Nu, Nu_{avg}, Nu distribution plots, flow visulization, \frac{H}{D} = 4, S = [0 - 0,98]$

Table 6. Summary of Numerical investigations of jet impingement with swirl adapted from Ahmed (2016).

Study	Re	Turbulence models	Parameters
Angioletti, Nino and Ruocco (2005)	1000-4000	<i>RNG k - ε, SST k - ω, RSM</i>	$ V , Nu, H/D = 4.5, S = 0$
Behnia, Parneix and Durbin (1998)	23,000–70,000	<i>STD k - e, v²- f</i>	$ V , Nu, k, \frac{H}{D} = 2 - 6, S = 0$
Craft, Graham and Launder (1993)	23,000–70,000	<i>Low - Re k - e, RSM, and two SMC models</i>	$ V , u_i, \overline{u_i' u_j'}, Nu, k, \frac{H}{D} = 2 - 6, S = 0$
Dianat, Fairweather and Jones (1996)	23,000	<i>STD k - e, RSM</i>	$ V , u_i, \overline{u_i' u_j'}, Nu, k, \frac{H}{D} = 2 - 12, S = 0$
Isman, Pulat, Etemoglu, and Can (2008)	4000–12,000	<i>STD k - e, RNG k - e, two other nonlinear models</i>	$ V , Nu, \frac{H}{D} = 4 - 10, S = 50$
Jaramillo, Pérez-Segarra, Rodriguez and Oliva (2008)	23,000 and 700,000	<i>Different k - e, k - ω models</i>	$ V , Nu, \frac{H}{D} = 2 - 6, S = 0$

Study	Re	Turbulence models	Parameters
Merci and Dick (2003)	23000	<i>Low – Re k – e, Low – Re nonlinear k – e</i>	$ V , u_i, \overline{u_i' u_j'}, Nu, k, \frac{H}{D} = 2 - 6, S = 0$
Ortega-Casanova (2012)	7000–18,000	<i>SST k – ω</i>	$Nu, \frac{H}{D} = 5 - 30, S = 0.15 - 0.43$
Pulat, Isman, Etemoglu, and Can (2011)	4000–12,000	<i>Different k – e, k – ω models</i>	$Nu, \frac{H}{D} = 6$
Ramezanpour, Mirzaee, Firth and Shirvani (2007)	4000–16,000	<i>RNG k – e, RSM</i>	$Nu, \text{Streamlines}, \frac{H}{D} = 4 - 10, S = 0$
Sagot, Antonini, Christgen and Buron (2008)	23000	<i>Realizable k – e, RNG k – e, STD k – ω, SST k – ω</i>	$Nu, \frac{H}{D} = 2, S = 0$
Ahmed, Al-Abdeli and Guzzomi (2015a)	18000 and 23000	<i>Realizable k – e, STD k – e RNG k – e, STD k – ω, SST k – ω, RSM</i>	$ V , u_i, \overline{u_i' u_j'}, k, \tau_w, \langle u_i \rangle, Cp, \text{Inlet profile velocity}, \frac{H}{D} = 0.5 - 1.9, S = 0 - 0.5$

Swirling impinging jet literature

The literature on swirling impinging jets is limited. The experimental work focused geometric swirl generators consisting of twisted tape inserts. Aerodynamically generated swirl was investigated by Ahmed *et al.* (2015a). A small jet offset of $H/d \leq 1$ is not investigated by most authors and the focus is on bigger jet offset distances.

Most of the numerical simulations are only for $S = 0$. The effect of swirl on the heat transfer is not investigated. Most authors suggest the use of the SST $k - \omega$ turbulence model. The increase in Re increases heat transfer. The closer the nozzle to the impingement surface, the higher the heat transfer.

The work by Ahmed *et al.* (2015a) is of particular interest where the authors investigated the application of SIJ and experimentally measured the fluid's velocity profile and pressure distributions. The authors changed the swirl number with tangential inlet jets.

Ortega-Casanova (2011), Ortega-Casanova (2012), and Ortega-Casanova and Castillo-Sanchez (2017) investigated the effect of heat transfer in SIJ. The authors found that the SST $k - \omega$ was the best turbulence model and used it for a 2D axi-symmetric optimisation study. The authors found that the increase in Re increased the peak and average Nusselt numbers. The closer the nozzle to the impingement surface, the higher the average Nusselt number on the surface.

Swirling impinging jets are of interest to enhance heat transfer for a solar receiver design. The literature shows mixed results for improving heat transfer. Fully turbulent SIJ are of particular interest where the swirl is generated aerodynamically. From the numerical investigations the $k - \omega$ model shows the best results for modelling SIJ.

2.9 Influencing solar receiver designs

The following receiver designs are presented as they are of interest to the research being conducted. Each of the designs presented addresses a unique application of a novel concept to enhance heat transfer particularly taking advantage of the reradiation to heat transfer surfaces and the use of jet impingement.

External pyramid receiver

An investigation of hexagonal-pyramid based receivers' thermal efficiency was done by Garbrecht *et al.* (2013). Numerical simulations were carried out for the pyramids of the receiver and radiation was simulated. A specified incoming radiation was specified to obtain temperature profiles within the receiver. The receiver's temperature profiles were then used to determine the net emission losses.

Convective losses were approximated using work done by Siebers and Kraabel (1984). The geometry of the receiver is depicted in Figure 21. The pyramid design is depicted in Figure 22 (a).

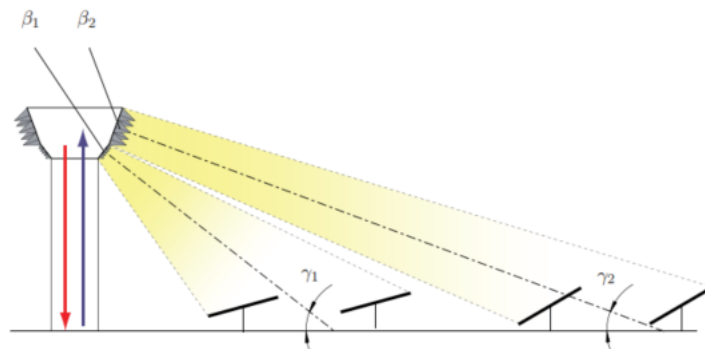


Figure 21. External pyramid receiver central receiver schematic proposed by Garbrecht *et al.* (2013). The receiver acts as a heat trap at the base and has achieved a 91% thermal efficiency. High surface temperatures of 1050 K are reached in the design which might need to be reduced as depicted in Figure 22(b). The emission and radiation losses account for 4.1% of losses due to the heat trap effect. The streamlines of the HTF flow within the pyramid are depicted in Figure 22 (c).

The external pyramid receiver shows promise in terms of limiting radiation losses. In order to make this concept viable, the limitations of the work must be addressed, namely:

- The inclusion of an accurate implementation for a solar heat source.
- Natural convection can be investigated numerically.
- The numerical model used has also been shown to be inferior to alternative models available.
- The consideration of conduction losses through the base of the receiver can be included.
- The given design can then be further analysed and optimised.
- The external surface temperature needs to be reduced.

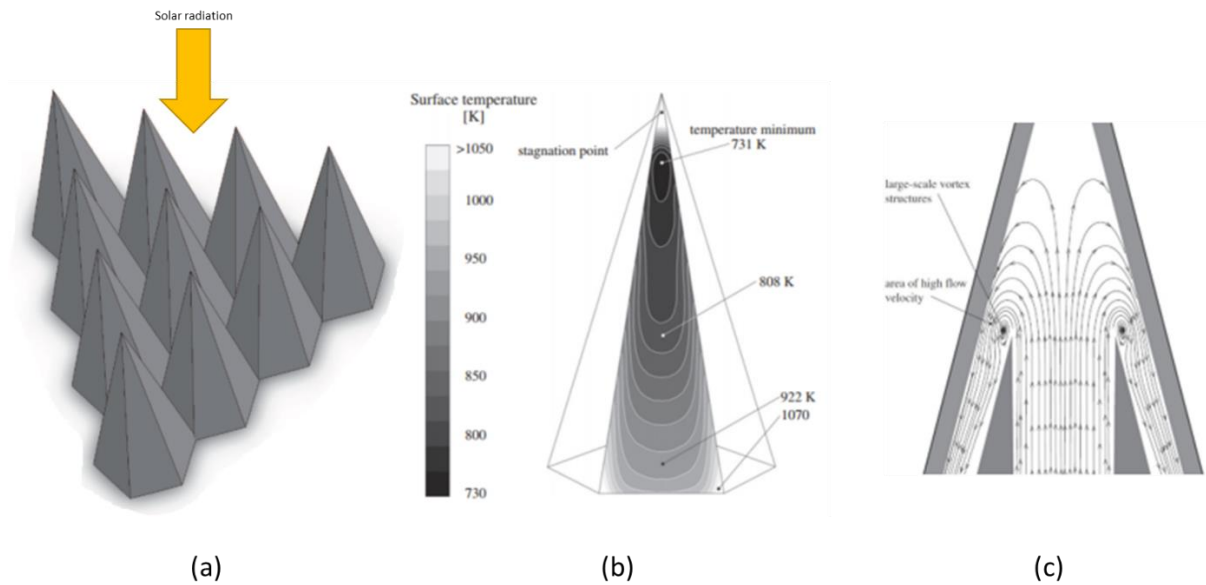


Figure 22. (a) External pyramid outer surface temperature contour. (b) Net flux absorbed by pyramid contour. (c) HTF streamlines for pyramid (Garbrecht *et al.*, 2013).

Spiky central receiver air pre-heater receiver

A spiky central receiver air pre-heater (SCRAP) receiver was proposed by Lubkoll *et al.* (2015). The proposed receiver schematic is depicted in Figure 23 (a). This novel external receiver aimed to overcome the practical limitation of other pressurised air systems, the low heat transfer coefficient on the gas side using internal fins. The interesting geometry used long cylindrical spikes as the absorption surfaces. These spikes act as a radiation trap because of the high view factor between spikes and reduce the radiative losses, thereby improving performance. The spikes have internal fins to enhance the heat transfer to the air as depicted in Figure 23 (b).

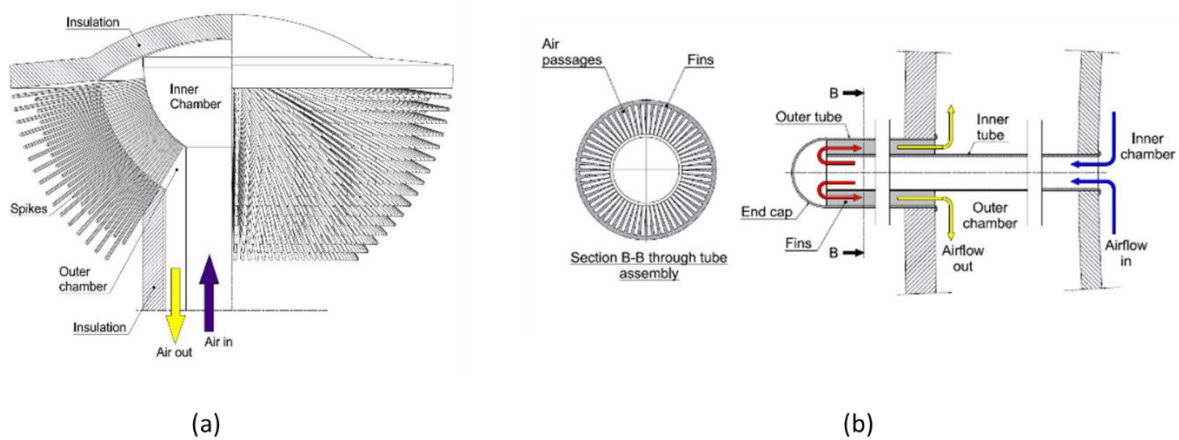


Figure 23. (a) Schematic of SCRAP receiver. (b) Internally finned tube sectional view (Lubkoll *et al.*, 2015).

The SCRAP receiver design is still being developed and an experimental setup has been created (Lubkoll, Harms & Von Backström 2017). The objective is to enhance the heat transfer whilst still maintaining an acceptable pressure drop. This receiver is similar to the receiver proposed by Garbrecht *et al.* (2013). Both designs use a radiation trap effect between absorbing surfaces.

Jet impinging receiver for solar dish Brayton cycles

An investigation of and impinging receiver for a gas dish Brayton cycle was done in a study conducted by Wang *et al.* (2015). Wang *et al.* (2015) concluded that impingement heat transfer is very effective for cavity receivers with non-uniform heat flux as it improves uniformity with high local heat transfer coefficients.

Wang *et al.* (2015) used a non-sequential ray tracing model and used the output flux as a thin heat source for ANSYS for a computational fluid dynamics (CFD) simulation. All the temperature related properties were fit with a polynomial and implemented as a user-defined function in ANSYS. The proposed receiver design is depicted in Figure 24 (a). A sectional view of the receiver is depicted in Figure 24 (b).

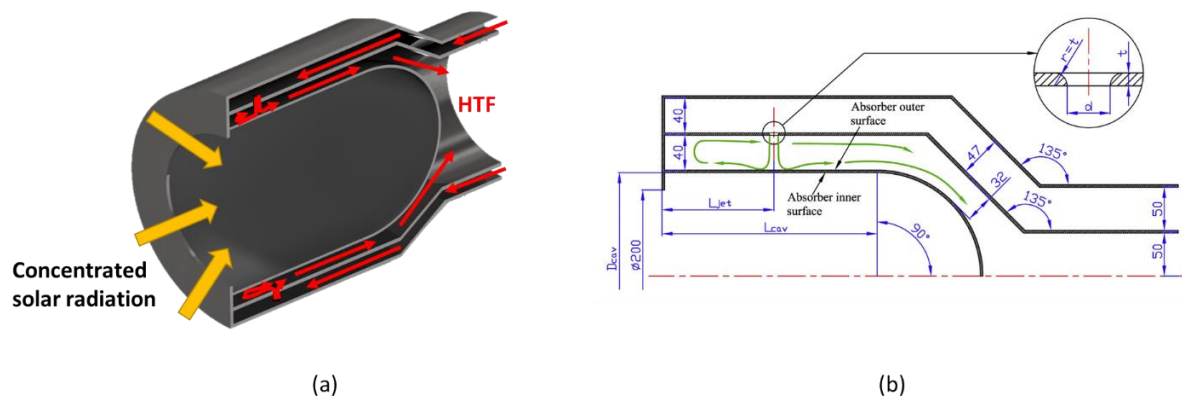


Figure 24. (a) Geometric model of proposed jet impingement solar dish receiver. (b) Schematic of proposed jet impingement solar dish receiver (Wang *et al.*, 2015).

The local Nusselt number is plotted over the absorber surface to depict the enhanced heat transfer in Figure 25. The following was observed by Wang *et al.* (2015): the Nusselt number distribution influenced the surface temperatures; radiation losses typically dominate where 6300 W is lost due to radiation compared to 1050 W to natural convection; and natural convection losses are typically only 40% of radiation losses.

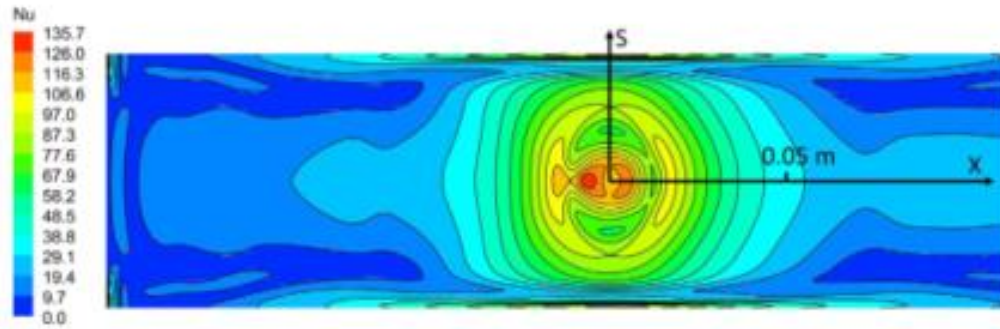
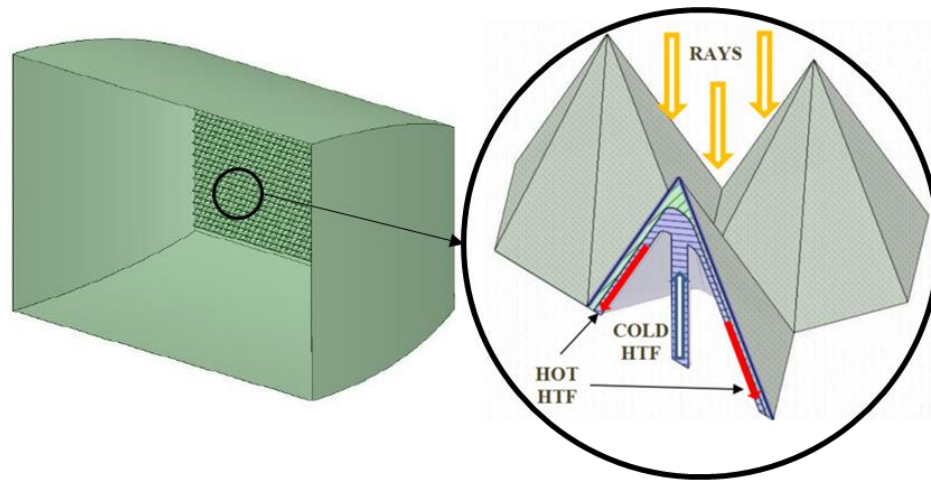


Figure 25. Local heat transfer Nusselt number over cylindrical surface (Wang *et al.* 2015).

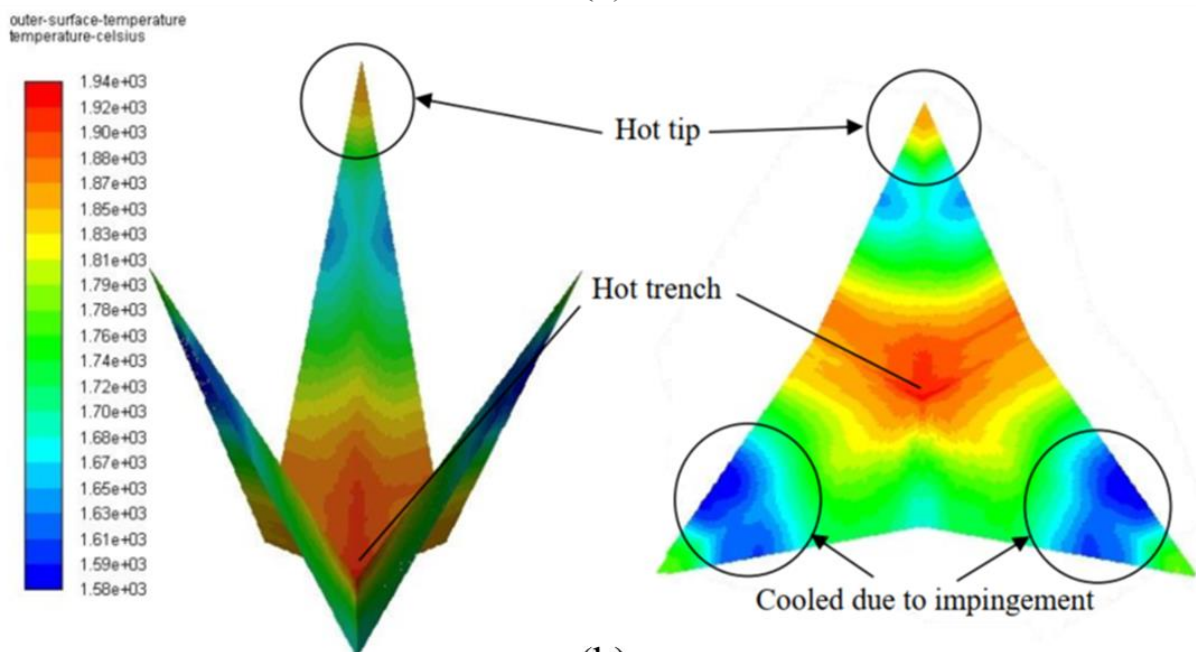
Current receiver design

The proposed receiver design is a cavity receiver with a hexagonal pyramid array forming the absorbing surface of the receiver depicted in Figure 26(a). Within each pyramid is a confined nozzle that impinges the HTF onto a concave surface. The HTF of the receiver is molten salt. The use of molten salt is becoming more and more popular for higher operational temperatures due to its inherent advantages for thermal storage. The receiver has the goal of reducing the thermal losses of the system by acting as a radiation trap. The receiver design allows the concentrated solar radiation to enter the aperture but cannot be reflected directly out of the aperture, as shown in Figure 26(b).

The cavity design can reduce the radiation losses of the receiver, which is dominant at higher temperatures. In addition, the concept uses an array of impinging jets at the absorber to enhance the heat transfer rates achieved as depicted in Figure 26(a). The cavity of the receiver is also beneficial as it limits the convective losses of the receiver and the pyramid arrangement absorbs majority of the reradiation, of nearby pyramids.



(a)



(b)

Figure 26. Hexagonal pyramid receiver design (a) secondary concentrator and pyramid with internal flow arrangement (b) pyramid surface temperature and hot spots (Slootweg *et al.*, 2019).

This type of pyramid receiver has been investigated by Garbrecht *et al.* (2013) and Slootweg (2018). One of the limitations of the receiver is the upper operational temperature for the steel surface. The surface can reach temperatures of above 1070 K (Garbrecht *et al.*, 2013). With more accurate optical models and thermal models, it has been shown that the pyramid surface can achieve temperatures of up to 1940 K (Craig *et al.*, 2018; Slootweg, 2018). The heat transfer rates must be improved and optimised in order to fully use this type of receiver. Internal fins similar to the SCRAP receiver design were suggested by Garbrecht *et al.* (2013), to enhance heat transfer to the HTF. As previously stated, one of the limitations on the investigation by Garbrecht *et al.* (2013) is the realistic flux profile on the receiver.

To address the research limitations the optical and thermal modelling is investigated in the solar application in Chapter 5.

The design of Sloomweg (2018) was not effective and had limitations on the practicality of the design. The limitations for the design can briefly be summarised with the following points:

- The design had excessively high surface temperatures of 1940 °C. This would result in the melting of most steels.
- The hexagonal pyramid would produce a large thermal stress on the absorbing surface.
- No internal fins were implemented which can enhance the heat transfer rates achieved.
- The outlet temperature of the receiver HTF of 563.9 °C. The usable limit of molten salt is 600 °C and the outlet temperature is only achievable with high surface temperatures.
- The absorbing surface design and heat transfer could benefit from optimisation.

2.10 Optical modelling in literature

To accurately simulate the energy captured by the collector and receiver, numerical optical models are used. The model needs to be a validated and be able to evaluate complex light particle interactions with the collectors, while also considering wavelength and temperature dependence of the rays' interaction with absorbing and reflecting surfaces. The optical performance of the receiver field must be simulated accurately by considering the sun shape, sun angle, blocking, shadowing, aiming strategies, absorptivity and reflective errors. For this purpose, Monte-Carlo ray tracing (MCRT) has proven effective (Ardekani, 2017; Asselineau, 2017; Craig et al., 2018; Sloomweg et al., 2019). A summary of the literature on MCRT is provided and discussed below.

Monte-Carlo ray tracing

MCRT methods are some of the most robust modelling techniques for SPT receiver simulations. MCRT is a statistical method that makes use of the Markov chain. The Markov chain is a sequence of events where the probability of the succeeding event is not influenced by the previous event. This produces a probability distribution by repeating these events multiple times (Walsh, 2004). As a result, the accuracy of the method is proportional to the number of iterated events. MCRT methods make use of averaged results from individual samples but do contain fluctuations around the mean. Therefore, the accuracy can be improved through more iterations.

As a statistical method MCRT models can incorporate spatial, angular, spectral and temporal variations of radiative intensity for reflective, opaque and transmitting surfaces (Asselineau, 2017; Howell, 1998). MCRT methods can be applied to solar radiation by assigning a discrete number of rays. The flux distributions can therefore be computed by determining the number of intercepting rays over an area

with the energy contained by each ray. Based on the geometry surface properties the reflection, absorbance and transmittance of each ray can be statistically determined (Shuai, Xia & Tan, 2008). MCRT comes in a variety of methods from basic collision-based methods to advanced methods such as the pathlength method.

MCRT is used to develop codes such as SolTrace, a free software developed by the National Renewable Energy Laboratory (Wendelin, 2003). SolTrace is suitable for complex geometries and has been widely used for CSP optical performance (e.g., Li *et al.*, 2016). An optical model using SolTrace and scripting has been developed by Slootweg *et al.* (2018). The developed and validated model can accurately: convert complex geometries from ANSYS mesh files, be used for different heliostat field layouts, and be simulated for different days using the Iqbal DNI model. This developed model can overcome the limitations of SolTrace and provides accurate optical simulations (Iqbal, 1983; Slootweg *et al.*, 2018). It will be used in Chapter 5 to generate a realistic heat source when evaluating a swirling jet receiver.

2.11 Thermal modelling in literature

The concentrated solar radiation that reaches the receiver is subjected to multiple heat transfer mechanisms from the absorbing surface. With the complicated geometry of the receiver no analytical solution exists to the problem. The heat transfer is enhanced using impinging jets which causes complex flow. In order to model the complex flow within the receiver particularly for jet impingement with swirl, CFD is needed, and the literature is surveyed for work relating to jet impingement.

2.11.1 Computational fluid dynamics

CFD is employed in research as it can be used numerically solve partial differential equations. CFD allows us to visualise flow patterns and capture the physics of these systems in more detail. This will help us understand the flow better and make better approximations of real systems. However, CFD does have its inherent disadvantages as numerical approximation errors are introduced. It is critical to understand these errors associated with CFD. Furthermore, simplifying assumptions are made about the underlying physics of the problem which may result in incorrect solutions. Numerical results must be critically evaluated and validated to ensure the results obtained are reliable (Tu, Yeoh & Liu, 2013).

CFD has been employed by various authors to simulate CSP receivers (see Garbrecht *et al.*, 2013; Guan, Zhang & Shan, 2017a; Guan, Zhang, Shan & Hang, 2017b; Guan, Zhang & Shan, 2018; Roldán & Fernández-Reche, 2015; Uddin, 2008; Wang *et al.*, 2015; Yu, Zhang & Shan, 2015). Several authors have used CFD to model jet impingement with good agreement to experimental work (see Ab Kadir *et*

al., 2010; Craig *et al.*, 2018; Garbrecht *et al.*, 2013; Guan *et al.*, 2017a; Koseoglu & Baskaya, 2010; Seifi *et al.*, 2017; Sharif & Mothe, 2010; Uddin, 2008; Violato, Ianiro, Cardone & Scarano, 2012; Wang *et al.*, 2015; Yang, Chang, Zhao & Leng, 2017; Yang, Wei & Wang, 2011; Yu *et al.*, 2015; Yu, Zhang & Xu, 2014; Zuckerman & Lior, 2006). The other heat transfer mechanisms present within the receiver have also been subject to investigation. These include the modelling of the radiative, convective and conductive losses within cavity receivers. A detailed discussion on CFD and jet impingement numerical modelling is presented next.

2.11.2 Jet impingement numerical modelling

Many industrial applications of jet impingement involve turbulent flow within the whole domain, downstream of the nozzle. As previously described turbulence results in the formation of eddies (section 2.7.1). The eddies generated by the flow vary over a wide range of length scales and interact in a dynamically complex way. Therefore, the modelling the flow presents significant difficulties when trying to accurately predict the behaviour of turbulent jets (Versteeg & Malalasekera, 2007).

A substantial amount of research has been conducted to develop numerical methods that are capable of capturing the turbulence effects. These methods may be grouped into the following categories:

- Turbulence models for Reynolds-averaged Navier-Stokes (RANS) equations.
- Large Eddy simulation (LES).
- Direct numerical simulation (DNS).

Reynolds-averaged Navier-Stokes

The RANS methods focus on the mean flow while modelling the effects of turbulence on the flow's properties. After substituting a mean and fluctuating term for each flow variable, the Navier-Stokes equations are time-averaged (Versteeg & Malalasekera, 2007). Extra terms appear in the equations as a result. In the RANS approach, the additional terms are modelled with classical turbulence models based on their general principles of operation and the suitability of the model. The models typically used are the $k - \varepsilon$ standard model, $k - \varepsilon$ realisable model, $k - \omega$ model, Reynolds stress model (RSM), $v^2 - f$ model, and shear stress transport (SST) model.

RANS models have had mixed results for predicting jet impingement flow. From all of the RANS models the superior models for accuracy are the $k - \omega$ SST model and the Transition SST model (Zuckerman & Lior, 2006). The Transition SST ($\gamma - \overline{Re}_{\theta,t}$) model is applicable for turbulent flows where a significant portion of the boundary layer is laminar (ANSYS Inc, 2013). This is a significant consideration for jet impingement as in the stagnation region the flow stagnates, relaminarises and

develops into a turbulent flow along the impingement surface. The heat transfer rates achievable for flow is largely dependent on the flow regime and therefore must be accurately captured by the numerical model. Historically RANS models do not predict the transition location correctly. This issue is addressed using the Transition SST model which extends to SST model by adding two additional equations for the transport of intermittency and the Reynolds number based on momentum thickness. The Transition SST is a hybrid model like the SST model, and combines the $k - \omega$ and $k - \varepsilon$ models to take advantage of their respective strengths. This is achieved by using the $k - \omega$ model near the wall and the $k - \varepsilon$ model for regions further away from the wall. A weighting function is used based on the distance from the wall to provide a smooth transition between both models (Zuckerman & Lior, 2006). For jet impingement problems, it has been found that the SST model is capable of predicting Nusselt numbers within 20% of experimental results and within a 5% of those predicted by the v^2f model (Menter, Thomas & Wolfgang, 2003). This makes the SST model an attractive choice due to the high accuracy at low computational costs and with its Transition model extensions, able to evaluate laminar to turbulent transition downstream of the impingement point.

Large Eddy simulations

The LES model is an intermediate form of turbulence calculations, that tracks the behaviour of larger eddies. The method uses spatial filtration of the Navier-Stokes equations before the computation allowing the larger eddies to pass and rejecting the smaller eddies (Versteeg & Malalasekera, 2007). LES has recently become more popular and has provided more insight into the formation, propagation and effects of flow eddies on the velocity fields and jet flow characteristics. The downfall of LES is the substantial computational power required to produce results that are both accurate and stable (Zuckerman & Lior, 2006).

The Governing equations are presented for the solution in the form of the filtered Navier-Stokes equations. Filtering is the formal cutting off of the small scale eddy, in the case of LES low-pass filtering is used to cut off the small scale eddies and leave the large scale eddies untouched. This is achieved by filtering the time dependent Navier-Stokes equations in either the Fourier space based on the wave-number or in the physical space. Effectively eddies with a scale smaller than the filter width or grid spacing are removed. The filtering process is therefore affected by the mesh sizing, this is linked to the priori process of mesh refinement based on the turbulent scale mesh refinement used to capture 80% of the kinetic energy.

In space the filter acts as a running average based on requirements of the simulation and the model. The filter in the spectral/Fourier space is evaluated by averaging the complex exponential of the field where it becomes a multiplicative function. The filter can be applied to specification to achieve sharper filters

for the flow. The simulation program used is ANSYS Fluent where the finite volume discretisation provides the filtering operation.

Sub-grid scale model

Due to the filtering of the eddies captured by the LES model modelling of the small-scale eddies is required. The role of the subgrid model is therefore to approximate the dissipation of the smallest scale eddies in the flow. The models used in ANSYS Fluent employ the Boussinesq hypothesis to model the subgrid scale stresses from

$$\tau_{ij} - \frac{1}{3} \tau_{kk} \sigma_{ij} = -2\mu_t \overline{S_{ij}} \quad (18)$$

For incompressible flows the subgrid-scale stresses τ_{kk} is not modelled but can be added to the filtered pressure. In ANSYS Fluent there are four models for μ_t : the Smagorinsky-Lilly model, the dynamic Smagorinsky-Lilly model, the Wall-Adapting Local Eddy-Viscosity (WALE) model, and the dynamic kinetic energy subgrid-scale model.

From the literature review conducted and the work done relating to the subgrid-scale models the primary model used in the investigation is the WALE model. This model has shown superior performance compared to the other models used as it provides the correct near wall asymptotic behaviour and the formulation of the model does not require explicit filtering and is suited well to unstructured grids (Durbin & Reif, 2011). The distinct advantage for the required investigation is that the model returns $\mu_t = 0$ for laminar shear flows, unlike the Smagorinsky-Lilly model. The use of the WALE model is best suited for the given flow as the jet encounters a relaminarisation of the flow in the impingement region for low swirl numbers and the use of the other models will lead to errors (ANSYS Inc, 2013).

WALE model

Near to a wall the subgrid shear stress should approach $0 \propto y^3$ therefore as the wall is approached the $u \rightarrow O(y)$, $v \rightarrow O(y^2)$, and $w \rightarrow O(y)$. Indicating that the errors are proportional to the cell size near the wall and the strain rate will be of magnitude of the order of 1. This shows that the Smagorinsky-Lilly model is not consistent with the described scaling. As an alternative the WALE model was proposed by Ducros, F. & Franck, Nicoud & Poinso, Thierry (1998). The essence of the model is in the correction of the gradient term considering the strain rate and vorticity to reduce perpendicular to the wall and use the velocity gradient for the calculation of the subgrid viscosity.

Direct numerical simulations

The DNS of turbulent flows takes the Navier-Stokes equations as a starting point and develops a transient solution on a sufficiently fine spatial mesh. With sufficiently small-time steps, this enables the

model to resolve the smallest of the turbulent eddies and fastest fluctuations in the flow (Versteeg & Malalasekera, 2007). The long computational times do limit the practical use of such a method to low Reynolds numbers, not usually encountered in realistic JIHT applications (Zuckerman & Lior, 2006). The DNS method is, therefore, not a practical method for numerical simulation of jet impingement-related problems currently; but with improvements in computational power DNS can provide more insight for complex flows in future.

Summary of turbulence models

The turbulence models described each have their own benefits and costs associated. The balance between accuracy and the computational cost is the key to providing researchers with timely and reliable results. Table 7 presents an overview of the models discussed and the applicability to jet impingement simulations. The table is an adaptation of the work done by Zuckerman and Lior (2006).

Table 7. Comparison of CFD turbulence models for jet impingement (Zuckerman & Lior, 2006).

Turbulence Model	Computational cost (time required)	Impinging jet transfer coefficient prediction	Ability to predict secondary peak of Nusselt number
The $k - \epsilon$ standard model	Low	Poor: Nu errors of 15-60%	Poor
The $k - \omega$ standard model	Low-moderate	Poor-fair: Nu errors of at least 10-30%	Fair: may have incorrect location/magnitude
The $k - \epsilon$ (Realisable) and other $k - \epsilon$ models	Low	Poor-fair: Nu errors of at least 15-30%	Poor-fair: may have incorrect location/magnitude
Reynolds Stress Model	Moderate-high	Poor: Nu errors of 25-100%	Fair: may have incorrect location/magnitude
Shear stress transport, hybrid model	Low-moderate	Good: Typical Nu errors of 20-40%	Fair
The $v^2 - f$ model	Moderate	Excellent: Nu errors of 2-30%	Excellent
Direct numerical simulation/Large Eddy simulation models	Extremely high	Good-excellent	Good-excellent

The described numerical models do not incorporate the additional complexity of modelling swirl flows. However, as highlighted in section 2.8, the modelling of swirling jets is complex and largely dependent on the flow field domain therefore the best practices of modelling swirling jets are investigated in Chapter 3.

2.12 Optimisation

To improve the efficiency of the receiver, various design parameters can be considered and optimised. Optimisation studies for cavity receivers have been investigated in literature. With the tools available for modelling the optical performance of the receiver and heat transfer within the receiver numerical optimisation may be used. Typically, geometric parameters of the receiver are investigated with the associated trade-offs in performance metrics. These geometric parameters are then optimised for the required objective. To evaluate the optimal design, a fundamental understanding of optimisation is necessary.

2.12.1 Optimisation fundamentals

The general optimisation problem is formulated as:

$$\min_{w.r.t\ x} f(x)$$

Subject to the constraints:

$$\begin{aligned} g_j(x) &\leq 0, & j &= 1, \dots, m \\ h_j(x) &= 0, & j &= m, \dots, r \end{aligned}$$

where x is a vector of variables, $f(x)$ is the objective function, $g_j(x)$ are the inequality constraints, and $h_j(x)$ are the equality constraints. The constraints impose feasible solutions criteria on the solution. Based on the available information and the nature of the objective function and constraints, various methods are employed to solve the optimisation problem (Snyman & Wilke, 2018). Optimisation techniques used are grouped as either mathematical programming or simulation optimisation. Mathematical programming does have the distinct underlying downfall by assuming local convexity of the function. This assumption drives the method to the optimal solution of the convex domain (Asselineau, 2017). Traditional mathematical programming optimisation requires the adoption of a stochastic nature (based on probabilities) and need to be modified to overcome these shortcomings. Multiple methods have been developed to overcome these.

Optimisation methods

Sample average methods estimate gradients to progress towards a solution. Stochastic approximation methods mimic gradient based methods for nonlinear problems (Snyman & Wilke, 2018). With no gradient information available random search methods may be used. Heuristics and metaheuristics are specific random search methods, these do not solve the problem but find approximate solutions within given time constraints. Heuristics and metaheuristics are population-based approaches where the search presents a population of candidate solutions. These populations can then be reduced or evolved with

improved results and progress towards a solution. Genetic and particle swarm algorithms are examples of metaheuristic methods. Simulation optimisation makes approximations of the objective function using simulations. Simulation optimisation regroups these methods to solve these problems (Asselineau, 2017). The methods described can be readily applied to a single objective function, but with design problems, there may be multiple objectives to optimise.

Multi-objective optimisation

Multi-objective optimisation is the sub-field of optimisation used to optimise a set of objective functions. Multiple optimisation metrics are scalarised to produce a single optimisation metric. Scalarisation requires an informed decision on the relationships of the objectives and their associated trade-offs (Asselineau, 2017). This scalarisation cannot be carried out when the objective function is not known and approximated only. For an approximated function, the Pareto dominance concept may be applied to the problem. A set of Pareto optimal points can be generated to form a front or limit of the multi-objective optimisation (Marler & Arora, 2004). The Pareto front gives a range of designs for the best performance of each objective function. From here trade-offs can be evaluated to determine the best compromise.

2.12.2 Receiver optimisation

For receiver design parametric studies are typically used. This is due to the computational expense of complex flow and radiation modelling. Coupled heat transfer problems are dependent on the geometry and are inherently non-linear functions. As such, traditional gradient-based algorithms are ineffective (Marler & Arora, 2004). Numerical optimisation tools are used to solve these problems but introduce numerical errors. In literature, multiple optimisation studies and parametric studies have been done to produce better receiver designs.

Early works on receiver optimisation were done by Steinfeld and Schubnell (1993). The optimum aperture size for a cavity receiver was investigated with an empirical method for maximum thermal efficiency. Experimentally a test case was investigated to measure the flux distribution. For the given flux distribution, the centre point was determined, and the corresponding radius of the aperture and operational temperature determined. The overall efficiency was then modelled for a range of operational temperatures and cavity radii. Additionally, the authors numerically investigated the effects of sun shape, with MCRT, on the flux distribution and consequentially the efficiency. The work found that above 700 K radiation losses become significant and efficiency drops monotonically for the measured case. As the operational temperature increases the optimal absorber radius decreases along with the efficiency. An optimal parameter can be determined based on the flux distribution radius and temperature. For the Gaussian distribution of flux, the optimal range is defined as a narrow range of

size over a large range of peak fluxes 2.4 to 2.9 standard deviations. The sun shape considerably influences the both the optimal radius and the optimal temperature but more so on the radius (Steinfeld & Schubnell, 1993).

Optimisation studies conducted for jet impingent heat transfer have been investigated. The optimisation strategies adopted are typically response surface optimisation and regression analysis of this response surface with the use of genetic algorithms. The use of a coupled response surface and genetic algorithm was used by Yang *et al.* (2013). The authors found that using this approach and direct CFD simulations resulted in a 2% difference for optimal parameters. The response surface is used to generate the objective function of the design and the genetic algorithm is used to find optimal points for the geometry improving the design efficiency.

Ardekani (2017), conducted a multi-objective optimisation for a multiple tube, LFC cavity receiver. The investigated receiver was thermally and optically modelled using CFD and SolTrace. The multiple objectives were to maximise solar collection, minimise thermal losses, and minimise the plant cost. The ANSYS environment was used to create a response surface of the function and a multi-objective genetic algorithm was used to solve the problem. The algorithm produced Pareto candidates for the receiver geometry. The implementation of this method was successful and resulted in interesting and unique receiver designs (Ardekani, 2017).

The entire shape of a cavity receiver was investigated by Asselineau (2017). Gradient free, stochastic and multi-objective optimisation was carried out for the receiver design. The result was a new “Multi-Objective Evolutionary Progressive Monte-Carlo Evaluation Optimization method”. The proposed method reduced computation time and produced geometrical concept receivers capable of maintaining high efficiencies at a moderate receiver total mass (Asselineau, 2017).

2.13 Conclusion

The comprehensive literature review presented gives the required background for the investigation to be conducted in this dissertation. The literature review is detailed as the investigation is highly multidisciplinary and involves complex topics that must be understood in order for the need for the research to be highlighted and to ensure that the observations and results of the work may be understood.

From the established literature it can be deduced that there is a need for further improvements in CSP. SPT technologies hold significant promise for future improvements that can be made for high temperature receiver designs. To investigate high temperature receiver designs multiple designs are

presented and discussed from literature. The variation of the design is based on the application of the receiver as the receiver design becomes a trade-off problem between multiple parameters. For this research a novel receiver concept is investigated. Based on the unique application of the receiver, the various parts that make up the CSP plant can be optimised to improve the overall efficiency.

Improving the performance of SPT systems is complex as it cannot be constructed and tested until a final prototype is developed. To evaluate the performance of a receiver, the physics and development of the receiver must therefore be numerically simulated. The performance of the receiver and the collector is inherently coupled, and both need to be modelled accurately for realistic results. A discussion of the modelling of the proposed receiver is discussed, in particular the thermal modelling. Based on the model of the receiver performance, the parameters of the receiver can be optimised.

JiHT is complex to simulate accurately and inexpensively. The nature of jet impingement and the benefits it provides for heat transfer must be understood to ensure the simulations capture the physical behaviour. The theory behind the physics was presented along with important considerations made for the nature of the flow. The modelling of the flow, and the turbulence effects, are described and the numerical methods of evaluating this flow are discussed. The heat transfer can be further enhanced if required, based on classical heat transfer enhancement methods. Other methods also exist that are of more interest for jet impingement, such as swirling flows and different nozzle geometry effects. Based on the numerical modelling considerations relating to JiHT, the proposed receiver design can be investigated, inexpensively, with the Transition SST model. The method of imparting swirl within the impinging jet setup shows promise in achieving higher heat transfer rates, therefore, swirling impinging jets will be the primary focus of improving the concentrated solar receiver design. From the literature the complexities associated with swirl flows and jet impingement are clear. Considering the theory and physics of the flow behaviour, the numerical modelling can consider the flow phenomena and accommodate these considerations in the investigation. The investigation of swirling jet impingement is limited in literature and as a result this study will contribute to the body of knowledge for similar flows.

All of the receiver designs in literature that make use of jet impingement (section 2.9) stand to benefit from the addition of swirl. The accurate prediction of swirling jet impingement with numerical models is therefore vital for more general applications. In order to ensure that swirling impinging jets can be accurately modelled a validation study is required.

3 NUMERICAL VALIDATION OF SWIRLING JET IMPINGEMENT

3.1 Introduction

The objective of this chapter is to investigate the use of swirl impinging jets (SIJ) in a production CFD environment. The study focuses on the validation of the numerical model by analysing the accuracy of the model when compared to experimental results. The validation is investigated numerically with ANSYS FLUENT.

For the validation, two test cases are used, namely an impinging jet with aerodynamically generated swirl, and swirl generated using a geometric insert. The experimental methods and results for each case are presented in sections 3.2.1 and 3.2.2 respectively. Two cases are used to ensure that the selected models will be able to predict the Nusselt number distribution and simultaneously be able to predict the influence of swirl on the impinging jet flow behaviour. The validation study investigates models of varying complexity from 2D axisymmetric studies (section 3.5), 3D steady RANS simulations (section 3.6 and 3.7), 3D Unsteady RANS (URANS) simulations (section 3.6), and finally LES (section 3.8).

The complexity of the fluid flow must be captured for both of these flow situations to be considered accurate for the intended CSP application and for optimisation of the flow parameters for heat transfer to be described in later chapters. The varying degrees of numerical modelling complexity form a foundation for the applicability of the models used later in the dissertation. The applicability of each of the models is summarised in the conclusions in section 3.9.

3.2 Validation experiments

In order to ensure the numerical model accurately captures the physics and complex flow of the swirling jet, the numerical model is validated against experimental work. Based on the literature for swirling impinging jets, there are few sources that can be used to validate the numerical work (for aerodynamically generated swirl) and as such, a variety of sources are consulted for this problem. For the validation multiple models of varying complexity are presented to investigate the applicability of the assumptions made for the validation. Keeping this in mind, the experimental methods and results must be well understood to assess the accuracy of the model.

3.2.1 Aerodynamically generated swirl

The primary experimental work consulted is based on the doctoral thesis of Ahmed (2016). This work consists of a series of papers published, namely, Ahmed *et al.* (2015a), Ahmed *et al.* (2016b), Ahmed, Al-Abdeli and Guzzomi (2016a), Ahmed, Al-Abdeli and Guzzomi (2017), Ahmed, Al-Abdeli and Matthews (2015b). The experiments used for the validation study are for jet impingement with aerodynamically imparted swirl using tangential inlet ports. The air is compressed and fed into the base of the nozzle and through the tangential ports. The fluid, air, then flows through a pipe where the flow further develops and exits out of the nozzle where after it impinges on a flat plate supplied with a uniform heat flux. The required swirl rates are achieved by varying the flow from the inlet ports (flow rates are presented in Appendix A). A dual wire (X-wire) CTA probe is used to measure the nozzle exit flow conditions, namely the axial and tangential velocity components. The accuracy of the mean velocity components is estimated and verified with pitot tube measurements to be 2 – 4% of the centreline velocity (Ahmed *et al.*, 2016b).

For the heat transfer measurements an infrared camera is used operating at a 7.5 – 13 μm wavelength range. The infrared camera is used as a non-intrusive measurement, has a high sensitivity (mK) and has low response times (Carlomagno & Cardone, 2010). The measurements of the heat transfer coefficients are conducted using the steady-state heated tin-film technique. At steady state, the heat flux distribution without an impinging jet measured circumferentially at $r/d = 2$ varies by 2% (Ahmed *et al.*, 2016b). The steady-state temperature distribution over the foil was measured to be within a variation of 0.3°C. The temperature distributions for the foil with jet impingement are determined by taking 150 thermal images at five frames per second and post-processed to give the time-averaged temperature distributions after steady-state conditions were met. The authors include a detailed analysis for how they compensated for the conduction of heat through the foil, the radiative properties of the foil, the calibration of equipment and the uncertainty errors of the experiment (Ahmed *et al.*, 2016b). The maximum uncertainties for Re and Nu are determined to be $\pm 4\%$ and $\pm 5\%$, respectively. The authors then validated the experiment with experiments conducted by other authors (for the no swirl case) and found that the Nu distribution are within good agreement within 4% for the impingement region where $r/d < 2$. The variation was attributed to the nozzle size and the boundary conditions at the exit plane.

The experimental work done is for a swirling jet impingement on a flat plate focused primarily on the near field impingement characteristics, like heat transfer characteristics and the pressure distribution. The same experimental setup was used for multiple domain geometries. The experimental setup is depicted in Figure 27.

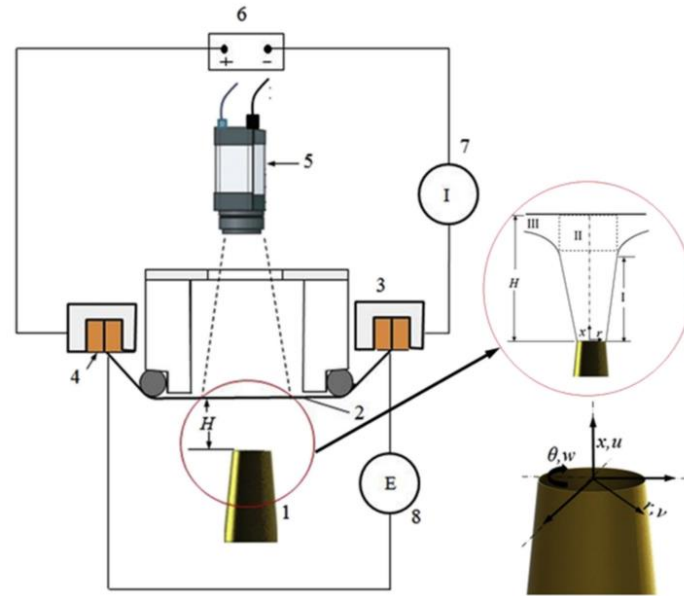


Figure 27. Vertical round jet impingement on a flat surface, experimental test setup schematic from Ahmed et al. (2017). Key: 1. Swirl nozzle, 2. Stainless steel foil (impingement surface), 3. Aluminium assembly to hold copper busbars, 4. Copper busbars, 5. Infrared camera, 6. DC Power supply, 7. Clamp meter to measure current at steel foil, 8. Digital multimeter to measure voltage across steel foil.

The swirl generator geometry is of significance for the numerical study as the inlet flow conditions have a significant effect on the swirling jet impingement characteristics. The tangential and axial jet volume flow rates are varied to achieve the desired swirl number, S , described by equation (17). The swirl nozzle with the flow conditioner and inlet jets as used for the experiment are depicted in Figure 28.

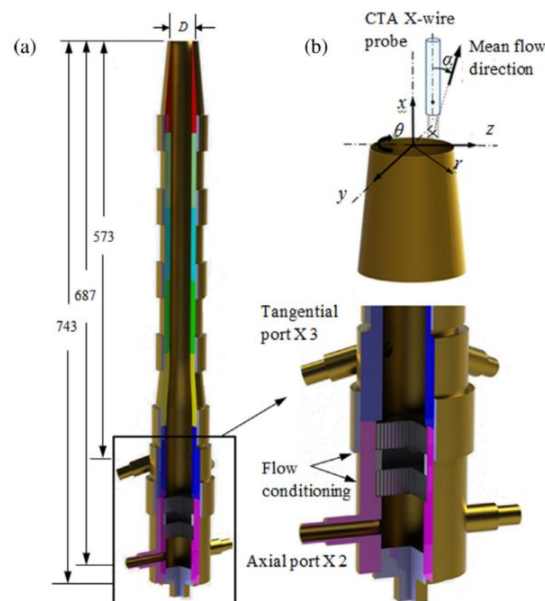


Figure 28. Sectional CAD drawing of swirl nozzle and inlet jets (Ahmed *et al.*, 2016b). (a) Full sectional view (dimensions in *mm*). (b) Setup for CTA measurements and coordinate system used.

3.2.2 Geometrically generated swirl

The use of geometric inserts do show a pattern for the oil film flow visualisations such as those experiments conducted by Mohamed Illyas, Ramesh Bapu and Venkata Subba Rao (2018), Nuntadusit *et al.* (2012a), and Nuntadusit, Wae-Hayee, Bunyajitradulya and Eiamsa-Ard (2012b).

For the application of SIJ the use of geometric swirl generators is investigated. The investigation is for helical vane inserts where the swirl is generated based on the vane's orientation within the exit nozzle. The study of geometric swirl generators can serve as a direct comparison for aerodynamically generated swirl where heat transfer and pressure drop can be compared. The method of swirl generation in the proposed solar receiver is not fixed and therefore a viable alternative can be investigated for optimal performance. The validation is conducted to ensure that the numerical model used for modelling the swirl flow can predict swirl generated geometrically as a form of passive velocity excitation.

In Hee, Youl, Taek and Suk (2002), the authors recorded the Nusselt number distribution over the impinging plate is recorded using thermochromatic liquid crystal spayed on the impingement surface and image processing system. The maximum uncertainty for the recorded Nu is 3.33% for the test case where $H/d = 10$, $S = 0.77$, and $Re = 23\ 000$.

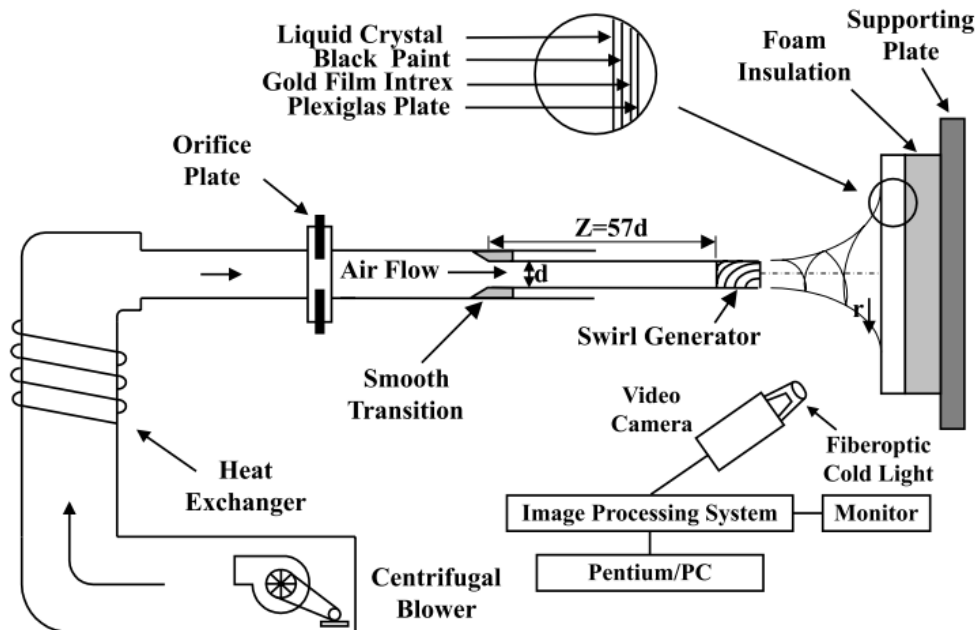


Figure 29 Experimental setup of jet impingement with geometric insert.

3.3 CFD model settings

This section describes the general settings for the simulations conducted. The computational inputs and the modelling techniques are similar for all five cases considered. The assumptions made for the numerical models are described in section 3.3.1, the fluid properties are presented in section 3.3.2 and the solution algorithm described in section 3.3.3.

3.3.1 Assumptions

For aerodynamically-generated swirl, the computational fluid domain investigated is based on the given geometry presented in Figure 28. Initially, a 2D axi-symmetric domain is generated with axi-symmetric swirl enabled. Ahmed *et al.* (2016b) have shown at selected reference radii that the temperature distribution varies by as little as 2% circumferentially from the mean temperature value within the near field impingement zone. The axisymmetric nature of swirl flows has been used for numerical investigations by multiple authors for jet impingement such as Ortega-Casanova (2011), Ortega-Casanova (2012), Ortega-Casanova and Castillo-Sanchez (2017).

The selection of the axi-symmetric condition is substantiated due to the aerodynamic generation of swirl as opposed to the geometric generation of swirl with inserts which requires 3D modelling. The implementation of a 2D axi-symmetric study has numerous advantages to predict flow behaviour and heat transfer at a relatively low numerical cost compared to larger 3D simulations. The 2D simulations can be parametrically studied for multiple flow conditions and give a better understanding for the physics governing the flow.

3.3.2 Fluid properties

The fluid used in the experiment was air. Air enters the experimental setup at the ambient temperature of $T_{in} = 293\text{ K}$; the inlet temperature is reported to vary by only 2% (Ahmed *et al.*, 2016b). The air properties used by the experimenters are provided at the inlet and presented in Table 8. For additional information on fluid properties refer to appendix A.

Table 8. Fluid properties for the flat plate JIHT validation.

Property	Value	Reference
Density	$\rho = 1.225\text{ kg/m}^3$	(Ahmed <i>et al.</i> , 2017)
Thermal conductivity	$k(T_j) = 0.0264\text{ W/m}\cdot\text{K}$	(Ahmed <i>et al.</i> , 2017)
Dynamic viscosity	$\nu = 15.11 \times 10^{-6}\text{ Ns/m}^2$	(Ahmed <i>et al.</i> , 2017)
Specific heat	$c_p = 1007\text{ J/kgK}$	(Ahmed <i>et al.</i> , 2017)

3.3.3 Solution algorithm

The solution algorithm used for all validation cases is the pressure-based Coupled algorithm. The solution was obtained by applying a second-order upwind scheme for the pressure and energy terms. Special considerations were made for the pressure scheme, the PRESTO! scheme is used as this has produced the most reliable results for capturing high-pressure gradients typically found in swirl flows. No convergence criteria were implemented. The residuals were monitored by inspection until the residuals stabilised, typically over 1 000 iterations. This was achieved when all residuals were below 10^{-5} . As the residuals are scaled, additional monitors are used in order to check the convergence of the solution. The solution methods for all of the simulation cases are summarised in Table 9.

Table 9. Summary of simulation numerical controls.

	Case 3.1	Case 3.2	Case 3.3	Case 3.4	Case 3.5
2D/3D	2D	3D	3D	3D	3D
Cell count	6.00E+06	2.00E+07	2.00E+07	1.50E+06	2.60E+07
Steady?	Steady	Steady	Transient	Transient	Transient
Turbulence	Transition SST	Transition SST	Transition SST	Transition SST	LES
Discretisation Schemes	2 nd order	2 nd order	2 nd order	2 nd order	2 nd order
Pressure-velocity coupling	Coupled	Coupled	Coupled	Coupled	Coupled
Pressure	PRESTO!	PRESTO!	PRESTO!	PRESTO!	PRESTO!
Momentum	2 nd order	2 nd order	2 nd order	2 nd order	2 nd order
Density	2 nd order	2 nd order	2 nd order	2 nd order	2 nd order
Energy	2 nd order	2 nd order	2 nd order	2 nd order	2 nd order
Turbulence	2 nd order	2 nd order	2 nd order	2 nd order	2 nd order
Time step	-	-	5.80E-04	-	1.00E-08
Maximum Residual	1.00E-04	1.00E-04	1.00E-05	1.00E-07	1.00E-06

3.4 General boundary conditions

The boundary conditions are relatively similar for all of the simulations. The models use velocity inlets for the inlets of the experiments. The outlets are modelled as zero pressure outlets. The ambient fluid surfaces at the top of the domain are specified with zero-gauge pressures. The models have a constant heat flux on the impingement surface. All pipe walls are adiabatic. The boundary conditions are summarised in Table 10. Where additional boundary conditions are considered the inputs will be presented. For each case the boundaries will be presented for each subsection.

Table 10. Summary of boundary conditions.

Boundary	Property	Case 3.1	Case 3.2	Case 3.3	Case 3.4	Case 3.5
Inlet	Velocity Temperature	v_{ax} = 13.6 m /s v_{tan} = 15.26 m /s 293 K	v_{ax} = 2.59 m /s v_{tan} = 33.98 m /s 293 K	v_{ax} = 2.59 m /s v_{tan} = 33.98 m /s 293 K	v_{ax} = 10.6 m /s 300 K	v_{ax} = 2.59 m /s v_{tan} = 33.98 m /s 293 K
Swirl	-	0 - 1.05	0 - 1.05	0 - 1.05	0 - 1.05	0.77
Outlet	Pressure Temperature	Zero pressure gradient T_{out} = 293 K	Zero pressure gradient T_{out} = 293 K	Zero pressure gradient T_{out} = 293 K	Zero pressure gradient T_{out} = 300 K	Zero pressure gradient T_{out} = 293 K
Impingement surface	Heat flux	q_w = 1120 W	q_w = 1120 W	q_w = 1120 W	q_w = 1000 W	q_w = 1120 W
Axis of symmetry	-	yes	no	no	no	no
Pipe wall	-	No slip conditions, Adiabatic	No slip conditions, Adiabatic	No slip conditions, Adiabatic	No slip conditions, Adiabatic	No slip conditions, Adiabatic
Time	-	Steady	Steady	0.06	Steady	0.025

3.5 2D axisymmetric swirl

The 2D axisymmetric swirl implies that the flow is symmetric about the central axis with a constant circumferential velocity. The investigation of swirl in literature has shown to exhibit this behaviour and this was observed for the experimental results.

3.5.1 Domain parameterisation and grid generation

The computational domain is generated in ANSYS SpaceClaim; the use of SpaceClaim allows for geometry generation to be scripted for analysis. The parametric fluid domain, the boundary conditions used for the simulations (listed in section 3.4) and the geometry zones are presented in Figure 30.

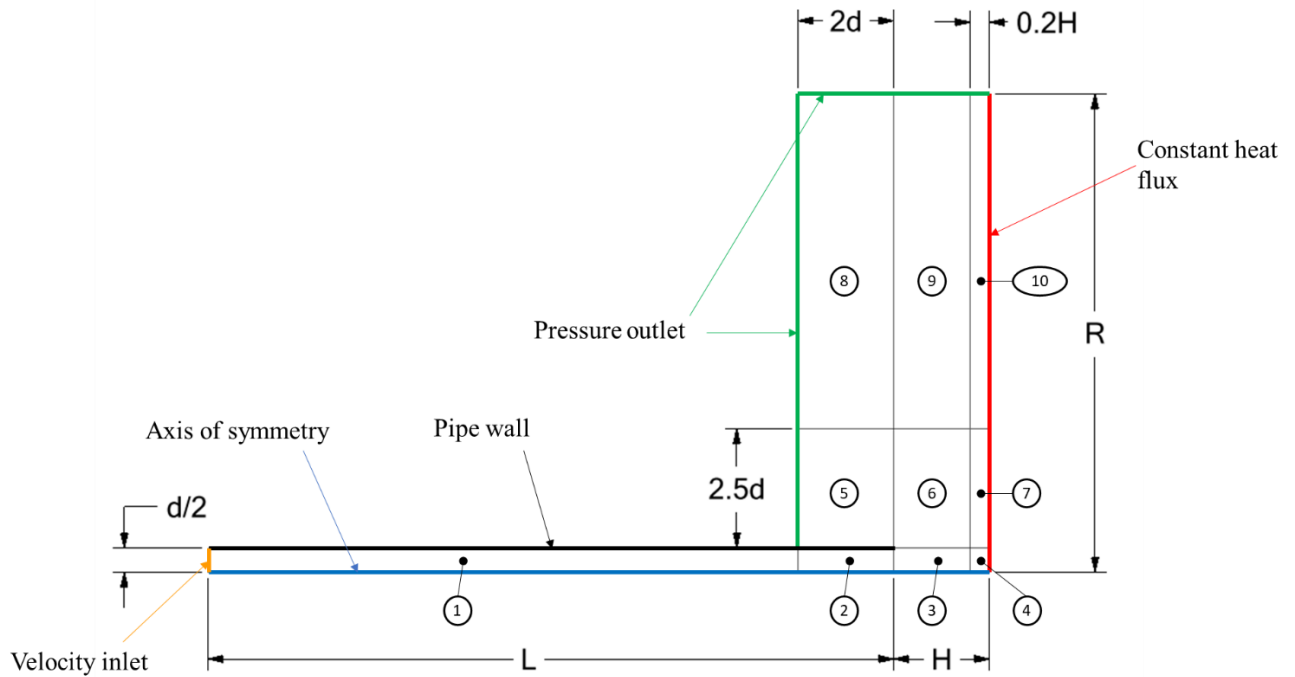


Figure 30. ANSYS 2D axisymmetric computational domain for flat plate swirling jet impingement.

The colouring of the geometry describes the boundary conditions used and the encircled numbers refer to the zones. The zones are of significance to the mesh generation strategy used where each zone's mesh is refined based on the required accuracy or number of cells needed in each zone to accurately capture the flow physics.

The fluid domain generated was used to investigate the effect of the size boundary conditions relative to one another. The geometry parameters used for the investigation with $H = 2d$ and their descriptions are given in Table 11.

Table 11. Domain geometric parameters and descriptions.

Parameter	Description	Value
d	Nozzle diameter	40mm
L	Entrance length	573mm
H	Nozzle exit to impingement surface length	80mm
R	Exit length of domain in the radial direction	400mm

The entrance length used is based on the described CAD geometry for the experimental setup. The length used is for the length of the 40mm pipe downstream of the tangential jets.

The mesh was generated using ANSYS Meshing. Quadrilateral face meshing with specified number of divisions and biases was applied to zones 1,2,3,4,6,7 and 10 (see Figure 30). Unmapped

quadrilateral/triangular meshes with specified element sizing were applied to zones 5, 8 and 9. The mesh is generated in this manner to allow the user to allocate more cells in the zones of interest and along the impingement wall. The number of divisions for each zone and the face sizing are input parameters that can be modified in the ANSYS Workbench environment. A coarse mesh of 11 831 cells is depicted in Figure 31.



Figure 31. Depiction of a coarse mesh, with the applied mesh refinement, of 11 831 cells for the axisymmetric 2D flat plate JIHT.

The mesh depicted is too coarse for the CFD analysis and is presented to show the mesh strategy and refinement of the mesh. The final mesh used (with a cell count of six million cells) is selected based on a mesh independence study (see appendix B). For this purpose, the quantities used to ensure mesh independence is the y_{avg}^+ and the Nu_{avg} over the entire impingement surface.

For the final mesh, the y_{max}^+ on the impingement surface was ensured to be $y_{max}^+ < 1$. Further details can be found in appendix B where the quality of the mesh and a detailed mesh independence study are presented.

3.5.2 Turbulence Model selection

The turbulence model used for the SIJ and conventional JIHT is investigated. The turbulence models selected for comparison are the SST $k - w$, $k - \omega$, $k - \epsilon$, kkl , RKE - EWT and Transition SST models. The turbulence model selection and the mesh generated are inherently coupled and the mesh used is important for capturing the turbulence within the fluid. For the investigation, a sufficiently refined mesh is used based on the mesh independence study further discussed in appendix B. The Nusselt number distribution over the impinging surface is used for the comparison as presented in Figure 32.

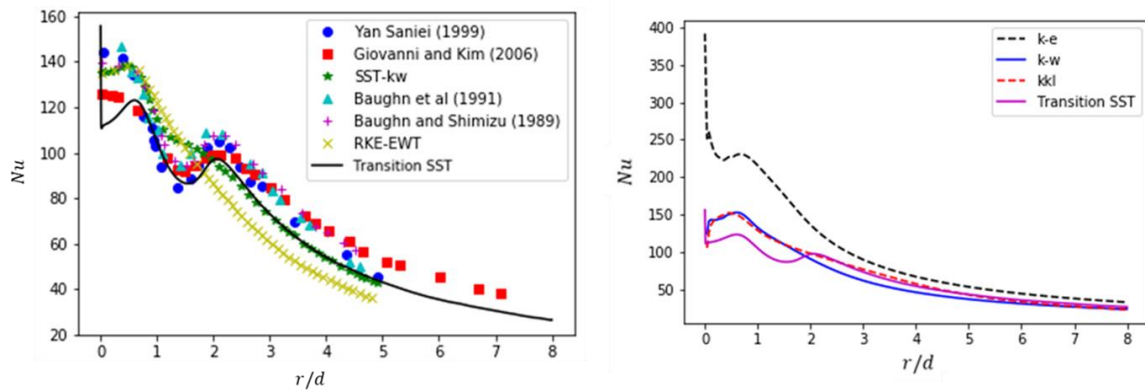


Figure 32. Nu vs r/D for different turbulence models for a conventional impinging jet.

As can be seen, the Transition SST model is the best able to approximate the experimental results as the second peak in the Nusselt number is evident. The other models do not accurately capture the Nusselt number as they do not allow for the laminar to turbulent transition.

3.5.3 Results for various swirl numbers (Case 3.1)

The best model in terms of mesh and turbulence model is used for comparison to the experimental results. The Nu distribution is plotted for the near field impingement region, where $r/d < 2$, with the experimental results measured from Ahmed (2016). The numerical results obtained are plotted individually for various nozzle to impingement surface heights and are consistent with the experimental heights used. The Nusselt distributions are presented in Figure 33 to Figure 36 for different H/d values.

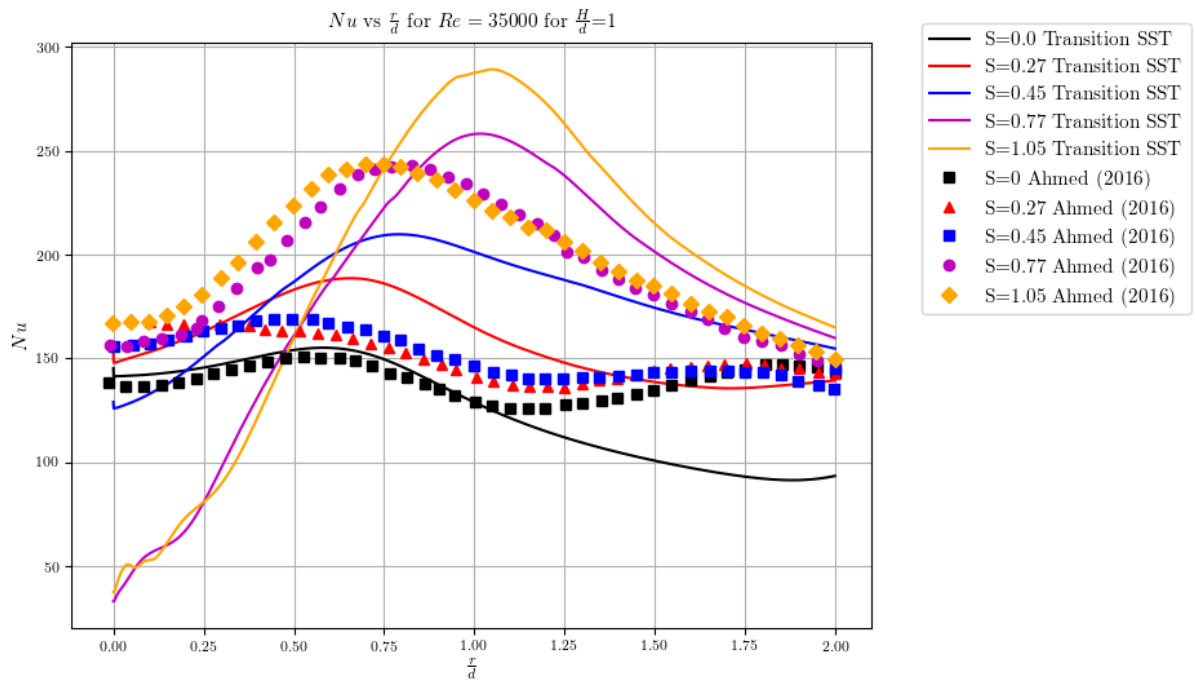


Figure 33. Nu vs r/d for experimental and numerical results for SIJ for $Re = 35\ 000$, $H/d = 1$, $d = 40\text{mm}$ and $S = 0, 0.27, 0.45, 0.77, 1.05$.

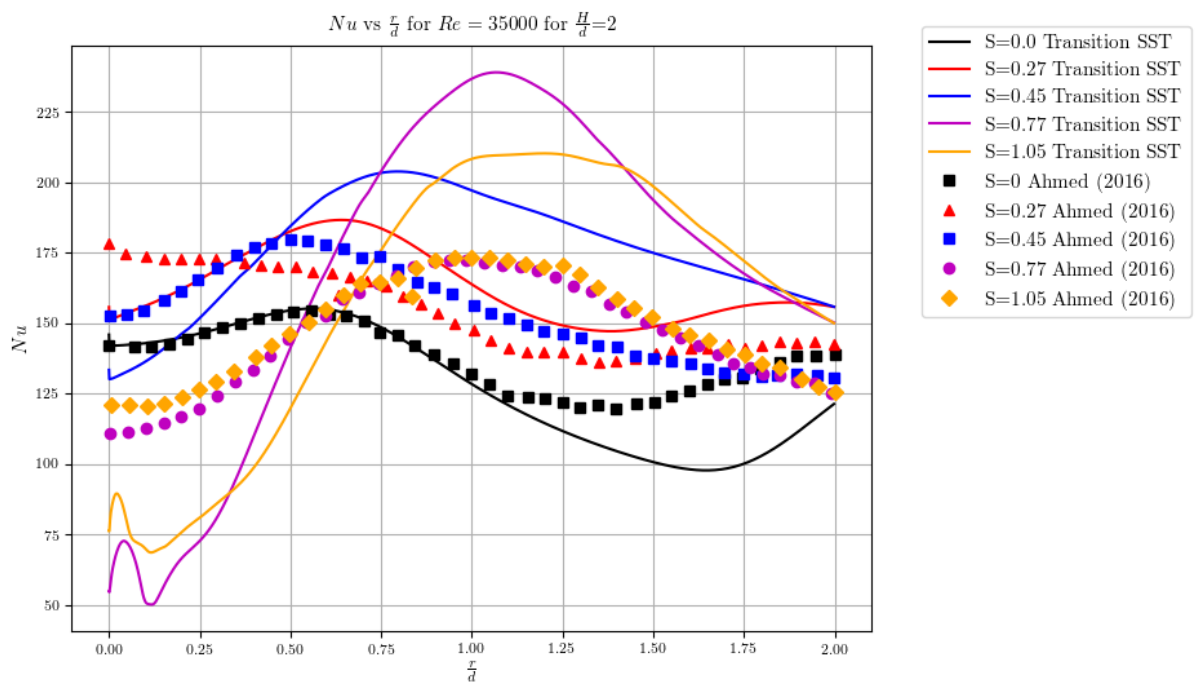


Figure 34. Nu vs r/d for experimental and numerical results for SIJ for $Re = 35\ 000$, $H/d = 2$, $d = 40\text{mm}$ and $S = 0, 0.27, 0.45, 0.77, 1.05$.

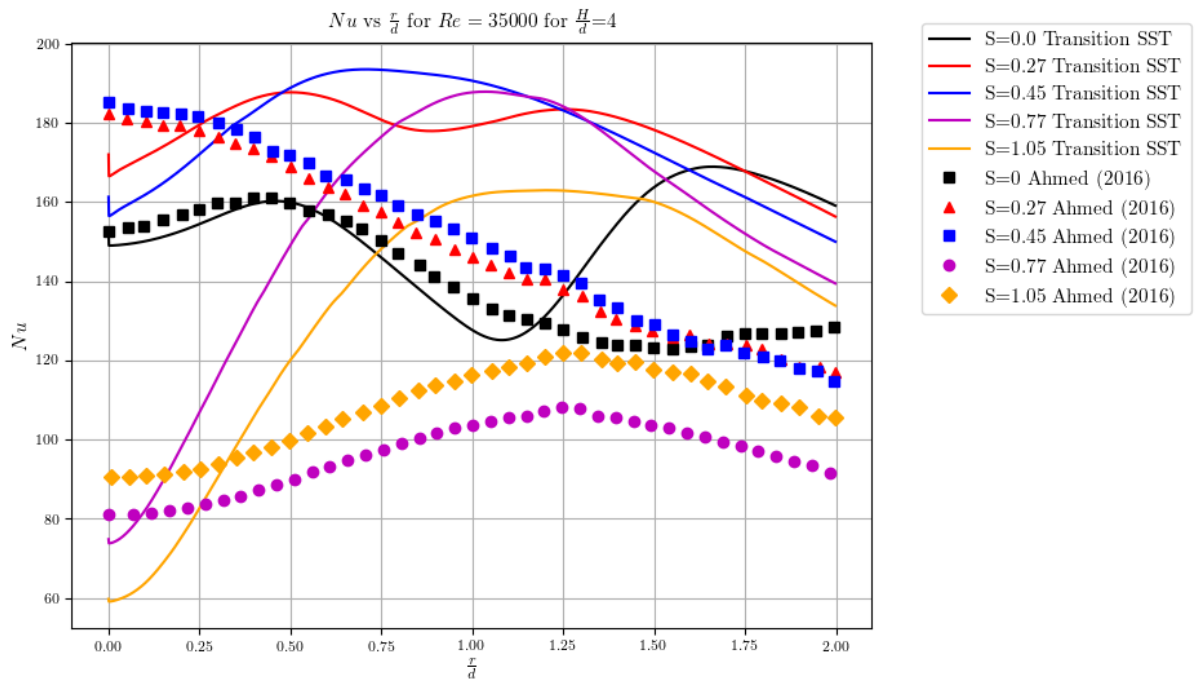


Figure 35. Nu vs r/d for experimental and numerical results for SIJ for $Re = 35\ 000$, $H/d = 4$, $d = 40\text{mm}$ and $S = 0, 0.27, 0.45, 0.77, 1.05$.

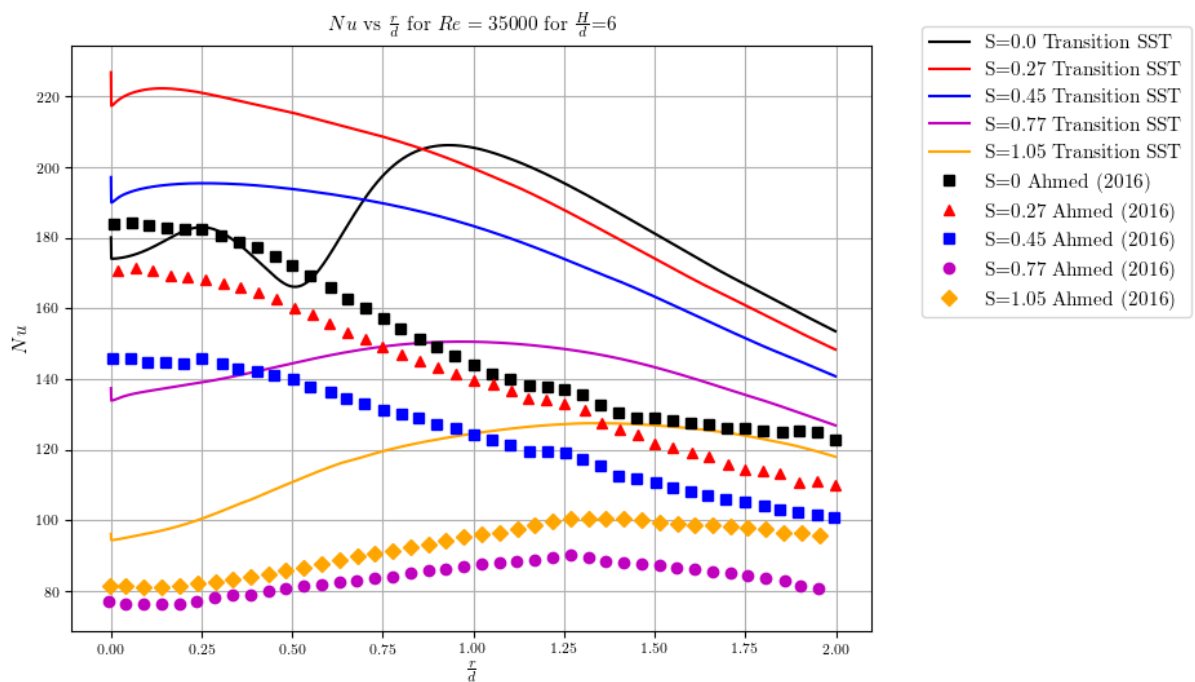


Figure 36. Nu vs r/d for experimental and numerical results for SIJ for $Re = 35\ 000$, $H/d = 6$, $d = 40\text{mm}$ and $S = 0, 0.27, 0.45, 0.77, 1.05$.

Discussion

Although the comparison between the experimental and numerical results is not good, the numerical simulation results follow the general trend depicted in the experimental results where the location of the Nu_{max} shifts radially outwards away from the axis of symmetry with an increase in swirl. This is likely attributed to the centrifugal force generated within the flow pushing the flow radially outwards as it exits the nozzle. Additionally, the increase in swirl at low nozzle to plate heights show decrease in the Nu_{st} accompanied with an increase in Nu_{max} . The net result of the swirl is to increase the average Nusselt number in the near-field impingement zone. The addition of swirl shows how the heat transfer can be enhanced but also how through the use of swirl the location of the maximum heat transfer can be manipulated to match the heat flux on the impingement surface. The use of swirl also shows a more uniform Nu distribution over the impingement surface, this can allow for a more uniform heat transfer over the surface particularly at high nozzle to plate heights.

The numerical simulations results compare better to the experimental results for smaller nozzle to impingement heights. The results do however show similar phenomena that were captured in other numerical studies of a similar nature by other authors such as Ahmed *et al.* (2017), Ortega-Casanova (2012), and Ortega-Casanova and Castillo-Sanchez (2017).

The errors and discrepancies between the numerical and experimental results may be due to the influence of the upstream conditions, underlying assumptions or the numerical model errors. The use of boundary conditions in FLUENT for the axisymmetric swirls may not capture complex interactions within the impingement region. The axisymmetric nature of the flow is largely dependent on the flow conditions namely S and Re , where there exists a critical Re for each S as discussed in section 2.4. The flow may in fact not be axisymmetric in nature and therefore the use of axisymmetric swirl will present erroneous results. The axisymmetric assumption is challenged for the simulation and may need to be neglected for the study of SIJ.

The upstream conditions for where the flow mixes after the swirl is generated are not reported on in the experimental paper. The complex nature of vortex shedding and the interactions of such vortices may not be captured in a steady RANS simulation and have been shown to have a transient nature. In the experimental findings of Ahmed (2016) the RMS nature of the flow on the impingement zone is highly variable. This indicates that over time the heat transfer on the impingement plane is highly variable, therefore assuming steady flow might not be adequate to predict the heat transfer over the impingement surface numerically.

The discrepancy of the results for higher swirl numbers at the stagnation point can be attributed to the observed recirculation zone in that region. The recirculation zones are known to be dependent on the flow domain, for high swirl numbers the recirculation region is expected at $x/d \approx 2$, as can be seen in

the simulation results Figure 34 the stagnation region has a slight peak (Gupta *et al.*, 1984). This peak may be due to the enhancing effects of the recirculation region at this jet offset distance. The recirculation zone may create a washup effect at this point and a reduction zone along the r/d direction resulting in the peak and dip in this region. In the near field impingement, the recirculation region effect is evident but not as pronounced as the $H/d = 2$ results as the recirculation zone is expected to only be fully developed by $x/d \approx 2$, therefore there is a slight instability in the region but as the recirculation region does not have the space to fully develop the effect, is not as pronounced. For the larger jet offsets the recirculation zone is fully developed and is further upstream of the impingement surface resulting in a reduction of heat transfer near the stagnation region as the axial velocity is significantly reduced. Hence for higher offset distances larger errors in the Nu distribution is predicted.

In the literature, the physics and flow behaviour of JIHT *without* swirl have shown large errors between the numerical and experimental results of errors between 20 – 40% (Zuckerman & Lior, 2006). The addition of swirl to the flow problem further complicates the flow and tests the limitations of turbulence models. The addition of swirl generates high pressure gradients within the flow, a finer mesh is therefore required to capture these gradients and not all numerical turbulence models have shown good accuracy at predicting these gradients.

It is evident that the model shows excellent correlation in some cases and poor performance in other cases. The models accuracy across the scope of all the cases is not reliable and therefore a more robust model should be developed. The improvement of the model can be achieved by conducting more experiments for SIJ and improvement of turbulence models that can further predict this type of flow. For large H/d distance the Transition SST model does show it may not be reliable for conventional JIHT. This may be further amplified by the addition of swirl within the flow domain. The model has shown to over predict the heat transfer rate significantly by up to 52% for conventional JIHT and up to 53% for SIJ.

The use of the axi-symmetric simulations may be justified in the sense that they present reasonable accuracy at smaller H/d distances. The simulations can also predict the trends of the heat transfer well when compared to the experimental results, the location of the Nu peaks, the \overline{Nu} over the impingement surface correlate well with experimental results (Ahmed *et al.*, 2016b). For the suggested study the use of axisymmetric swirl for concave surfaces is therefore justified as:

- The 2D simulations are relatively cheap to run.
- The integrated quantities such as \overline{Nu} are predicted reasonably well.
- The trends shown for the Nu distribution over the impingement surface are predicted for the numerical simulation.

In Chapter 4, the use of the 2D axisymmetric swirl case will be used to study the effects of concavity of the impingement surface and for an optimisation study. This is justified as for the described solar receiver application the nozzle to wall distance are required to be small and the use of axi-symmetric simulations Transition SST results are reasonable accurate. For the required application the turbulence model is further investigated for the 3D case discussed next and validated with experimental results.

3.6 3D RANS Simulations

In this section, the investigation is extended to a 3D domain where the upstream condition of the flow can be accurately captured by modelling the swirl generator based on the work of Ahmed (2016) (aerodynamically-generated swirl) and for geometric swirl generating inserts investigated by authors Fénot, Dorignac and Lalizel, 2015.

3.6.1 Ahmed swirl generator (Case 3.2)

For the aerodynamically generated swirl a 3D case is further investigated. The swirl is generated with axial and tangential inlet port and the fluid impinges on a flat surface. The swirl generator and the flow rates through each of the inlet ports control the swirl.

Swirl generator

The case used for validation is the same as the 2D case however the inlet geometry can now be resolved in 3D. The CFD model of the swirl generator is depicted in Figure 37.

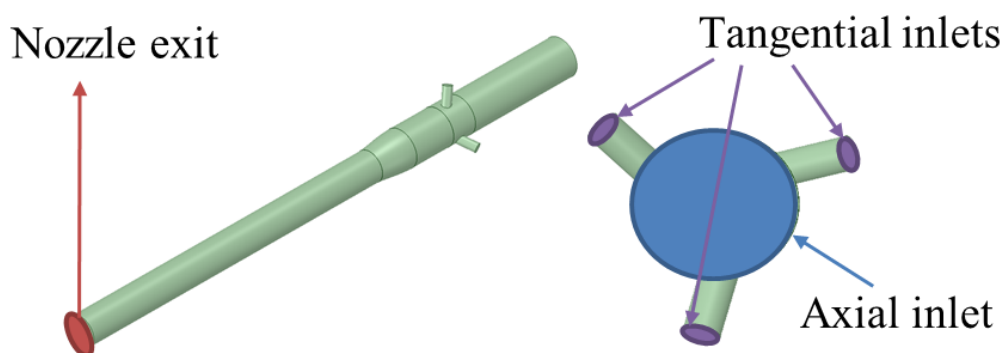


Figure 37. Ahmed aerodynamic swirl generator.

Swirl generator flow rates

The Reynolds number and swirl number are controlled in the experiment through varying the flow rate through the inlet ports. The range of swirl numbers considered, and the corresponding axial and tangential velocity components are shown in Table 12.

Table 12. Swirl intensities, volumetric flow rate and velocity components.

\dot{Q}_t/\dot{Q}_T	S	\dot{Q}_T (m ³ /s)	\dot{Q}_t (m ³ /s)	u_t (m/s)	u_{ax} (m/s)
0.00	0.00	0.0166	0	0.00	8.46
0.32	0.16	0.0166	0.0053	15.55	5.77
0.47	0.27	0.0166	0.0078	23.03	4.48
0.61	0.45	0.0166	0.01	29.72	3.33
0.69	0.77	0.0166	0.0115	33.98	2.59
0.84	0.83	0.0166	0.014	41.27	1.33
1.00	1.05	0.0166	0.0166	48.97	0.00

Fluid domain

The fluid domain is investigated for a constant jet offset distance of $H/d = 2$. The computational domain is kept constant for all the considered swirl numbers and is shown in Figure 38.

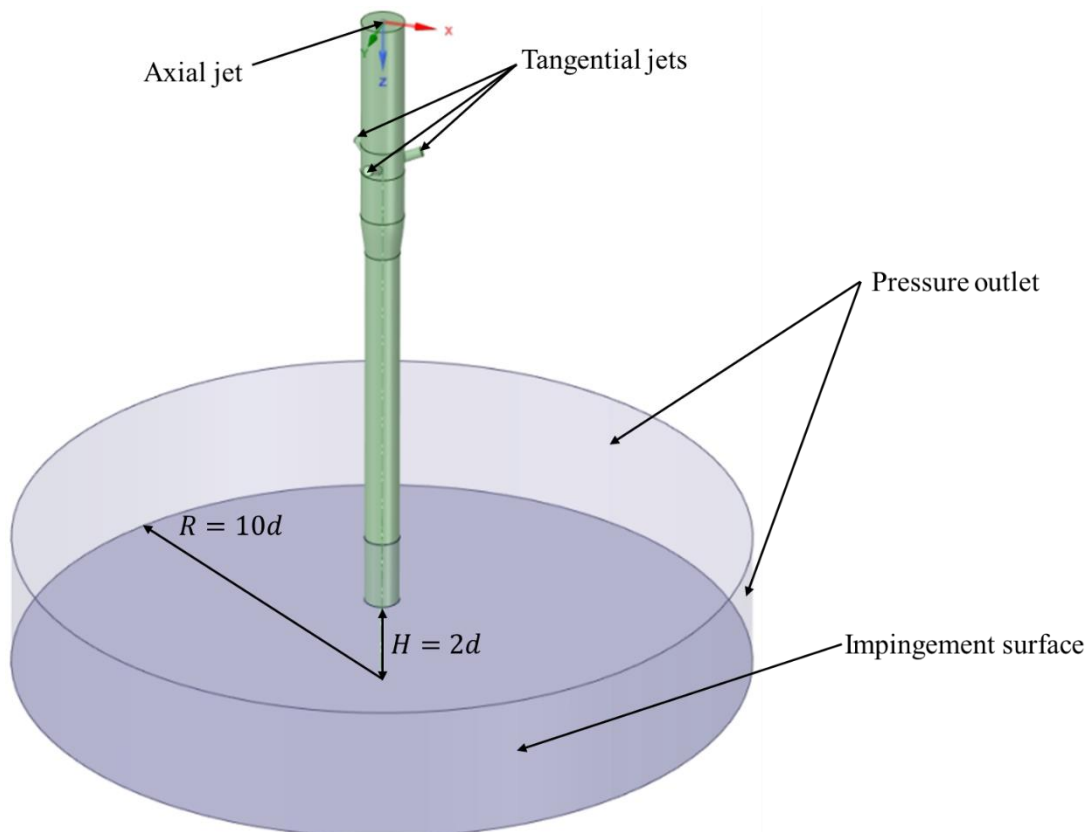


Figure 38. 3D SIJ domain for flat impingement surface based on the work of Ahmed.

The domain is further sub-divided into sections. This is done to allow for better mesh refinement controls within the domain allowing for more cells to be allocated in regions of interest. Several methods of sub-division and meshing are investigated for the case.

Meshing

The meshing of the geometry is always one of the most important considerations for CFD. The mesh size, strategy and cell type used can have a considerable effect on the results of the simulation therefore a significant amount of time is dedicated to mesh investigations to ensure that the solution is mesh independent and that the mesh is able to capture the physics governing the flow and reducing numerical errors introduced with the mesh. The detailed analysis of the mesh methods is presented in appendix B.

The mesh generated for the investigation is a structured mesh comprising of predominantly hexahedral elements and very few prisms located in the region where the tangential jets generate the swirl. This is used to ensure a high-quality mesh in the region. View of the mesh is presented in Figure 39.

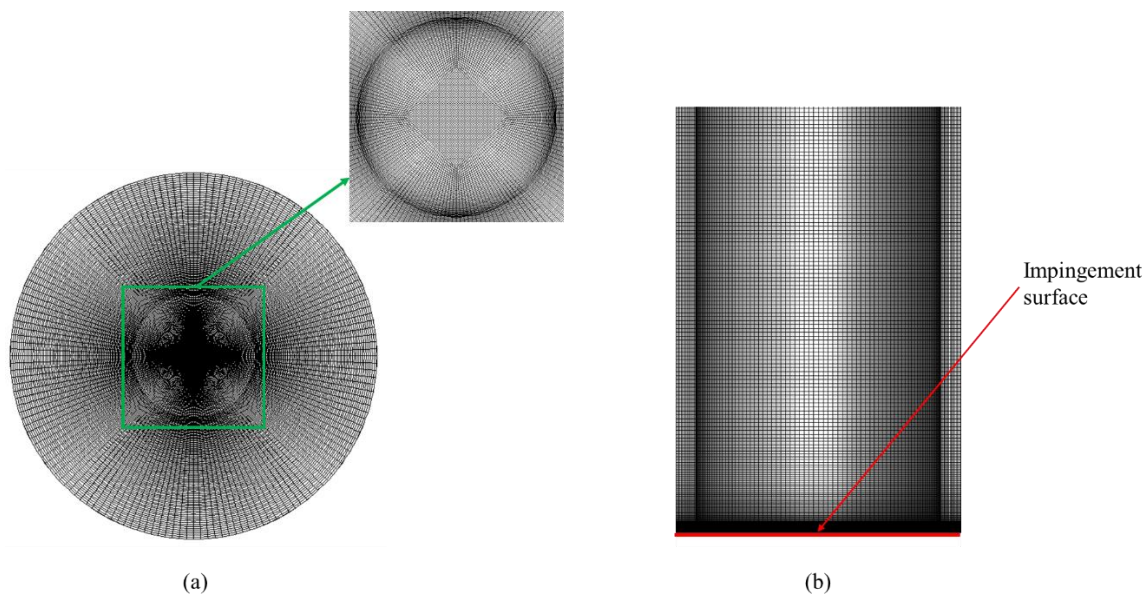


Figure 39. 3D SIJ mesh (a) Mesh on flat impingement surface (b) Mesh refinement near impingement surface in axial direction.

Fluid properties

The fluid properties and model selection for the case is the same as for the 2D axi-symmetric case presented in section 3.5. The fluid properties can be found in section 3.3.2.

Boundary conditions

The boundary conditions used are the same as for the 2D case where the wall boundaries and outlet boundaries are consistent. The velocity inlet boundary conditions differ in the sense that there are four inlet boundaries, however, the three tangential jets are identical. The velocity inlet conditions are set to be constant and normal to the boundary face with the velocity magnitude specified.

Results

The 3D validation results are compared to the experimental results. The experimental results are depicted in appendix A. The agreement is satisfactory for the mean flow as the major flow features are captured reasonably well when comparing the Nu distribution over the plate (Figure 42) and the velocity profiles through the domain (Figure 40 and Figure 41).

As can be seen from the Nu distribution on the impingement surface the stagnation point Nu still is predicted to be lower than the experimental results and the peak Nu is over predicted when compared to the experimental results (refer to Figure 87 in Appendix A). The location of the peak Nu is not located at the same radial position of $r/d = 0.985$ but at $r/d = 0.726$. The location of the peak Nu is located where the radial velocity reaches a maximum near the impingement surface, this has been found to be the case in the experimental results for impinging jets without the addition of swirl depicted in Figure 42. As can be seen from the Nu distribution over the impingement surface the Nu contours show that the distribution does vary in the circumferential direction. The variation in the distribution may be due to the inability of the mesh to capture the vortex core region and the vortex breakdown that occurs after the flow exits the jets nozzle.

The velocity magnitude is plotted on a central plane of the geometry in Figure 40. From the velocity field a recirculation zone is observed near the stagnation point in the impingement region. The recirculation of the flow appears not only in the axial but also in the tangential and radial velocity components this may be the reason for the reduction in heat transfer at the stagnation region. The results compare well to the observed profiles in the 2D cases.

The velocity profiles at the nozzle exit for various swirl numbers are depicted in Figure 41. The velocity comparison highlights the deficiency experienced in the 2D simulations where the velocity profiles are not accurately captured at the nozzle exit, due to the circumferential variation. The sensitivity of the model to the upstream conditions are extremely important for the accurate modelling of the SIJ. This cannot be captured in the 2D simulations as the complex flow interactions from swirl generator are not axisymmetric.

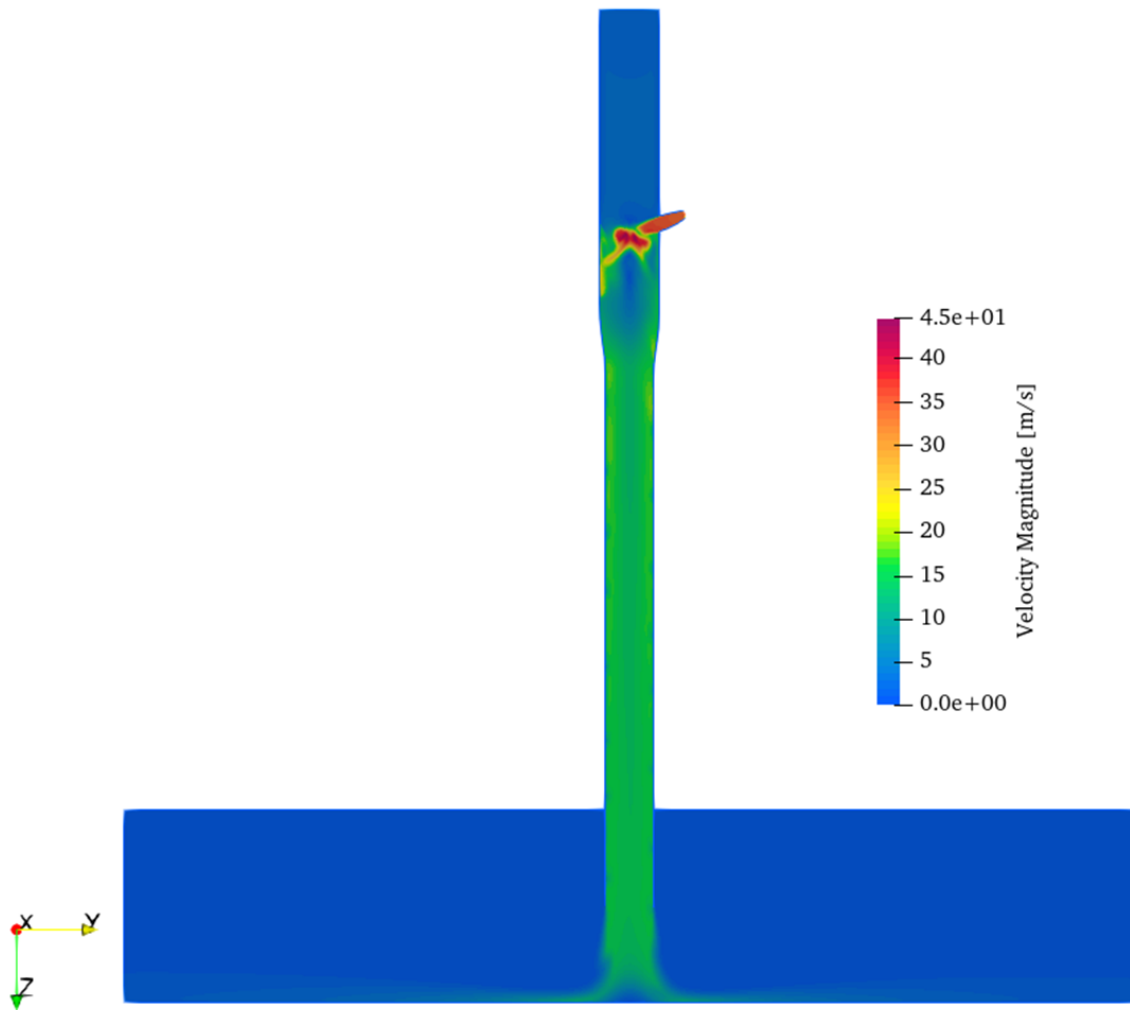


Figure 40. 3D SIJ velocity magnitude where $H/d = 2$ and $S = 0.77$.

A common behaviour for SIJ is observed where despite the reduction in the stagnation point Nusselt number the peak Nu is considerably enhanced along with the \overline{Nu} over the impingement surface. The Nusselt number contour plots show that local hotspots are formed as lobes (Figure 42). From the steady analysis it is evident that the heat transfer on the impingement surface is not uniform. In order to determine if this is due to the numerical scheme forcing the flow to be steady or if this is in fact a characteristic behaviour of the flow a transient RANS simulation is conducted.

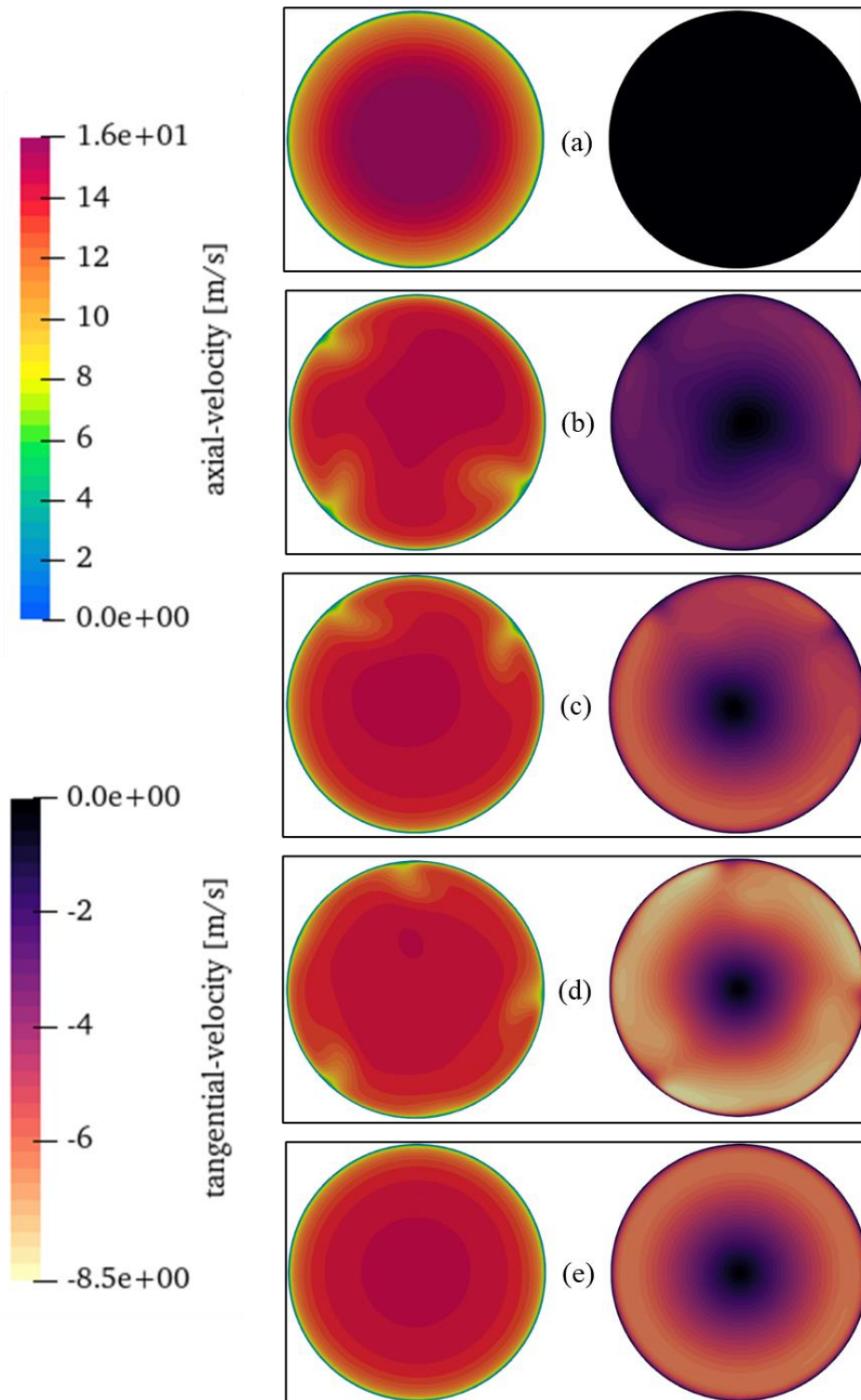


Figure 41. Nozzle exit axial and tangential velocity profiles for (a) $S = 0$ (b) $S = 0.27$ (c) $S = 0.45$ (d) $S = 0.77$ (e) $S = 1.05$.

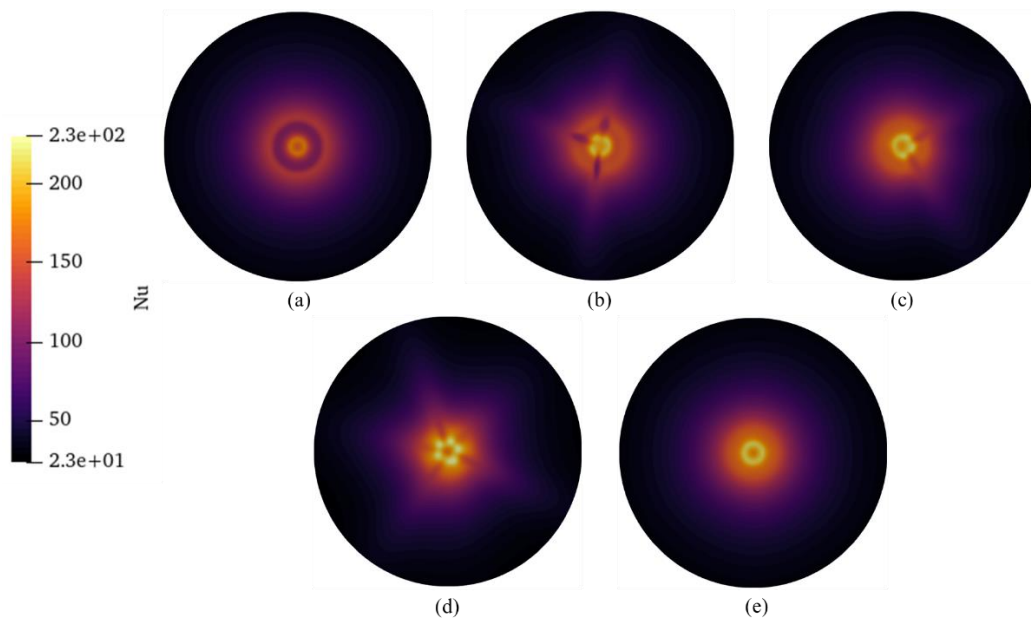


Figure 42. Nusselt number distributions on impingement surface where (a) $S = 0$ (b) $S = 0.27$ (c) $S = 0.45$ (d) $S = 0.77$ (e) $S = 1.05$.

3.6.2 Transient analysis (Case 3.3)

For the transient analysis the simulation is initialised from the steady RANS results of Case 3.2. The same controls are used but the time accurate solution and time are set up based on the solution stability to ensure the CFL number ensures stability the numerical controls are summarised in section 3.3.3. The boundary conditions are exactly the same as the steady 3D case.

Results

Based on the transient time accurate solution the Nusselt number distribution is monitored on the impingement plate and depicted in Figure 43 as a time series.

As is evident from the figure the maximum Nusselt number shows a periodic behaviour. The maximum Nusselt number rotates around the plate as a function of time. The rotational behaviour can be attributed to the complex flow mixing and large-scale vortex breakdown.

Vortex breakdown is dependent not only on the swirl number but also the Re of the flow. For high swirl numbers the vortex breakdown is axisymmetric and reaches the wall of the swirl generator. This only occurs in swirl jets when $S \geq 1$. For other high swirl cases the vortex breakdown is either spiral or double helix in shape (Gupta *et al.*, 1984). This phenomenon is evident in the Nu distributions on the impingement surface where at $S = 1.05$ the distribution is axisymmetric (Figure 42). Disruptions in the upstream conditions dramatically affect the flow behaviour. Swirl flow literature emphasize the flow

instabilities in the vortex core region. The vortex core is more unstable for lower swirl numbers and when high swirl is present the flow becomes more symmetric. Figure 42 indicates that the flow instability due to the vortex core breakdown may be true but this is not conclusive. The transient effects of the vortex core break down may provide a better explanation (Figure 43). The Nusselt number distribution is shown to be unstable and the lobes move around on the impingement surface. The lobes may be more influenced by the flow instabilities than can be predicted by the steady solutions. The stagnation point Nusselt number is shown to be higher than predicted by the 2D cases and steady cases.

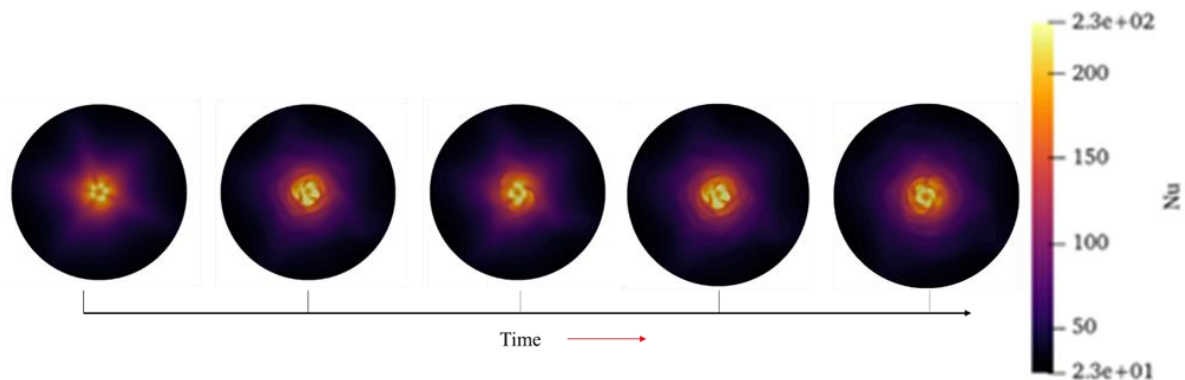


Figure 43. Nusselt number distribution on flat surface as a function of time where $Re = 35\ 000$ and $S = 0.77$.

For comparison the transient results are circumferentially averaged, and time averaged for the Nusselt number on the impingement surface. The URANS averaged results are depicted in Figure 44. As can be seen the Nusselt number is over predicted but the stagnation point Nusselt number is better predicted than for the 2D case. The difference could be due to the simulation time (0.5 seconds) compared to the realistic time of the experiment. The heat transfer may be over predicted due to the turbulence model however the most appropriate RANS model is used. The differences again may be due to upstream conditions not being accurately captured.

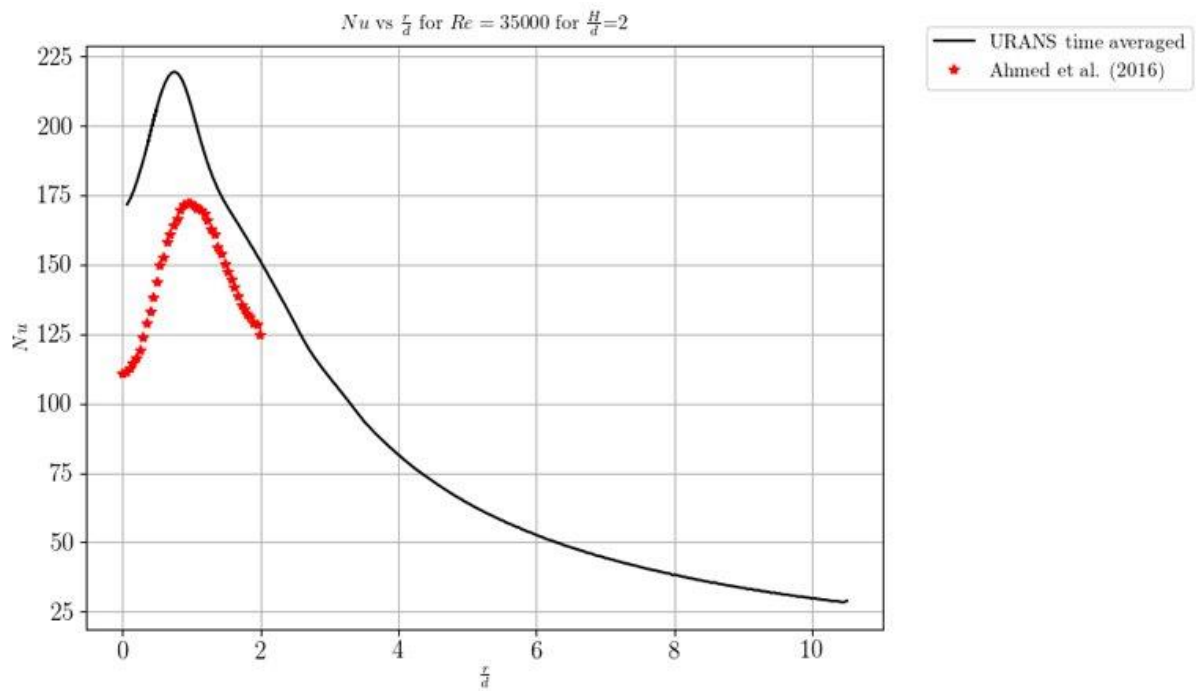


Figure 44. Time averaged Nusselt number in the radial direction.

3.7 Geometric swirl generator (Case 3.4)

To investigate a variety of methods of swirl generation, a geometric swirl generator is also investigated. This will highlight the differences in the heat transfer as a result of a geometric swirl generator.

Fluid domain

The CFD domain investigated is depicted in Figure 45. The common parameters as investigated in the previous studies remain consistent such as the height, inlet and exit domain extent.

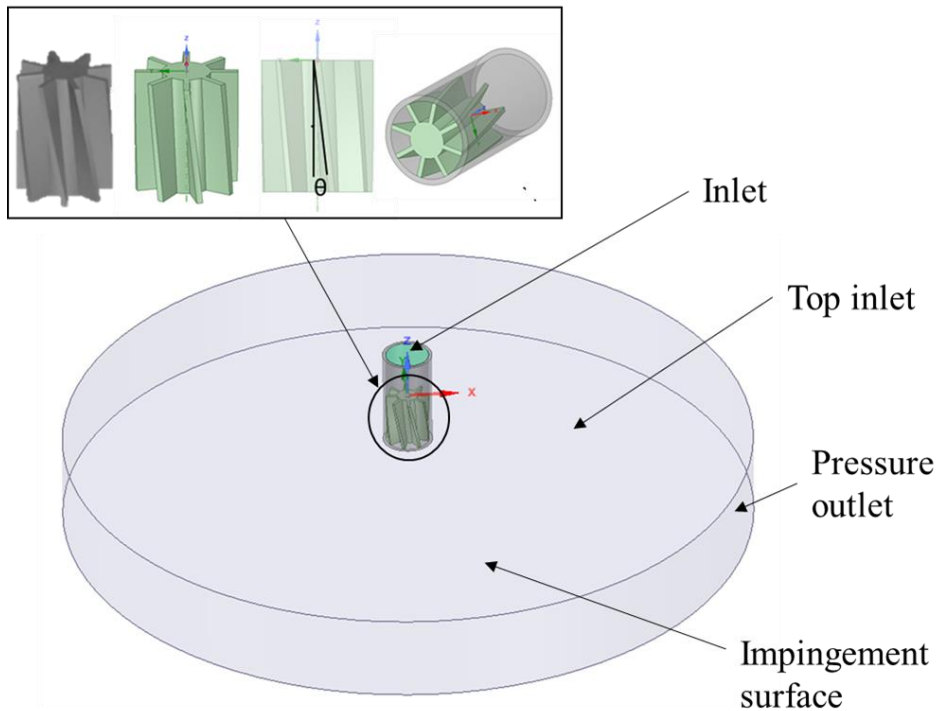


Figure 45. Flow domain with geometric swirl generator.

Fluid properties

The fluid properties remain consistent with the properties of air described for the previous cases.

Results

The effect of the Nu distribution due to the insert is compared to the experimental results in Figure 46, when evaluated along the radial direction corresponding to a lobe. As can be seen the experimental and numerical results are in strong agreement where the peak Nu is fairly well predicted and the corresponding location of the peak Nu . The stagnation point Nu is however not well captured by the simulation results and is severely under predicted by 77%. Also evident from this figure is the general increase in convection heat transfer due to swirl, compared to the no swirl case.

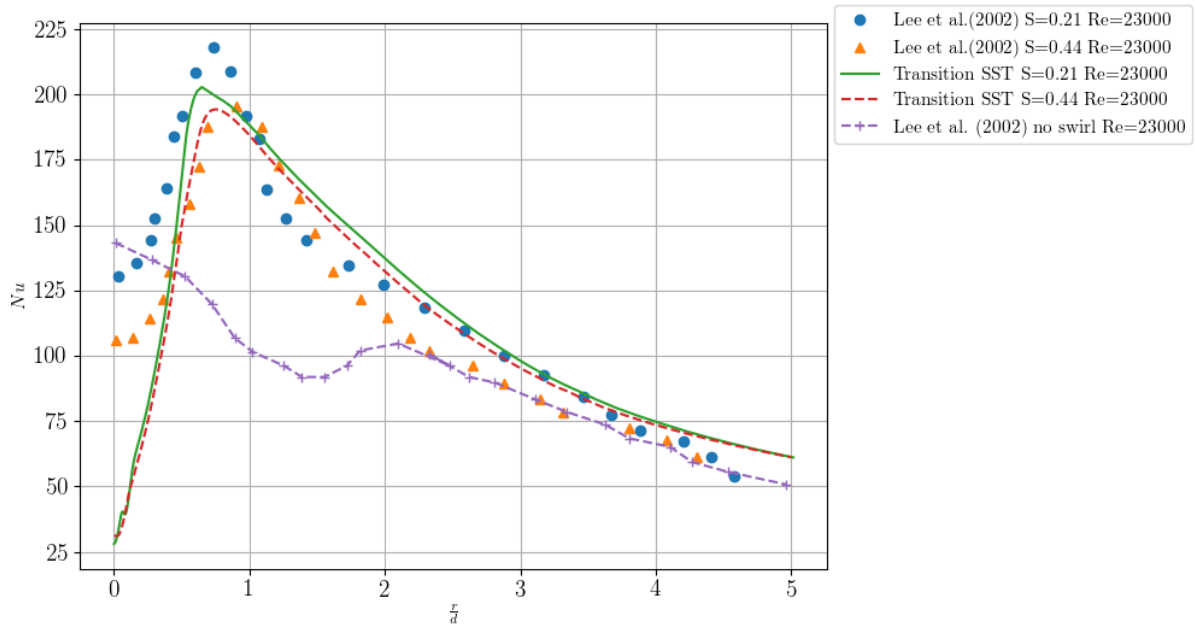


Figure 46. Nusselt number in the radial direction validation.

The Nu distribution on the impingement surface where $H/d = 2$, $Re = 23\,000$, and $S = 0.44$ is depicted in Figure 47.

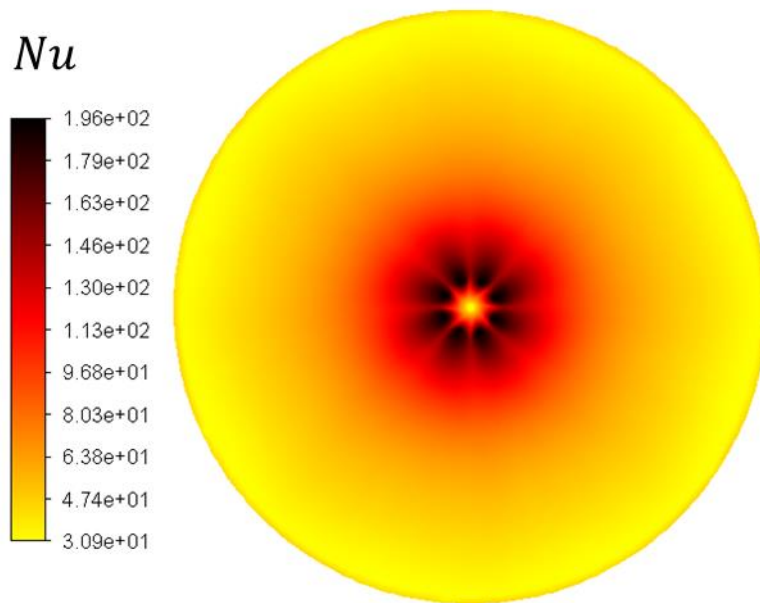


Figure 47. Nusselt number distribution on impingement surface due to geometric insert.

As is evident from the figure, the insert creates a footprint on the Nu distribution. The Nu distribution results in a fairly uniform heat transfer over the impingement region with distinct lobes occurring due to the multi-channel separation of the fluid when it exits the nozzle. The heat transfer is further enhanced by the multiple jet interactions along with the addition of swirl.

The maximum Nu does not occur at the stagnation point but rather at the location where $r/d = 0.74$ due to the swirl generator blockage effects (Figure 46). The multiple jets and the swirl effect become a maximum near the jet edge where a strong shear layer is present with large momentum enhancing the heat transfer. The velocity contours within the domain are presented in Figure 48.

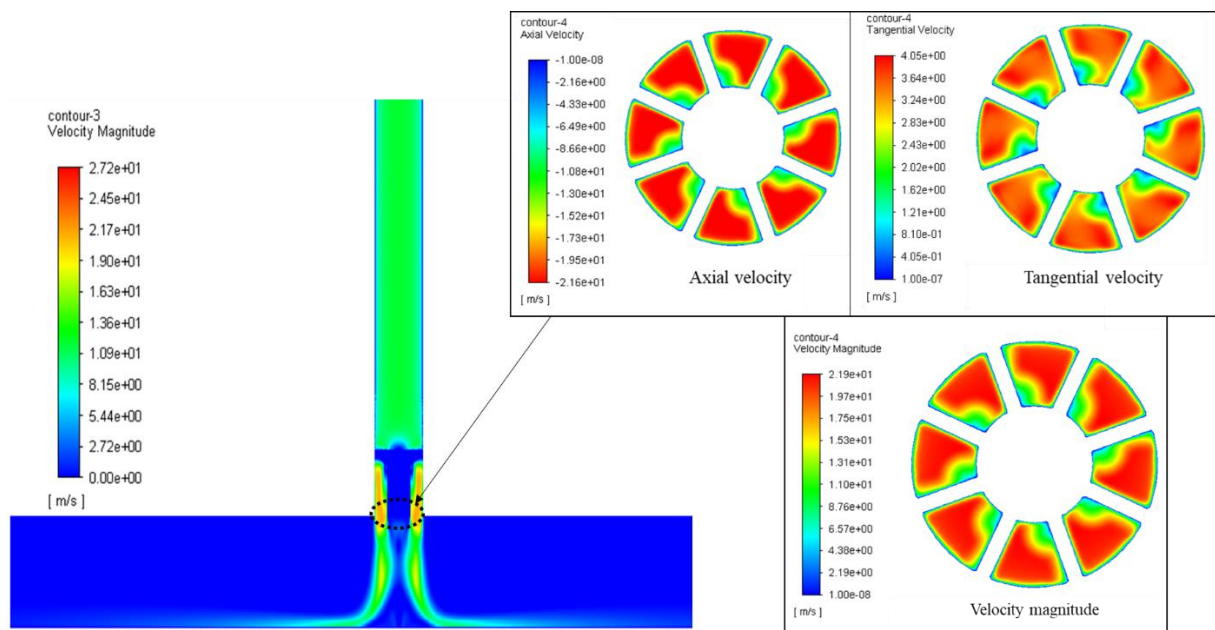


Figure 48. Velocity magnitude on mid plane and velocity distributions at nozzle exit.

As is evident from Figure 48, the swirl generator effectively imparts a tangential velocity in the flow and dramatically increases the velocity of the flow. There is a core region that develops in the impingement region due to the multichannel effect of the swirl generator. This can be the major factor reducing the stagnation point Nu .

For the geometric swirl generator investigated the use of steady RANS simulations show excellent results when compared to the experimental results, this comparison has also been shown in literature to be the case for multiple other geometric swirl generators such as twisted tape inserts and annular flow swirl generators.

3.8 Large Eddy Simulation (Case 3.5)

To address the limitations of the RANS models used in the study LES is used for a single case because of its high cost. LES has shown in the past to overcome the RANS limitations and provide more accurate simulations for JIHT. The use of LES for accurate predictions of JIHT is well documented in literature and has led to further insight into the mechanisms governing the flow (Grenson & Deniau, 2017; Uddin *et al.*, 2019).

A major issue is the size of the grid required for the LES simulation some authors have used about 26 million cells (Grenson & Deniau, 2017) and mentioned the LES simulation is not “adequate” for the investigation of $Re = 10\,000$. Therefore, the following is only a preliminary study to gain further insight into SIJ flow behaviour.

3.8.1 Domain and mesh strategy

For the mesh of the solution domain the requirements of the cell size are strongly linked to the Re of the jet. For the cell sizing requirement for mesh independence the mesh is successively refined to the point where the solution does not practically change, this can be done as shown in previous chapters by monitoring selected properties and showing mesh independence or quantitatively using the grid convergence index. For LES there is no grid independence as the small-scale eddies are explicitly described as a function of the grid through the use of the subscale model. It can be stated that DNS is the grid independent limit of LES, however the grid refinement does affect the solution and is considered for accuracy purposes. The sufficiency for LES simulations is when the statistics of the flow are insensitive to grid refinement. This an extremely costly procedure to follow as it requires the simulation of the flow for multiple grids through the required number of cycles and the statistics of the simulations to be calculated.

Inaccuracy for LES is due to 3 sources: numerical discretisation, limitations of the subgrid model and slow statistical convergence. There are always numerical errors as LES is under resolved.

Typically, in literature the grid is defined based on the dimensionless grid parameters in each of the dimensions. The viscous length of the domain is the defining characteristic used to ensure the mesh is sufficiently refined for wall resolved constraints (Grenson & Deniau, 2017; Uddin, Weigand & Younis, 2013; Uddin *et al.*, 2019). The viscous length is defined as

$$l_v = \frac{\mu_t}{\nu} \quad (19)$$

Therefore, it is desired that the cell size in each direction be sufficiently resolved such that the following are met:

$$\Delta x^+ = \frac{\Delta x}{l_v} = 25$$

$$\Delta y^+ = \frac{\Delta y}{l_v} = 25$$

$$\Delta z^+ = \frac{\Delta z}{l_v} = 2$$

where the refinement on the impinging plate in the axial direction is the smallest as that is the direction of the boundary layer growth as the fluid flows towards the outlets.

The mesh strategies followed the same guidelines where the objective of the study was to compare the results obtained to experimental results for a primary flow cases where $S = 0.77$. In addition, the mesh quality metrics, steady resolved flow fields and heat transfer characteristics were analysed before the implementation of the LES simulations. The mesh strategy used for the Steady 3D cases are used where a final cell count of 26 million cells are used. Additional cells would be used however the memory limit of the available computer was reached with 26 million cells.

3.8.2 Numerical solution procedure

The numerical solution procedure is consistent with previous cases and is summarised in Table 9. The only significant difference is the use of the WALE subgrid scale viscosity model. The WALE model has been shown to be the best subgrid scale viscosity model for impinging jets in literature (Arya & De, 2019; Dairay, Fortune, Lamballais & Brizzi, 2015; Grenson & Deniau, 2017).

Simulation duration

The simulation duration for the LES simulation is characterised based on the cycle time characterised by the time taken for the fluid to flow through the domain from the inlet to the exit. The through flow time is defined as the domain length divided by the bulk velocity (Durbin & Reif, 2011), typically 5-10 flow times are required for statistical steady state to be achieved. Additionally, the cycle time can be based on the oscillatory frequency of the flow which is defined as the dimensionless unit the Strouhal number. The Strouhal number is typically given in the form of equation (29).

$$St = \frac{fL}{U_b} \quad (20)$$

The St is presented for the period of the column mode of a free jet where $St \approx 0.4$ (Gupta *et al.*, 1984). The basis of determining the frequency in this manner is commonly adopted for LES in literature from

multiple authors (Dairay *et al.*, 2015; Grenson & Deniau, 2017; Uddin *et al.*, 2013). Based on the nature of the free jet the frequency is dependent on the bulk fluid velocity and the diameter of the nozzle.

The St number in the literature is always referred to for a free jet as being $St \approx 0.4$. This is considered where the simulation is conducted typically for eight to 12 cycles of the frequency based on the U_b and the D (Dairay *et al.*, 2015; Grenson & Deniau, 2017; Uddin *et al.*, 2013). The maximum number of cycles used was 20 for statistical analysis. For the given flow conditions, the f is calculated to be 170 therefore it is estimated that 170 cycles are completed every second. A full cycle is then determined to be 0,0058823529 *seconds*. It is then estimated that the complete solution of 12 cycles will be completed after 1 411 765 iterations.

Typically, a dimensionless time step is used and CFL is smaller than one. The dimensionless time step proposed by (Uddin, 2008; Uddin *et al.*, 2013) is:

$$\Delta t \frac{U_b}{D} = 7E - 8$$

For $Re = 23\ 000$ the physical time step used was $5.07E - 10$ seconds. Additionally, the authors Grenson and Deniau (2017) have proposed a similar approach however ensuring that the CFL remains less than 1.4 in the simulation resulting in a non-dimensional time step of $\Delta t \frac{U_b}{D} = 3E - 5$ giving a physical time step of $7E - 8$ *seconds*. From the required number of cycles the statistical field for the simulation can be computed and analysed.

Results

To visualise the complexities of the flow an instantaneous snapshot of the flow eddies, velocity profile, and Nusselt number are depicted in Figure 49.

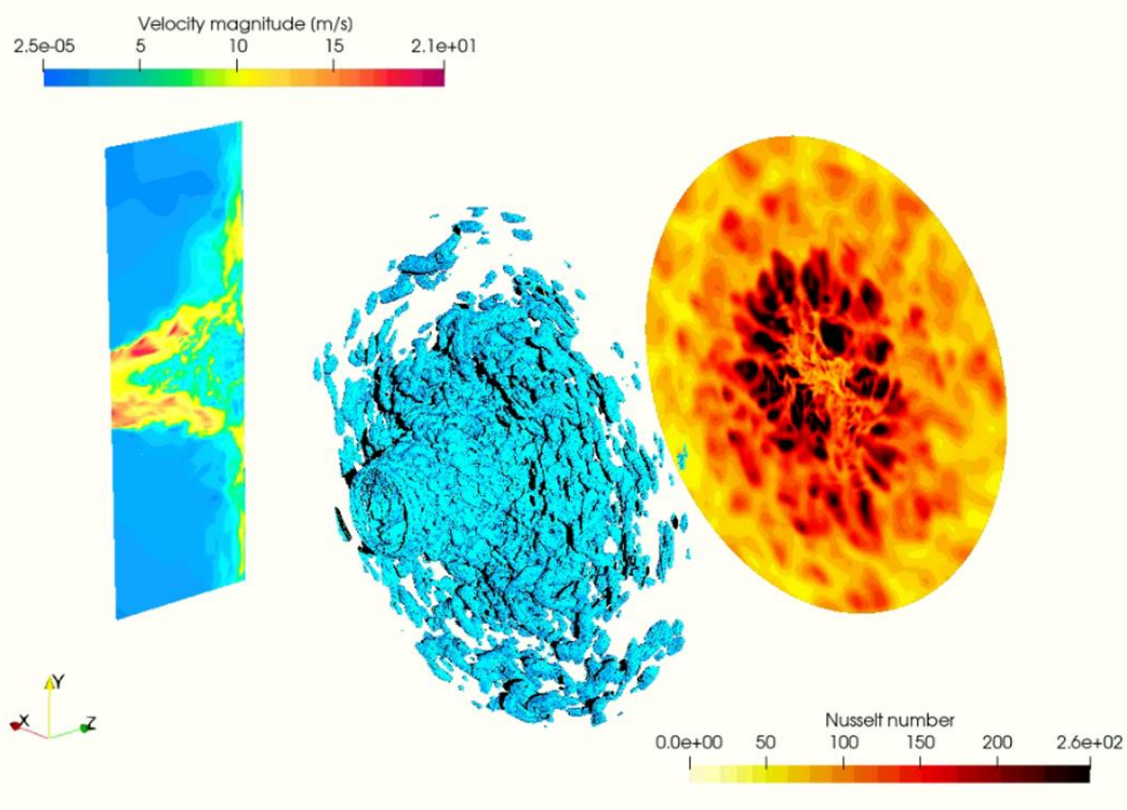


Figure 49. LES instantaneous velocity magnitude contours in central plane and on Q-criterion iso-surfaces, and Nusselt number distribution on impingement surface.

As can be seen, the flow is highly complex with the vortices visualised with the contours of the Q-criterion. The velocity contour plot shows the complex mixing in the stagnation region. The mixing in the stagnation region may be the reason why the 2D and RANS are not able to accurately predict the Nusselt number in this region. The Nusselt number contours on the impingement surface show a large number of local hot spots are created, this may be due to the small-scale eddies in the flow. The maximum Nusselt number is significantly higher than in the RANS models, this may be due to a small-scale wash up effect on the impingement surface.

The LES simulation Nusselt number distribution on the impingement surface is time averaged and circumferentially averaged. The averaged result is plotted against along the radial direction in Figure 50. The LES simulation shows a very accurate prediction of the Nusselt number on the impingement surface with the peak Nusselt number the stagnation point Nusselt number, the location of the peak Nusselt number is slightly off. The most likely reason for the superior performance of the LES model is due to the small-scale vortices being simulated which may be an underlying phenomenon that enhances heat transfer as has been shown in literature for conventional impinging jets without swirl. The LES simulations shows a lot of promise but need to be investigated further. Finally, the power

spectral density (PSD) of the axial velocity is plotted against the Kolmogorov constant showing that the energy spectra decay is captured accurately, as depicted in Figure 51.

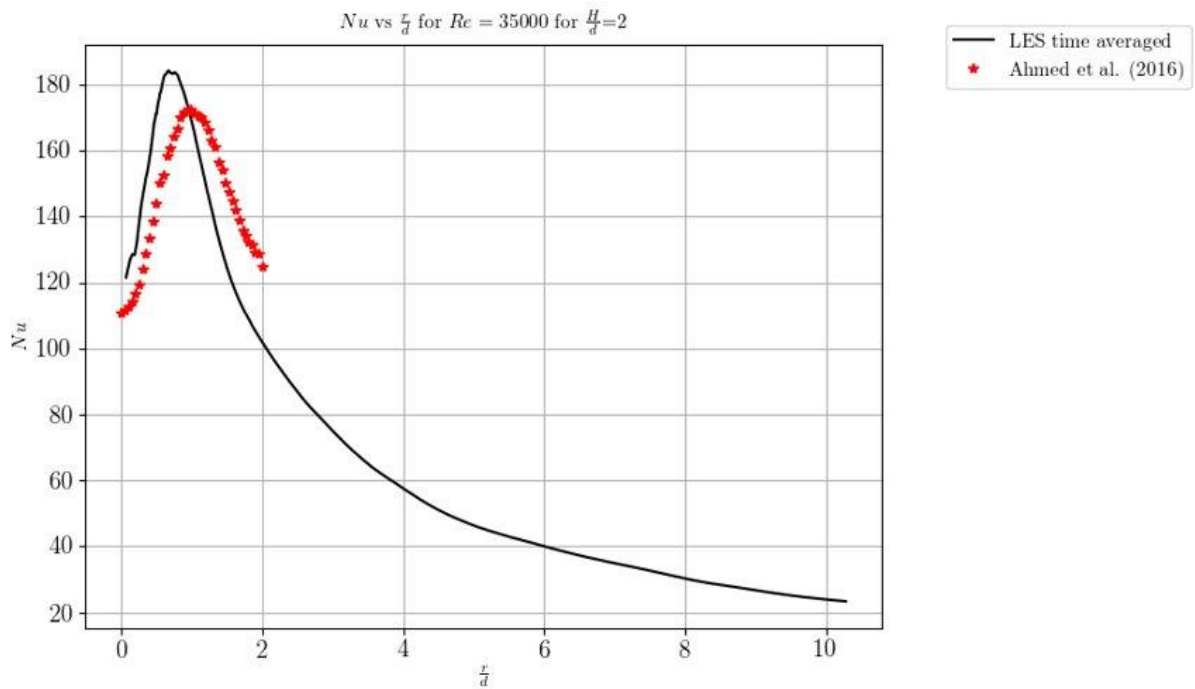


Figure 50. LES time averaged Nusselt number distribution on impingement surface in the radial direction.

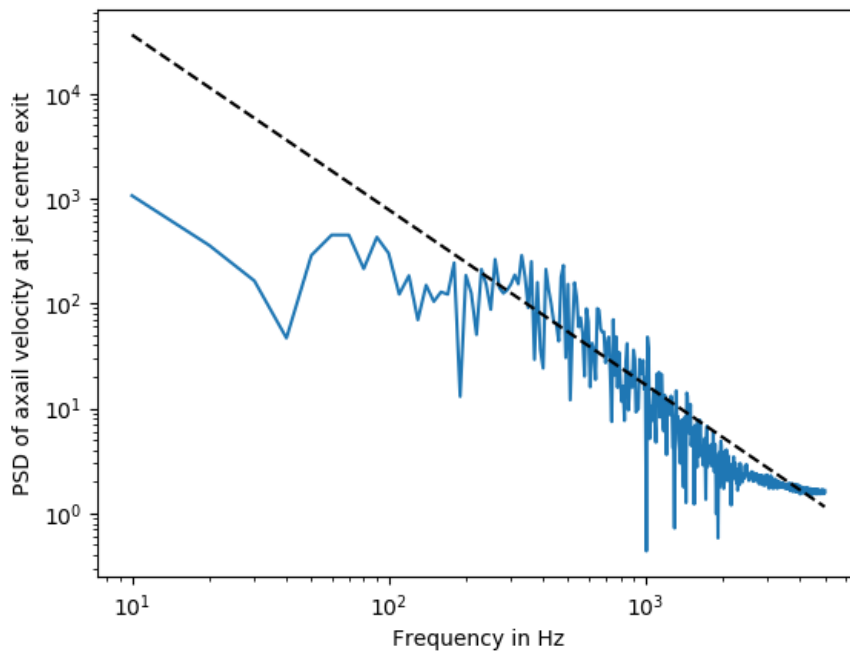


Figure 51. PSD of axial velocity at jet centre exit, Kolmogorov constant plotted for reference.

3.9 Conclusion

CFD simulation presents the most accurate way of modelling JIHT flows. For the researcher's investigation, the Transition SST model has proven reliable for JIHT analysis. Although there are numerical errors associated, JIHT can be further investigated with LES for enhanced accuracy (Craig *et al.*, 2018). The validation of the experiments considered show the trends of the heat transfer. The magnitude of the local maximum heat transfer coefficients, for the double humps, were not accurately captured. From the initial validation, a thermal model of the proposed receiver can be carried out using the Transition SST model.

Case 3.1 showed that the 2D axi-symmetric model does not do a good job at predicting the Nusselt number for most cases. The stagnation Nusselt number and location were not predicted well. The model's prediction was worse for higher jet offset distances. The peak Nusselt number was consistently over predicted. The swirl generator was not considered and the flow was assumed to be axi-symmetric. The performance of the axi-symmetric model cast doubt on the question as to whether the flow is axi-symmetric in nature or if this only appears when it is spatially averaged in 3D.

Case 3.2 modelled the aerodynamic swirl generator in 3D. 3D simulations have limitations due to a higher computational expense in comparison to 2D simulations. The swirl generator showed a difference in comparison to the flow profiles of the 2D cases. The importance of modelling the swirl generator is highlighted by the 3D cases. Evidence of flow instabilities for lower swirl numbers are suspected from the Nusselt number distribution and the incorrect prediction of the steady-state profiles.

Case 3.3, investigated the transient effects of the flow. The transient effects showed that a spatial and time averaging is an important consideration for the flow. The flow instabilities present created a non-uniform peak Nusselt number distribution on the impingement surface. The instabilities further influenced the heat transfer with local hotspots, and when averaged, the Nusselt number is over predicted.

In Case 3.4, a geometric swirl generator was investigated in 3D. Geometrically generated swirl showed a distinct imprint from the swirl generator insert. The Nusselt number is not uniform as the flow splits and act as multiple jets. The peak Nusselt number was accurately predicted but the stagnation point Nusselt number was not well predicted.

Case 3.5 showed the complex flow behaviour of a SIJ by modelling it using LES. The effect of smaller eddies on the heat transfer was shown to be significant to accurately predict the heat transfer behaviour. The flow showed complex mixing and smaller local heat transfer hot spots. The consideration of the

small scale eddies and the transient behaviour show an excellent prediction of heat transfer averaged over time.

From all of the cases solved, the lessons learnt from the modelling approaches can be summarised in Table 13.

Table 13. Summary of modelling approaches.

Model	Applicability
2D axi-symmetric swirl	<ul style="list-style-type: none"> • Fails to adequately predict the stagnation point Nu • Reasonable estimate of average heat transfer • Predicts the location of peak Nu reasonably well • Possible use for fundamental optimisation
3D Steady RANS	<ul style="list-style-type: none"> • Fails to adequately predict the stagnation point Nu • Provides far better predictions of Nu distribution • Predicts geometric generated swirl very well • Can be used for optimisation of internal flow geometry
LES	<p>Based on preliminary investigation:</p> <ul style="list-style-type: none"> • Predicts Nu distribution well for geometric and aerodynamic generated swirl • Predicts the stagnation point Nu far better • Possibly the only method of predicting high swirl flows accurately, due to unsteady vortices

4 NUMERICAL OPTIMISATION OF CONCAVE SWIRLING JET IMPINGEMENT AND CONE RECEIVER

4.1 Introduction

For the investigation of the effect of surface curvature on SIJ there are no prior experimental or numerical studies. In order to give credibility to this investigation case, the previous results from the flat surface impingement validation case (described in Chapter 3) are used and the validation of a secondary case for impingement on a curved surface without the addition of swirl is used. Using the two additional cases where SIJ and surface curvature are investigated separately, a generalisable numerical model can be used to capture both cases physics where no experimental results are available. The simulations for RANS are to the author's knowledge the first investigation of its kind for SIJ on a concave surface.

The subsections are presented in a similar format to the validation Chapter 3 with the considerations of the additional complexity involved with the concave surface. The experiment used for comparison where swirl is not present is described in section 4.2. The fluid properties remain consistent with the last chapter (unless otherwise stated) and all properties are presented in section 4.3. The numerical considerations and model selection are presented in section 4.4. The investigation first looks at the 2D axi-symmetric case section 4.6, and then the 3D case is presented for RANS models in section 4.7.

4.2 Experimental validation case

The experiment used for a proxy validation without the addition of swirl is from the authors Lee *et al.* (1999) and is depicted in Figure 52. It is used to show that a conventional impinging jet on a concave surface without swirl can be reasonably well predicted with CFD. The addition of swirl adds additional complexity and as no validation case exists all of the defining parameters of the simulation are investigated.

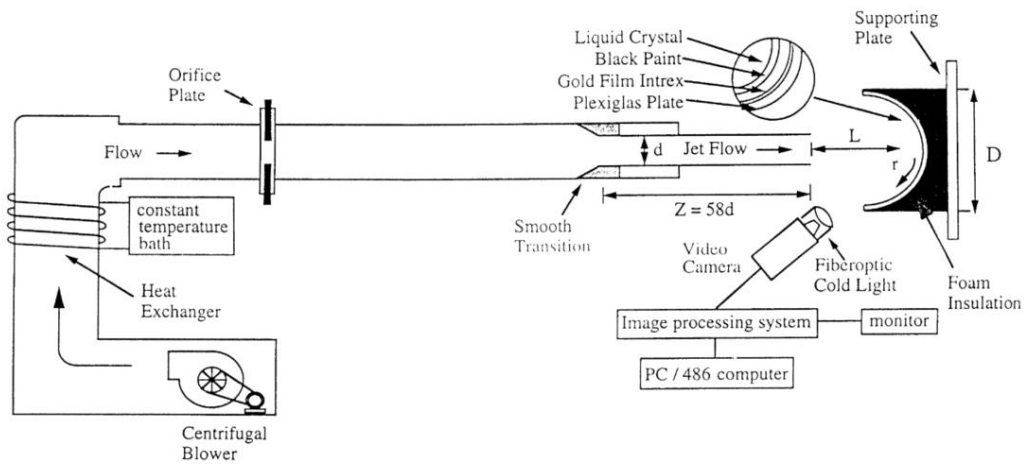


Figure 52. Vertical round jet impingement on a concave surface, experimental test setup schematic (Lee *et al.*, 1999).

The experiment investigated the effect of concavity and jet offset distance for an air impinging jet. The authors recorded the Nusselt number distribution over the impinging plate using a thermochromatic liquid crystal sprayed on the impingement surface and determining the temperature distribution using an image processing system. The maximum uncertainty for the recorded Nu is 4.5%. The jet exit temperature is controlled by the heat exchanger and did not vary by more than ± 0.2 °C (Lee *et al.*, 1999).

4.3 Fluid properties

The fluid used in the experiment was air with properties defined at the inlet conditions. The fluid properties are used in the simulation and are defined as piece-wise linear functions of temperature in ANSYS Fluent. The properties of air were presented in section 3.3.2.

4.4 Computational setup

The solution algorithms used are consistent with Chapter 3. The solution is also monitored in a consistent manner when compared to Chapter 3. A summary of the key considerations made for the simulations and input variables are summarised in Table 14.

Table 14. Summary of simulations numerical controls.

	Case 4.1	Case 4.2	Case 4.3	Case 4.4
2D/3D	2D	2D	3D	2D

	Case 4.1	Case 4.2	Case 4.3	Case 4.4
Cell count	5.00E+06	1.40E+07	2.00E+07	1.50E+07
Steady?	Steady	Steady	Steady	Steady
Turbulence	Transition SST	Transition SST	Transition SST	Transition SST
Discretisation Schemes	2 nd order	2 nd order	2 nd order	2 nd order
Pressure-velocity coupling	Coupled	Coupled	Coupled	Coupled
Pressure	PRESTO!	PRESTO!	PRESTO!	PRESTO!
Momentum	2 nd order	2 nd order	2 nd order	2 nd order
Density	2 nd order	2 nd order	2 nd order	2 nd order
Energy	2 nd order	2 nd order	2 nd order	2 nd order
Turbulence	2 nd order	2 nd order	2 nd order	2 nd order
Time step	-	-	-	-
Maximum Residual	1.00E-04	1.00E-04	1.00E-05	1.00E-04

4.5 Boundary conditions

The boundary conditions applied for the analysis are consistent with the boundary conditions used for a flat plate in Chapter 3. The domain and applied boundary conditions are depicted in the following sections for each case. The magnitude of the input boundary conditions is based on the experimental values for the validation cases such as the inlet velocities and the impingement surface heat flux. The boundary conditions applied are summarised in Table 15.

Table 15. Summary of simulations boundary conditions.

Boundary	Property	Case 4.1	Case 4.2	Case 4.3	Case 4.4
Inlet	Velocity Temperature	v_{ax} = 10.6 m/s 300 K	v_{ax} = 13.6 m/s v_{tan} = 15.27 m/s /s 293 K	v_{ax} = 2.59 m/s v_{tan} = 33.98 m/s /s 293 K	v_{ax} = 0.91 m/s v_{tan} = 1.06 m/s /s 563 K
Swirl	-	0	0 - 1.05	0 - 1.05	0 - 1.5
Surface curvature		0.089	0.056-0.089	0.089	1 - 3

Boundary	Property	Case 4.1	Case 4.2	Case 4.3	Case 4.4
Impingement height		2	1 - 6	2	0.2 – 1.5
Outlet	Pressure Temperature	Zero pressure gradient $T_{out} = 300 K$	Zero pressure gradient $T_{out} = 293 K$	Zero pressure gradient $T_{out} = 293 K$	Zero pressure gradient $T_{out} = 600 K$
Impingement surface	Heat flux	$q_w = 1120 W$	$q_w = 1120 W$	$q_w = 1120 W$	$q_w = 1 MW$
Axis of symmetry	-	yes	yes	no	yes
Pipe wall	-	No slip conditions, Adiabatic	No slip conditions, Adiabatic	No slip conditions, Adiabatic	No slip conditions, Adiabatic
Time	Time	Steady	Steady	Steady	Steady

4.6 2D axi-symmetric without swirl (Case 4.1)

The 2D simulations are validated against the experimental case. The effects of swirl are then investigated for a concave impingement surface.

Geometry and parameterisation

The 2D domain models the experimental domain of Lee *et al.* (1999), Lee *et al.* (2004), Lee and Lee (2000), and Lee, Lim, Lee, Yoon and Sung (2007), which is depicted in Figure 53. The domain consists of a pipe radius $d/2$ where the fluid enters at a velocity inlet the pipe and flow a length of L/d to the nozzle exit. The axis of symmetry is depicted as the centre axis of the domain. The impingement surface is represented by a curved arc at the defined curvature of d/D , located H/d downstream of the nozzle exit, that extends until it is perpendicular with the centre point of the arc. The ambient exit pressure outlet extends an additional $2d$ upstream of the centre point of the impingement surface curvature.

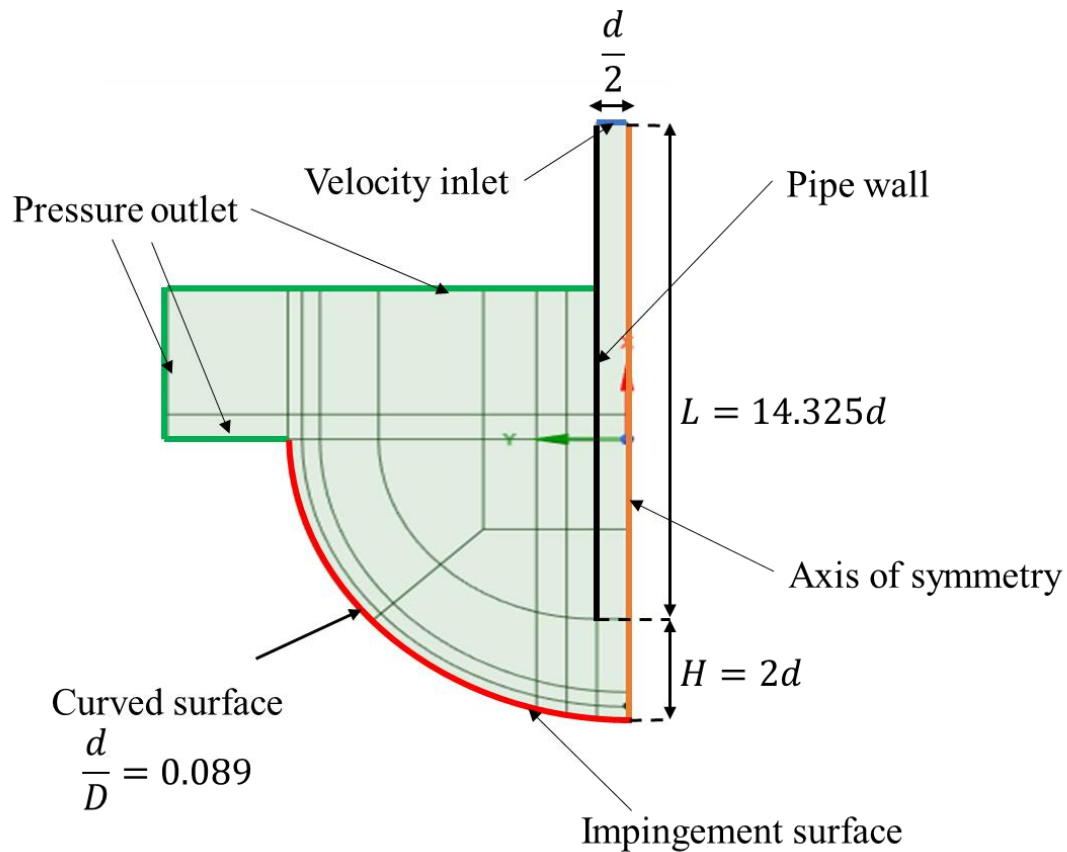


Figure 53. 2D Axi-symmetric fluid domain and boundary conditions.

Mesh strategy

For the 2D axisymmetric domain a structured mesh consisting of only quadrilateral elements is generated. The mesh is refined in the regions of interest. The mesh is refined sufficiently such that the quality remains high and the cell growth rate is limited to a difference of 20% to the adjacent cell. The final mesh consisted of four million quadrilateral mesh elements. A coarse mesh (100 000 cells) of the proposed strategy is depicted in Figure 54.

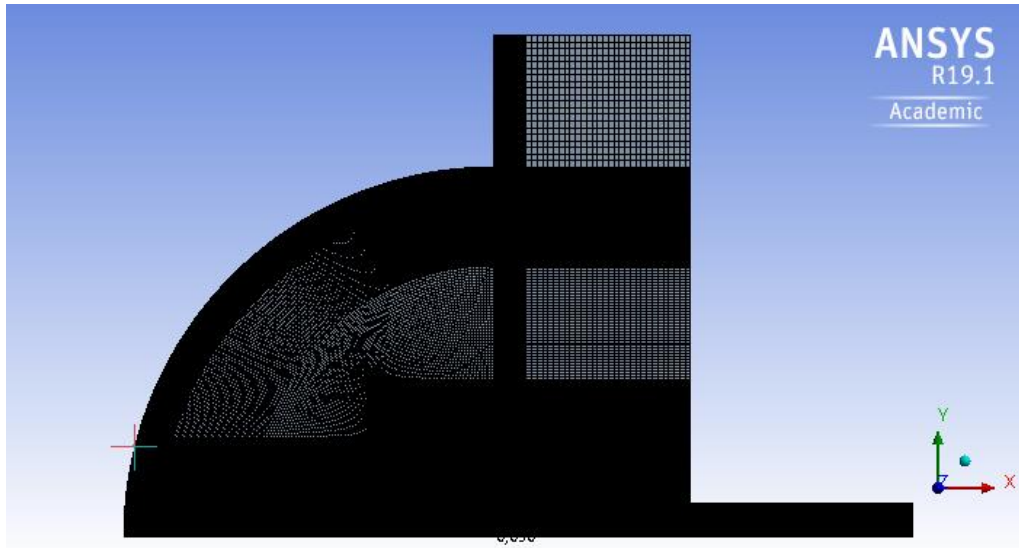


Figure 54. Coarse mesh of the 2D axisymmetric mesh.

Boundary conditions

The boundary conditions for the simulation are defined based on the experimental results of Lee *et al.* (1999) and are depicted in Figure 53. The fluid enters the domain via a velocity inlet, the velocity is specified as constant axial magnitude normal to the flow. At the defined Reynolds number of $Re = 23\,000$ resulting in a bulk flow rate of $u_{ax} = 10.6$ m/s. Pressure outlet conditions are applied at the outlet with a zero-pressure gradient. On the impingement surface a constant heat flux is applied of 1200 W.

Results

The heat transfer numerical results are plotted in the form of Nu versus the non-dimensional radial distance, r/d against the experimental results in Figure 55. The results compare well with the experimental results with deviations evident in the stagnation region and the exact location of the second hump in the Nu distribution. As for flat impingement surfaces, an increase in the Reynolds number an inlet turbulence leads to an increase in Nusselt number and a more distinct second hump. The results for the case where $Re = 23\,000$, $H/d = 2$, $d = 34$ mm, $d/D = 0.089$, and $L = 10d$ are presented in more detail. The velocity magnitude contour plot is plotted over the domain to depict the flow speed, presented in Figure 56. The velocity plot indicates that a strong recirculation region is present due to the curvature of the impingement surface.

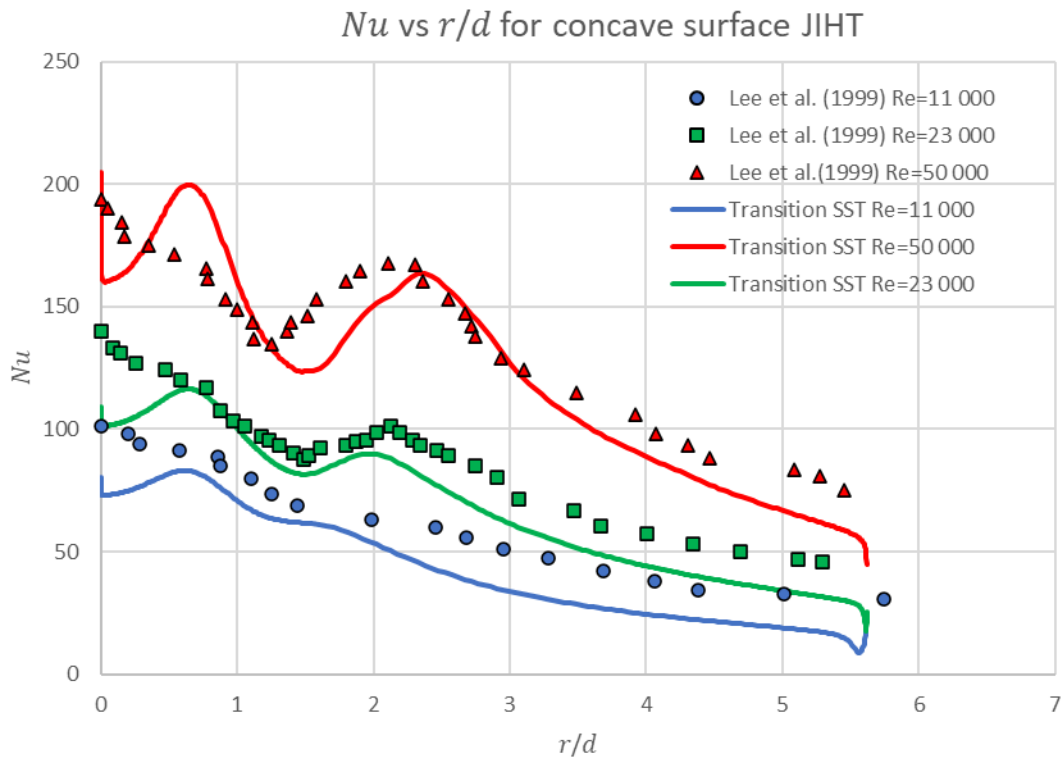


Figure 55. Nu vs r/d for experimental and numerical results for concave JIHT for $Re = [11\ 000, 23\ 000, 50\ 000]$, $H/d = 2$, $d = 34\text{mm}$, $d/D = 0.089$, and $L = 10d$.

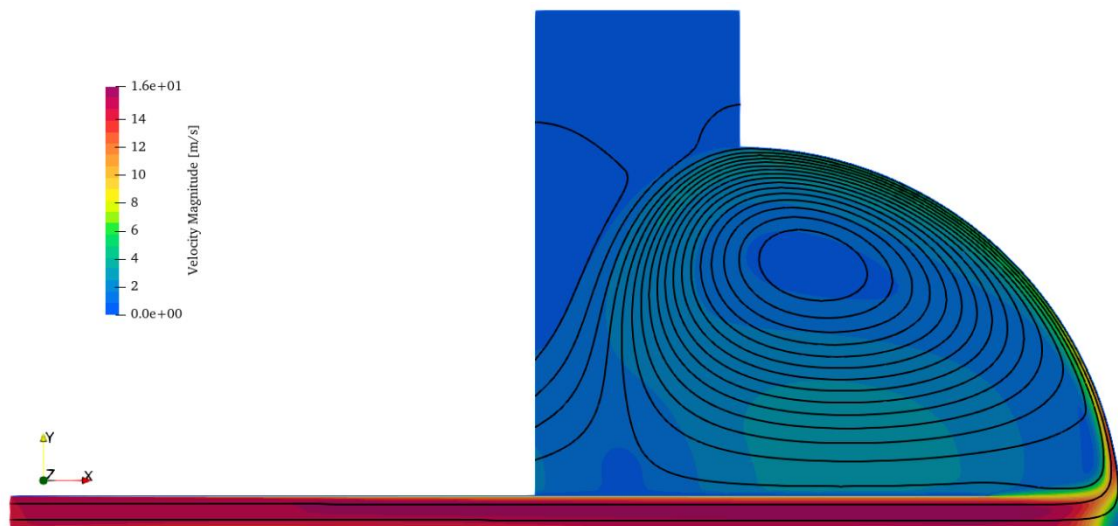


Figure 56. Vertical round jet impingement on a concave surface, velocity magnitude and streamlines. (Case 4.1)

From the velocity plot, the theory for jet impingement is seen. The ambient fluid is then entrained in the jet flow, as seen by the increase in fluid velocity by the nozzle. From here the core region is formed by the high-speed fluid, which widens after exiting the nozzle, indicated by the high velocity magnitude

region. The stagnation region forms with low velocity fluid and flows along the wall. The boundary layer forms and grows along the constant heat flux wall and recirculation occurs at the end of the wall. Contrary to the flat impingement surface of Chapter 3, here the flow is accelerated as it moves away from the impingement location due to the surface curvature.

From the results of the numerical simulation, the Transition SST model proves reliable again in predicting trends. The accuracy of the solution is reasonable considering how inexpensive the computational cost is relative to other simulations. It is seen that the Nu increases generally for increasing Re . The double hump can be described due to the stagnation point heat transfer and transition to turbulent flow. From comparing the Nu plot, Figure 55, and the velocity plot, Figure 56, the turbulent intensity is the highest for where the peaks occur, this corresponds directly to the kinetic turbulent energy (Behnia *et al.*, 1999; Narayanan *et al.*, 2004). Concave heat transfer increased 20% over flat plate JIHT increase this is more applicable for small nozzle to surface distances (Lee *et al.*, 1999). The numerical stagnation region is wider than the experimental stagnation results. The far field heat transfer is found to be lower than the experimental results. The loss of accuracy may be attributed to unclear experimental results as the exit velocity profile is not known (Craig *et al.*, 2018).

From the validated model and the investigation of the flat plate case, the parameters and boundary conditions can be investigated to further enhance the heat transfer on the impingement surface.

4.6.1 Swirling impinging jet on concave surface parameter investigation (Case 4.2)

The influence of swirl number and the geometry is evident and has a profound effect on the heat transfer rates achieved. From the limited experimental results and the validated numerical model, the effect of the described parameters can be investigated further and, in more detail, to further understand the physics governing the flow.

Boundary conditions

The boundary conditions applied for the simulations correspond to Ahmed (2016), Ahmed *et al.* (2015b), and Ahmed *et al.* (2016b). The fluid enters the domain via a velocity inlet, the velocity is specified as constant axial and tangential components. The components are determined by the flow rate and the defined swirl number. At the defined Reynolds number of $Re = 35\,000$ resulting in a bulk flow rate of $u_{ax} = 13.6\text{ m/s}$. The tangential component is determined based on equation (17). The axisymmetric boundary conditions are applied as the Nusselt number distribution does not vary dramatically around the circumference from the experimental results. Pressure outlet conditions are

applied at the outlet with a zero-pressure gradient. On the impingement surface a constant heat flux is applied of 1120 W .

For the given domain, the boundary conditions were implemented as indicated in Figure 53. The boundary conditions values are based on the available information from the experimental results. The boundary conditions applied are consistent with Chapter 3 investigations.

Results

Four parameter combinations were chosen as representative and the Nusselt number distributions are plotted in Figure 57. Additional results are available in appendix C.

Shown in Figure 57 are the effects of swirl, jet impingement distance offset and surface curvature. The general trends observed can be summarised as follows:

- The maximum Nusselt number increases with a smaller jet offset distance.
- The maximum Nusselt number increases with swirl number.
- The maximum Nusselt number location shifts away from the nozzle centre with an increase in swirl number.
- An increase in curvature results in a more uniform Nusselt number for variable swirl numbers.

From the observable trends the heat transfer characteristics and flow field are consistent with the findings of Chapter 3.

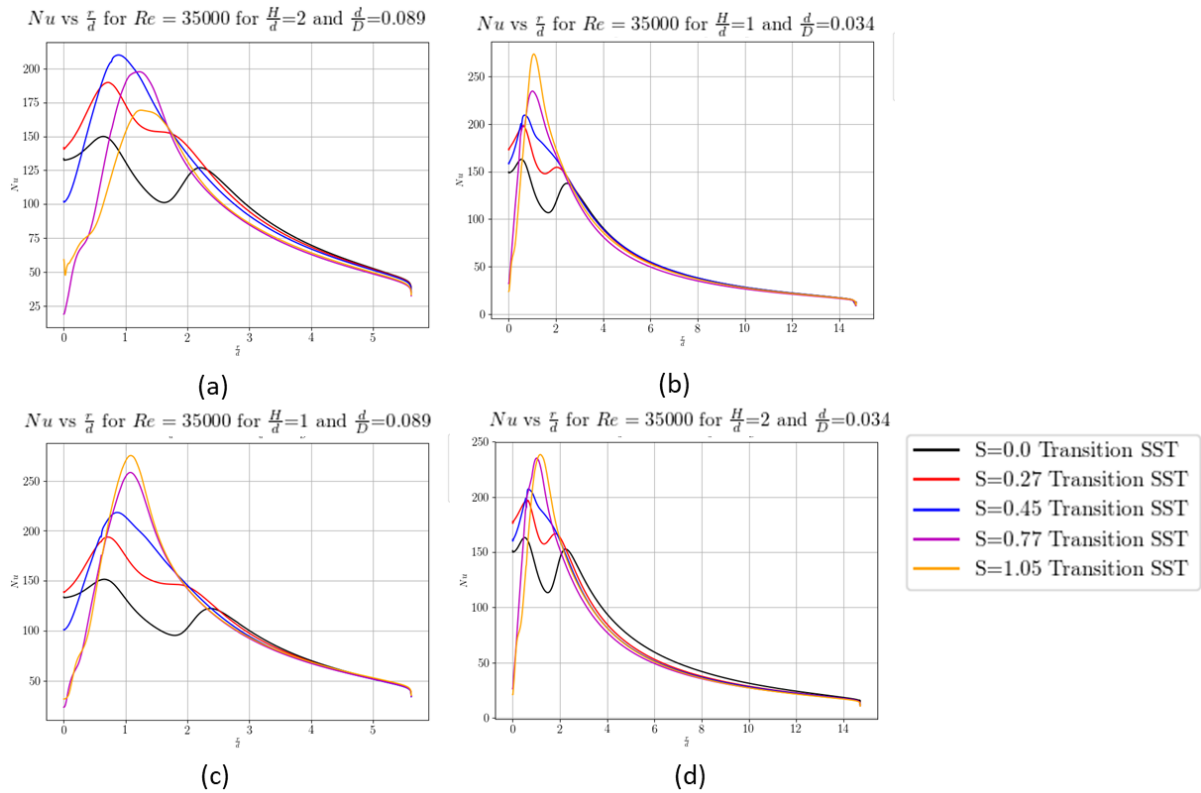


Figure 57. Nusselt number distribution in radial direction (a) $H/d = 2, d/D = 0.089$ (b) $H/d = 1, d/D = 0.034$ (c) $H/d = 1, d/D = 0.089$ (d) $H/d = 2, d/D = 0.034$.

To further investigate the flow field and flow field characteristics, the flow variables for a selected case ($S = 0.77, H/d = 2, d/D = 0.089$) are presented in Figure 58. The velocity magnitude plot shows that the peak velocity location on the impingement surface corresponds with the location of peak Nusselt number. The pressure is highest on the pipe wall due to the swirl flow and low in the central vortex and recirculation zone. The swirl velocity and axial velocity show the key flow profile and correspond with the velocity magnitude indicating how the swirl and axial velocity peaks shift radially away from the centre of the pipe. The size of the recirculation zone on the impingement surface is depicted by the velocity plots. A strong recirculation zone is formed. The high turbulent kinetic energy is located where the swirl velocity is the highest and at the nozzle exit where the ambient fluid is entrained into the jet flow.

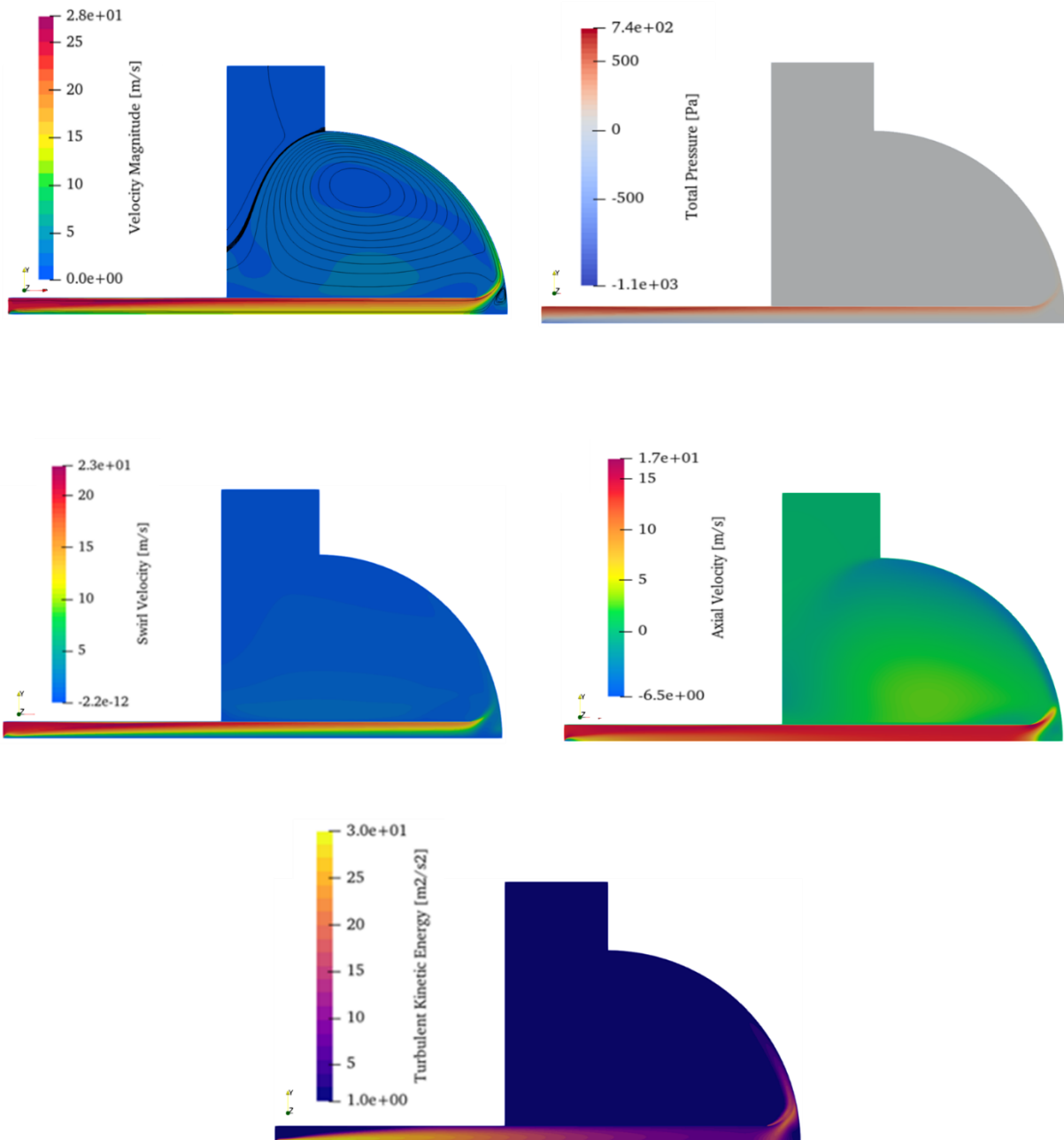


Figure 58. Flow variables of SIJ o a concave surface where $S = 0.77, H/d = 2, d/D = 0.089$ velocity magnitude, total pressure, swirl velocity, axial velocity and turbulent kinetic energy (Case 4.2).

4.7 3D SIJ (Case 4.3)

The aerodynamic swirl generated using tangential jets from Ahmed *et al.* (2016b) is applied to a concave surface in a 3D model. By comparing the same swirl generation method, the effect of concavity is the investigation parameter. By comparing the cases on a like for like basis the multiple methods of heat

transfer enhancement discussed in literature can be compared to the swirl case to evaluate the prospective enhancements that can be made.

Domain

The fluid domain investigated numerically is depicted in Figure 59. The dimensions of the domain aside from the surface curvature are consistent with Chapter 3.

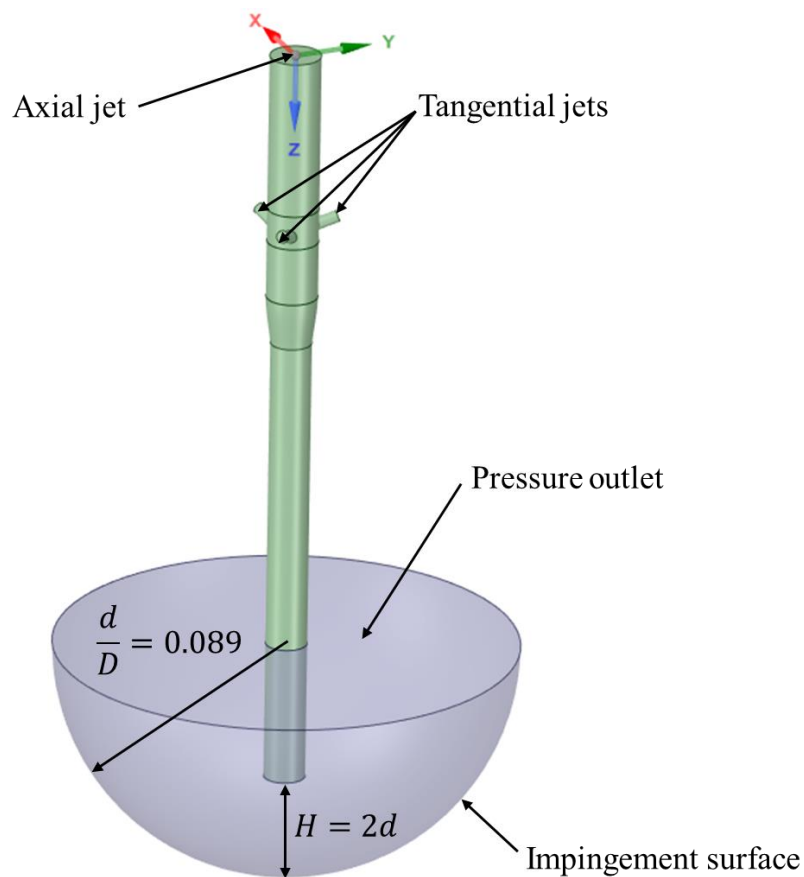


Figure 59. 3D fluid domain for SIJ on a concave surface.

Mesh

The domain is sub-divided in order to improve the mesh control and provide more cells in the areas of interest. The final mesh used for the investigation consisted of 20 million cells. For additional information on the mesh and mesh dependency refer to appendix C.

Boundary conditions

The boundary conditions applied for the simulation correspond with the experimental conditions of Ahmed *et al.* (2015b), Ahmed (2016), Ahmed *et al.* (2016b), and Ahmed *et al.* (2017), however, the impingement surface has a curvature over which a constant heat flux is applied. As with the other cases investigated the boundary conditions are summarised in Table 15.

Numerical scheme

The numerical scheme remains consistent and is summarised in Table 14.

Results

Five parameter combinations are used to display the results, plotted as Nusselt number contours on the impingement surface in Figure 60. Additional results are shown in appendix C.

The general trends observed for the investigation are:

- The maximum Nusselt number increases with swirl number.
- There appear to be lobe regions of high Nusselt number that form.

In addition, there appears to be a flow instability for the medium swirl numbers, this is consistent with the flat plate validation findings, which are suspected to be transient. The lobes were therefore averaged out along the circumferential direction. The circumferential averaged Nusselt number distribution is plotted in Figure 61 for five swirl numbers for a specific geometry.

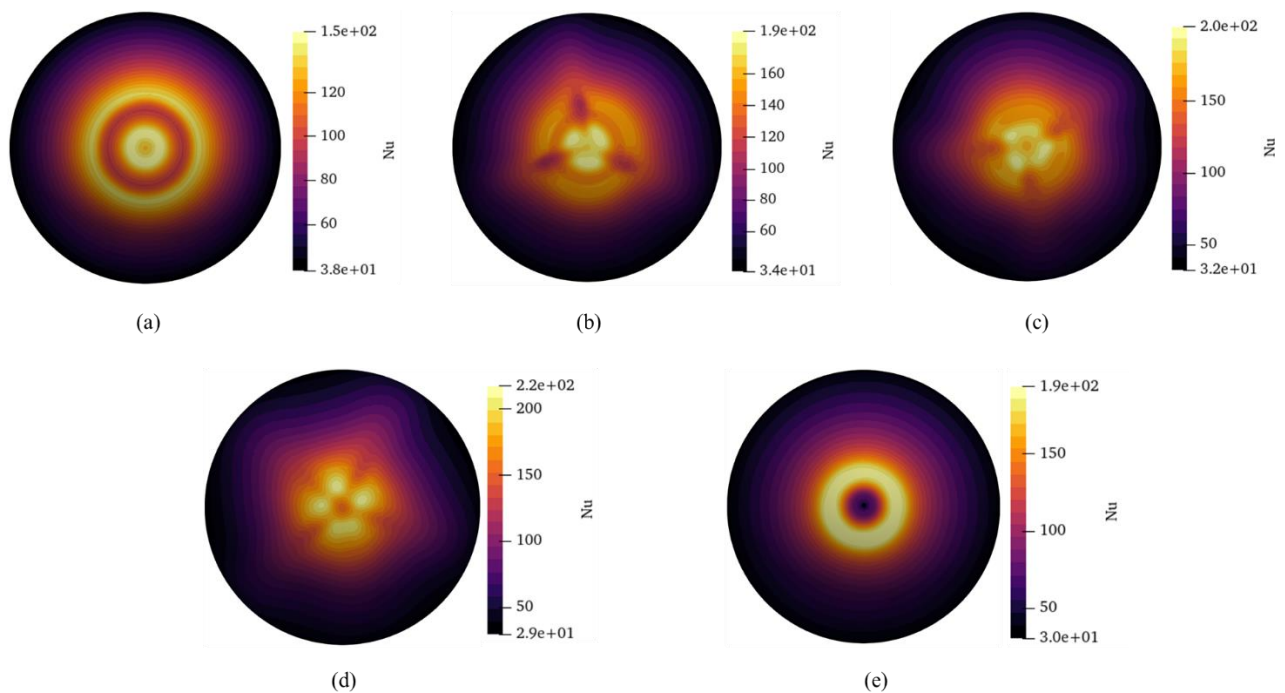


Figure 60. Nusselt number distribution of SIJ on a concave surface where $H/d = 2$, $d/D = 0.089$ (a) $S = 0$ (b) $S = 0.27$ (c) $S = 0.45$ (d) $S = 0.77$ (e) $S = 1.05$.

From the circumferentially averaged Nusselt number plots the general expected trends are similar to the 2D case and the flat case from Chapter 3. The 3D case shows that the stagnation point Nusselt number is under-predicted for the 2D cases particularly for $S = 0.77$ (when comparing Figure 61 with Figure 34). The axi-symmetric case was shown to not accurately predict the stagnation point Nusselt number. The Nusselt number distribution is improved by curvature but there appears to be a “sweet spot” for the swirl number for a given flow configuration. This motivates the need for an optimisation study to improve heat transfer.

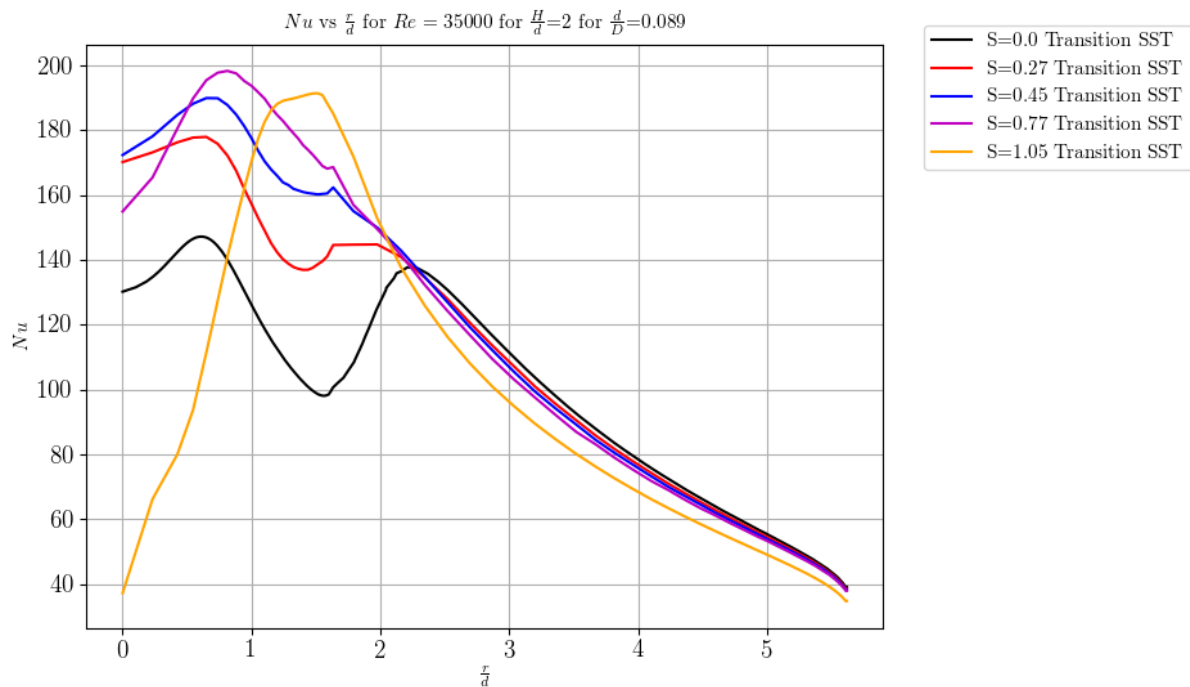


Figure 61. Nusselt number distribution in radial direction where $H/d = 2$, $d/D = 0.089$.

4.8 Optimisation of receiver cone

The geometry is considered first as a 2D axi-symmetric domain, this is used due to lower computational expense. This forms the base proxy analysis where the general dimensions and flow conditions are modelled without the swirl generator and the swirl is imposed as a boundary condition. This study allows for more studies to be conducted for the receiver geometry in a shorter time. The study allows for the heat transfer rates and the outlet fluid temperature to be maximised. The pressure losses of the system are not considered as the neglected swirl generator will determine the pressure drop. The study will give a good indication of the principal components/parameters influencing heat transfer and the outlet temperature achieved. A solar salt HTF is used in this section to prepare for the realistic heat source 3D model of the next chapter.

4.8.1 2D cone optimisation (Case 4.4)

The 2D cone design is based on the previous design described in section 2.9. The cone receives the solar radiation on the shell outer surface. On the internal cone surface there is an impinging jet with a swirl generator. The cone shell is made of a carbon steel and the HTF investigated is solar salt. The cone design, parameters and boundary conditions used for the simulations are depicted in Figure 62.

Material properties

The use of carbon steel and solar salt is to compare the performance relative to the previous design (Slootweg (2018)) and due to the use of the chosen materials in industry. The cone is manufactured from carbon steel (0.08 C, 0.3 Mn) and the HTF used is solar salt, a eutectoid mixture of ~60% sodium nitrate ($NaNO_3$) and ~40% potassium nitrate (KNO_3). For the simulation, the material properties are specified in Table 16.

Table 16. Material properties for the cone and HTF.

Material	Density, ρ (kg/m^3)	Specific heat, C_p (J/kg · K)	Thermal conductivity, k (W/m · K)	Dynamic viscosity, μ (kg/m · s)	Reference
Solar Salt	2263.641 – 0.636 · T	1396.044 + 0.172 · T	0.45	0.07543937 – 2.77 $\times 10^{-4} \cdot T$ + 3.49 $\times 10^{-7} \cdot T^2$ – 1.47 $\times 10^{-10} \cdot T^3$	(Serrano-López, Fradera & Cuesta-López, 2013)
Carbon steel	8030	502.8	Piecewise linear function (refer to Appendix D)	-	(Morrell, 2017)

Cone simulation parameters

The cone is parameterised in the 2D domain for all design parameters. The design parameters considered for the study are presented in Table 17.

Table 17. Input Parameters used for Concave SIJ Investigations of one Axisymmetric Cone in the Receiver.

Parameter	Description
t_f/H	The return flow annulus thickness
ts	The thickness of the steel shell
d	Pipe diameter
R/d	The concave surface radius to nozzle diameter ratio
H/d	Nozzle height to nozzle diameter ratio

Parameter	Description
Re	Reynolds number
S	Swirl number decomposed into the axial and tangential velocities.
θ	The cone inclination angle relative to the flat absorber surface.

The geometry is parameterised in the SpaceClaim scripting environment, the script used to generate the 2D flow domain is presented in Appendix E. The parameterised geometry and the design parameters are presented in Table 17 and Figure 62. The surfaces coloured in blue indicate the fluid domain and the faces coloured in green indicate the solid cone shell domain.

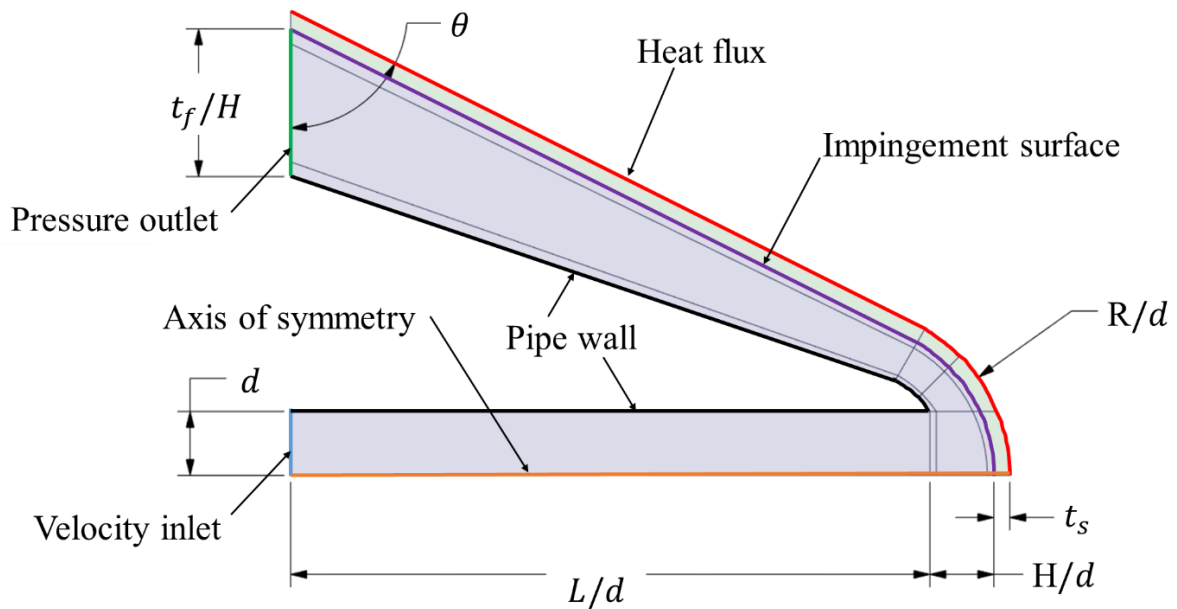


Figure 62. 2D cone parametric domain with indicated design parameters and boundary conditions.

For the receiver optimisation, the multi-objective functions are defined as follows:

$$\begin{aligned}
 & \min_{w.r.t x} -h_{avg,shell}(x) \\
 & \min_{w.r.t x} -T_{avg,outlet}(x) \\
 & \min_{w.r.t x} T_{max,shell}(x)
 \end{aligned}$$

where $x = [d, Re, S, t_s, t_f, L, R, \theta]$.

The design is also constrained in the sense that there are limitations imposed on the geometric dimensions such that the parameters cannot produce a non-feasible solution for the cone. During the validation studies certain parameters were observed to enhance heat transfer and others reduced the heat

transfer. It was observed that smaller surface curvature ratios d/D resulted in heat transfer enhancement. Smaller nozzle offset distances H/d have shown to enhance heat transfer particularly with higher swirl rates. A higher fluid flow velocity Re has shown to increase heat transfer therefore only fully developed turbulent flow is considered. The larger the cone is the larger the surface area over which heat transfer occurs, this is however not a direct design variable but is a function of the following design variables: L, H, θ, R and t_s .

From the described observations the following parameter constraints are imposed on the optimisation variables:

$$10\text{mm} \leq d \leq 50\text{mm}$$

$$1\text{mm} \leq t_s \leq 10\text{mm}$$

$$0.5 \leq t_f/H \leq 2$$

$$0.2 \leq H/d \leq 1.5$$

$$1 \leq R/d \leq 3$$

$$5 \leq L/d \leq 15$$

$$5\,000 \leq Re \leq 60\,000$$

$$0 \leq S \leq 1.5$$

$$10^\circ \leq \theta \leq 90^\circ$$

Imposing the described inequality constraints on the impinging cone and with no required equality constraints, the cone geometry can be optimised. For the optimisation a response surface optimisation study is conducted. In order for the surrogate model to be investigated the selection of the parameters for each design point are used to populate the design space. Latin hypercube sampling is used for the design of experiments to randomly and uniformly populate the design space.

The design of experiments sample space is populated for the nine design parameters with 147 samples specified for the analysis, each sample is described as a new design point (DP) from DP0 to DP147. This provides a random yet uniformly distributed design space. A sample for the larger design space used for the surrogate model is presented in Table 18.

Table 18. Design point sample space populated with LHS.

DP	d (mm)	t_s (mm)	t_f/H	H/d	R/d	L/d	θ (°)	Re	S
0	37.07	2.24	0.35	0.28	2.48	12.52	36.28	72500.00	1.07
1	32.72	2.46	0.83	0.34	2.42	9.80	32.74	58214.29	0.61
2	39.52	3.61	0.38	0.61	2.84	14.22	42.91	143214.29	1.37

DP	d (mm)	t_s (mm)	t_f/H	H/d	R/d	L/d	θ (°)	Re	S
3	27.55	8.01	0.23	0.73	1.64	12.11	64.13	46071.43	0.42
4	22.38	8.39	1.27	0.94	2.89	12.04	48.66	79642.86	1.46
5	46.60	6.82	0.54	0.36	1.52	11.97	52.64	106071.43	1.33
6	13.40	7.58	0.88	0.37	2.75	14.83	51.31	57500.00	1.35
7	37.07	2.24	0.35	0.28	2.48	12.52	36.28	72500.00	1.07

Due to the change in geometry the mesh is defined in such a way that the sizing functions scale with the geometry. The mesh uses the findings from the mesh independence study in appendix C while simultaneously ensuring that $y^+_{max} \leq 1$ on the impingement surface. A sample mesh generated for the optimisation study is presented in Figure 63.

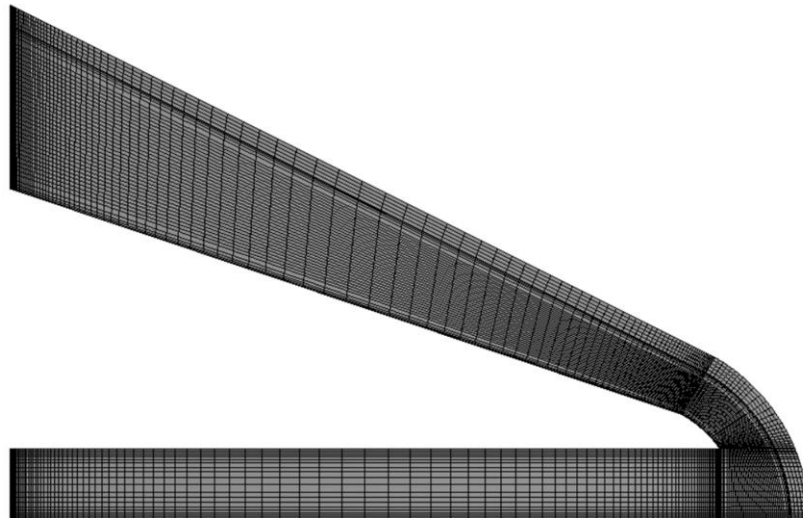


Figure 63. 2D axi-symmetric cone mesh of 9000 cells.

The optimisation study considers a simplified heat source as the heat flux boundary condition. The applied heat flux used is a typical maximum heat flux experienced on the receiver absorbing surface of $1 \text{ MW}/\text{m}^2$. A constant heat flux is used for the design as non-uniform heat fluxes cannot be investigated in a 2D model.

Other solution controls and methods are similar to those used for the validation cases in Chapter 3.

4.8.2 Results

From the optimisation study the influence of the design parameters on the cone performance are analysed. The optimisation of the cone is analysed using the programming language python.

Sensitivity study

Before a full optimisation study, a sensitivity analysis is conducted on the input parameters and a linear regression analysis is conducted for the key output parameters. The linear regression analysis is performed by subdividing the data into a test and training set of results. The test and training data are scaled for each of the respective input and output parameters. The scaling of the data is important as this provides a more accurate comparison between design variables as the scale of the design variables range from values of the magnitude 10^{-4} and 10^5 . The regression analysis is done for the training set and compared to the results of the test data. The sensitivity of the training and test data analysis is beyond the scope of this document and focuses primarily on the implementation of the numerical methods in the python environment.

From the scaled regression analysis the data are fitted for the following key output variables which have a significant influence on the cone design: $T_{max,shell}$, T_{outlet} and $Nu_{avg,shell}$. The key parameters are selected as the purpose of the design optimisation is to enhance heat transfer and lower the maximum operational temperature of the shell.

Table 19 provides the regression coefficients for each parameter and the variance score for the parameters and the output parameter.

Table 19. Linear regression coefficients of design inputs to performance outputs.

	d	L/d	H/d	R/d	t_{shell}	θ	t_f	Re	S	Variance
$Nu_{avg,shell}$	-0.67	-0.54	-0.12	-0.09	0.1	0.44	-0.06	0.37	0.08	0.86
T_{outlet}	0.49	0.5	0.06	0.07	0.03	-0.44	-0.01	-0.38	0.03	0.79
$T_{max,shell}$	0.48	0.38	0.26	-0.01	0.21	-0.52	0.11	-0.31	-0.05	0.66

One can see the sensitivities of the performance metrics based on each parameter. From the analysis observations can be made. From the study the nozzle diameter is shown to have a high regression coefficient, this is expected as the geometry dimensions all scale with the size of the nozzle. With the proportional scaling a different observation may be made, the diameter is an indication of the cone size. Based on the cone size it can be seen that the maximum shell temperature and the outlet fluid temperature are largely influenced, as expected for the available heat transfer surface area. For most input parameters excluding $\frac{R}{d}$, t_f and S , the design parameters for the outlet temperature and maximum shell temperature show similar trends, this shows the dependency between the parameters. As the

maximum surface temperature increases the outlet temperature also increases. A detailed pair plot figure is provided in appendix E depicting the correlation between investigated parameters.

The variable that shows a disproportionate behaviour is R/d , as the curvature increases the outlet temperature can be enhanced and the maximum surface temperature reduced. The influence of the surface curvature is complex but as was noted for the impinging jet investigation in sections in 4.6 and 4.7, the reduction in curvature results in higher heat transfer. The surface curvature may also influence the recirculation that occurs at the cone tip.

The return flow annulus thickness reduces the maximum surface temperature and increases the outlet temperature. The return flow annulus thickness can increase the velocity of the fluid flow and therefore enhance heat transfer by reducing the cross-sectional flow area. The enhancement of heat transfer therefore reduces the maximum surface temperature and increases the outlet temperature. A benefit of this parameter that will be further investigated is the reduction of flow area that may help recapture the pressure loss for the cone.

The swirl although not significant, shows an enhancement in heat transfer resulting in a reduction of the maximum surface temperature and increase in outlet temperature. The addition of swirl prolongs the time the fluid spends in the receiver as the flow will return in a helical flow pattern increasing the time the fluid spends within the cone and increasing the outlet temperature. The centrifugal force induced may also reduce the pressure losses within the cone.

Response surface surrogate model

The optimisation of the design is done using a response surface surrogate model. The response surface used is a robust zero-order-only radial basis function of nine dimensions corresponding to each of the input parameters. A radial basis function approximates a non-linear function $f(\mathbf{x})$ as a linear combination of p basis function:

$$\phi_j(x, x_c^j), \quad j = 1, \dots, p$$

This allows for the surrogate model of:

$$f(x) \approx \sum_{j=1}^p w_j \phi_j(x, x_c^j) = \tilde{f}(x), \quad j = 1, \dots, p$$

where w_j are the estimated linear weights of the function. The weights are determined using a least-squares optimum regression fit. The radial basis surrogate model is selected as there are a few design vectors and the non-linear function expected for fluid flow problems can be adequately approximated and optimised inexpensively for the design space (Snyman & Wilke, 2018).

Separate response surfaces are used for each output objective and a weighted multi-objective surface. The radial basis function uses a gaussian basis function to create a smooth surrogate model. The response surface is used for an interpolation function for the scattered data and the test and training data are used to optimise for the shape parameter (ϵ). The radial basis function can be formulated as follows:

$$\phi_j(x, x_c^j) = e^{(-\epsilon r_j(x)^2)}$$

The shape parameter is optimised with the test data using k -fold cross validation where the least squares error is minimised (Snyman & Wilke, 2018). This proposed method used to generate the surrogate is described in detail in the works of Snyman and Wilke (2018). Additionally, information and source code for the optimisation may be found in Appendix E.

Optimisation

The objective function to be optimised for the design is based on a weighted objective function where the weightings of each functions are allocated based on the design considerations. The weightings are also manipulated for multiple values and the perceived global minimum of each case are compared. From the study the selected objective function is presented:

$$\min_{w.r.t x} -(0.2)h_{avg,shell}(x) - (0.5)T_{out}(x) + (0.3)T_{max,shell}(x)$$

The optimisation is implemented for the surrogate model using the python library `scipy.optimize`. For the optimisation multiple methods are available for the optimisation algorithm. Multiple algorithms and start points are used for a sensitivity study. The optimiser used is Sequential Least Squares Programming (SLSQP) (Snyman & Wilke, 2018). This optimiser has shown superior results for non-linear, bounded and zero order optimisation (Snyman & Wilke, 2018). The multi-start strategy is used to try and locate the global minimum result for the design space. The start points are uniformly distributed within the design space and the radial basis functions are evaluated at each design point to determine the global minimum. For the study 100 start points are used and optimised for in the 9-dimensional space.

For the optimisation study several candidate points are available based on the objective. Form the generated candidate points several points are located within a similar sub-space. The bounded sub-space was found to be within the following ranges:

$$22mm \leq d \leq 46mm$$

$$3mm \leq t_s \leq 8mm$$

$$0.2 \leq t_f/H \leq 1.32$$

$$0.26 \leq H/d \leq 0.93$$

$$1.5 \leq R/d \leq 1.9$$

$$6.7 \leq L/d \leq 14.5$$

$$18\,000 \leq Re \leq 22\,000$$

$$0.23 \leq S \leq 1.4$$

$$33^\circ \leq \theta \leq 84^\circ$$

Of the optimal candidate points the top three points are selected for the validation test case by using the input parameters in the simulation code. Only candidate points that meet the design requirements are considered (as the applied heat source is over estimated a relaxation of 10% is given for the $T_{max,shell}$ and T_{outlet}). The candidate points approximated results from the surrogate model and the simulation results are compared. The input parameters for the candidate points are presented in Table 20.

Table 20. Candidate points parameters.

	CP 1	CP 2	CP 3
d [mm]	26.16	36.8	29.04
L/d	11.39	6.89	12.14
H/d	0.87	0.26	0.21
R/d	1.51	1.5	1.5
t_s [mm]	3.01	6.23	7.12
θ [°]	84	60.59	77.9
t_f/H	0.5	1.13	0.2
Re	18688	19516	15286
S	0.38	0.78	1.33

From the constructed response surface, the design points are validated by running a CFD simulation with the described inputs. The output parameters are compared in Table 21.

Table 21. Candidate points performance and validation.

	CP 1		CP 2		CP 3	
	RBF	CFD	RBF	CFD	RBF	CFD
$Nu_{shell,avg}$ [$W/m^2 \cdot K$]	3451	2806	3372	2606	3776	3502
T_{outlet} [K]	673	613	664	615	711	653
$T_{max,shell}$ [K]	1507	2345	1488	3622	1587	1378

The surrogate model seems to predict the heat transfer rates and outlet fluid temperature within a reasonable accuracy. The maximum shell temperature however is not predicted accurately. This may be due to the inability of the surrogate model to capture the non-linear behaviour of the fluid resulting

in an inaccurate prediction of the maximum shell temperature. As the maximum shell temperature only occurs in select regions of the material, the surrogate model has difficulty in predicting this whereas for the average properties the surrogate model shows superior performance. With the validation results CP1 and CP2 do not meet the design requirements.

Based on the optimum zone, a global optimum is selected considering the insights gained from the sensitivity study. The considerations made are as follows: The jet offset distance is minimised as this results in higher heat transfer rates to the fluid. The curvature ratio is minimised as this has shown to increase heat transfer rates. The cone angle selected is a maximum as this will increase the radiation view factor to adjacent cones. The material thickness is maximised to reduce thermal creep effect over longer operational times and the intense thermal cycling encountered. The return flow area is minimised to achieve a similar flow area to reduce the pressure losses expected to be encountered and increase the flow rate and heat transfer rate near the cone base. For the flow conditions with the observable effects such as the need for low Re and high S the heat transfer and pressure can be optimised in Chapter 5. For the optimal candidate point the geometric parameters are simplified to ensure a manufacturable design is chosen.

Candidate point

Of the candidate points, the best performer was CP3. This design produced a high outlet temperature for the HTF and maintained a relatively cool shell temperature when compared to the other candidate points. The optimised solution's geometry and simulation results are presented to give a comprehensive overview of the fluid dynamics and heat transfer within the receiver. This same geometry is investigated in 3D with a realistic heat source in Chapter 5.

The flow distributions for the optimised candidate point are presented in Figure 64 and Figure 65. The Velocity profiles for the axial and swirl flow show a similar flow profile to the validation cases. The high turbulent kinetic energy corresponds with the peak velocities as expected. The velocity magnitude profile correspond with the axial and tangential velocity profiles. The static temperature achieved is limited below melting temperature and the maximum temperature occurs near the cone exit.

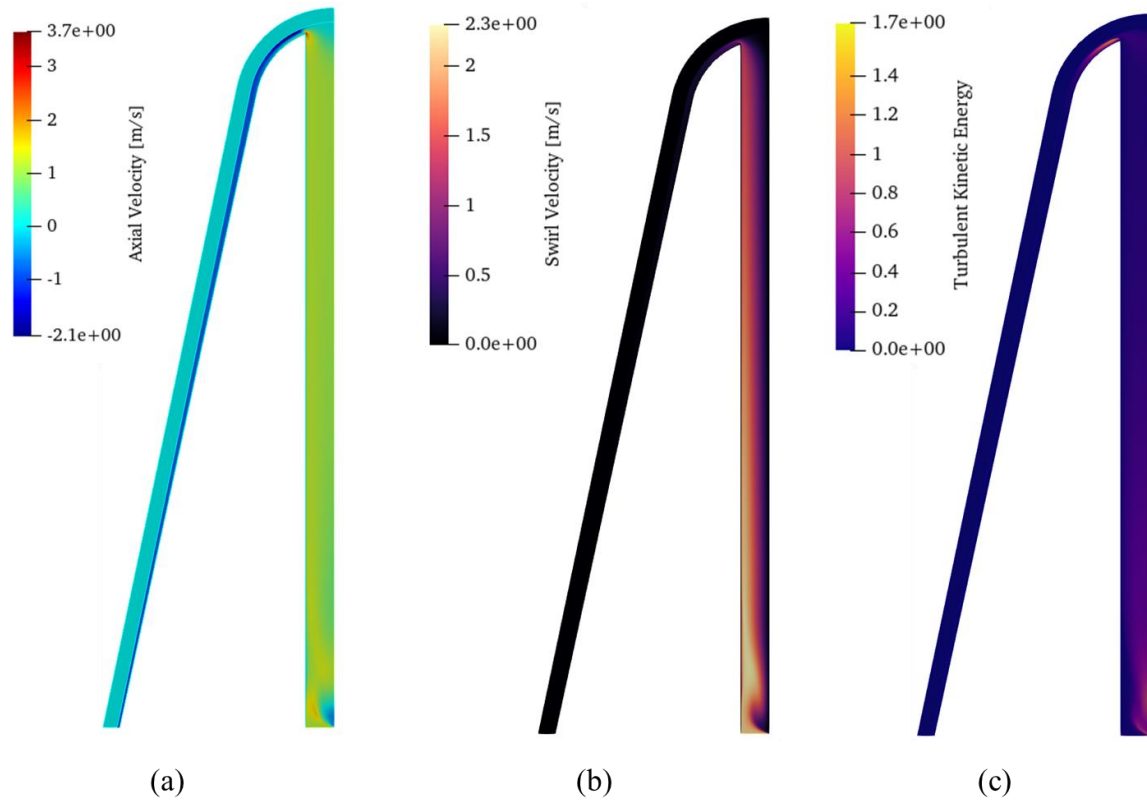


Figure 64. Flow variables for optimised design of SIJ in a solar receiver cone CP3 (a) Axial velocity (b) Swirl velocity (c) Turbulent kinetic energy.

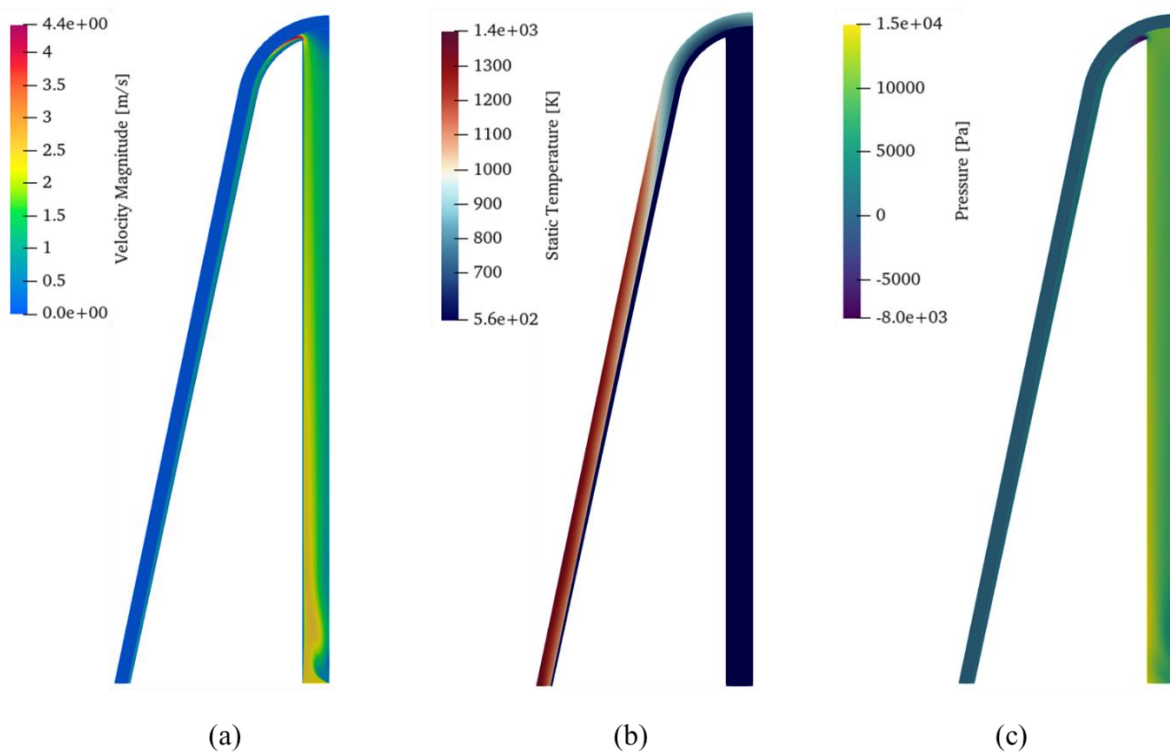


Figure 65. Flow variables for optimised design of SIJ in a solar receiver cone CP3 (a) Velocity magnitude (b) Static temperature (c) Static pressure.

4.9 Conclusion

In this chapter, novel applications for SIJ were investigated in conjunction with a concave impingement surface. Based on the simulations conducted the following conclusions can be made:

- Surface curvature has an effect on the heat transfer for a SIJ. The curvature not only can enhance heat transfer but can change the flow characteristics to change the location of the peak heat transfer. The surface curvature can be detrimental to heat transfer too depending on the flow configuration.
- The validation of 2D simulations show that the heat transfer can be predicted within reasonable accuracy for no swirl cases.
- The inclusion of surface curvature has not been investigated in literature and the simulations need to be further developed and investigated with experimental results.
- The general trends of the domain parameters are consistent with the flat impingement surface study. The 2D and 3D domains show consistent trends in comparison to the flat case, but the 3D simulations give additional insight into some flow instabilities that may be present. The 3D case also shows that there may exist an optimal swirl for a given domain that was not evident in the 2D simulations.
- With better understanding of the model limitations in 2D, the 2D models may be useful for an initial optimisation study as the 3D simulations are computationally expensive.
- The effect of various input parameters are considered and correlated linearly to the output parameters to give an indication of the key input parameters to optimise the output parameters.
- The optimisation study used a surrogate model to optimise the design. From the optimisation study an optimal zone was identified with three candidate designs selected for further investigation.
- Of the candidate designs an optimised design is chosen for further investigation in the next chapter.

5 SWIRLING JET IMPINGEMENT IN A CONCENTRATED SOLAR TOWER RECEIVER FOR REALISTIC HEAT SOURCE

5.1 Introduction

To model the performance of the proposed receiver some of the previous assumptions must be questioned. It was previously highlighted that the concentrator and receiver are inherently coupled and that the performance of the collector influences the design of the receiver. This coupling is addressed in this chapter by modelling the performance of the collector in conjunction with the receiver.

Whilst modelling the collector and receiver the key objectives should be kept in mind, namely:

- to model a realistic solar flux on the receiver;
- to increase heat transfer; and
- reduce the maximum surface temperature on the absorbing surface.

First an overview of the design and the modelling approach are discussed. The collector used for concentrating the solar rays on the absorbing surface is modelled using the methodology proposed by Slootweg *et al.* (2019). The concentrated heat flux obtained from the optical model is used as a heat source in the CFD analysis to investigate a more realistic application than the uniform heat source of previous chapters. The effects of radiation losses from the cone are investigated without and with neighbouring cones being present. Finally, a comparison is then made between the cone using SIJ and jet impingement with and without swirl, to evaluate if a SIJ will help meet the receiver's design objectives.

5.2 Design overview

The proposed concept of the receiver uses developed receiver designs as the foundation and attempts to double down on these designs' advantages. The initial concept is discussed in section 2.9. This concept was an enhanced version the external pyramid receiver proposed by Garbrecht *et al.* (2013). The new design aims to improve on prior designs by using SIJ.

The investigation of the receiver considers two aspects of the design, the optical performance, and the thermal performance. The focus of this investigation is to improve heat transfer and reduce the maximum surface temperature of the receiver, for a more practical receiver design. As the optical design and optical optimisation was extensively studied by Slootweg *et al.* (2019), the developed optical model developed by that author is used for the ray tracing.

The absorbing surface of the receiver is made up of many cones. Each cone has an SIJ on the interior that impinges on the tip of the cone and flows back out at the base of the cone. The cone uses three tangential inlet ports and one axial inlet port to create the SIJ. The HTF impinges on the cone near the tip and then flows in an annulus back towards the cone base. The cones act as a heat trap (taking advantage of adjacent cones' large view factor) to reduce the radiation losses to the environment. Simultaneously the cones utilise SIJ to improve heat transfer at the tip, where the highest concentrated solar irradiation is present and where the cone has a large view factor to the environment. The layout of the cones is and the dimensions of the optimal cone are depicted in Figure 66. The green section represents the solid shell and the blue section is the fluid domain.

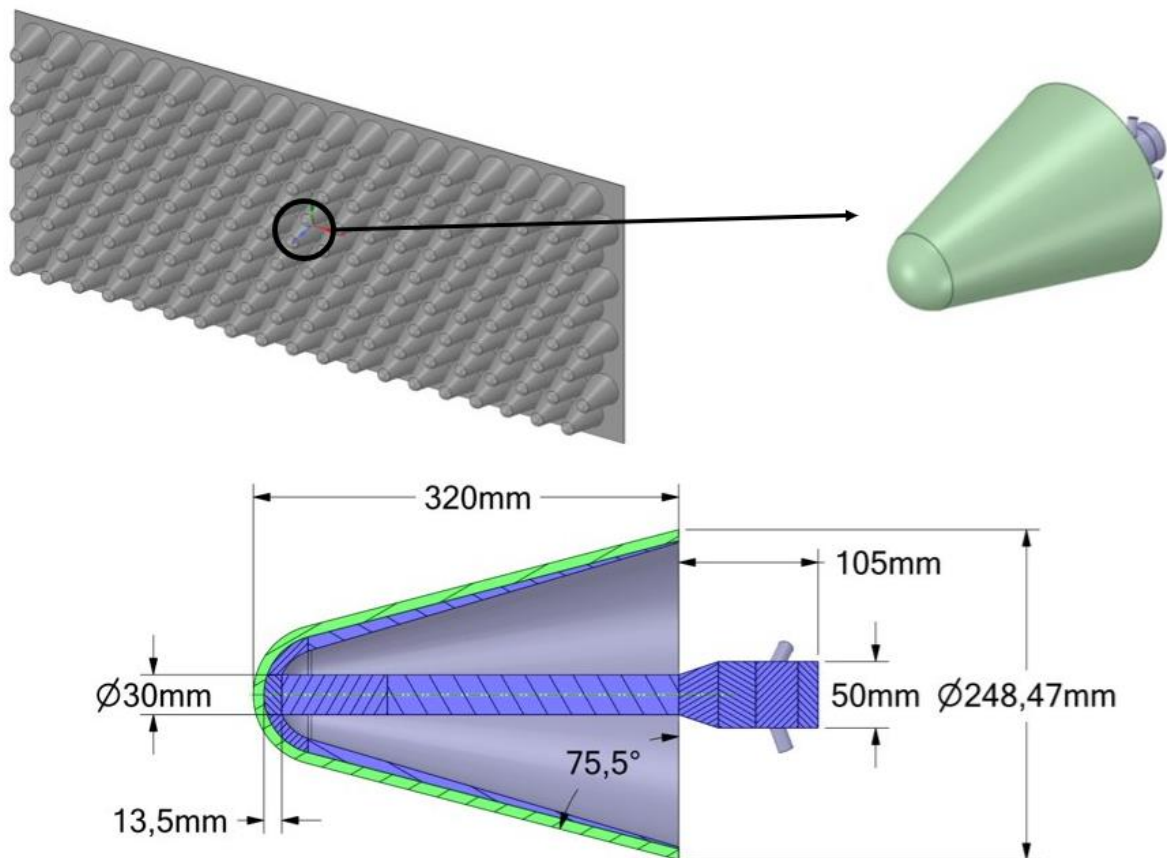


Figure 66. Receiver absorbing surface with SIJ cones and the dimensions of the optimised cone design.

5.3 Optical modelling

The optical modelling of the receiver considers a realistic heat source from the concentrated solar radiation due to a heliostat field and a secondary concentrator. The non-uniformity of the heat flux on

the surface is an important consideration not only to realistically predict the thermal performance of the receiver but to optimise the upstream flow conditions for thermal efficiency.

The optical performance of the receiver is modelled using a tool developed by M. Sootweg where the complex geometry of the receiver can be modelled in SolTrace. SolTrace is a solar ray tracing software that can predict the light interactions with multiple reflective and refractive surfaces. SolTrace uses a Monte Carlo ray tracing method to simulate the sun's ray interactions with the heliostats and finally produce a heat flux distribution on the receiver. The heat flux distribution on the receiver is used as a volumetric heat source on the absorbing material in the CFD model. The use of a heat source allows the internal convective heat transfer to be modelled as well as the external conditions such as the radiation and convection.

The heat flux for the receiver is determined for a test case using the PS-10 heliostat field and central tower in Spain. The simulated case is only considered for an instantaneous time on the selected julian day 180 at solar noon (Sootweg et al., 2019). The day of selection is used as this will provide a good average estimation for the heat flux on the receiver. The ray tracing is computationally expensive and may require billions of rays for a converged flux distribution. The model is simplified to a smaller region of cones and not the entire absorbing surface, this is done based on the assumption that for a given region the view factors of neighbouring cones will dominate the radiation effects.

5.3.1 Optical model inputs

As mentioned, the PS-10 heliostat field is used for the investigation. The PS-10 solar power plant in Seville, Spain has undergone extensive research. The key parameters used to model the PS-10 solar field and the tower are summarised in Table 22.

Table 22. Computational settings for optical model of PS-10.

Location	Latitude [°]	37.44, North
	Longitude [°]	6.25, West
	Altitude [m]	7
	Greenwich Mean Time [hours]	+1/+2
Tower	Height [m]	115
Aperture	Angle [°]	11.5/12.5
	Width [m]	13.72
	Height [m]	12
Heliostat	Type	Sanlúcar 120
	Width [m]	12.84
	Height [m]	9.45

	Reflectivity	0.88
	Transmissivity	0
	Slope error	0.71
	Specularity error	0.14
	Error type	Gaussian

The tool makes use of a clear sky assumption for the DNI radiation modelling. This is used as the effect of weather on the DNI is not considered for the developed tool. The clear sky assumption is justified as CSP plants are only operational when a minimum DNI threshold is met. SolTrace only uses primitive geometries, to incorporate more complex geometries, let us consider a previous model investigated by Slootweg *et al.* (2019).

Initially we have CAD geometry which in this case consists of solid hexagonal pyramids depicted in Figure 67 (a). The CAD is then discretised into cells making up a surface mesh using triangular elements depicted in Figure 67 (b). The discretisation is done using Ansys Mesher based on the method used by Ardekani (2017), Craig *et al.* (2018), and Slootweg *et al.* (2019). The surface mesh is used as the geometry in Soltrace where the rays are traced from the sun, reflected onto the receiver and onto the absorber depicted in Figure 67 (c). For each element, the number of rays is summed and the power per ray is defined based on the model inputs. The total flux on each cell is then assigned as a local flux for in interpolation file that can then be applied as heat source for the thermal analysis depicted in Figure 67 (d).

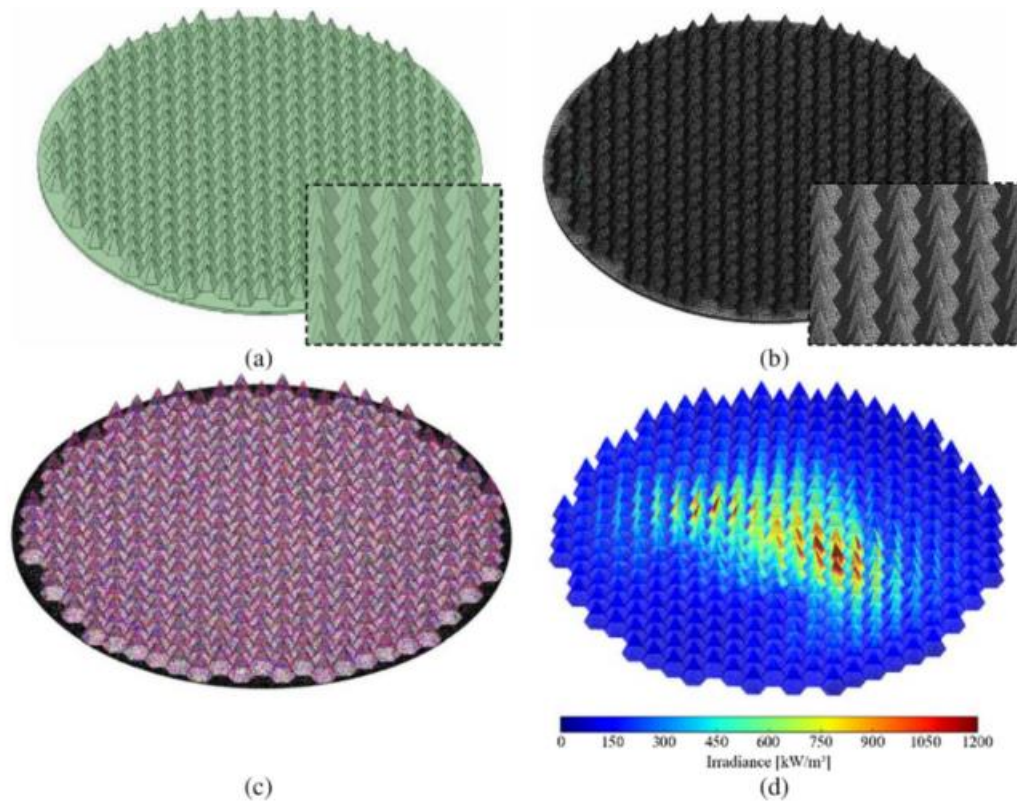


Figure 67. Optical model geometry (a) Cad geometry (b) Surface mesh of geometry (c) Rays on the receiver surface (d) Solar heat source.

With the discretised absorbing surface, the optical properties are required to determine the heat absorbed. The surface mesh of the absorbing surface contained 23 000 elements for the ray tracing model. The sun input assumes 1000 W/m^2 with a pillbox shape and 9.3 mrad angle. The optical properties of the absorbing cones and the reflective surfaces of the base are presented in Table 23.

Table 23. Optical material properties of receiver/absorber for SolTrace simulation.

	Reflectivity	Transmissivity	Slope error	Specularity error
Absorptive	0.05	0	0.95	0.2
Reflective	0.95	0	0.71	0.14

For the ray-tracing model, the accuracy of the flux distribution is proportional to the number of rays simulated (as is common with Monte Carlo simulations). As it is not computationally feasible to simulate infinite rays, a ray independence monitor is used where the proportional change in absorbed energy and distribution is compared to the required additional rays simulated. For the final surface flux distribution 315 million rays were simulated for the receiver. The total heat on the receiver cone converged to approximately 168 kW . The number of rays show convergence as the residual change in the heat flux approaches 0 as seen in Figure 68.

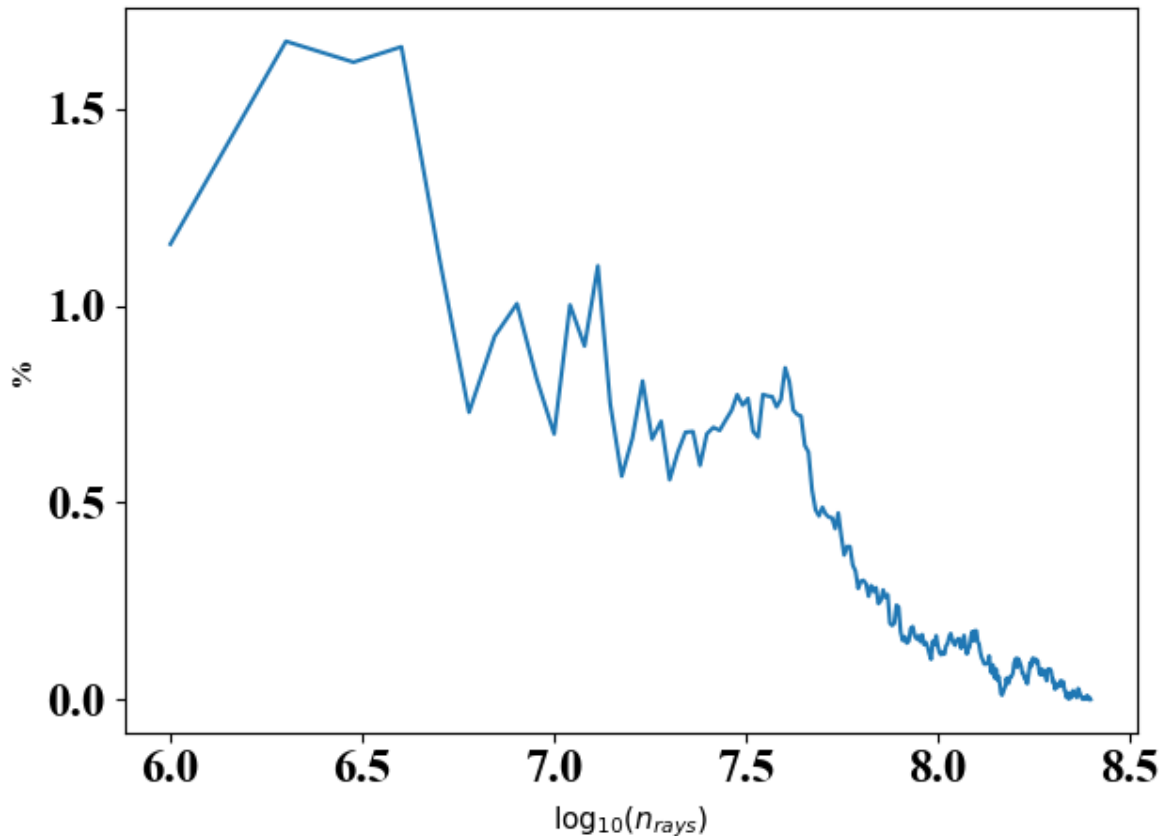


Figure 68. SolTrace ray convergence on absorbing surface.

5.3.2 Optical simulation results

The result of the Soltrace simulation is a heat flux map of the absorbing surface. Figure 69 shows that we will have a different heat flux distribution on each cone. The central cones experience a higher peak heat flux of about 2500 kW/m^2 , the outer cones show a lower peak heat flux of below 1500 kW/m^2 . Cones at different locations might therefore have different cooling requirements. The cones also show a preferential heat flux on the upper surface of the cone. This may be due to the height of the cones or the collector aiming point. This may need to be a consideration for optimising heat transfer in the future.

Figure 70 depicts a detailed heat flux map on the central cone. The peak is a lobe near the tip of the cone at 3000 kW/m^2 . One side receives most of the concentrated solar radiation. The flux map demonstrates that the consideration of a uniform heat flux over the absorbing area is incorrect. To investigate the influence of the non-uniform heat flux distribution on the heat transfer the central cone is considered. The aiming strategy and blockage effects must be considered in future studies.

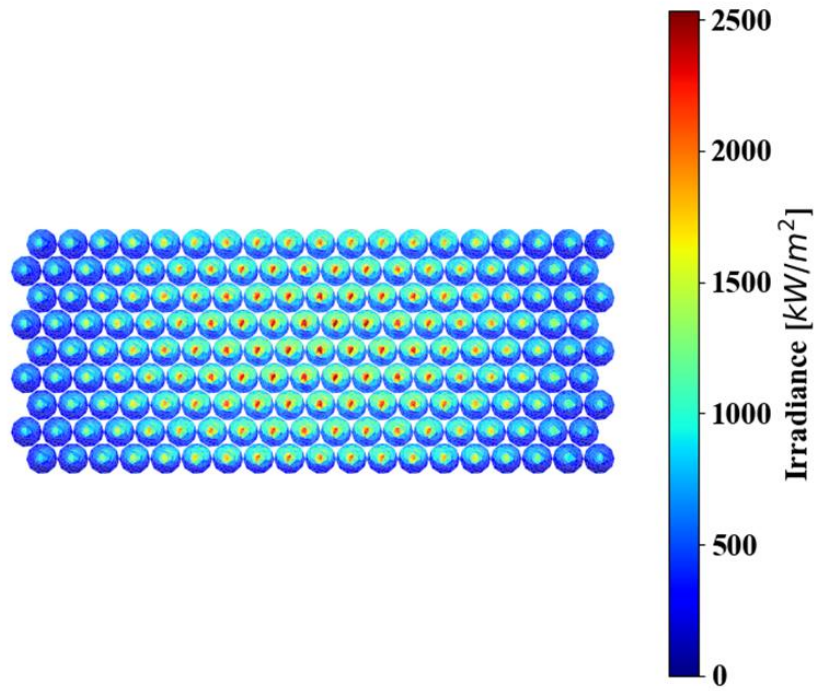


Figure 69. Heat flux distribution on absorber surface.

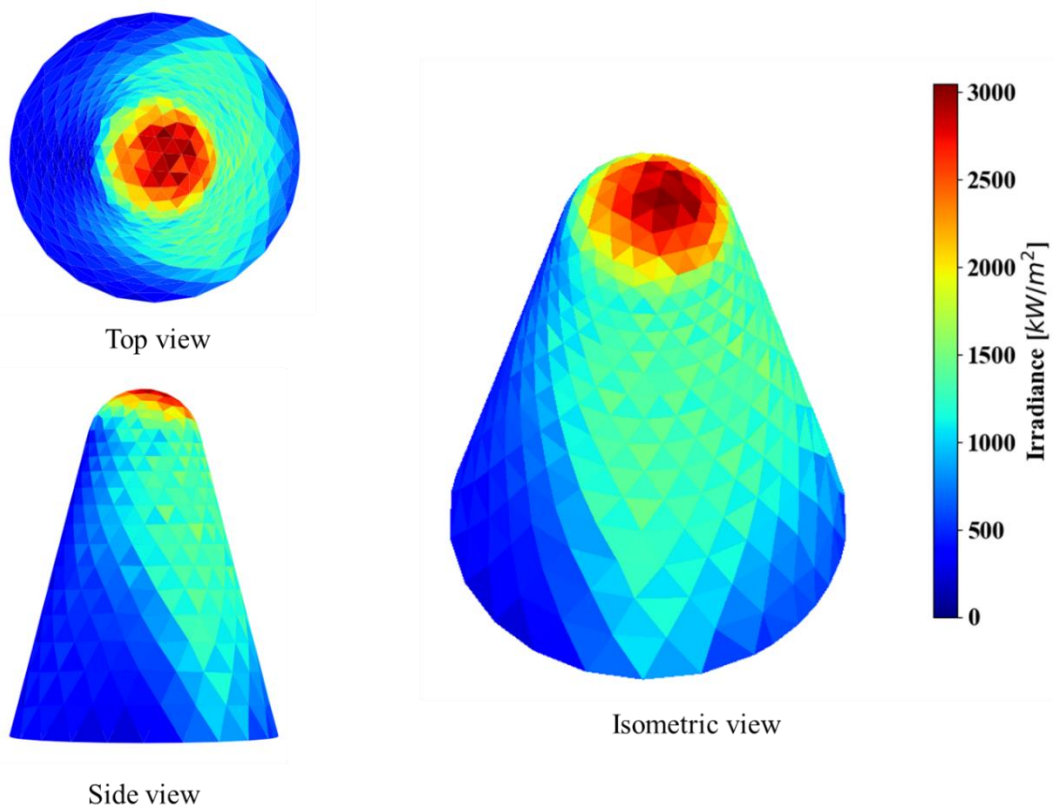


Figure 70. Heat flux distribution on central cone of the receiver.

5.4 Single cone analysis

Based on the previous analyses for the cone optimisation study a single cone is investigated in 3D with a realistic heat flux. The single cone investigation will give a direct comparison between a uniform heat flux and a realistic on-sun condition.

5.4.1 Domain and mesh

For the numerical domain considered a single cone is modelled at the centre of the receiver (Figure 71). The cone's dimensions are based on the optimal design parameters from the optimisation study. Included in the domain is the surrounding air as a hexagonal region surrounding the cone or shuttlecock, depicted in Figure 71. The hexagonal air domain is included to capture the radiation heat transfer between the cone, the adjacent cones, and the environment. The air is modelled as a transparent solid, hence any external convection is not considered for the simulation. The computational domain makes use of symmetry boundary conditions as indicated in the boundary conditions section to simplify the analysis.

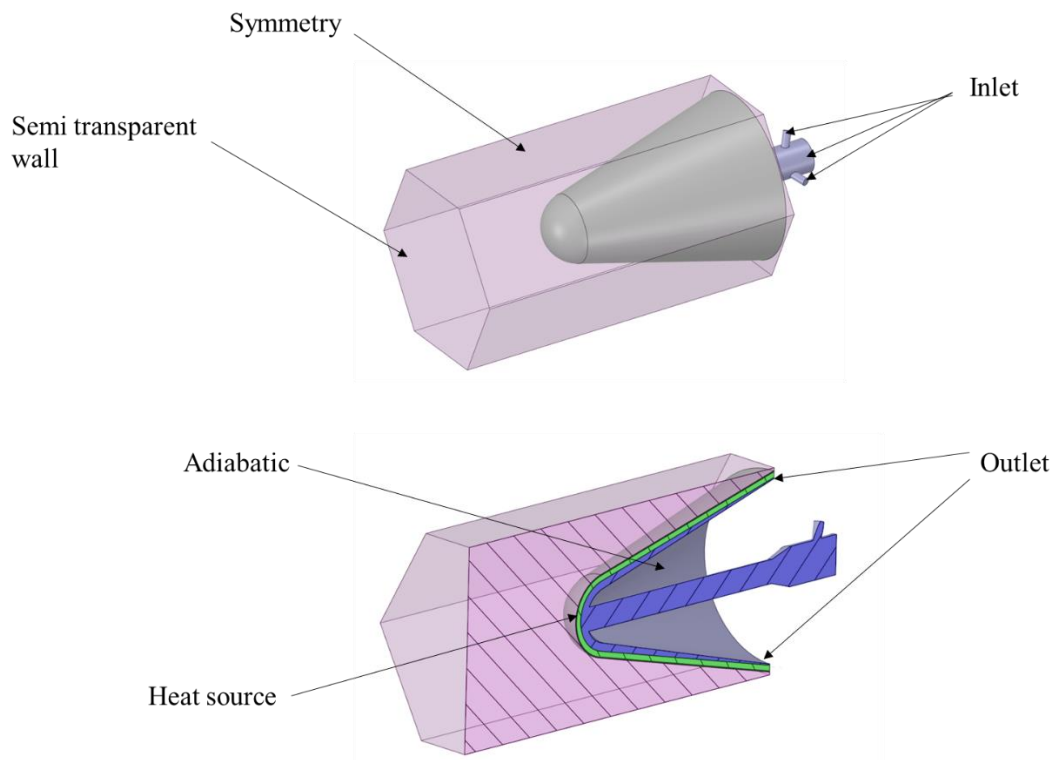


Figure 71. Single central cone CFD domain with solar heat source.

For the meshing strategy, the fluid domain is sub divided into mesh refinement regions. The mesh refinement regions are depicted in Figure 72.

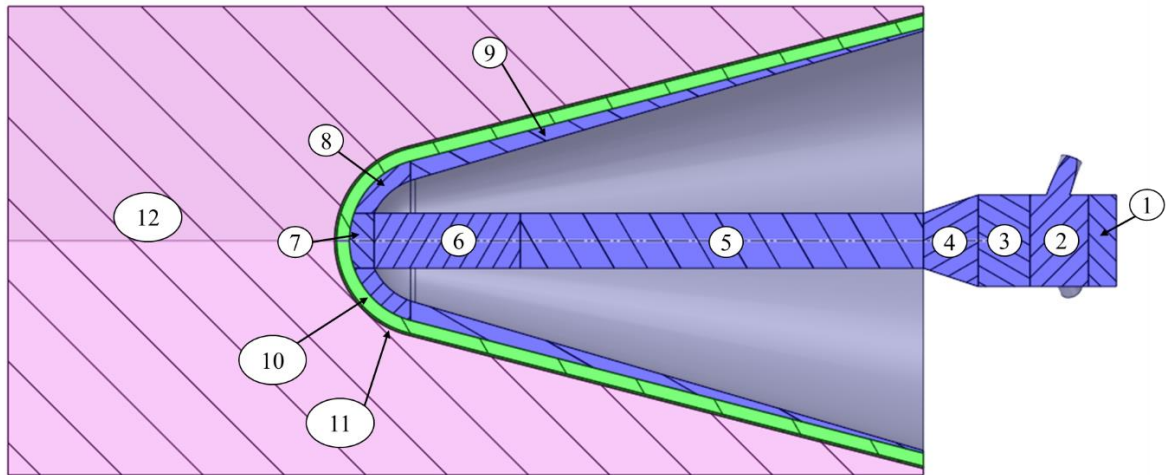


Figure 72. Shuttlecock regions for mesh refinement.

The mesh consists of polyhedral cells. Polyhedral cells are good for reducing the required number of cells and provide a good mesh for complex flows where the mesh cannot be well aligned with the flow direction. The expected flow patterns are complex, and change based the flow conditions such as swirl, therefore polyhedral cells are preferred.

The mesh refinement allows for a better control over the mesh density and the different areas of the fluid domain. The 2D simulations of previous chapters gave a good indication of the areas where complex flow is present and where mesh refinement is needed. In the fluid domain a body of influence sizing is used for mesh refinement. The boundary layer is captured using 10 inflation layers near the walls in the fluid cell zones, with a growth rate of 1.2. The cell sizes used to refine the mesh are summarised in Table 24.

Table 24. Mesh controls for central cone.

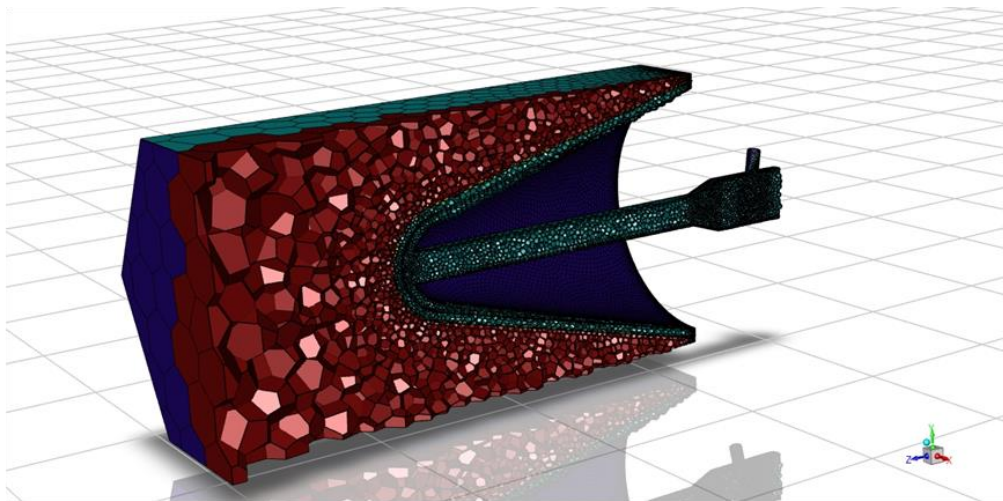
Region	Cell sizing [mm]	Growth rate
Region 1	0.8	1.3
Region 2	0.5	1.1
Region 3	0.65	1.05
Region 4	0.8	1.05
Region 5	1	1.1
Region 6	0.8	1.1
Region 7	0.35	1.05

Region	Cell sizing [mm]	Growth rate
Region 8	0.5	1.05
Region 9	1	1.5
Region 10	1.5	1.5
Region 11	0.5	2
Region 12	20	3

The solid cell zones of the domain are of interest mainly for thermal conduction and radiation. To capture thermal conduction in the solid regions a minimum of three cells are specified across the gap. In the solid air domain, a much larger cell size is specified as a body sizing on 20 mm. The mesh strategy produces a fine mesh in the fluid domain and grows the resulting surface mesh into the solid cell zones resulting in a conformal mesh. The final mesh consists of 14 million polyhedral cells. For illustrative purposes, a coarse mesh of the entire domain is depicted in Figure 73.



Front view



Isometric view

Figure 73. Coarse mesh depicting the meshing strategy for the SIJ shuttlecock receiver.

5.4.2 Material properties

For the computational setup, the work is a natural extension of the previous work (Chapter 4) using the same HTF and cone material. The cone is manufactured from carbon steel (0.08 C , 0.3 Mn) and the HTF used is solar salt, a eutectoid mixture of $\sim 60\%$ sodium nitrate ($NaNO_3$) and $\sim 40\%$ potassium nitrate (KNO_3). The solid air is simulated as a transparent solid in steady state, therefore only thermal conductivity is of interest. The material properties are specified in Table 25.

Table 25. Material properties for Shuttlecock domain.

Material	Density, ρ (kg/m^3)	Specific heat, C_p (J/ $kg \cdot K$)	Thermal conductivity, k (W/m · K)	Dynamic viscosity, μ ($kg/m \cdot s$)	Reference
Solar Salt	2263.641 $- 0.636 \cdot T$	1396.044 $+ 0.172 \cdot T$	0.45	0.07543937 $- 2.77 \times 10^{-4} \cdot T$ $+ 3.49 \times 10^{-7} \cdot T^2$ $- 1.47 \times 10^{-10} \cdot T^3$	(Serrano-López, Fradera & Cuesta-López, 2013)
Carbon steel	8030	502.8	Piecewise linear function (refer to Appendix E)	-	(Serrano-López, Fradera & Cuesta-López, 2013)
Solid air	1.225	1006.43	0.0242	-	(ANSYS, 2013)

5.4.3 Boundary conditions

The boundary conditions of the simulation are similar to the previous simulations and are depicted in Figure 71. The optimal flow conditions of the optimisation study are used for the velocity inlets. The outlet of the cone is a pressure outlet. The pipe walls are assumed to be adiabatic.

The swirl is generated using tangential inlet ports with a constant velocity. The flow is channelled between the carbon steel shell and the inner adiabatic pipe wall. The outer shell cell zone is a heat source mapped from the optical simulations. The external solid air conducts heat from the cone and allows for radiation heat transfer. The six outer solid air walls are symmetry boundary conditions and the top wall of the solid air is a semi-transparent wall region that allows radiation to leave the simulation domain as heat loss. The details of the boundary conditions are summarised in Table 26.

Table 26. Boundary conditions for shuttlecock receiver.

Boundary	Value	Comment
Heat source	Profile	Profile from SolTrace
Velocity inlet	$u_{ax} = 0.8 \text{ m/s}$ $u_{\theta} = 2.6 \text{ m/s}$ $T_j = 563 \text{ K}$	Used for jet inlet momentum and thermal conditions.
Pressure outlet	Zero pressure gradient $T_{out} = 585 \text{ K}$	

5.4.4 Numerical scheme

The numerical scheme specifications of the simulations numerical methods are summarised in section 4.4. The steady-state RANS simulation used the Transition SST turbulence model based on the validation studies. The radiation model used is the discrete ordinates (DO) method. In each quadrant, the polar (θ) and azimuthal (ϕ) angles were divided into three divisions as control angles with three subdivisions (pixels) for each angular discretisation, respectively. The radiation is only solved for the solid air zone.

5.4.5 Simulation results

The cone is simulated with a heat flux distribution from the SolTrace heat source. The simulations results are summarised in Table 27.

Table 27. CFD results for shuttlecock central cone.

Property	Value
Inlet pressure axial (<i>kPa</i>)	30
Inlet pressure tangential (<i>kPa</i>)	34
Inlet temperature (<i>K</i>)	563
Outlet temperature (<i>K</i>)	582
Maximum cone temperature (<i>K</i>)	1663

As can be seen in Figure 74 the tangential inlets create a higher vorticity in the pipe. The peak velocity is reached near the impingement surface in the channel region. A high heat transfer rate is expected to occur in this region of high velocity flow.

The total pressure is depicted in Figure 75. As can be seen the highest total pressure is at the tangential inlet ports. The pipe creates friction losses that are enhanced due to swirl. After the fluid leaves the nozzle the lowest negative pressure region is formed in the recirculation zone. The flow stagnates on the impingement surface and begins to flow towards the outlet. Some of the pressure loss is recuperated near the outlet as the channel has a taper allowing for a similar equivalent outlet flow area, to the inlet flow areas.

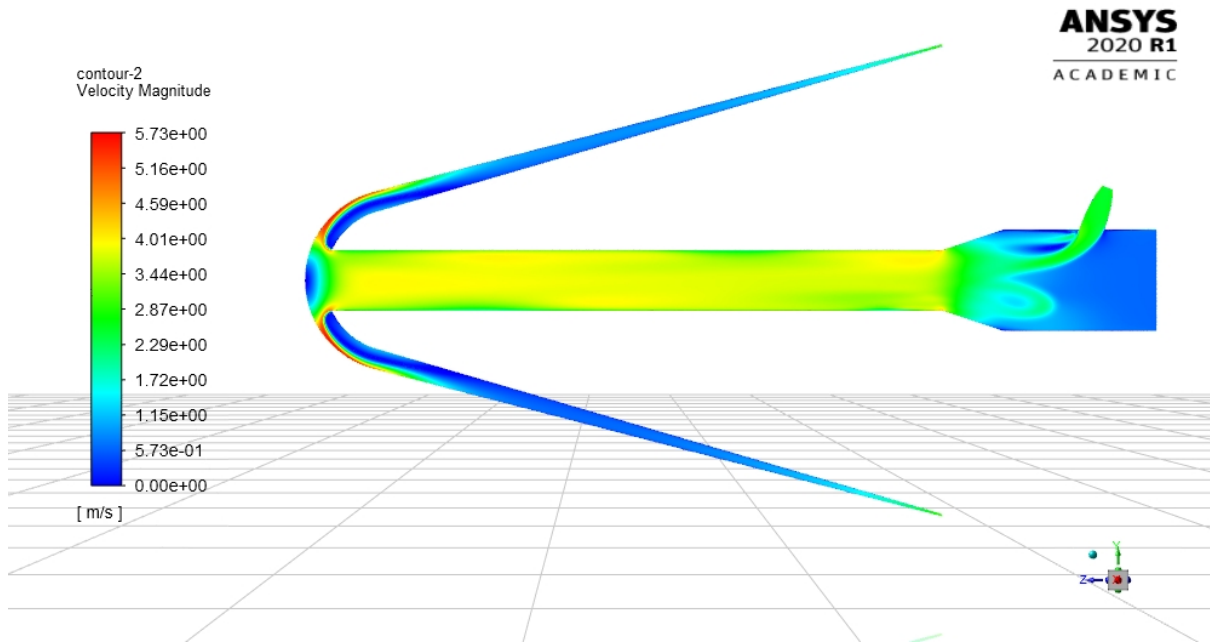


Figure 74. Velocity magnitude contours for shuttlecock cone on central plane.

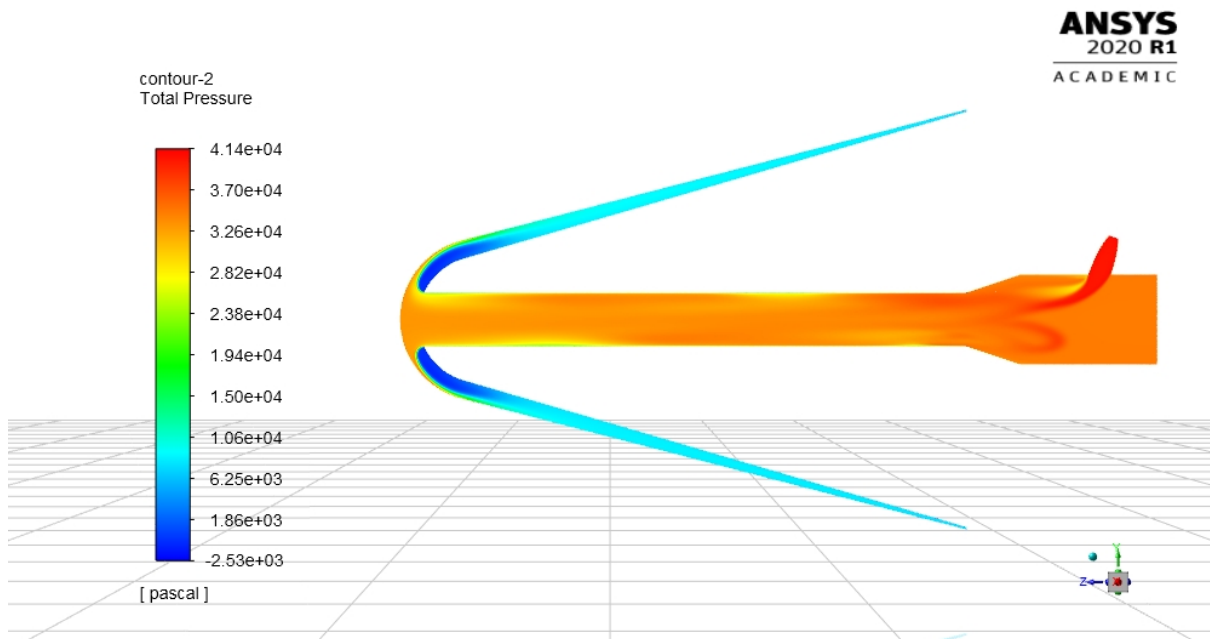


Figure 75. Total pressure contours for shuttlecock cone on central plane.

From the temperature contour plot of the domain (Figure 76), it can be seen that the peak temperature is located near the tip of the cone. The temperature profile is lob-sided due to the non-uniform incident radiation profile. The addition of swirl moves the maximum Nusselt number away from the central axis and can be used to remove the off-axis peak solar radiation more effectively.

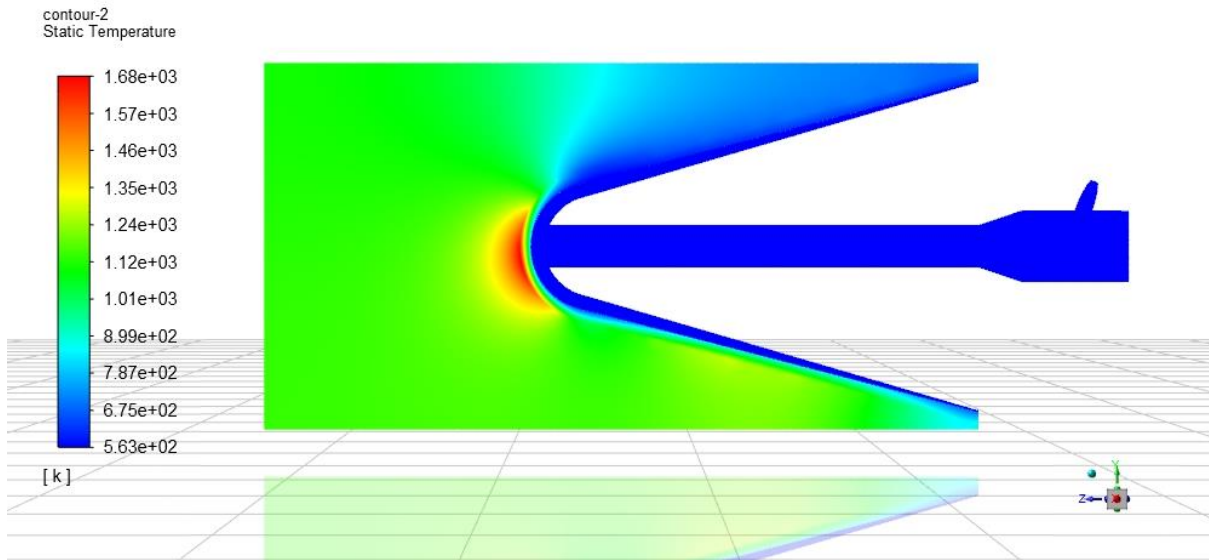


Figure 76. Static temperature for shuttlecock cone.

The temperature profile on the outer surface of the cone is depicted in Figure 77. The non-uniform heat flux on the receiver creates a local hotspot at the receiver's tip of 1663 K. The hotspot is not ideal because this spot will radiate towards the environment and is not radiated towards the adjacent cones. The maximum surface temperature is lower than the melting temperature of the carbon steel therefore demonstrating that swirl does have an advantage for this application.

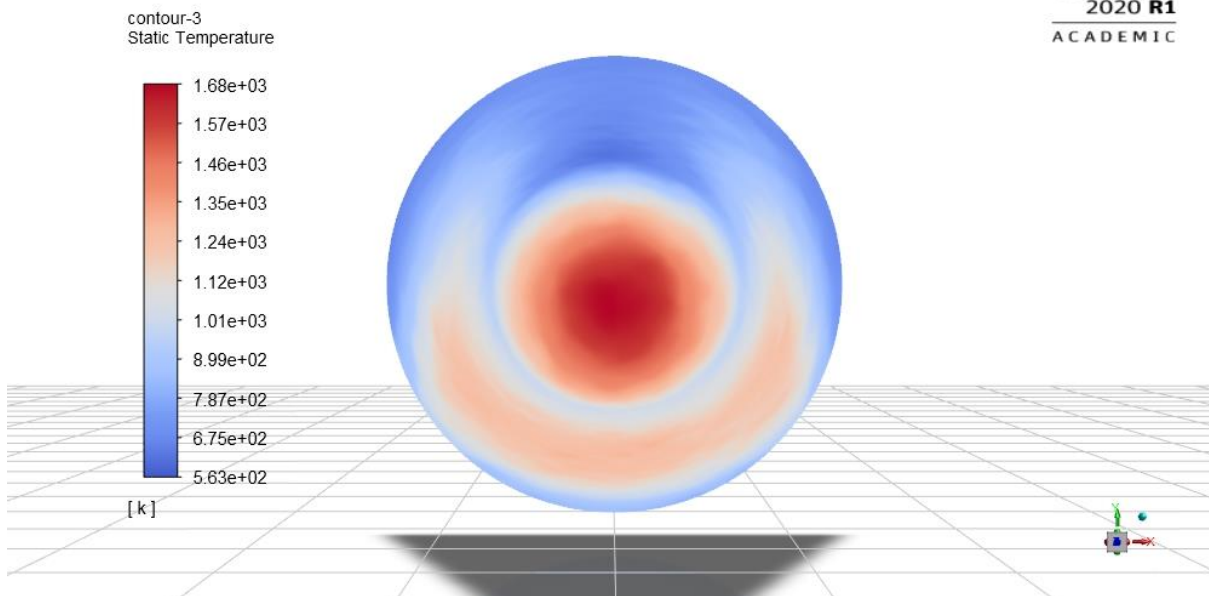


Figure 77. Static temperature [K] on shuttlecock cone absorbing surface.

The realistic heat source obtained from the PS-10 ray tracing simulations has a considerable effect on the temperature distribution. The non-uniformity creates local hot spots on the cone of near 1407 °C and 967°C at the tip and near the middle of the cone respectively. From the analysis it is shown that the cone does not allow the steel shell to exceed the melting temperature of the carbon steel of (1425 – 1540 °C) (Suzuki, Nishimura & Nakamura, 1984). The limitation of the receiver design is the maximum surface temperature of the steel cone as discussed by Sloomweg *et al.* (2019).

Despite the improved performance and heat transfer a disadvantage is the low outlet temperature for the cone HTF. The low thermal conductivity of the HTF negatively impacts the design and limits the heat transfer rates achievable. If the desired high fluid outlet temperature is required, the system may need for multiple flow-throughs and not a once-through configuration. This allows for the outer cones with lower thermal radiation intensities to act as preheaters for the fluid and as the flow is routed to the centre of the aperture the final outlet temperature required may be achieved.

The on-sun conditions show how the uniform heat flux is not a good assumption for a solar receiver. The total energy is significantly less and is focused on a smaller area of the entire cone. This affects the maximum achievable outlet temperature, the maximum surface temperature, and the location of the maximum surface temperature.

The effect of natural convection is not considered for the receiver design. The primary objective of this dissertation is to look at swirling impinging jets for solar tower receivers. The numerical expense is significantly larger when considering external natural or forced convection. The effect of thermal reradiation with the adjacent cones is however predicted to have a significant effect on the results and is investigated next.

5.5 Multiple cones radiation

The single cone was first considered with simplifying assumptions especially assuming symmetry conditions to replace the effect of surrounding cones. This assumption is oversimplified but is useful for gaining insight of how an on-sun condition influences the cone performance.

The domain is further extended to incorporate the adjacent cones depicted in Figure 78. The initial simulation's shell surface temperature is used in an iterative simulation approach. The adjacent cones are patched with the temperature profile of the central cone from the first analysis and the heat transfer is solved for the central cone, depicted in Figure 79 (a). The new temperature profile is then exported and patched to the adjacent cones and repeated until a converged solution is reached, depicted in Figure

79 (b) and Figure 79 (c). This method assumes that the cones are experiencing a similar irradiation profile from the heliostat field due to their proximity in the receiver (Figure 69).

The adapted case allows for more accurate heat transfer analysis accounting for more accurate radiation heat transfer between cones. The outer walls of the enlarged solid air zone are still assumed to be symmetry walls.

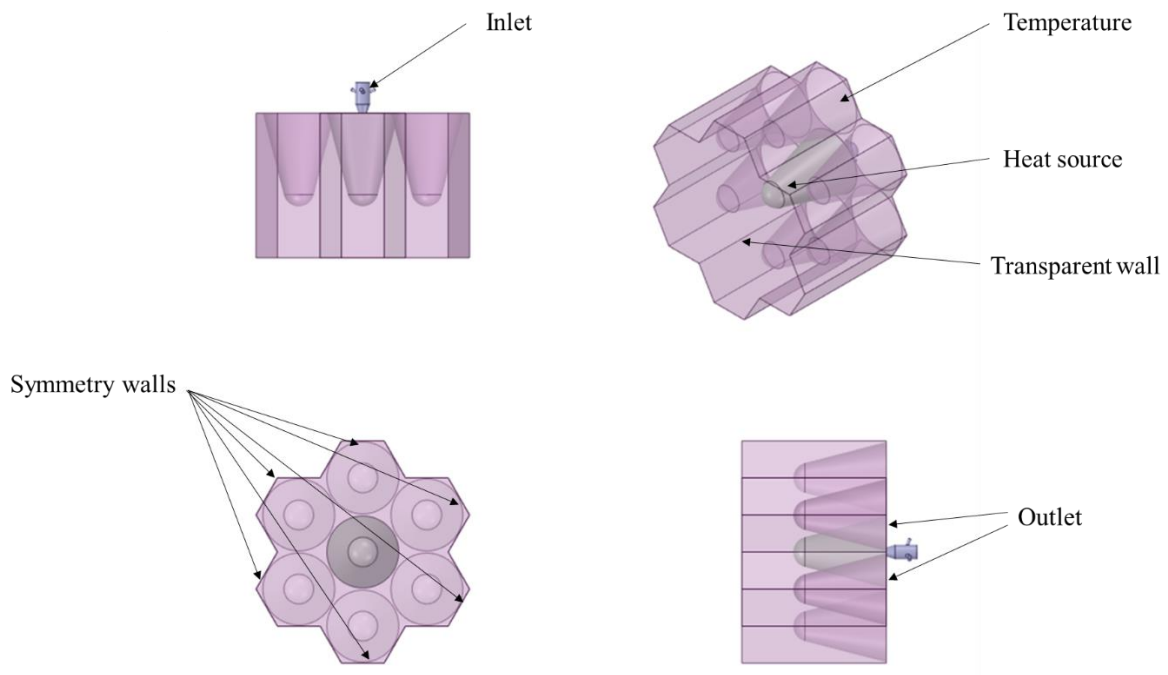


Figure 78. CFD domain for central shuttlecock cones and surrounding air.

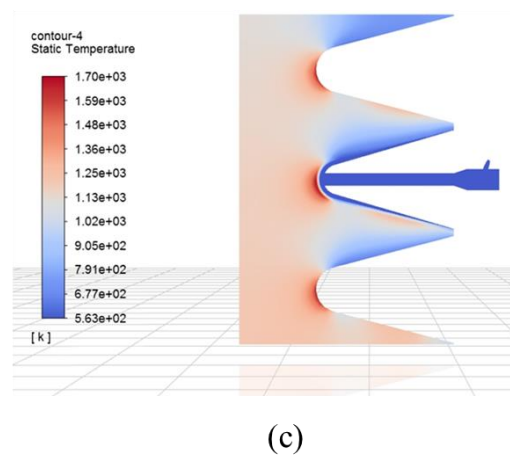
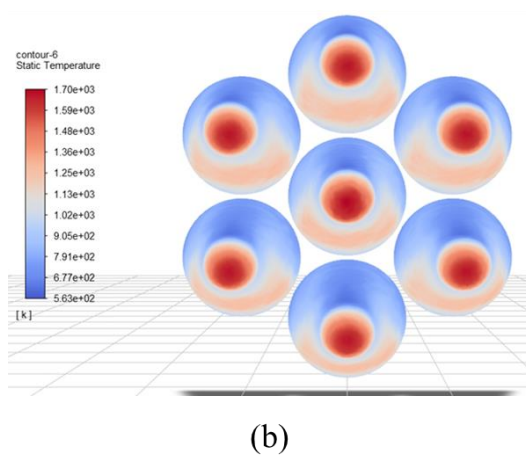
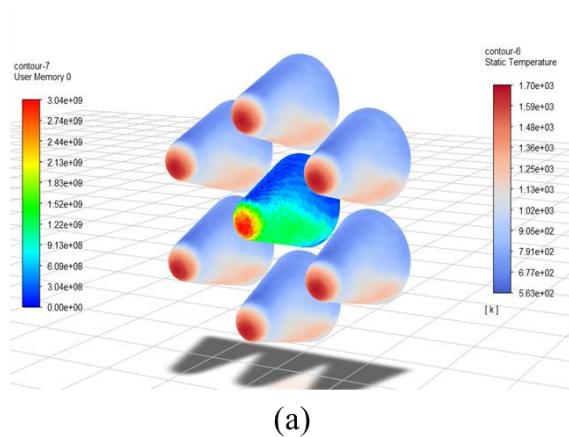


Figure 79. Static temperature on shuttlecock cone absorbing surface boundary conditions (a) heat source and surrounding cones static temperature (b) Patched static temperature from central cone (c) Side view of static temperature distribution.

The inclusion of the neighbouring cones for the radiation model changes the temperature distribution on the central cone. The peak temperature is increased by 20°C at the tip where the carbon steel is near melting temperature (Figure 79 (b) and Figure 79 (c)).

The net radiation heat flux for the cones is depicted in Figure 80. Most of the radiation emitted occurs at the tips of the cone where the local hot spot occurs. The areas where the radiation is being absorbed is near the base of the cone, acting as a radiation trap between cones. The areas of high radiation emission to the environment occur near the peak surface temperature.

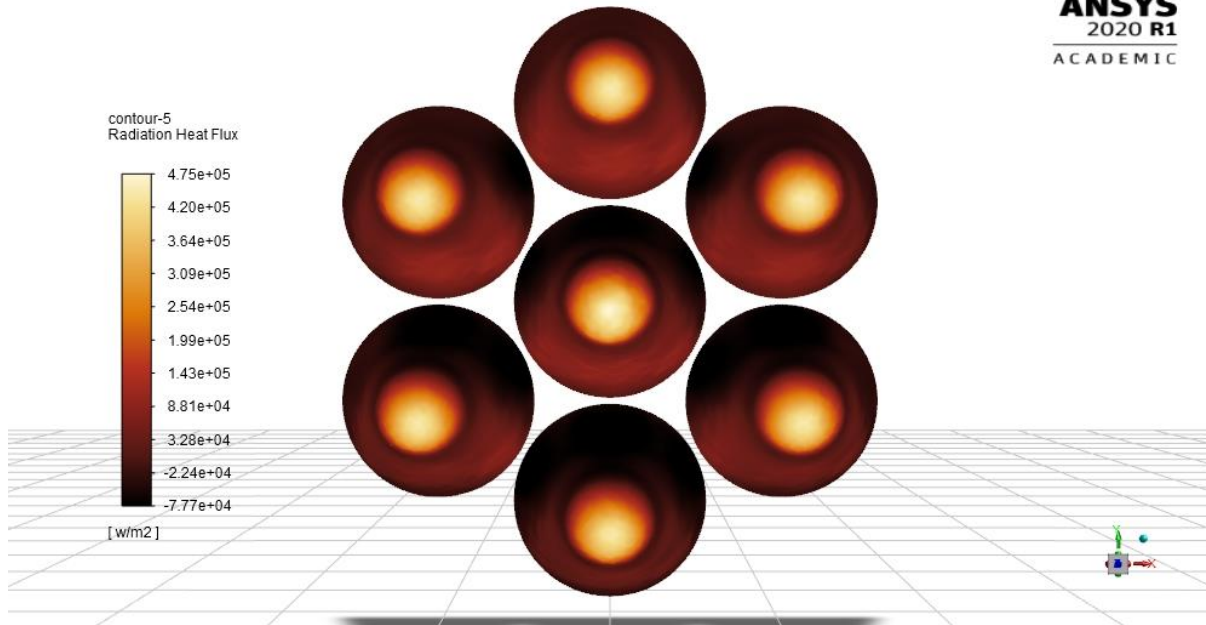


Figure 80. Radiation heat flux on absorbing surface.

The emitted radiation of the central cone is approximately 6 kW (or 4%) of the 168 kW being supplied to this cone from the heliostat field via the ray-tracing model. The energy absorbed by the HTF (in the absence of any external convection losses) is 161.8 kW. This result will be compared to a cone without swirl in the next section.

5.5.1 Swirl and no swirl comparison

To conclusively evaluate the benefit of SIJ, two additional cases are evaluated. The first case is for a conventional impinging jet without swirl and the second where the swirl is increased.

A summary of the results is presented in Table 28. The heat absorbed by the HTF is not significantly impacted by the presence of swirl with a slight reduction in radiation losses. The maximum surface temperature of the cone is however significantly impacted by the presence of swirl.

Table 28. CFD results for shuttlecock central cone for different swirl numbers.

Property	$S = 0$	$S = 0.3$	$S = 1.2$
Total (integrated) solar heat source (kW)	168.2	168.2	168.2
Pressure drop of HTF axial (kPa)	29.89	30	45.9
Pressure drop of HTF tangential (kPa)	0	34	50.2
Inlet temperature (K)	563	563	563
Outlet temperature (K)	585.23	585.11	585.34

Property	$S = 0$	$S = 0.3$	$S = 1.2$
Heat gain by heat transfer fluid (W)	161.8	162.8	162.7
Maximum receiver temperature (exposed to sun) (K)	1782.3	1702.25	1616.74
Radiation heat lost through aperture (W)	6175.4	5535.3	4771.7

The temperature profile along the radial direction is depicted in Figure 81. The solid line indicates the maximum temperature on the cone in the radial direction and the transparent points indicate the temperature distribution. The design tries to capture the heat and reduce the radiation losses with high view factors to adjacent cones. Only the tip radiates most of the energy to the environment. The lower maximum temperature may also have operation lifetime and maintenance benefits. The additional cost for the receiver design is the increase in required pressure for the inlets and manufacturing of the swirl inlet geometry. The maximum surface temperature was reduced by 166 °C for high swirl flow compared to no swirl. The reduced maximum surface temperature is near the tip which has a high view factor to the environment. Near the base of the cone the swirl did not have a significant effect on the surface temperature.

The surface temperature contours are depicted in Figure 82 to Figure 84. The temperature profile peaks and valleys correspond well with the applied heat source distribution. The addition of swirl seems to reduce the hotspot size at the tip. The effect of the symmetry boundaries is shown in the side views for the midplane temperature plot for each simulation. Some cones lose less radiation on the cold side and more on the hot side, due to the symmetry assumption. The inclusion of the adjacent cones shows an effect on the radiation losses the central. The inclusion of the adjacent cones changed the radiation losses by 1 kW with a single cone model overestimating the radiation losses.

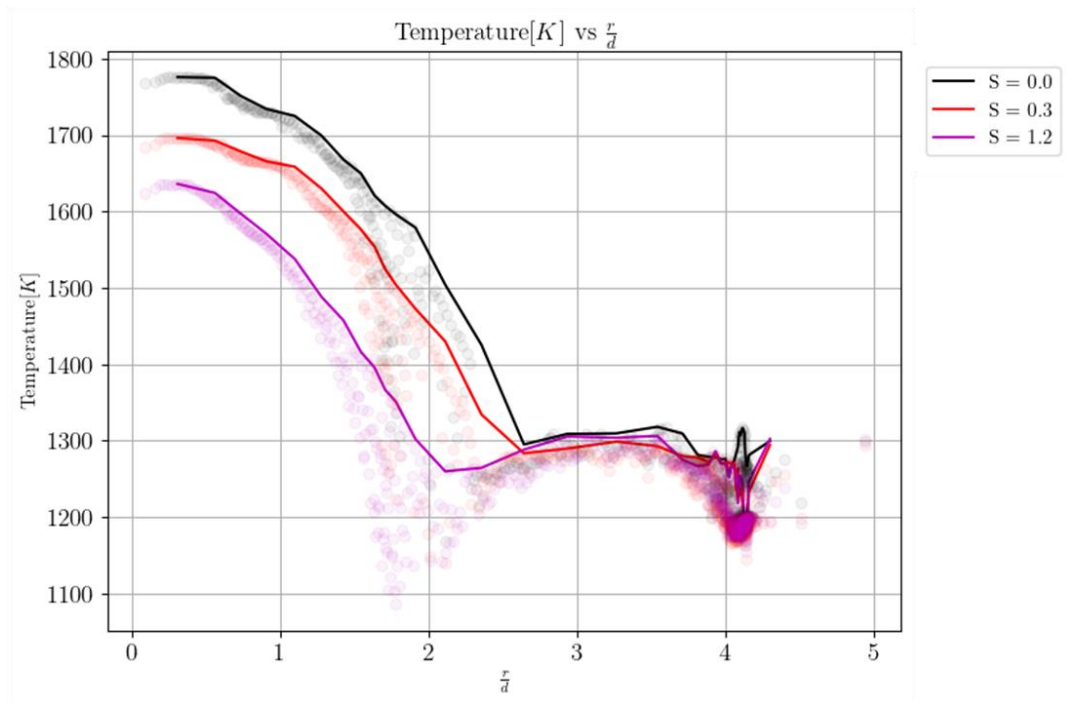


Figure 81. Static temperature on shuttlecock cone absorbing surface in the radial direction for different swirl numbers.

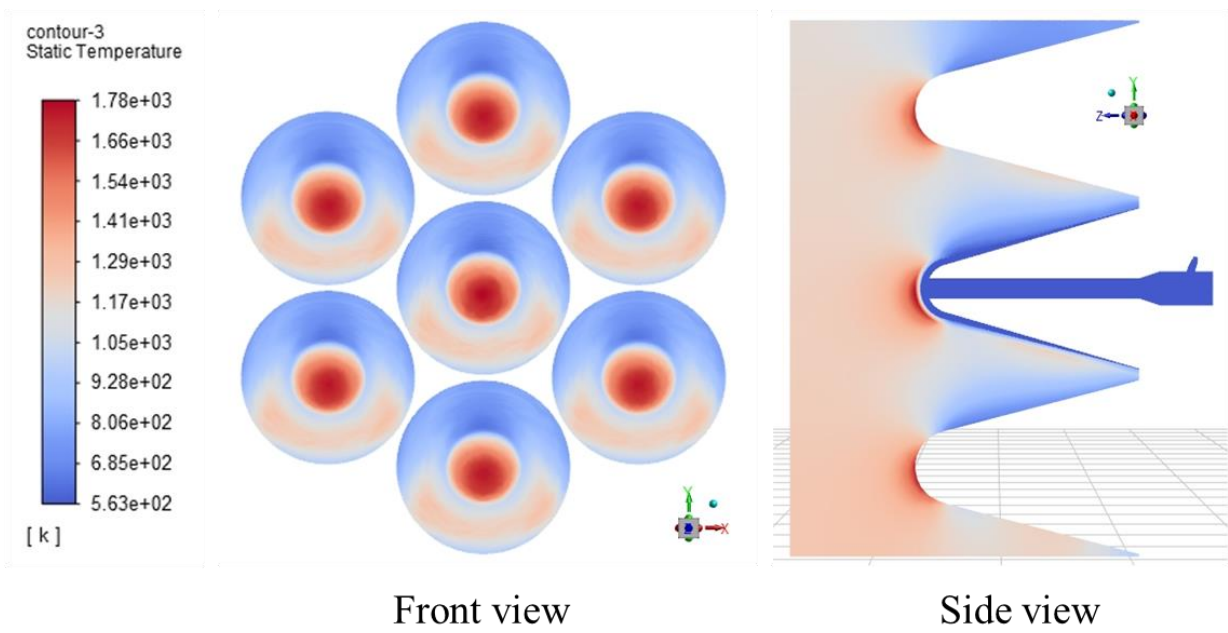


Figure 82. Static temperature on shuttlecock cone where $S = 0$.

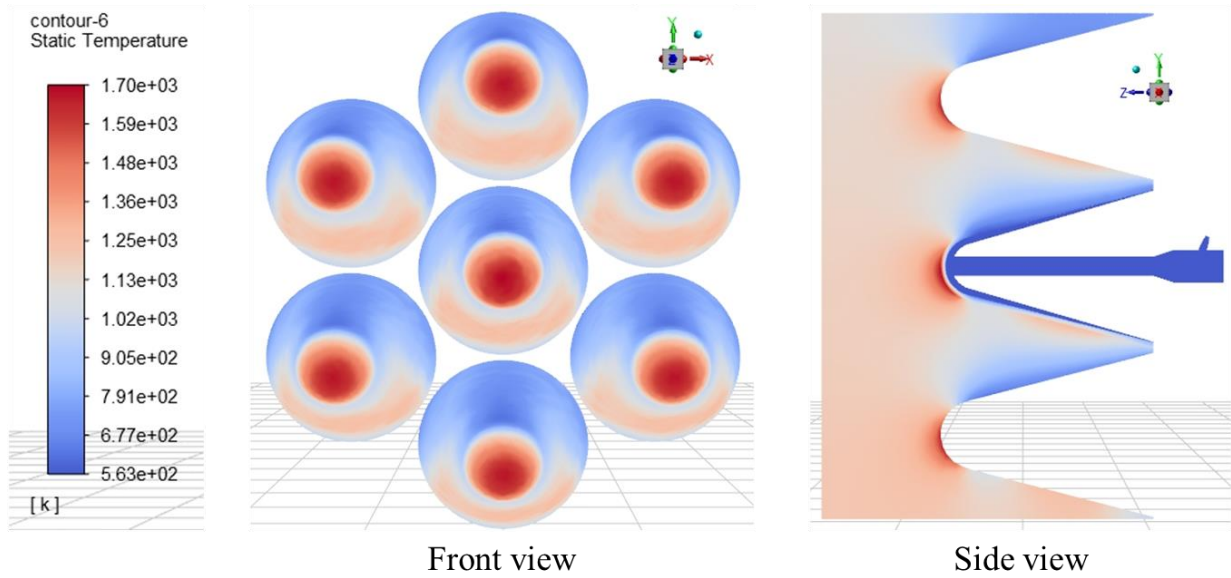


Figure 83. Static temperature on shuttlecock cone where $S = 0.3$.

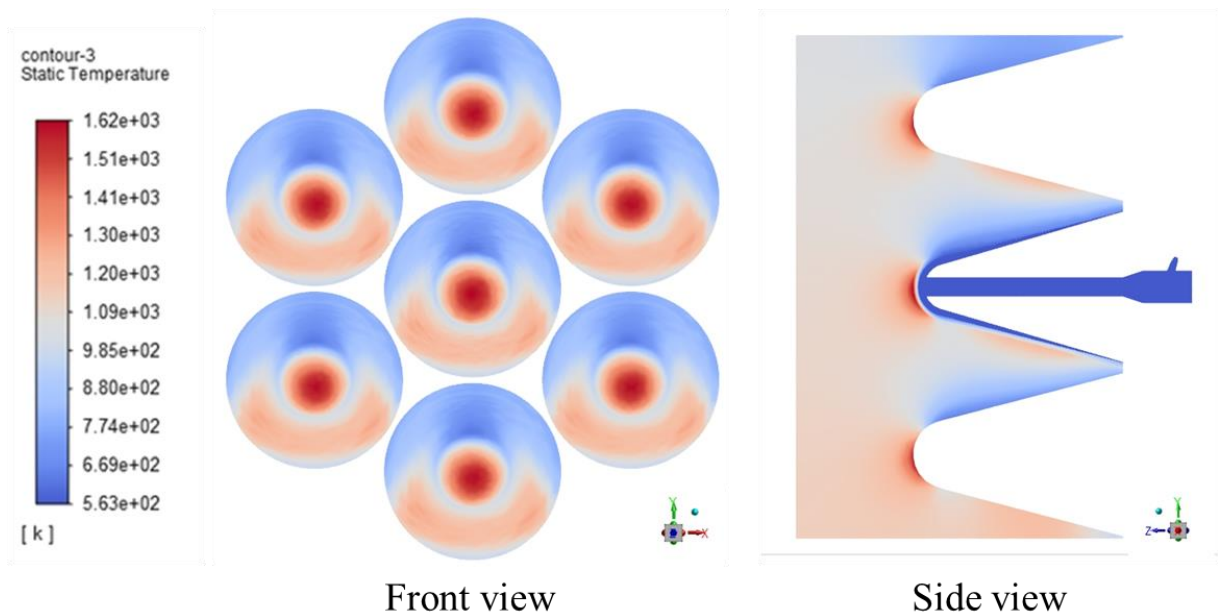


Figure 84. Static temperature on shuttlecock cone where $S = 1.2$.

The reduced surface temperature may be due to the improved heat transfer near the tip. The non-dimensional Nusselt numbers normalised by the no-swirl case are depicted in Figure 85. It is clear that the high swirl case has a higher heat transfer near the tip and more uniform on the tip. The lower heat transfer near the outlet for all swirls is similar.

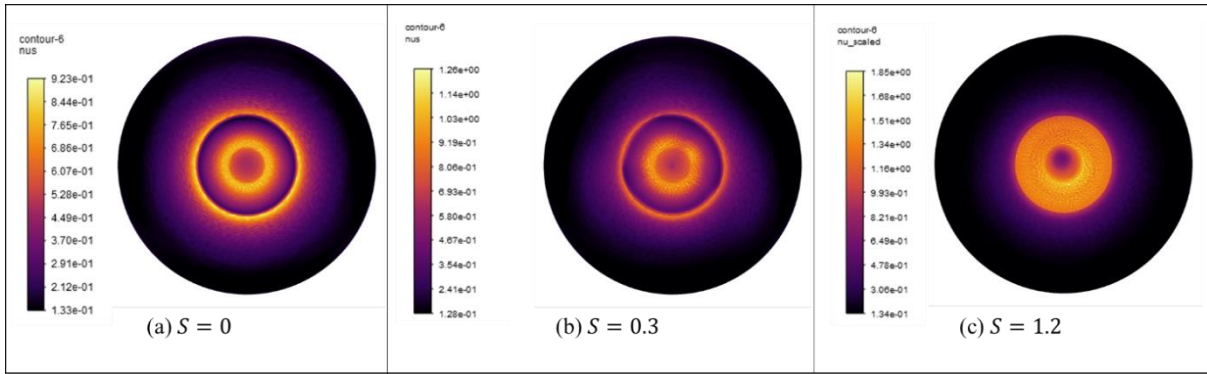


Figure 85. Non-dimensional Nusselt number on impingements surface for different swirl intensities.

The non-dimensional Nusselt number is plotted against a non-dimensional radius in Figure 86. It is clear that the swirl improved the heat transfer in the impingement region. As the flow approaches the outlet the heat transfer rates are similar. The heat transfer has been significantly enhanced compared to no-swirl case by 2.3% on average and the peak is enhanced by 19%. The enhancement allows for a reduction in the surface temperature of the cone.

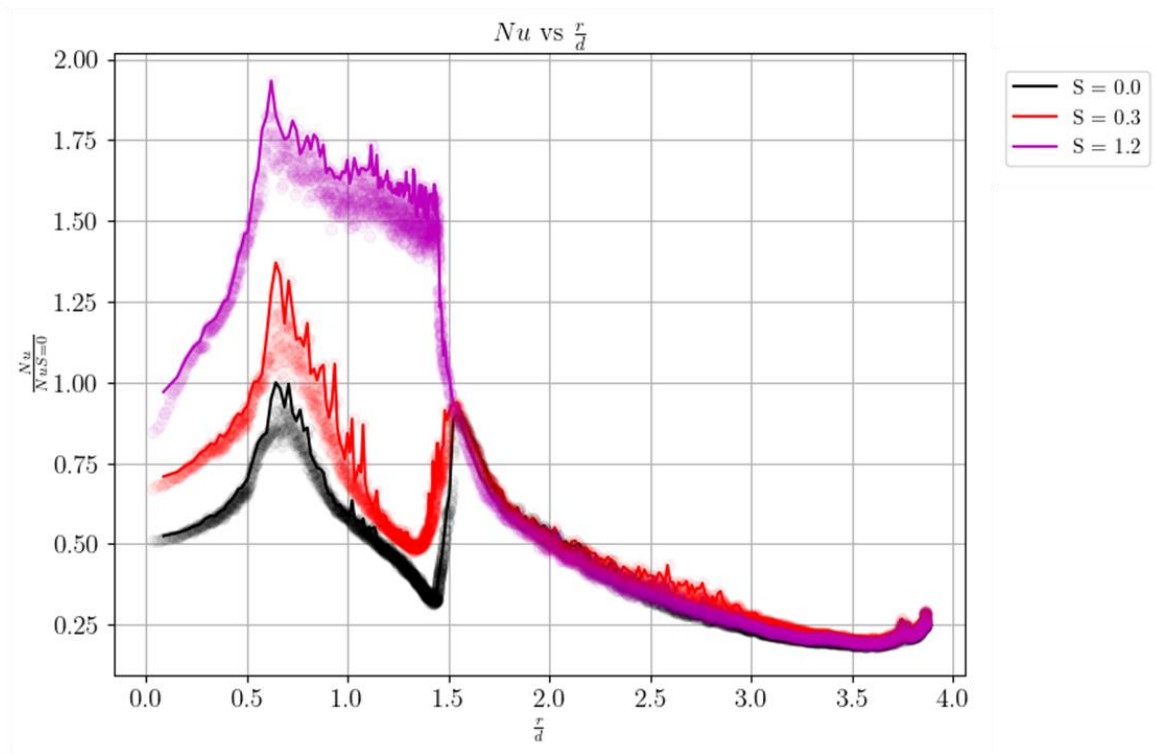


Figure 86. Non-dimensional circumferentially averaged Nusselt number on impingement surface for different swirl intensities.

Based on the simulation the cone is not achieving a desired increase in heat transfer to the HTF. In order to achieve a higher outlet temperature, the heat flux on the cone must be increased by the collector or by increasing the size of the cone to intercept more solar radiation. The disadvantage of using swirl is

however the increased pumping requirements at the inlets. Both the pressure losses and heat transfer enhancements must be considered for a final design.

5.6 Conclusions

This chapter focused on the thermal performance of the receiver under more realistic flux distributions. From the results of the study the following conclusions can be made:

- The receiver design can be improved despite the use of enhanced heat transfer obtained with SIJ.
- The application of a realistic heat flux over the absorber surface is important. The non-uniformity of the heat flux can change the heat transfer requirements of the design.
- The effect of radiation heat transfer is important for the design.
- The non-uniform heat flux must be considered at the optimisation stage of the design.
- The use of molten salt for advancing STP is not promising. The salt limits the achievable heat transfer and the upper usable limit of the salt hinders the maximum achievable thermal efficiency due to the HTF specific heat.
- Significantly less total energy enters the system compared to the optimisation studies. Due to the applied heat flux on the receiver in comparison to the realistic heat flux.
- The use of swirl has potential applications for reducing radiation losses and reducing the maximum operating temperature of the receiver.

6 CONCLUSIONS AND FUTURE WORK

6.1 Conclusions

The dissertation aimed to investigate a novel proposed receiver design for an SPT. The investigation introduced the need for renewable energy and highlighted the potential of CSP. CSP technologies being used in industry have potential for improvement. The CSP technology with the most potential is SPT.

The objectives defined in Chapter 1 have mostly been reached. Table 29 presents the defined objectives and the outcome of the objectives.

Table 29. Achievement of dissertation objectives

Objective	Completion
Investigate the fundamentals of SPT receivers	✓
Research methods used for improving receiver efficiencies	✓
Develop a thermal model for a proposed SPT receiver	✓
Validation of the thermal model	
2D axi-symmetric model	✗
3D aerodynamic swirl generator	✓
3D geometric swirl generator	✓
Investigate the use of swirl with impinging jets for heat transfer enhancements	✓
Investigate effect of surface curvature on SIJ	✓
Use swirl to enhance heat transfer	
Improve heat transfer	✗
Address design limitations	✓
Optimise receiver design	✓
Investigate realistic solar flux on receiver	✓

In Chapter 2, the literature pertaining to the topic was researched. It can be concluded that CSP holds promise for the renewable energy industry particularly SPT. The need for SPT receivers to operate at higher temperatures is the key to improving the technology. To do this, the SPT plant components and the interactions between components must be understood. The interaction between the collector and receiver is inherently coupled and both components influence the efficiency of the system. The designs of receivers that are capable of operating at high temperatures are presented. From the receiver designs, the heat transfer enhancement techniques of jet impingement and swirl were highlighted.

A novel receiver design is proposed for the study. The receiver aims to address the limitations of historical designs and improve the receiver's efficiency using SIJ. The modelling of JIHT and swirl are considered for CFD. To validate the CFD approach several experimental setups are replicated. The experiments selected include:

1. A jet impinging on a flat surface without swirl.
2. A jet impinging on a flat surface with aerodynamically generated swirl.
3. A jet impinging on a flat surface with geometrically generated swirl.
4. A jet impinging on a concave surface without swirl.

Chapter 3 described the validation of the CFD model for SIJ on a concave surface. From the results obtained, it can be concluded that:

- 2D axi-symmetric models predict impinging jets without swirl well, with at least 20% accuracy for a flat surface and concave surface when using the Transition SST RANS turbulence models.
- LES is the best turbulence modelling approach and captures SIJ heat transfer the best. LES can predict the location of the peak Nusselt number and the magnitude of the peak Nusselt number within 5% and 9%, respectively. LES is however extremely computationally expensive and not feasible for the scope of the dissertation that also involved optimisation.
- The 2D axi-symmetric models do not predict the location of the peak Nusselt number accurately. The peak Nusselt number is predicted within 16 - 75% accuracy.
- The advantage of the 2D simulations is that the average Nusselt number is predicted within 12% accuracy. The 2D simulations are inexpensive to run and therefore can be justified for a reduced-order optimisation model.
- The 3D simulations predict the average heat transfer of geometrically-generated swirl within 13%. The 3D RANS cases do not however predict the stagnation point Nusselt number accurately, with a 48% error.

Optimisation methods were implemented in Chapter 4 to determine the influence of various parameters. The following conclusions can be drawn:

- From the concave SIJ investigation a 2D optimisation is done for the receiver design parameters. In total nine parameters were investigated. A radial basis function surrogate model was used with a latin hypercube sample space to perform a multi-objective optimisation of the cone with three candidate points identified and validated.

Finally, Chapter 5 investigated the candidate design from Chapter 4 in 3D with a realistic heat source obtained from SolTrace. Only radiation losses were considered with external natural convection not modelled. From the simulations the following conclusions can be drawn:

- The realistic heat source must be considered for the optimisation study as the non-uniform heat flux influences the maximum temperature on the cone shell and the achievable outlet temperature.
- For a molten salt inlet temperature of 563 K and a mass flow rate of 4.89 kg/s the thermal efficiencies for $S = 0$, $S = 0.3$ and $S = 1.2$ are 96.2%, 96.79 and 96.74%, respectively. The addition of swirl did not have a significant effect on the outlet temperature.
- The addition of swirl improved heat transfer rates by 2.3% on average and by 19.7% for the peak heat transfer coefficient.
- The most significant effect of the addition of swirl was to reduce the maximum cone surface temperature by more than 160 °C. This is of particular interest as this reduction improves the operational life of the receiver and widens the gap to the melting temperature of the cone.
- The reduction of peak surface temperature reduced the radiation heat losses to the environment from 6.2 kW to 4.8 kW.

Detailed results of temperature and heat transfer distributions as determined in this dissertation can allow for better estimations and predictions for SIJ for heat transfer applications. The investigation for SIJ on a concave surface is in its infancy but hopefully this study can serve as a baseline for future studies to improve numerical models of SIJ. The detailed numerical method and results can aid in improving the development of SPT receivers.

6.2 Future work and Recommendations

From the investigation, potential areas that may be further investigated were found. For future research, the proposed receiver design can be optimised to achieve better thermal efficiencies. Specific items that can be investigated, are:

- Optical modelling can be used to investigate a realistic solar flux distribution on the receiver with SolTrace for different sun angles and annual variations.
- The secondary concentrator and aiming strategies can be investigated to determine the optimal cavity design to achieve more uniform heat fluxes for the variation in incoming radiation.
- External natural and forced convection due to wind need to be included in the thermal performance assessment as the cavity receiver is still open to the environment.

- The parametric analysis can be extended when optimising the JIHT pyramid design. Parameters for investigation are suggested by Sloomweg (2018). As an example, the investigation of pressure losses and heat transfer can be optimised using multi-objective optimisation.
- Additional methods of heat transfer enhancement (such as fins) can be investigated to improve the heat transfer performance as suggested by Garbrecht *et al.* 2013, Lubkoll *et al.* (2015), and Sloomweg (2018).
- The optical modelling makes simplifying assumptions such as all of the heliostats surfaces are flat. Optical modelling with ray tracing can be developed further. Modelling tools such as those from Sloomweg *et al.* (2019) can offer potential to consider the combination of optical modelling and thermal modelling.
- The limitations on the computing time hindered further investigations for LES. LES should be used to further investigate this type of flow as other models are sufficiently accurate at predicting SIJ heat transfer.

REFERENCES

- Ab Kadir, M.Z.A., Rafeeu, Y. & Adam, N.M. 2010. Prospective scenarios for the full solar energy development in Malaysia. *Renewable and Sustainable Energy Reviews*, 14(9):3023-3031.
- Abe, K.I. & Suga, K. 2001. Large eddy simulation of passive scalar in complex turbulence with flow impingement and flow separation. *Heat Transfer—Asian Research: Co-sponsored by the Society of Chemical Engineers of Japan and the Heat Transfer Division of ASME*, 30(5):402-418.
- Abrantes, J.K. & Azevedo, L.F.A., *Fluid flow characteristics of a swirl jet Impinging on a flat plate*. Paper presented at the 13th International Symposium on Applications of Laser Techniques to Fluid Mechanics, Lisbon, Portugal, 26-29 June.
- Africa, T.W. 1975. Archimedes through the looking-glass. *The Classical World*, 68(5):305-308.
- Ahmed, Z.U. 2016. *An experimental and numerical study of surface interactions in turbulent swirling jets*. Unpublished doctoral thesis, Perth, Australia: Edith Cowan University. [Online] Available from: <https://ro.ecu.edu.au/theses/1790>
- Ahmed, Z.U., Al-Abdeli, Y.M. & Guzzomi, F.G. 2015a. Impingement pressure characteristics of swirling and non-swirling turbulent jets. *Experimental Thermal and Fluid Science*, 68:722-732.
- Ahmed, Z.U., Al-Abdeli, Y.M. & Guzzomi, F.G. 2016a. Corrections of dual-wire CTA data in turbulent swirling and non-swirling jets. *Experimental Thermal and Fluid Science*, 70:166-175.
- Ahmed, Z.U., Al-Abdeli, Y.M. & Guzzomi, F.G. 2016b. Heat transfer characteristics of swirling and non-swirling impinging turbulent jets. *International Journal of Heat and Mass Transfer*, 102:991-1003.
- Ahmed, Z.U., Al-Abdeli, Y.M. & Guzzomi, F.G. 2017. Flow field and thermal behaviour in swirling and non-swirling turbulent impinging jets. *International Journal of Thermal Sciences*, 114:241-256.
- Ahmed, Z.U., Al-Abdeli, Y.M. & Matthews, M.T. 2015b. The effect of inflow conditions on the development of non-swirling versus swirling impinging turbulent jets. *Computers & Fluids*, 118:255-273.
- Alekseenko, S.V., Bilsky, A.V., Dulin, V.M. & Markovich, D.M. 2007. Experimental study of an impinging jet with different swirl rates. *International Journal of Heat and Fluid Flow*, 28(6):1340-1359.
- Angioletti, M., Nino, E. & Ruocco, G. 2005. CFD turbulent modelling of jet impingement and its validation by particle image velocimetry and mass transfer measurements. *International Journal of Thermal Sciences*, 44(4):349-356.
- ANSYS Inc. 2013. *ANSYS fluent theory guide*. Canonsburg: ANSYS Inc.

- Ardekani, M.M. 2017. *Optical, thermal and economic optimisation of a linear fresnel collector*. Unpublished doctoral thesis. Pretoria: University of Pretoria. [Online] Available from: <https://repository.up.ac.za/handle/2263/61313?show=full> [Accessed: 2018-09-07].
- Arya, N. & De, A. 2019. Effect of grid sensitivity on the performance of wall adapting SGS models for LES of swirling and separating–reattaching flows. *Computers & Mathematics with Applications*, 78(6):2035-2051.
- Asselineau, C.A. 2017. *Geometrical optimisation of receivers for concentrating solar thermal systems*. Unpublished doctoral thesis. Canberra, Australia: The Australian National University. [Online] Available from: <http://hdl.handle.net/1885/143561> [Accessed: 2018-08-31].
- Ávila-Marín, A.L. 2011. Volumetric receivers in solar thermal power plants with central receiver system technology: a review. *Solar Energy*, 85(5):891-910.
- Baig, H., Sarmah, N., Heasman, K. C. & Mallick, T. K. 2013. Numerical modelling and experimental validation of a low concentrating photovoltaic system. *Solar Energy Materials and Solar Cells*, 113:201-219.
- Behar, O., Khellaf, A. & Mohammadi, K. 2013. A review of studies on central receiver solar thermal power plants. *Renewable and Sustainable Energy Reviews*, 23:12-39.
- Behnia, M., Parneix, S. & Durbin, P.A. 1998. Prediction of heat transfer in an axisymmetric turbulent jet impinging on a flat plate. *International Journal of Heat and Mass Transfer*, 41(12):1845-1855.
- Behnia, M., Parneix, S., Shabany, Y. & Durbin, P. 1999. Numerical study of turbulent heat transfer in confined and unconfined impinging jets. *International Journal of Heat and Fluid Flow*, 20(1):1-9.
- Benoit, H., Spreafico, L., Gauthier, D. & Flamant, G. 2016. Review of heat transfer fluids in tube-receivers used in concentrating solar thermal systems: properties and heat transfer coefficients. *Renewable and Sustainable Energy Reviews*, 55:298-315.
- Bieber, M., Kneer, R. & Rohlf, W. 2017. Self-similarity of heat transfer characteristics in laminar submerged and free-surface slot jet impingement. *International Journal of Heat and Mass Transfer*, 104:1341-1352.
- Bilen, K., Bakirci, K., Yapici, S. & Yavuz, T. 2002. Heat transfer from a plate impinging swirl jet. *International Journal of Energy Research*, 26(4):305-320.
- Bradshaw, R. & Carling, R. 1987. A review of the chemical and physical properties of molten alkali nitrate salts and their effect on materials used for solar central receivers. In: Mamantov, G., Blander, M., Hussey, C., Mamantov, C., Saboungi, M. & Wilkes, J. (eds). *Proceedings of the Joint International Symposium on Molten Salts*, Pennington, NJ:959-969.
- Brown, K. J., Persoons, T. & Murray, D. B. 2010. *Heat transfer characteristics of swirling impinging jets*. Paper presented at the International Heat Transfer Conference, Washington, DC, 8-13 August:1-9.

- Butti, K. & Perlin, J. 1980. *A golden thread : 2500 years of solar architecture and technology*. Palo Alto, NY: Cheshire Books.
- Calise, F. & Vanoli, L. 2012. Parabolic trough photovoltaic/thermal collectors: design and simulation model. *Energies*, 5(10):4186-4208.
- Carlomagno, G.M. & Cardone, G. 2010. Infrared thermography for convective heat transfer measurements. *Experiments in Fluids*, 49(6):1187-1218.
- Cavallaro, F. 2009. Multi-criteria decision aid to assess concentrated solar thermal technologies. *Renewable Energy*, 34(7):1678-1685.
- Çengel, Y.A. & Ghajar, A.J. 2015. *Heat and mass transfer: fundamentals & applications*, New York, NY: McGraw-Hill Education.
- Chen, Y.T., Kribus, A., Lim, B.H., Lim, C.S., Chong, K.K., Karni, J., Buck, R., Pfahl, A. & Bligh, T.P. 2004. Comparison of two sun tracking methods in the application of a heliostat field. *Journal of Solar Energy Engineering*, 126(1):638-644.
- Chigier, N.A. & Chervinsky, A. 1967. Aerodynamic study of turbulent burning free jets with swirl. *Symposium (International) on Combustion*, 11(1):489-499.
- Chigier, N.A. & Dvorak, K. 1975. Laser anemometer measurements in flames with swirl. *Symposium (International) on Combustion*, 15(1):573-585.
- Choo, K.S. & Kim, S.J. 2010. Comparison of thermal characteristics of confined and unconfined impinging jets. *International Journal of Heat and Mass Transfer*, 53(15-16):3366-3371.
- Cooper, D., Jackson, D., Launder, B.E. & Liao, G. 1993. Impinging jet studies for turbulence model assessment—I. Flow-field experiments. *International Journal of Heat and Mass Transfer*, 36(10):2675-2684.
- Coventry, J., Andraka, C., Pye, J., Blanco, M. & Fisher, J. 2015. A review of sodium receiver technologies for central receiver solar power plants. *Solar Energy*, 122:749-762.
- Craft, T.J., Graham, L.J.W. & Launder, B.E. 1993. Impinging jet studies for turbulence model assessment—II. An examination of the performance of four turbulence models. *International Journal of Heat and Mass Transfer*, 36(10):2685-2697.
- Craig, K.J., Slootweg, M. & Meyer, J.P. 2018. *Heat transfer enhancement in molten salt central receiver using jet impingement*. Paper presented at the 5th Southern African Solar Energy Conference, Durban, 25-27 June.
- Dairay, T., Fortuné, V., Lamballais, E. & Brizzi, L.E. 2015. Direct numerical simulation of a turbulent jet impinging on a heated wall. *Journal of Fluid Mechanics*, 764:362-394.
- Dianat, M., Fairweather, M. & Jones, W. P., Predictions of axisymmetric and two-dimensional impinging turbulent jets. *International Journal of Heat and Fluid Flow*, 17(6):530-538.
- Dieterich, R. 2018. *24-hour solar energy: molten salt makes it possible, and prices are falling fast*. [Online] Available from: <https://insideclimateneeds.org/news/16012018/csp->

concentrated-solar-molten-salt-storage-24-hour-renewable-energy-crescent-dunes-nevada
[Accessed 2018-05-05].

- Durbin, P.A. & Reif, B.P. 2011. *Statistical theory and modeling for turbulent flows*. 2nd ed. West Sussex, UK: John Wiley & Sons.
- Ducros, F. & Franck, Nicoud & Poinso, Thierry. 1998. *Wall-Adapting Local Eddy-Viscosity Models for Simulations in Complex Geometries*. Numerical Methods for Fluid Dynamics VI.
- EIA see Energy Information Administration.
- Ellabban, O., Abu-Rub, H. & Blaabjerg, F. 2014. Renewable energy resources: current status, future prospects and their enabling technology. *Renewable and Sustainable Energy Reviews*, 39:748-764.
- Energy Information Administration. 2016. *International energy outlook 2016 with projections to 2040*. [Online] Available from: [https://www.eia.gov/outlooks/ieo/pdf/0484\(2016\).pdf](https://www.eia.gov/outlooks/ieo/pdf/0484(2016).pdf) [Accessed: 2018-06-07].
- Energy Information Administration. 2018. *Annual energy outlook 2018 with projections to 2050*. [Online] Available from: <https://www.eia.gov/outlooks/aeo/> [Accessed: 2018-06-07].
- Falcone, P.K. 1986. *A handbook for solar central receiver design*. Livermore, CA: Sandia National Labs.
- Fénot, M., Dornac, E. & Lalizel, G. 2015. Heat transfer and flow structure of a multichannel impinging jet. *International Journal of Thermal Sciences*, 90:323-338.
- Flamant, G., Hernandez, D., Bonet, C. & Traverse, J.P. 1980. Experimental aspects of the thermochemical conversion of solar energy: decarbonation of CaCO₃. *Solar Energy*, 24(4):385-395.
- Forsberg, C.W., Peterson, P.F. & Zhao, H. 2007. High-temperature liquid-fluoride-salt closed-brayton-cycle solar power towers. *Journal of Solar Energy Engineering*, 129(2):141-146.
- Fuqiang, W., Ziming, C., Jianyu, T., Yuan, Y., Yong, S. & Linhua, L. 2017. Progress in concentrated solar power technology with parabolic trough collector system: a comprehensive review. *Renewable and Sustainable Energy Reviews*, 79:1314-1328.
- Garbrecht, O., Al-Sibai, F., Kneer, R. & Wiegardt, K. 2013. CFD-simulation of a new receiver design for a molten salt solar power tower. *Solar Energy*, 90:94-106.
- Gardon, R. & Akfirat, J.C. 1965. The role of turbulence in determining the heat-transfer characteristics of impinging jets. *International Journal of Heat and Mass Transfer*, 8(10):1261-1272.
- Gau, C. & Lee, C.C. 1992. Impingement cooling flow structure and heat transfer along rib-roughened walls. *International Journal of Heat and Mass Transfer*, 35(11):3009-3020.
- Glynn, C., O'donovan, T., Murray, D. B. & Feidt, M. 2005. *Jet impingement cooling*. Paper presented at the 9th UK National Heat Transfer Conference, Manchester, England, September:5-6.
- Gomez-Vidal, J.C. & Tirawat, R. 2016. Corrosion of alloys in a chloride molten salt (NaCl-LiCl) for solar thermal technologies. *Solar Energy Materials and Solar Cells*, 157:234-244.

- Grenson, P. & Deniau, H. 2017. Large-Eddy simulation of an impinging heated jet for a small nozzle-to-plate distance and high Reynolds number. *International Journal of Heat and Fluid Flow*, 68:348-363.
- Guan, T., Zhang, J.Z. & Shan, Y. 2017a. Conjugate heat transfer on leading edge of a conical wall subjected to external cold flow and internal hot jet impingement from chevron nozzle – part 2: numerical analysis. *International Journal of Heat and Mass Transfer*, 106:339-355.
- Guan, T., Zhang, J.Z. & Shan, Y. 2018. Effect of offset-jets arrangement on leading edge hot-air heating effectiveness of engine inlet guide strut. *Applied Thermal Engineering*, 128:357-372.
- Guan, T., Zhang, J.Z., Shan, Y. & Hang, J. 2017b. Conjugate heat transfer on leading edge of a conical wall subjected to external cold flow and internal hot jet impingement from chevron nozzle – part 1: experimental analysis. *International Journal of Heat and Mass Transfer*, 106:329-338.
- Gupta, A.K. & Lilley, D.G. 1985. *Flowfield modeling and diagnostics*. Kent, UK: Abacus Press.
- Gupta, A.K., Lilley, D.G. & Syred, N. 1984. *Swirl flows*. Kent, UK: Abacus Press.
- Hee, L.D., Youl, W.S., Taek, K.Y. & Suk, C.Y. 2002. Turbulent heat transfer from a flat surface to a swirling round impinging jet. *International Journal of Heat and Mass Transfer*, 45(1):223-227.
- Ho, C.K. 2016. A review of high-temperature particle receivers for concentrating solar power. *Applied Thermal Engineering*, 109:958-969.
- Ho, C.K. 2017. Advances in central receivers for concentrating solar applications. *Solar Energy*, 152:38-56.
- Ho, C.K. & Iverson, B.D. 2014. Review of high-temperature central receiver designs for concentrating solar power. *Renewable and Sustainable Energy Reviews*, 29:835-846.
- Ho, C.K., Ortega, J., Christian, J.M., Yellowhair, J., Ray, D.A., Kelton, J.W., Peacock, G. & Andraka, C.E. 2016. *Fractal-like materials design with optimized radiative properties for high-efficiency solar energy conversion*. Albuquerque, NM: Sandia National Lab.
- Hoogendoorn, C.J. 1977. The effect of turbulence on heat transfer at a stagnation point. *International Journal of Heat and Mass Transfer*, 20(12):1333-1338.
- Howell, J.R. 1998. The Monte Carlo method in radiative heat transfer. *Journal of Heat Transfer*, 120(3):547-560.
- Ianiro, A. & Cardone, G. 2011. Heat transfer rate and uniformity in multichannel swirling impinging jets. *Applied Thermal Engineering*, 49:89-98.
- Ichimiya, K. 2003. Heat transfer characteristics of an annular turbulent impinging jet with a confined wall measured by thermosensitive liquid crystal. *Heat and Mass Transfer*, 39:545-551.
- International Renewable Energy Agency. 2018. *Renewable energy statistics 2018*. [Online] Available from: <http://www.irena.org/publications/2018/Jul/Renewable-Energy-Statistics-2018> [Accessed: 2018-09-02].
- Iqbal, M. 1983. *An introduction to solar radiation*. Toronto, Canada: Academic Press.
- IRENA see International Renewable Energy Agency.

- Islam, M.T., Huda, N., Abdullah, A.B. & Saidur, R. 2018. A comprehensive review of state-of-the-art concentrating solar power (CSP) technologies: current status and research trends. *Renewable and Sustainable Energy Reviews*, 91:987-1018.
- Islam, M.T., Shahir, S.A., Uddin, T.M.I. & Saifullah, A.Z.A. 2014. Current energy scenario and future prospect of renewable energy in Bangladesh. *Renewable and Sustainable Energy Reviews*, 39:1074-1088.
- Isman, M.K., Pulat, E., Etemoglu, A.B. and Can, M. 2008. Numerical investigation of turbulent impinging jet cooling of a constant heat flux surface. *Numerical Heat Transfer, Part A: Applications*, 53(10):1109-1132.
- Jaramillo, J.E., Pérez-Segarra, C.D., Rodriguez, I. & Oliva, A. 2008. Numerical study of plane and round impinging jets using RANS models. *Numerical Heat Transfer, Part B: Fundamentals*, 54(3):213-237.
- Kerzmann, T.L. 2010. *Energy and environmental analysis of a linear concentrating photovoltaic system*. Unpublished doctoral thesis. Pittsburgh: University of Pittsburgh. [Online] Available from: <http://d-scholarship.pitt.edu/8118/> [Accessed: 2018-08-25].
- Kinsella, C., Donnelly, B., O'Donovan, T. S. & Murray, D. B. 2008. *Heat transfer enhancement from a horizontal surface by impinging swirl jets*. Paper presented at the 5th European Thermal-Sciences Conference, Eindhoven, The Netherlands, 18-22 May.
- Koseoglu, M.F. & Baskaya, S. 2010. The role of jet inlet geometry in impinging jet heat transfer, modeling and experiments. *International Journal of Thermal Sciences*, 49(8):1417-1426.
- Kreith, F. & Goswami, D.Y. 2007. *Handbook of energy efficiency and renewable energy*. Boca Raton: CRC Press.
- Kuravi, S., Trahan, J., Goswami, D.Y., Rahman, M.M. & Stefanakos, E.K. 2013. Thermal energy storage technologies and systems for concentrating solar power plants. *Progress in Energy and Combustion Science*, 39(4):285-319.
- Lee, D.H., Chung, Y.S. & Won, S.Y. 1999. The effect of concave surface curvature on heat transfer from a fully developed round impinging jet. *International Journal of Heat and Mass Transfer*, 13(42):2489-2497.
- Lee, J. & Lee, S.J. 2000. The effect of nozzle configuration on stagnation region heat transfer enhancement of axisymmetric jet impingement. *International Journal of Heat and Mass Transfer*, 43(18):3497-3509.
- Lee, C.H., Lim, K.B., Lee, S.H., Yoon, Y.J. & Sung, N.W. 2007. A study of the heat transfer characteristics of turbulent round jet impinging on an inclined concave surface using liquid crystal transient method. *Experimental Thermal and Fluid Science*, 31(6):559-565.
- Lee, T., Lim, S., Shin, S., Sadowski, D.L., Abdel-Khalik, S.I., Jeter, S.M. & Al-Ansary, H. 2015. Numerical simulation of particulate flow in interconnected porous media for central particle-heating receiver applications. *Solar Energy*, 113:14-24.

- Lee, D.H., Song, J. & Jo, M.C. 2004. The effects of nozzle diameter on impinging jet heat transfer and fluid flow. *Journal of Heat Transfer*, 126(4):554-557.
- Lee, D.H., Won, S.Y., Kim, Y.T. & Chung, Y.S. 2002. Turbulent heat transfer from a flat surface to a swirling round impinging jet. *International Journal of Heat and Mass Transfer*, 45(1):223-227.
- Li, L., Coventry, J., Bader, R., Pye, J. & Lipiński, W. 2016. Optics of solar central receiver systems: a review. *Optics Express*, 24(14):A985-1007.
- Lubkoll, M., Harms, T.M. & Von Backström, T.W. 2017. *Introduction to heat transfer test setup for the SCRAP receiver*. Paper presented at the 22nd SolarPACES Conference, Abu Dhabi, United Arab Emirates, 11-14 October.
- Lubkoll, M., Von Backström, T.W., Harms, T.M. & Kröger, D.G. 2015. Initial analysis on the novel spiky central receiver air pre-heater (SCRAP) pressurized air receiver. *Energy Procedia*, 69:461-470.
- Lucca-Negro, O. & O'Doherty, T. 2001. Vortex breakdown: a review. *Progress in Energy and Combustion Science*, 27(4):431-481.
- Marler, R.T. & Arora, J.S. 2004. Survey of multi-objective optimization methods for engineering. *Structural and Multidisciplinary Optimization*, 26(6):369-395.
- Martin, D.T., Gouldin, F.C. & Yetter, R.A. 1975. *Preliminary evaluation of vortex breakdown stabilized combustor*. Ithaca, NY: Cornell University.
- Martinek, J. & Ma, Z. 2015. Granular flow and heat-transfer study in a near-blackbody enclosed particle receiver. *Journal of Solar Energy Engineering*, 137(5).
- Maurel, S. & Sollicec, C. 2001. A turbulent plane jet impinging nearby and far from a flat plate. *Experiments in Fluids*, 31(6):687-696.
- Menter, F., Thomas, E. & Wolfgang, V. 2003. *Heat transfer predictions based on two-equation turbulence models*. Paper presented at the 6th ASME-JSME 2003 Thermal Engineering Joint Conference, Kohala Coast, Hawaii, 16-20 March.
- Merci, B. & Dick, E. 2003. Heat transfer predictions with a cubic $k-\epsilon$ model for axisymmetric turbulent jets impinging onto a flat plate. *International Journal of Heat and Mass Transfer*, 46(3):469-480.
- Mohamed Illyas, S., Ramesh Babu, B.R. & Venkata Subba Rao, V. 2018. Heat transfer and flow visualization of swirling impinging jet on flat surface using helicoid inserts. *Journal of Visualization*, 21(5):729-749.
- Molana, M. & Banooni, S. 2013. Investigation of heat transfer processes involved liquid impingement jets: a review. *Brazilian Journal of Chemical Engineering*, 30(3):413-435.
- Morrell, R. (2017). *National Physical Laboratory: Kaye & Laby*. Retrieved October 15, 2018, from http://www.kayelaby.npl.co.uk/general_physics/2_3/2_3_7.html.
- Müller-Steinhagen, H. & Trieb, F. 2004. Concentrated solar power. *A review of the Technology. Ingenia—Quarterly of the Royal Academy of Engineering*, 18:43-50.

- Narayanan, V., Seyed-Yagoobi, J. & Page, R.H. 2004. An experimental study of fluid mechanics and heat transfer in an impinging slot jet flow. *International Journal of Heat and Mass Transfer*, 47(8-9):1827-1845.
- National Renewable Energy Laboratory. 2018. *Best research-cell efficiencies*. [Online] Available from: <https://www.nrel.gov/pv/assets/images/efficiency-chart.png> [Accessed: 2018-06-05].
- Neber, M. & Lee, H. 2012. Design of a high temperature cavity receiver for residential scale concentrated solar power. *Energy*, 47(1):481-487.
- Nozaki, A., Igarashi, Y. & Hishida, K. 2003. Heat transfer mechanism of a swirling impinging jet in a stagnation region. *Heat Transfer—Asian Research*, 32(8):663-673.
- NREL see National Renewable Energy Laboratory.
- Nuntadusit, C., Wae-Hayee, M., Bunyajitradulya, A. & Eiamsa-Ard, S. 2012a. Heat transfer enhancement by multiple swirling impinging jets with twisted-tape swirl generators. *International Communications in Heat and Mass Transfer*, 39(1):102-107.
- Nuntadusit, C., Wae-Hayee, M., Bunyajitradulya, A. & Eiamsa-Ard, S. 2012b. Visualization of flow and heat transfer characteristics for swirling impinging jet. *International Communications in Heat and Mass Transfer*, 39(5):640-648.
- Nuntadusit, C., Wae-hayee, M., Bunyajitradulya, A. & Shakouch, T. 2010. *Heat transfer enhancement for a swirling jet impingement*. Paper presented at the 14th International Symposium on Flow Visualization, Daegu, Korea, 21-24 June:1-9.
- Ortega-Casanova, J. 2011. Numerical simulation of the heat transfer from a heated solid wall to an impinging swirling jet. In: Ahsan, A. (ed.) *Two phase flow, phase change and numerical modeling*. IntechOpen.
- Ortega-Casanova, J. 2012. CFD and correlations of the heat transfer from a wall at constant temperature to an impinging swirling jet. *International Journal of Heat and Mass Transfer*, 55(21-22):5836-5845.
- Ortega-Casanova, J., Campos, N. & Fernandez-Feria, R. 2011. Experimental study on sand bed excavation by impinging swirling jets. *Journal of Hydraulic Research*, 49(5):601-610.
- Ortega-Casanova, J. & Castillo-Sanchez, S.I. 2017. On using axisymmetric turbulent impinging jets swirling as Burger's vortex for heat transfer applications. Single and multi-objective vortex parameters optimization. *Applied Thermal Engineering*, 121:103-114.
- Panwar, N., Kaushik, S. & Kothari, S. 2011. Role of renewable energy sources in environmental protection: a review. *Renewable and Sustainable Energy Reviews*, 15(3):1513-1524.
- Pritzkow, W.E.C. 1991. Pressure loaded volumetric ceramic receiver. *Solar Energy Materials*, 24(1-4):498-507.
- Pulat, E., Isman, M.K., Etemoglu, A.B. & Can, M. 2011. Effect of turbulence models and near-wall modeling approaches on numerical results in impingement heat transfer. *Numerical Heat Transfer, Part B: Fundamentals*, 60(6): 486-519.

- Ramezanpour, A., Mirzaee, I., Firth, D. & Shirvani, H. 2007. A numerical heat transfer study of slot jet impinging on an inclined plate. *International Journal of Numerical Methods for Heat & Fluid Flow*, 17(7):661-676.
- Rinaldi, F., Binotti, M., Giostri, A. & Manzoloni, G. 2014. Comparison of linear and point focus collectors in solar power plants. *Energy Procedia*, 49:1491-1500.
- Roldán, M.I. & Fernández-Reche, J.S.A. 2015. *CFD analysis of supercritical CO₂ used as HTF in a solar tower receiver*. Paper presented at the International Conference on Concentrating Solar Power and Chemical Energy Systems, Cape Town, 13-16 October.
- Sagot, B., Antonini, G., Christgen, A. & Buron, F. 2008. Jet impingement heat transfer on a flat plate at a constant wall temperature. *International Journal of Thermal Sciences*, 47(12):1610-1619.
- Sani, E., Mercatelli, L., Sansoni, P., Silvestroni, L. & Sciti, D. 2012. Spectrally selective ultra-high temperature ceramic absorbers for high-temperature solar plants. *Journal of Renewable and Sustainable Energy*, 4(3).
- Seifi, Z., Nazari, M.R. & Khalaji, E. 2017. 2D numerical simulation of impinging jet onto the concave surface. *Heat and Mass Transfer*, 53(1):59-72.
- Senda, M., Inaoka, K., Toyoda, D. & Sato, S. 2005. Heat transfer and fluid flow characteristics in a swirling impinging jet. *Heat Transfer—Asian Research*, 34(5):324-335.
- Serrano-López, R., Fradera, J. & Cuesta-López, S. 2013. Molten salts database for energy applications. *Chemical Engineering and Processing: Process Intensification*, 73:87-102.
- Sharif, M.A.R. & Mothe, K.K. 2010. Parametric study of turbulent slot-jet impingement heat transfer from concave cylindrical surfaces. *International Journal of Thermal Sciences*, 49(2):428-442.
- Shuai, Y., Xia, X.L. & Tan, H.P. 2008. Numerical study of radiation characteristics in a dish solar collector system. *Journal of Solar Energy Engineering*, 130(2).
- Siebers, D.L. & Kraabel, J.S. 1984. *Estimating convective energy losses from solar central receivers*. Livermore, CA: Sandia National Labs.
- Slootweg, M., 2018. *Numerical performance analysis of novel solar tower receiver*. Unpublished masters thesis. Pretoria: University of Pretoria. [Online] Available from: <http://hdl.handle.net/2263/70354>
- Slootweg, M., Craig, K.J. & Meyer, J.P. 2018. *Investigation into central receiver design for optimal optical and thermal performance*. Paper presented at the 5th Southern African Solar Energy Conference, Durban, 25-27 June.
- Slootweg, M., Craig, K.J. & Meyer, J.P. 2019. A computational approach to simulate the optical and thermal performance of a novel complex geometry solar tower molten salt cavity receiver. *Solar Energy*, 187:13-29.
- Snyman, J.A. & Wilke, D.N. 2018. *Practical mathematical optimization: basic optimization theory and gradient-based algorithms*. 2nd ed. Switzerland: Springer.

- SolarPaces. 2018. *Concentrating solar power projects*. [Online] Available from: <https://www.nrel.gov/csp/solarpaces/index.cfm> [Accessed: 2018-09-09].
- SolarReserve. 2015. *Crescent Dunes solar energy plant*. [Online] Available from: <https://www.solarreserve.com/en/newsroom/photos> [Accessed: 2018-09-20].
- Steinfeld, A. & Schubnell, M. 1993. Optimum aperture size and operating temperature of a solar cavity-receiver. *Solar Energy*, 50(1):19-25.
- Stine, W.B. & Geyer, M. 2001. *Power from the sun*. Power from the sun.net.
- Suzuki, H.G., Nishimura, S. and NAKAMURA, Y., 1984. Improvement of hot ductility of continuously cast carbon steels. *Transactions of the Iron and Steel Institute of Japan*, 24(1), pp.54-59.
- Syred, N. & Beér, J.M. 1974. Combustion in swirling flows: a review. *Combustion and Flame*, 23(2):143-201.
- The Highlanders. 2013. *The solar power towers of Seville, Spain*. [Online] Available from: <https://kitskinny.wordpress.com/2013/09/06/the-solar-power-towers-of-seville-spain/> [Accessed: 2018-09-10].
- The World Bank. 2017. *Solar resource data: solargis*. [Online]. Available from: <https://solargis.com/maps-and-gis-data/download/world/> [Accessed 2018-09-10].
- Tu, J., Yeoh, G.H. & Liu, C. 2013. *Computational fluid dynamics - a practical approach*. 2nd ed. Amsterdam: Elsevier/Butterworth.
- Uddin, N. 2008. *Turbulence modeling of complex flows in CFD*. Unpublished doctoral thesis. Stuttgart: University of Stuttgart. [Online] Available from: <http://dx.doi.org/10.18419/opus-3781> [Accessed: 2018-09-23].
- Uddin, N., Neumann, S.O. & Weigand, B. 2013. LES simulations of an impinging jet: on the origin of the second peak in the Nusselt number distribution. *International Journal of Heat and Mass Transfer*, 57(1):356-368.
- Uddin, N., Weigand, B. & Younis, B.A. 2019. Comparative study on heat transfer enhancement by turbulent impinging jet under conditions of swirl, active excitations and passive excitations. *International Communications in Heat and Mass Transfer*, 100:35-41.
- Ummadisingu, A. & Soni, M.S. 2011. Concentrating solar power – technology, potential and policy in India. *Renewable and Sustainable Energy Reviews*, 15(9):5169-5175.
- Vashishtha, S. 2012. *Comparison of CSP technologies*. [Online] Available from: <https://firstgreenconsulting.wordpress.com/2012/06/04/comparison-of-csp-technologies/comparison-of-csp-technologies/> [Accessed 2018-09-09].
- Versteeg, H.K. & Malalasekera, W. 2007. *An introduction to computational fluid dynamics: the finite volume method*. Harlow, England: Pearson Education.
- Vignarooban, K., Xu, X., Wang, K., Molina, E.E., Li, P., Gervasio, D. & Kannan, A.M. 2015. Vapor pressure and corrosivity of ternary metal-chloride molten-salt based heat transfer fluids for use in concentrating solar power systems. *Applied Energy*, 159:206-213.

- Violato, D., Ianiro, A., Cardone, G. & Scarano, F. 2012. Three-dimensional vortex dynamics and convective heat transfer in circular and chevron impinging jets. *International Journal of Heat and Fluid Flow*, 37:22-36.
- Viskanta, R. 1993. Heat transfer to impinging isothermal gas and flame jets. *Experimental Thermal and Fluid Science*, 6(2):111-134.
- Walsh, B. 2004. *Markov chain Monte Carlo and Gibbs sampling*. Tucson, AZ: Department of Ecology and Evolutionary Biology, University of Arizona.
- Wang, W., Laumert, B., Xu, H. & Strand, T. 2015. Conjugate heat transfer analysis of an impinging receiver design for a dish-Brayton system. *Solar Energy*, 119:298-309.
- Webb, B. & Ma, C.F. 1995. Single-phase liquid jet impingement heat transfer. *Advances in Heat Transfer*, 26:105-217.
- Wei, X., Lu, Z., Lin, Z., Zhang, H. & Ni, Z. 2008. Optimization procedure for design of heliostat field layout of a 1MWe solar tower thermal power plant. In: Li, j., Fan, Y., Wu, L., Zhang, Y.H., Coltrin, M.E., Zhao, Y., Chen, N., Andreev, V.M. & Singh, J. (eds). *Proceedings of SPIE*, March.
- Wen, M. & Jang, K. 2003. An impingement cooling on a flat surface by using circular jet with longitudinal swirling strips. *International Journal of Heat and Mass Transfer*, 46(24):4657-4667.
- Wendelin, T. 2003. *SolTRACE: a new optical modeling tool for concentrating solar optics*. Paper presented at the ASME 2003 International Solar Energy Conference, Kohala Coast, Hawaii, 15-18 March:253-260.
- Wu, W., Amsbeck, L., Buck, R., Waibel, N., Langner, P. & Pitz-Paal, R. 2014. On the influence of rotation on thermal convection in a rotating cavity for solar receiver applications. *Applied Thermal Engineering*, 70(1):694-704.
- Wu, W., Gobereit, B., Singer, C., Amsbeck, L. & Pitz-Paal, R. 2011. *Direct absorption receivers for high temperatures*. Paper presented at the 17th Annual SolarPACES Conference, Granada, Spain, 20-23 September.
- Yang, B., Chang, S., Wu, H., Zhao, Y. & Leng, M. 2017. Experimental and numerical investigation of heat transfer in an array of impingement jets on a concave surface. *Applied Thermal Engineering*, 127:473-483.
- Yang, Y.T., Lin, S.C., Wang, Y.H. & Hsu, J.C. 2013. Numerical simulation and optimization of impingement cooling for rotating and stationary pin-fin heat sinks. *International Journal of Heat and Fluid Flow*, 44:383-393.
- Yang, Y.T., Wei, T.C. & Wang, Y.H. 2011. Numerical study of turbulent slot jet impingement cooling on a semi-circular concave surface. *International Journal of Heat and Mass Transfer*, 54(1-3):482-489.

- Yu, Y.Z., Zhang, J.Z. & Shan, Y. 2015. Convective heat transfer of a row of air jets impingement excited by triangular tabs in a confined crossflow channel. *International Journal of Heat and Mass Transfer*, 80:126-138.
- Yu, Y.Z., Zhang, J.Z. & Xu, H.S. 2014. Convective heat transfer by a row of confined air jets from round holes equipped with triangular tabs. *International Journal of Heat and Mass Transfer*, 72:222-233.
- Yuan, Z., Chen, Y., Jiang, J. & Ma, C. 2006. Swirling effect of jet impingement on heat transfer from a flat surface to CO₂ stream. *Experimental Thermal and Fluid Science*, 31(1):55-60.
- Zhou, Y., Lin, G., Bu, X., Bai, L. & Wen, D. 2017. Experimental study of curvature effects on jet impingement heat transfer on concave surfaces. *Chinese Journal of Aeronautics*, 30(2):586-594.
- Zuckerman, N. & Lior, N. 2006. Jet impingement heat transfer: physics, correlations, and numerical modeling. *Advances in Heat Transfer*, 39:565-631.

APPENDIX A: EXPERIMENTAL RESULTS AND FLUID PROPERTIES

The details of the experimental work used for the validation of the CFD model are presented based on the work done by the authors Ahmed *et al.* (2015a); Ahmed *et al.* (2016b); Ahmed, Al-Abdeli and Guzzomi (2016a); Ahmed, Al-Abdeli and Guzzomi (2017); and Ahmed, Al-Abdeli and Matthews (2015b).

Nusselt number distribution

The measured experiment Nusselt number distribution is depicted in Figure 87, for the indicated flow conditions.

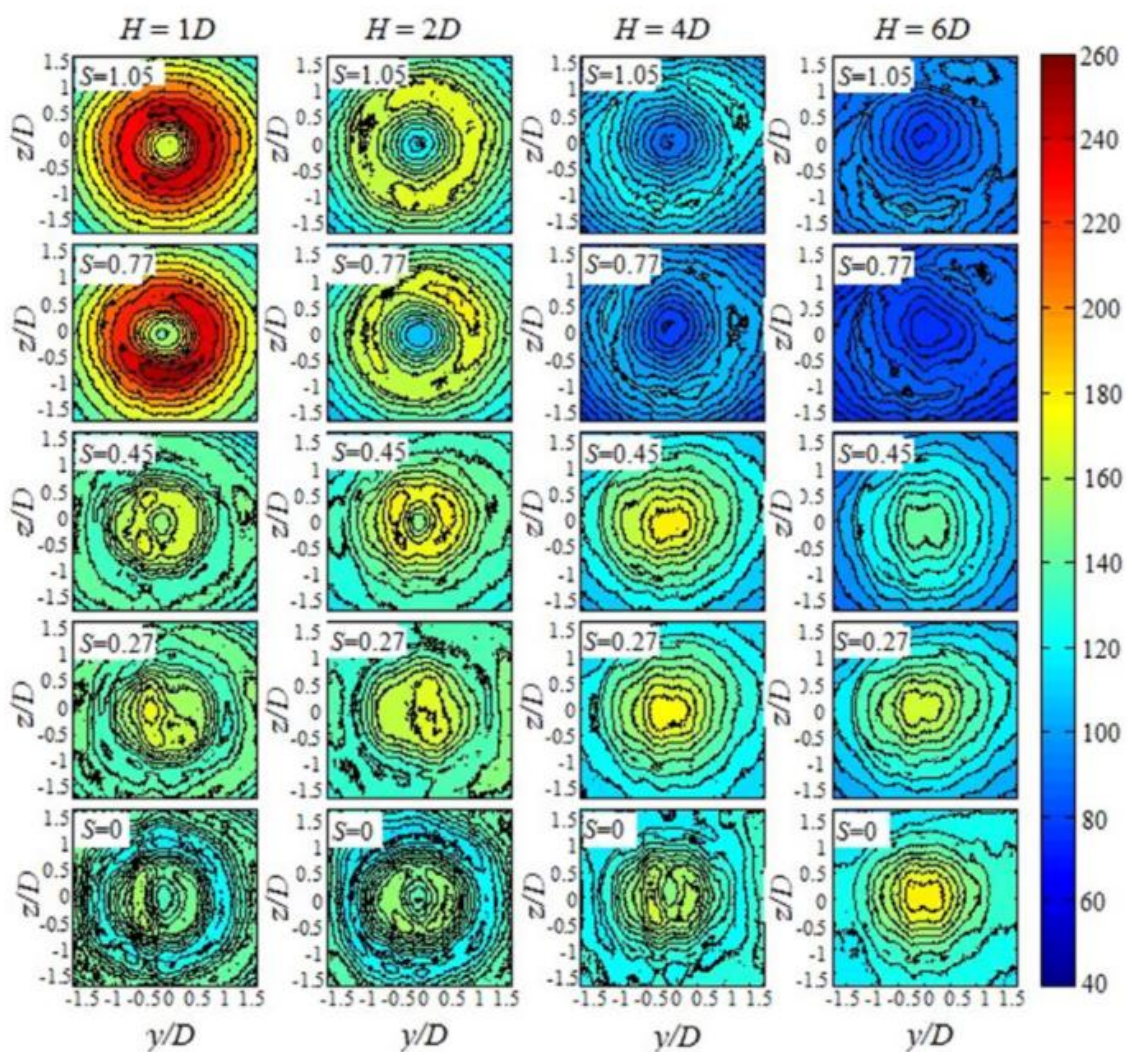


Figure 87. Nu contour plots for experimental results for SIJ for $Re = 35\,000$ and $S = 0, 0.27, 0.45, 0.77, 1.05$ (Ahmed, Al-Abdeli and Guzzom; 2016a).

Experimental conditions

The flow conditions reported by the authors presented below. The flow conditions describe the Reynolds number, axial and tangential flow velocity, the swirl number and the intermittency percentage in Figure 88.

No.	Re ($U_f D / \nu$)	U_b (m/s)	W_b (m/s)	S (W_b / U_b)	u' / U_b (%)
1	35,000 ± 4%	13.26	0.00	0.00	5.35
2		13.14	3.50	0.27	9.35
3		13.74	6.18	0.45	9.78
4		13.71	10.51	0.77	11.88
5		17.39	14.43	0.83	27.41
6		17.57	18.39	1.05	36.89
7	24,600 ± 3%	9.32	0.00	0.00	6.30
8		9.10	2.81	0.31	10.83
9		9.91	5.79	0.58	17.36
10		11.00	7.01	0.64	21.11
11		11.55	8.36	0.72	24.31
12		11.00	9.34	0.85	26.93
13	11,600 ± 6%	4.39	0.00	0.00	5.79
14		4.28	1.15	0.27	9.61
15		5.03	1.63	0.32	11.20
16		4.95	2.92	0.59	18.13
17		5.08	3.75	0.74	24.42

Figure 88. Flow conditions for experimental tests performed (Ahmed, Al-Abdeli and Guzzom; 2016a).

The inlet flow rates for the swirl generator are determined based on the measured swirl and volume flow rates. The measured swirl and required volumetric flow rates at selected Reynolds numbers are depicted in Figure 89.

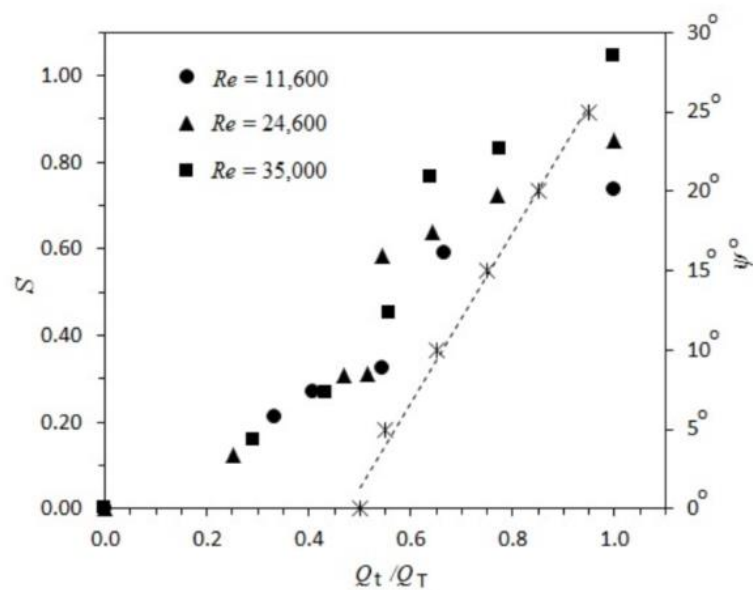


Figure 89. Swirl generator flow conditions and swirl number (Ahmed, Al-Abdeli and Guzzom; 2016a).

Fluid properties of air

The fluid properties of air are implemented as a piece-wise linear profile taken from Çengel & Ghajar, (2015). The code used to implement the air fluid properties are presented below.

```
define materials change-create air air yes piecewise-linear 26 150 2.355 200 1.767
250 1.413 260 1.360 270 1.311 280 1.265 290 1.220 300 1.177 310 1.141 320 1.106
330 1.073 340 1.042 350 1.012 360 0.983 370 0.956 380 0.931 390 0.906 400 0.883
500 0.706 600 0.589 700 0.507 800 0.442 900 0.392 1000 0.354 1500 0.235 2000 0.176
yes piecewise-linear 26 150 1017 200 1009 250 1009 260 1009 270 1009 280 1008 290
1007 300 1005 310 1005 320 1006 330 1006 340 1007 350 1007 360 1007 370 1008 380
1008 390 1009 400 1009 500 1017 600 1038 700 1065 800 1089 900 1111 1000 1130 1500
1202 2000 1244 yes piecewise-linear 26 150 0.0158 200 0.0197 250 0.0235 260 0.0242
270 0.0249 280 0.0255 290 0.0261 300 0.0267 310 0.0274 320 0.0281 330 0.0287 340
0.0294 350 0.03 360 0.0306 370 0.0313 380 0.0319 390 0.0325 400 0.0331 500 0.0389
600 0.0447 700 0.0503 800 0.0559 900 0.0616 1000 0.0672 1500 0.0926 2000 0.1149
yes piecewise-linear 26 150 10.64e-6 200 13.59e-6 250 16.14e-6 260 16.63e-6 270
17.12e-6 280 17.6e-6 290 18.02e-6 300 18.43e-6 310 18.87e-6 320 19.29e-6 330
19.71e-6 340 20.13e-6 350 20.54e-6 360 20.94e-6 370 21.34e-6 380 21.75e-6 390
22.12e-6 400 22.52e-6 500 26.33e-6 600 29.74e-6 700 33.03e-6 800 35.89e-6 900
38.65e-6 1000 41.52e-6 1500 53.82e-6 2000 64.77e-6 no no no
```

APPENDIX B: VERTICAL ROUND JET IMPINGEMENT HEAT TRANSFER ON A FLAT PLATE SENSITIVITY AND MESH ANALYSIS

Mesh extent investigation

The extent of the mesh height and length in the radial direction is investigated. The results are plotted for three investigated heights in Figure 90. The effect of the radial domain length adjustment is depicted in Figure 91.

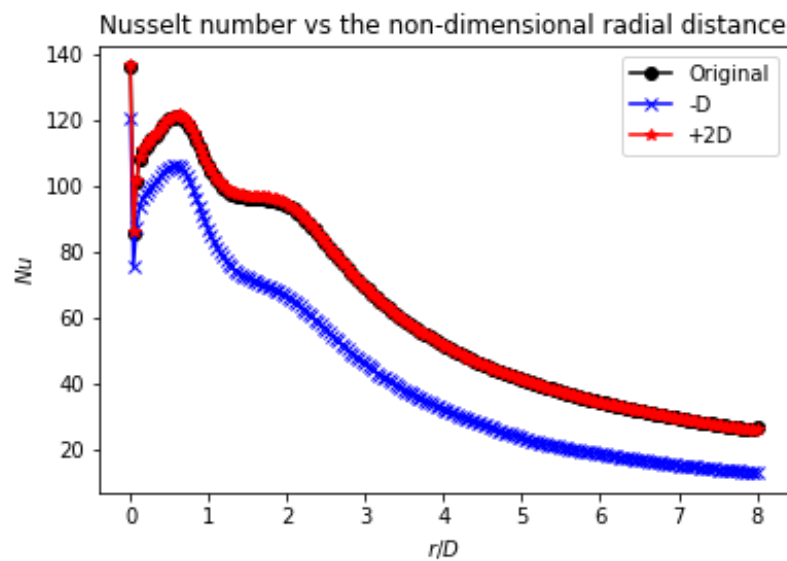


Figure 90. Nu vs r/D for different heights H/d for vertical JIHT.

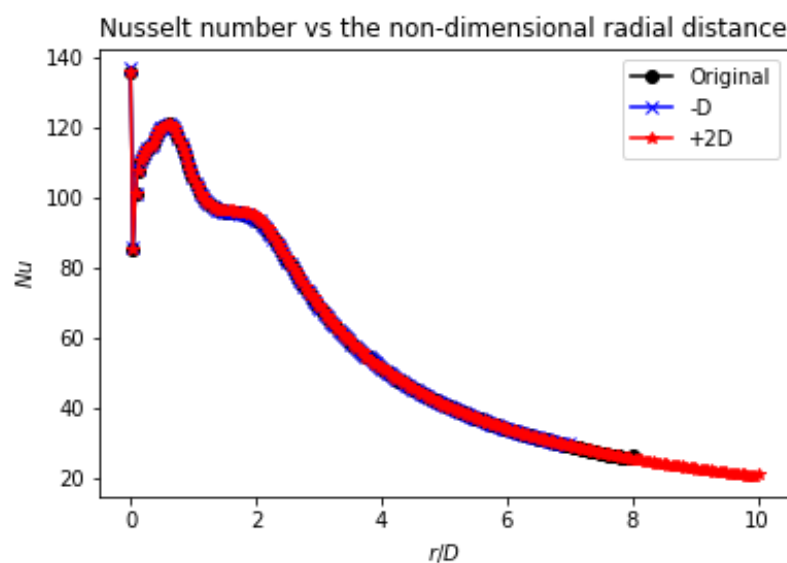


Figure 91. Nu vs r/D for different radial mesh extents for vertical JIHT.

Turbulence model investigation

The turbulence model is investigated for the simulations for the flat plate impingement. Different turbulence models are compared and plotted in Figure 92 and in Figure 93.

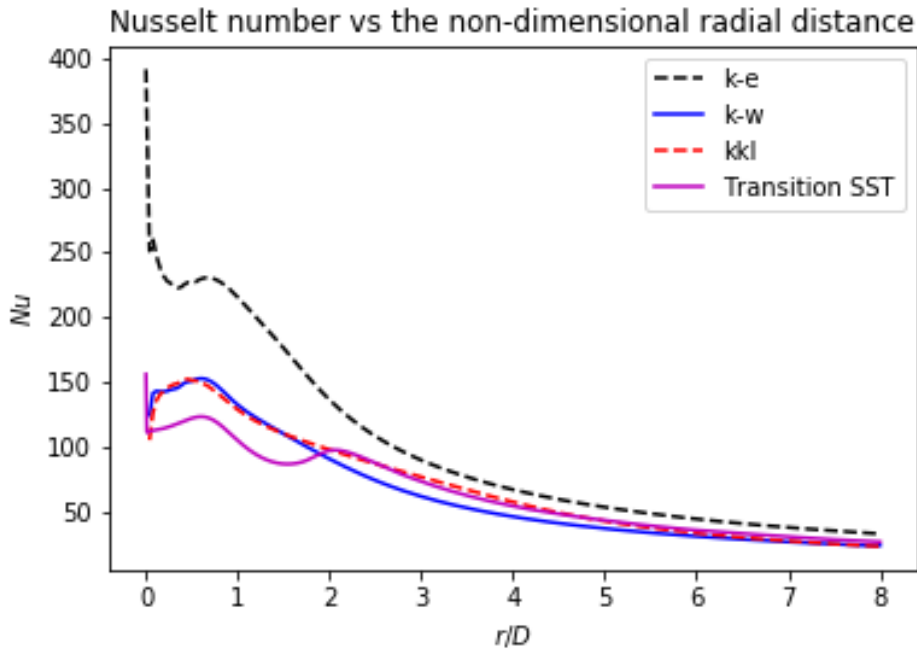


Figure 92. Nu vs r/D for different turbulence models for vertical JHT.

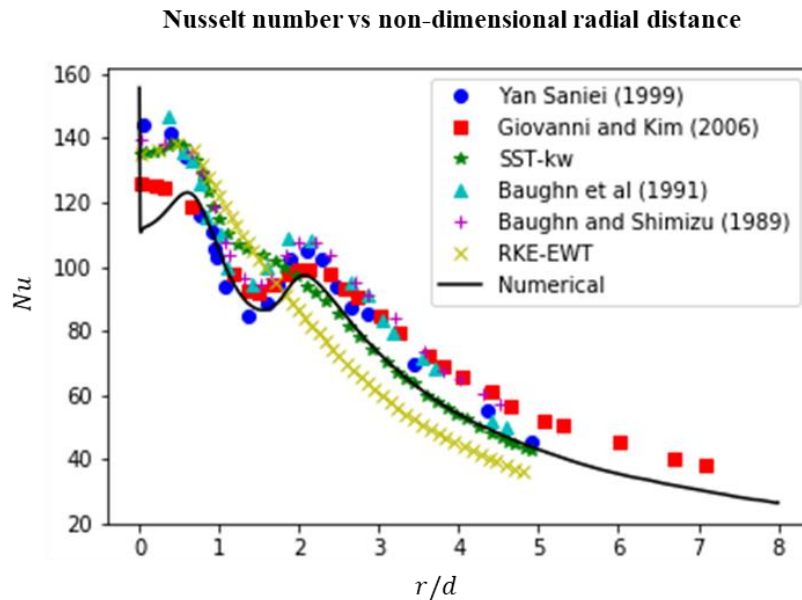


Figure 93. Nu vs r/d for experimental and numerical results of vertical jet validation, where numerical refers to the Transition SST turbulence model .

As can be seen the transition SST model is the best to approximate the experimental results as the second peak in the Nusselt number is evident. The other models do not accurately capture the Nusselt number when the flow transitions from laminar to turbulent flow. This is a consistent flow characteristic that must be considered for SIJ.

Impinging jet without mesh dependency

For the mesh independence study the grid size is changed and the results are compared. The primary investigation is on the Nu number over the domain, the metric for this is the average Nusselt number over the domain. For the investigation the number of cells is varied and the effect of the number of cells investigated on the quality and the area-weighted average Nu , these are depicted in Table 30.

Table 30. Mesh independence metric for vertical flat plate JIHT.

Number of cells	16700	66800	267200
Minimum quality	0.009	0.009	0.009
Maximum quality	0.99947	0.99947	0.99997
Average quality	0.7994	0.63555	0.94027
Nu average	64.574	65.615	66.164
GCI	-	-0.04271	-0.02221

For mesh independence the grid convergence index is used the condition to be met the performance parameter selected is the area weighted average Nu . For mesh independence the following must hold true.

$$\frac{GCI_{12}}{r^p GCI_{23}} \approx 1$$

For the given parameters the parameter calculated is

$$\frac{GCI_{12}}{r^p GCI_{23}} \approx 0.98414$$

The grid convergence index indicates that mesh independence has been achieved for the domain.

SIJ Mesh dependency study

For the mesh independence study, the grid size is changed, and the results are compared. The domain constraints and boundary conditions are held constant and only the meshing parameters are varied. The selected domain for the mesh independence study is for a considered base case with swirl. The SIJ is used as the mesh for the case with no swirl has been sufficiently studied and the modelling parameters for such a case are well defined. For the mesh dependency study the Nusselt number is used.

The Nu distribution over the impingement surface is the main focus of the study, for heat transfer applications. The mesh quantities used to determine if the mesh is sufficiently refined are considered and presented as in the dimensionless form as the y^+ value. To graphically determine the effect of the mesh on the solution of the simulation the meshing parameters are compared against the local Nu distribution of the impinging surface. The plots of the Nu for different number of elements is depicted in Figure 95.

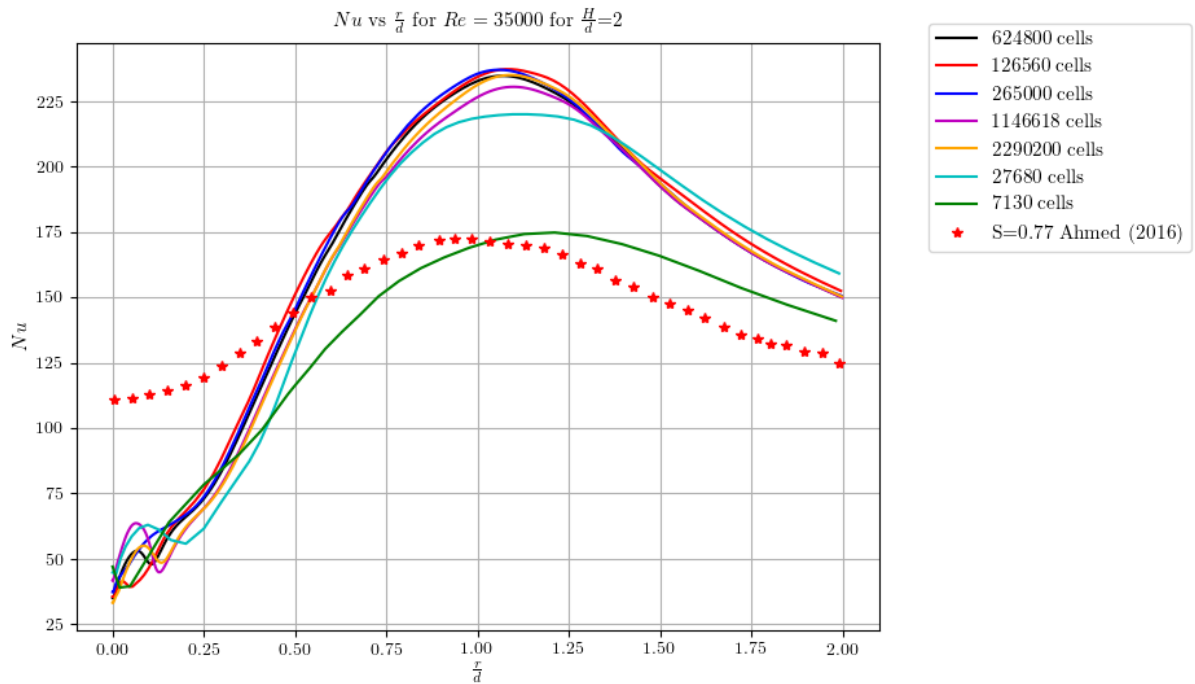


Figure 94. Nu vs r/D mesh dependency for $S = 0.77, H/d = 2$ where $r/D \leq 2$.

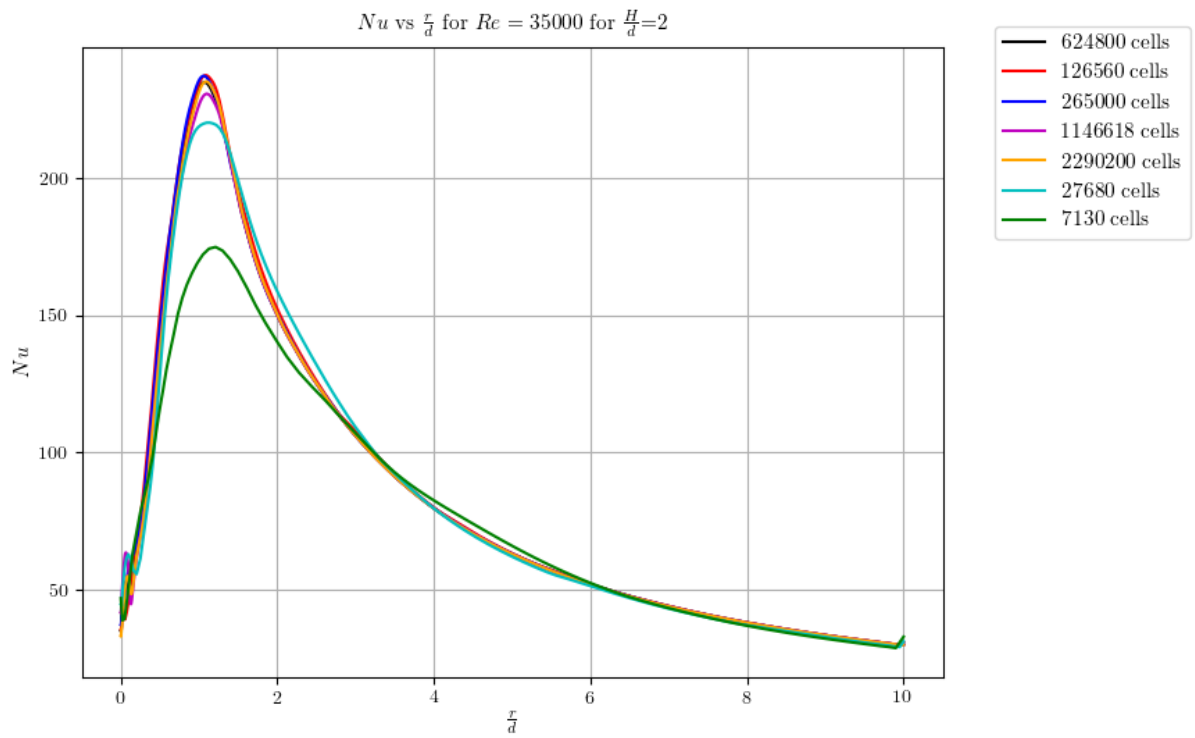


Figure 95. Nu vs r/D for $S = 0.77, H/d = 2$ over the entire impingement surface.

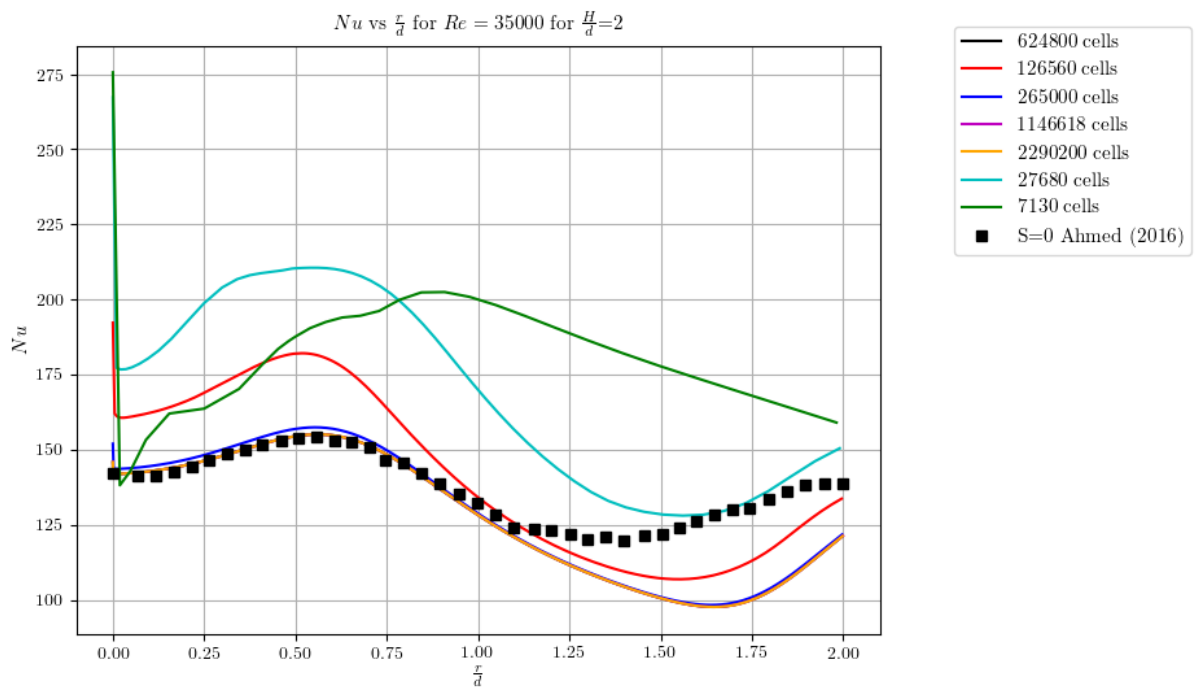


Figure 96. Nu vs r/D mesh dependency for $S = 0, H/d = 2$ where $r/D \leq 2$.

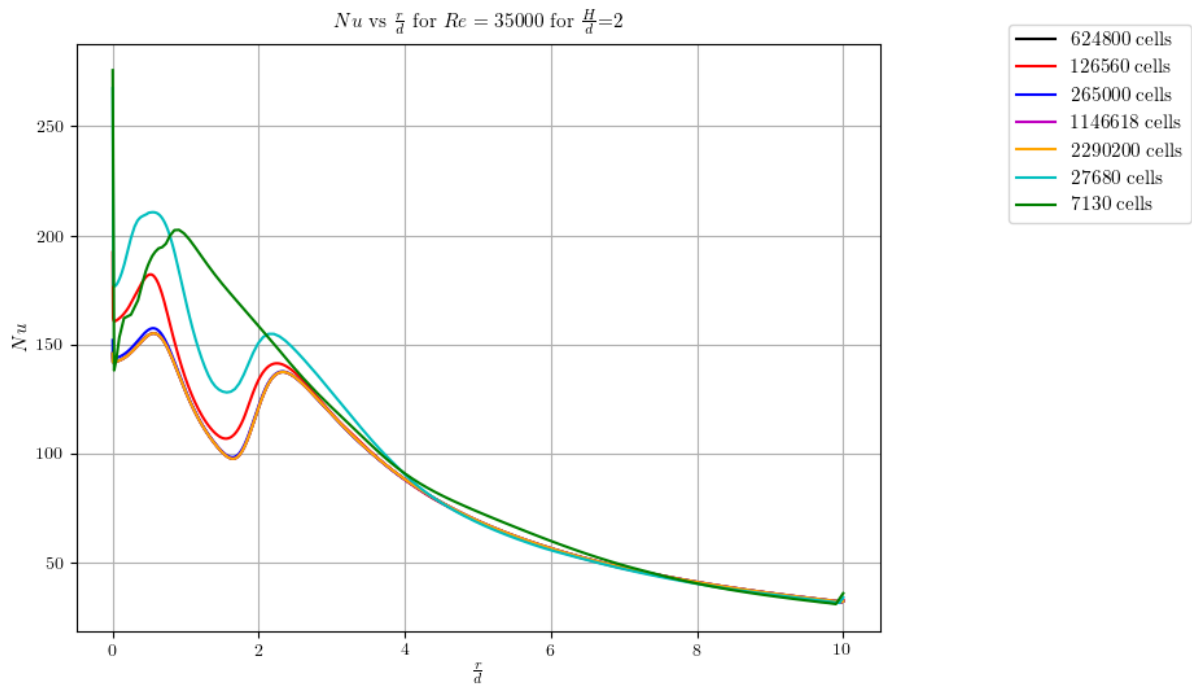


Figure 97. Nu vs r/D for $S = 0, H/d = 2$ over the entire impingement surface.

As can be seen, the effect of the mesh has a considerable effect on the results obtained. For the simulation the integrated average properties are of significance as the objective of the simulation is to improve heat transfer. The heat transfer described by the Nusselt number averaged over the impingement surface is significant as it will allow the designer of the impingement setup to predict the overall heat transfer achieved. The integrated parameters of interest for the simulation are compared for the mesh sizes to graphically determine the convergence of the mesh. The properties used for the mesh convergence study are the average Nusselt number (Figure 98), maximum Nusselt number (Figure 99) and maximum y^+ value on the impingement surface (Figure 100).

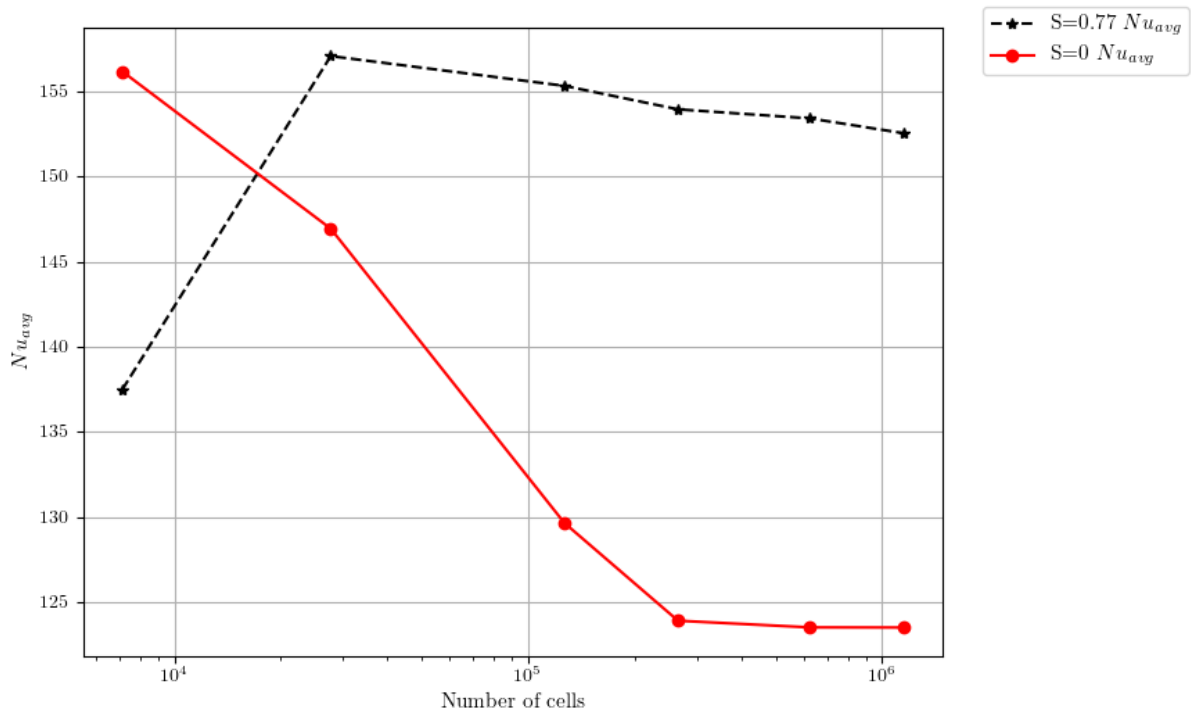


Figure 98. Average Nusselt number over the impingement surface vs number of cells for $S = 0$ and $S = 0.77$; $H/d = 2$.

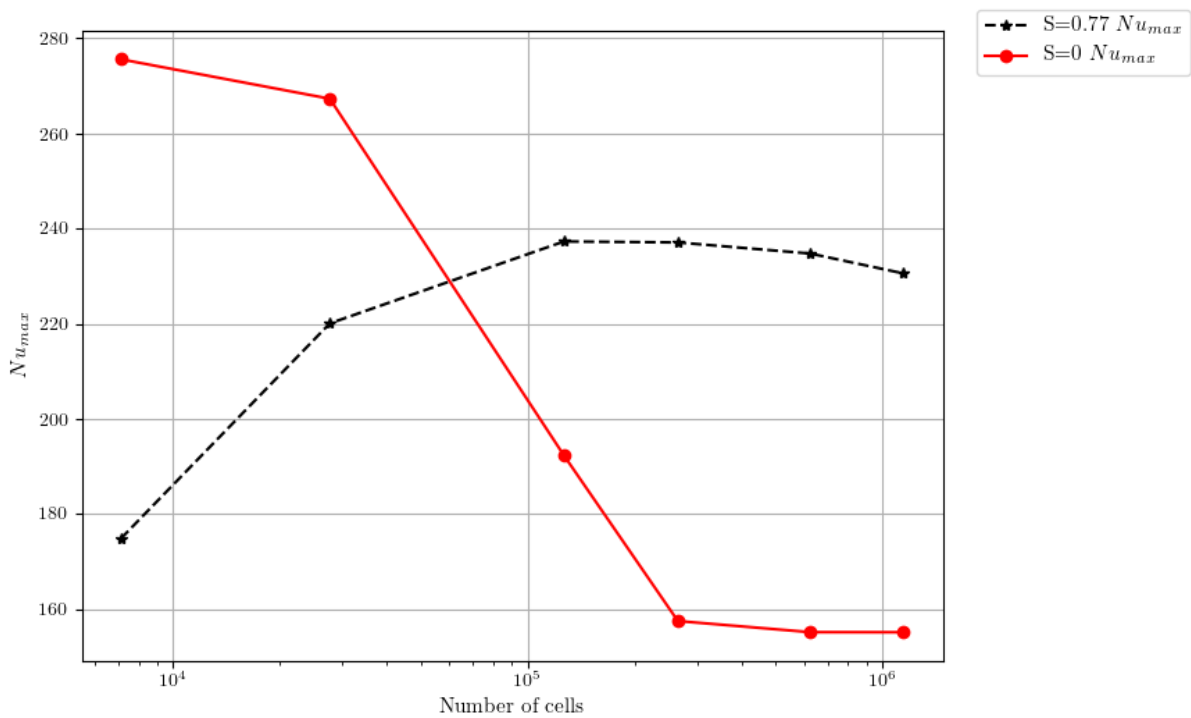


Figure 99. Maximum Nusselt number over the impingement surface vs number of cells for $S = 0$ and $S = 0.77$; $H/d = 2$.

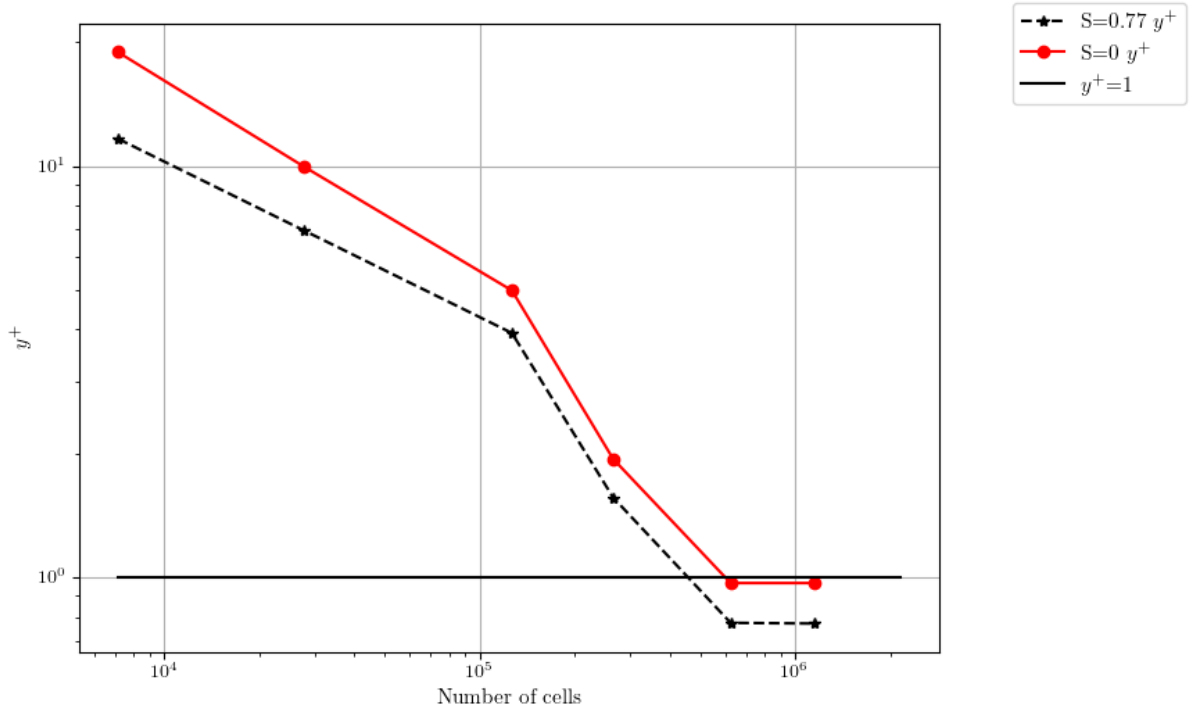


Figure 100. Maximum y^+ over the impingement surface vs number of cells for $S = 0$ and $S = 0.77$; $H/d = 2$.

The above figures illustrate graphically how the mesh independence study is conducted however the mesh refinement is not quantified. A method used in order to ensure that mesh independence is satisfied is the use of a mesh study using the Grid Convergence Index (GCI).

APPENDIX C: VERTICAL ROUND JET IMPINGEMENT HEAT TRANSFER FOR A CONCAVE SURFACE SENSITIVITY AND MESH ANALYSIS

For the vertical round impinging jet on a concave surface the work done by Lee *et al.* (1999). For the experiments a parametric analysis was conducted for air impingement. Different flow rates, nozzle to target distances and concave curvatures. A depiction of the experimental setup is presented in Figure 101.

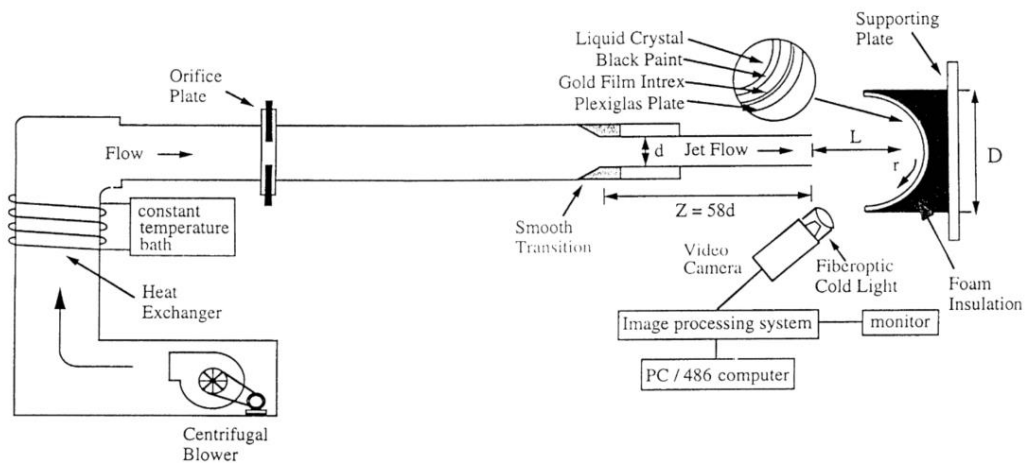


Figure 101. Vertical round jet impingement on a concave surface, experimental test setup schematic (Lee *et al.*, 1999).

The jet impingement on a concave surface is simulated. For the simulation multiple parameters were investigated to determine the sensitivity of the parameter on the simulation. For the numerical sensitivity analysis different turbulence models were investigated and a mesh independence study was done. Different turbulence models are compared and plotted in Figure 102.

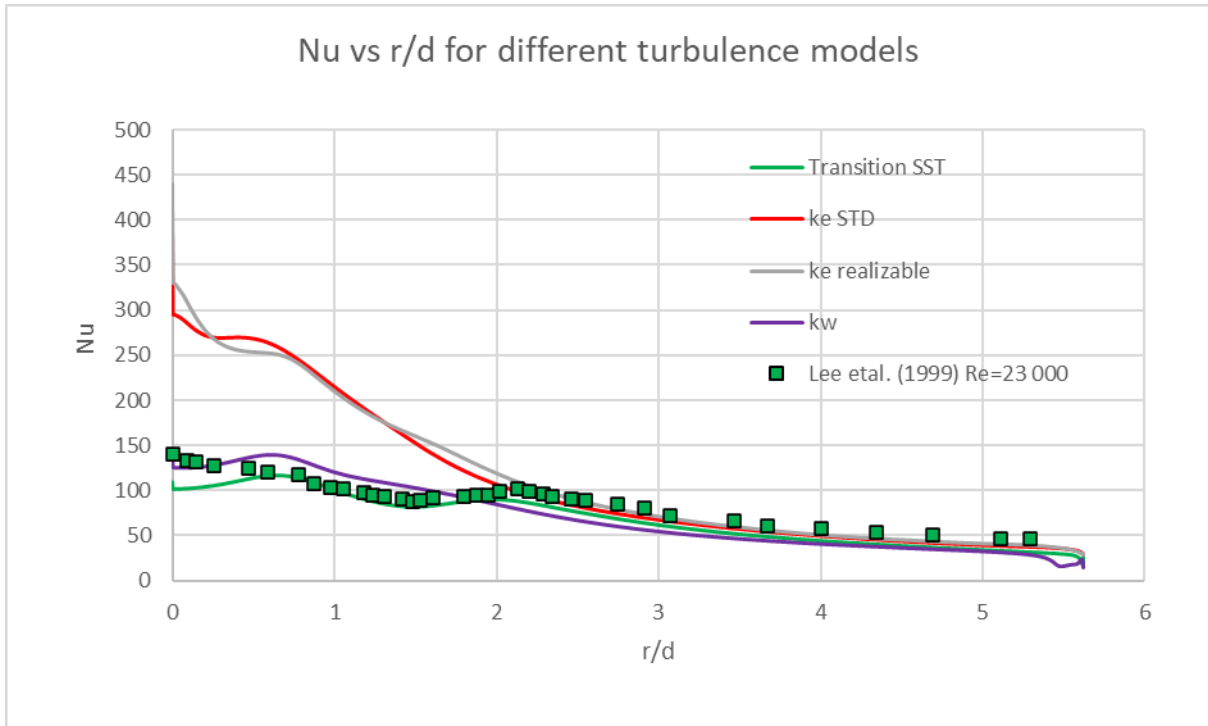


Figure 102. Nu vs r/D for different turbulence models for concave JIHT.

As can be seen the Transition SST model is the best to approximate the experimental results as the second peak in the Nusselt number is evident. The other models do not accurately capture the Nusselt number when the flow transitions from laminar to turbulent flow. For the mesh independence study the grid size is changed and the results are compared. The plots of the Nu for different number of elements is depicted in Figure 103.

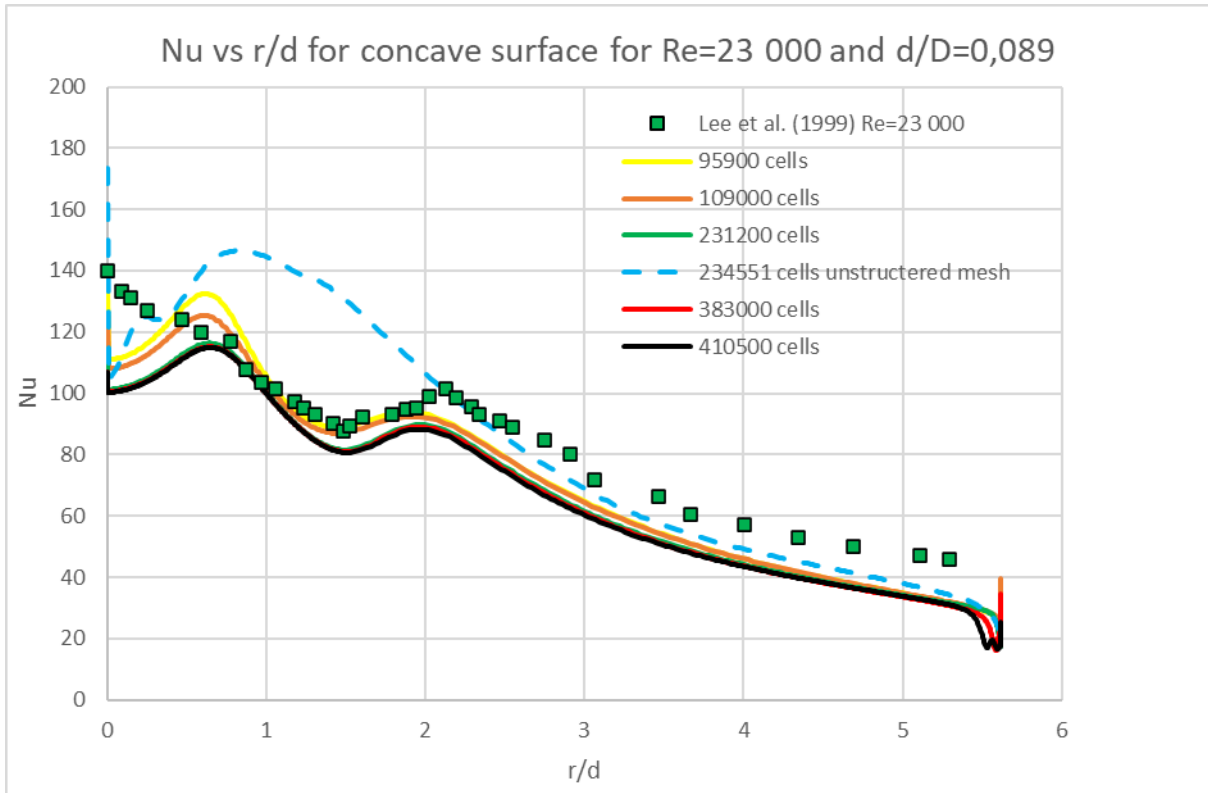


Figure 103. Nu vs r/D for different number of mesh cells for concave JIHT.

As can be seen, the effect of the mesh has a considerable effect on the results obtained. The unstructured mesh does not predict the Nu accurately or the double humps. The peaks of the humps do decrease as the mesh is refined and stabilise after 231 200 cells.

The numerical results are plotted against experimental results in Figure 104.

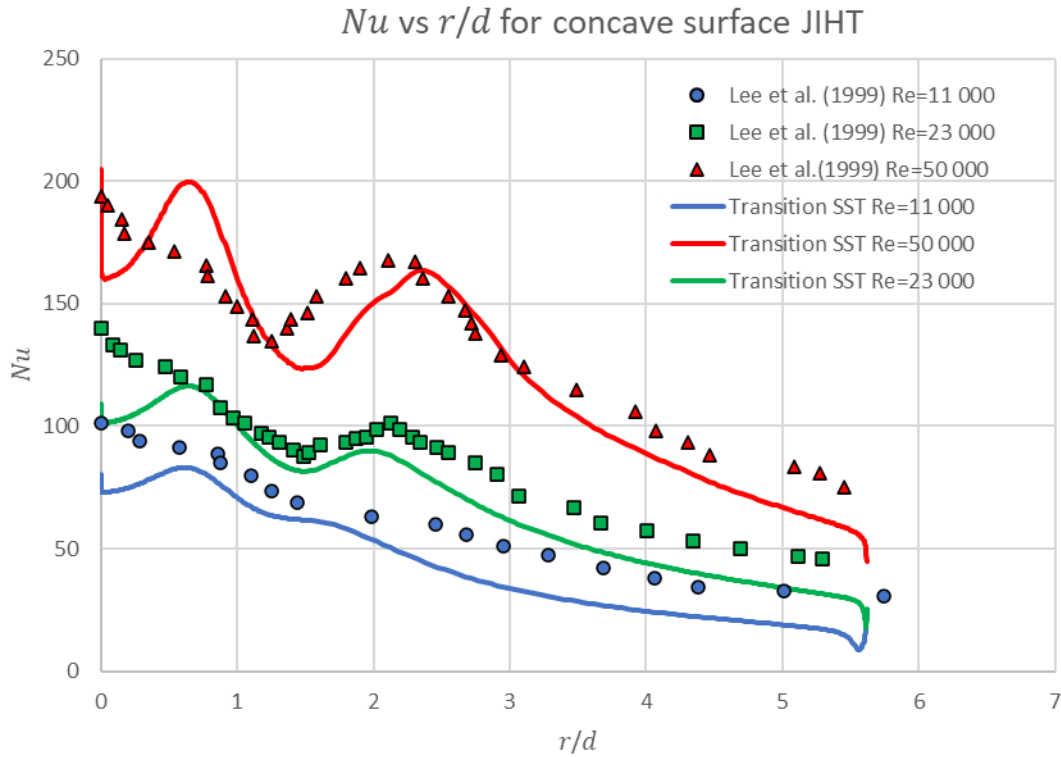


Figure 104. Nu vs r/d for experimental and numerical results for concave JIHT for $Re = [11\,000, 23\,000, 50\,000]$, $H/d = 2$, $d = 34\text{mm}$, $d/D = 0.089$, and $L = 10d$.

From the results of the numerical simulation, the Transition SST model proves reliable again in predicting trends. The accuracy of the solution is reasonable considering how inexpensive the computational cost is relative to other simulations.

Vertical swirling impinging jets on a concave surface results

The additional results for the concave impingement surface and SIJ investigation are presented as Nusselt number distributions from Figure 57 to Figure 111.

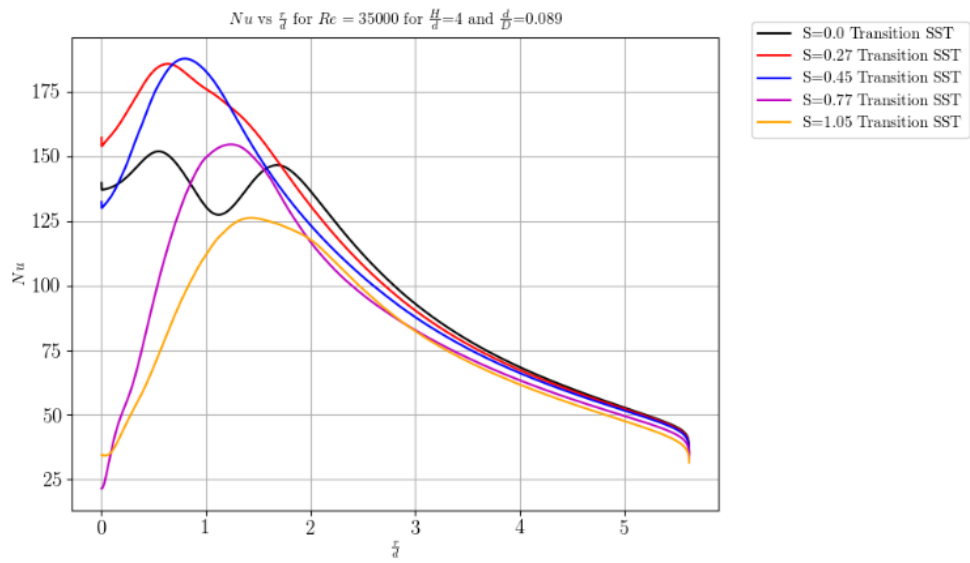


Figure 105. Nusselt number distribution in radial direction $H/d = 4, d/D = 0.089$.

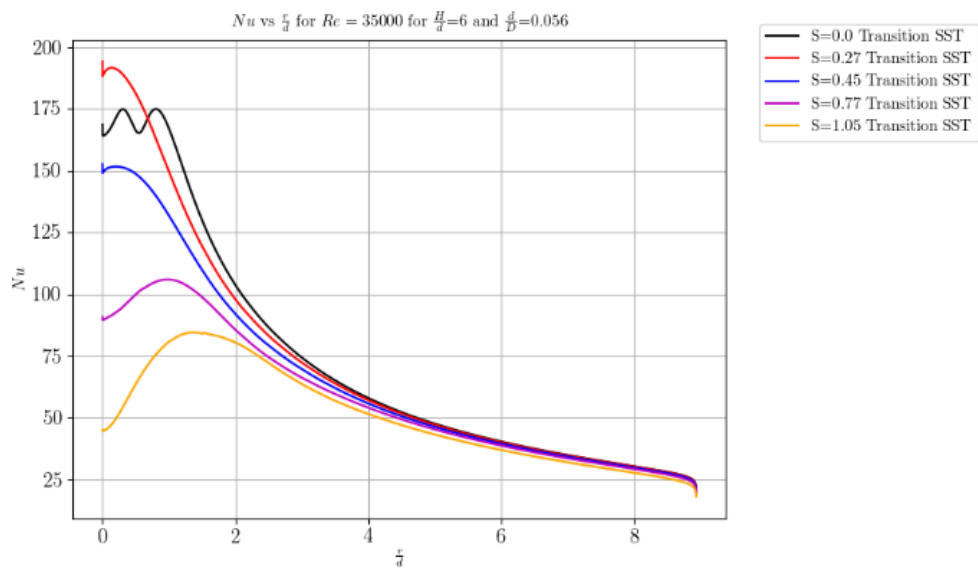


Figure 106. Nusselt number distribution in radial direction $H/d = 6, d/D = 0.056$.

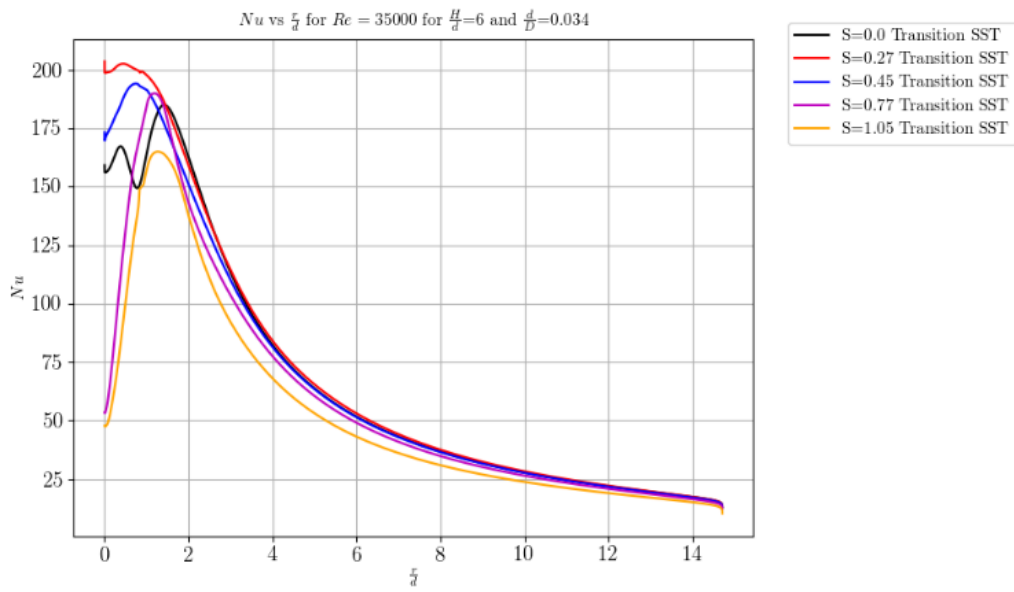


Figure 107. Nusselt number distribution in radial direction $H/d = 6, d/D = 0.034$.

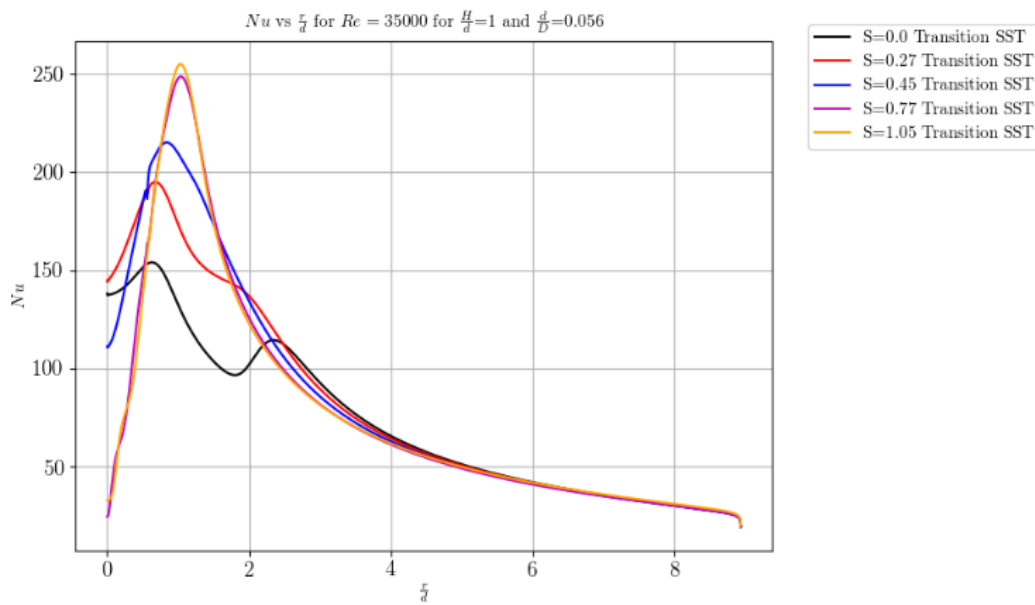


Figure 108. Nusselt number distribution in radial direction $H/d = 1, d/D = 0.056$.

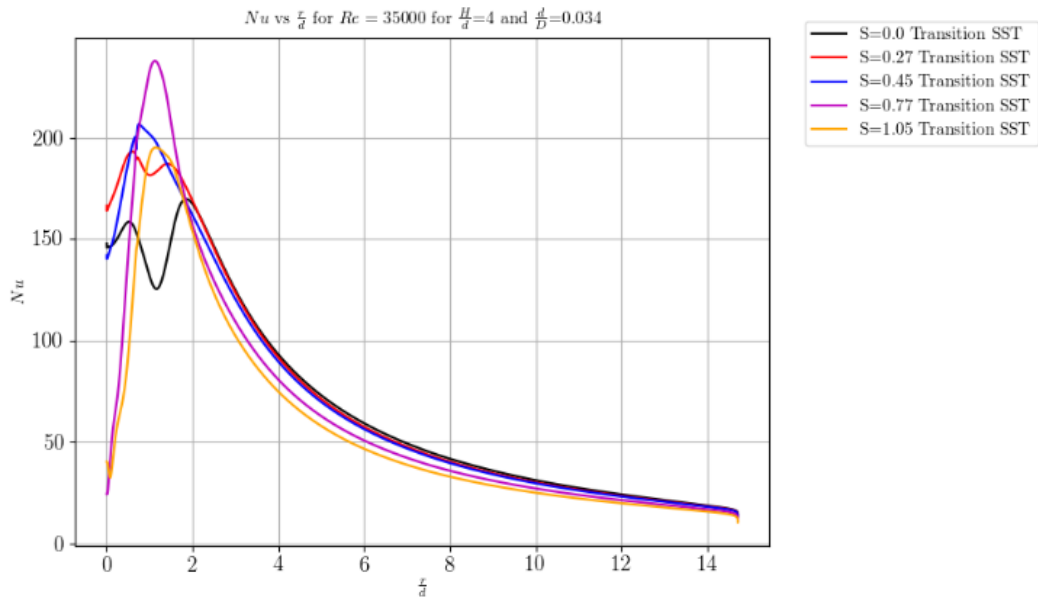


Figure 109. Nusselt number distribution in radial direction $H/d = 4, d/D = 0.034$.

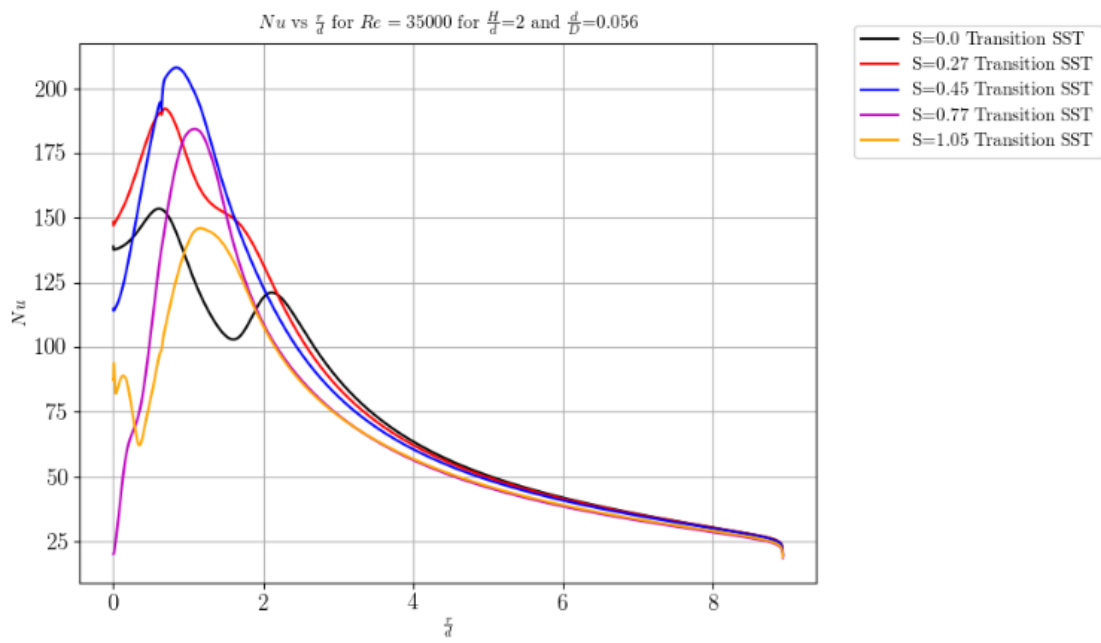


Figure 110. Nusselt number distribution in radial direction $H/d = 2, d/D = 0.056$.

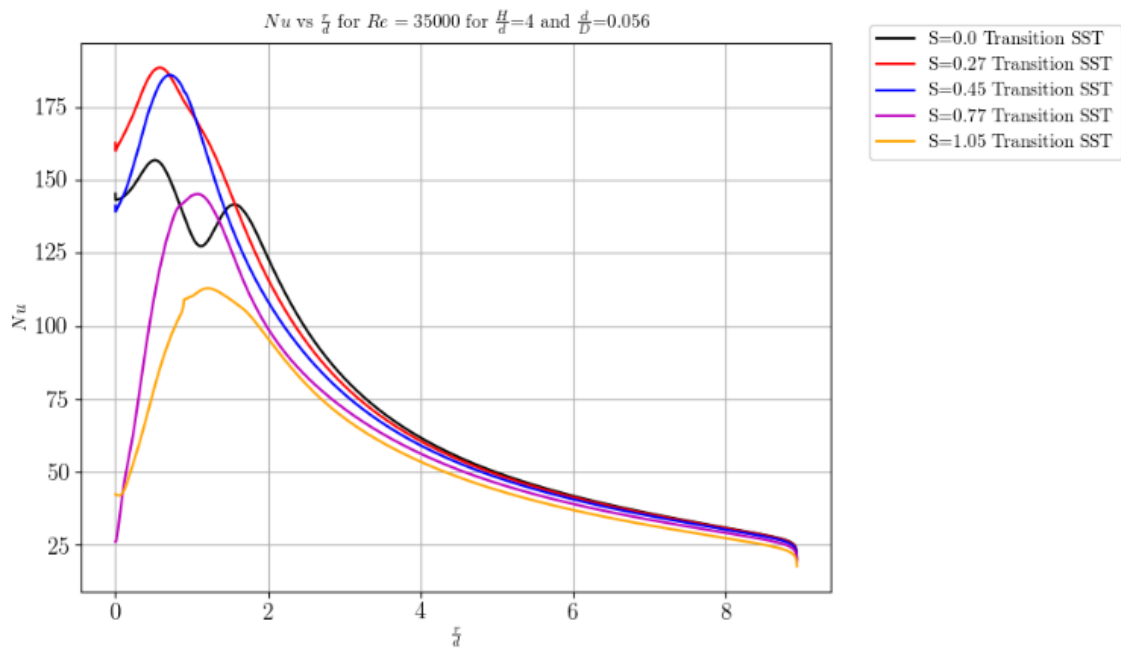


Figure 111. Nusselt number distribution in radial direction $H/d = 4, d/D = 0.056$.

APPENDIX D: SOURCE CODES FOR GEOMETRY AND SIMULATION AUTOMATION

The implementation of the geometry investigation to the implementation on a high performance computing cluster. The scripts are presented for each of the required scripting and implementation procedures.

Geometry

The geometry is scripted for the parametric investigation of the experimental test cases. The script used to automate the geometry and meshing strategy in SpaceClaim is presented below.

```
import math as m

selection = Selection.SelectAll()
result = Delete.Execute(selection)
# EndBlock

#diameter
d=30
#d=Parameters.d*1000
#entry length
Ld=10
#Ld=Parameters.Ld
L=Ld*d
#height
Hd=0.45
#Hd=Parameters.Hd
H=Hd*d
#concavity
Rd=1.5
#Rd=Parameters.Rd
R=Rd*d
#shell thickness
ts=8
#ts=Parameters.ts*1000
#center point of arcs
C=L+H-R
#division line 1 in degrees
adiv1=45
#division line 2 in degrees
adiv2=75
#adiv2=Parameters.adiv2
#outlet diffuser ratio
tf=0.1*H
#tf=Parameters.tf*H

p1x=0
p1y=0
p2x=L
p2y=p1y
p3x=L+0.1*H
p3y=p1y
p4x=L+0.9*H
p4y=p1y

p5x=L+H
p5y=p1y
p6x=p5x+ts
p6y=p1y
p7x=p1x
p7y=d/2
p8x=p2x
p8y=p7y
p9x=p3x
p9y=p8y
r1=((((p8x-C)**2)+(p8y**2))**0.5)
#r1=(p2x-C)/m.cos(m.atan(p7y/(p2x-C)))
r2=((p9x-C)**2+p9y**2)**0.5
r3=p2x-C+0.9*H
r4=p2x-C+H
r5=p2x-C+H+ts
p10x=C+(r3)*m.cos(m.asin(p7y/(r3)))
p10y=p7y
p11x=C+(r4)*m.cos(m.asin(p7y/(r4)))
p11y=p7y
p12x=C+(r5)*m.cos(m.asin(p7y/(r5)))
p12y=p7y
p13x=C+(r1)*m.cos((m.radians(adiv1)))
p13y=(r1)*m.sin((m.radians(adiv1)))
p14x=C+(r2)*m.cos((m.radians(adiv1)))
p14y=(r2)*m.sin((m.radians(adiv1)))
p15x=C+(r3)*m.cos((m.radians(adiv1)))
p15y=(r3)*m.sin((m.radians(adiv1)))
p16x=C+(r4)*m.cos((m.radians(adiv1)))
p16y=(r4)*m.sin((m.radians(adiv1)))
p17x=C+(r5)*m.cos((m.radians(adiv1)))
p17y=(r5)*m.sin((m.radians(adiv1)))
p18x=C+(r1)*m.cos((m.radians(adiv2)))
p18y=(r1)*m.sin((m.radians(adiv2)))
p19x=C+(r2)*m.cos((m.radians(adiv2)))
p19y=(r2)*m.sin((m.radians(adiv2)))
p20x=C+(r3)*m.cos((m.radians(adiv2)))
p20y=(r3)*m.sin((m.radians(adiv2)))
p21x=C+(r4)*m.cos((m.radians(adiv2)))
p21y=(r4)*m.sin((m.radians(adiv2)))
p22x=C+(r5)*m.cos((m.radians(adiv2)))
p22y=(r5)*m.sin((m.radians(adiv2)))
p23x=p1x

if tf<=H:
```

```

    p23y=p18y+p18x*m.sin((m.radians(90-
adiv2)))+(tf/m.sin(m.radians(adiv2)))
else:
    p23y=p18y+p18x*m.sin((m.radians(90-
adiv2)))-(tf/m.sin(m.radians(adiv2)))

p26x=p1x
p26y=p21y+p21x*m.sin((m.radians(90-
adiv2)))
p25x=p1x
p25y=p26y-
((0.1*tf)/m.sin(m.radians(adiv2)))
p27x=p1x
p27y=p22y+p22x*m.sin((m.radians(90-
adiv2)))
p23y=p26y-(tf/m.sin(m.radians(adiv2)))
p24x=p1x
p24y=p23y+((0.1*tf)/m.sin(m.radians(adiv2)
))

# Set Sketch Plane
sectionPlane = Plane.PlaneZX
result =
ViewHelper.SetSketchPlane(sectionPlane,
None)
# EndBlock

# Create Sweep Arc
origin = Point2D.Create(MM(C), MM(p1y))
start = Point2D.Create(MM(p4x), MM(p4y))
end = Point2D.Create(MM(p20x), MM(p20y))
senseClockwise = False
result = SketchArc.CreateSweepArc(origin,
start, end, senseClockwise)
# EndBlock

# Create Sweep Arc
origin = Point2D.Create(MM(C), MM(p1y))
start = Point2D.Create(MM(p5x), MM(p5y))
end = Point2D.Create(MM(p21x), MM(p21y))
senseClockwise = False
result = SketchArc.CreateSweepArc(origin,
start, end, senseClockwise)
# EndBlock

# Create Sweep Arc
origin = Point2D.Create(MM(C), MM(p1y))
start = Point2D.Create(MM(p6x), MM(p6y))
end = Point2D.Create(MM(p22x), MM(p22y))
senseClockwise = False
result = SketchArc.CreateSweepArc(origin,
start, end, senseClockwise)
# EndBlock

# Create Sweep Arc
origin = Point2D.Create(MM(C), MM(p1y))
start = Point2D.Create(MM(p8x), MM(p8y))
end = Point2D.Create(MM(p18x), MM(p18y))
senseClockwise = False
result = SketchArc.CreateSweepArc(origin,
start, end, senseClockwise)
# EndBlock

# Create Sweep Arc
origin = Point2D.Create(MM(C), MM(p1y))
start = Point2D.Create(MM(p9x), MM(p9y))
end = Point2D.Create(MM(p19x), MM(p19y))
senseClockwise = False
result = SketchArc.CreateSweepArc(origin,
start, end, senseClockwise)
# EndBlock

# Create Line
start = Point2D.Create(MM(p1x), MM(p1y))
end = Point2D.Create(MM(p2x), MM(p2y))
result = SketchLine.Create(start, end)
# EndBlock

# Create Line
start = Point2D.Create(MM(p2x), MM(p2y))
end = Point2D.Create(MM(p3x), MM(p3y))
result = SketchLine.Create(start, end)
# EndBlock

# Create Line
start = Point2D.Create(MM(p3x), MM(p3y))
end = Point2D.Create(MM(p4x), MM(p4y))
result = SketchLine.Create(start, end)
# EndBlock

# Create Line
start = Point2D.Create(MM(p4x), MM(p4y))
end = Point2D.Create(MM(p5x), MM(p5y))
result = SketchLine.Create(start, end)
# EndBlock

# Create Line
start = Point2D.Create(MM(p5x), MM(p5y))
end = Point2D.Create(MM(p6x), MM(p6y))
result = SketchLine.Create(start, end)
# EndBlock

# Create Line
start = Point2D.Create(MM(p1x), MM(p1y))
end = Point2D.Create(MM(p7x), MM(p7y))
result = SketchLine.Create(start, end)
# EndBlock

# Create Line
start = Point2D.Create(MM(p7x), MM(p7y))
end = Point2D.Create(MM(p8x), MM(p8y))
result = SketchLine.Create(start, end)
# EndBlock

# Create Line
start = Point2D.Create(MM(p8x), MM(p8y))
end = Point2D.Create(MM(p9x), MM(p9y))
result = SketchLine.Create(start, end)
# EndBlock

# Create Line
start = Point2D.Create(MM(p9x), MM(p9y))
end = Point2D.Create(MM(p10x), MM(p10y))
result = SketchLine.Create(start, end)
# EndBlock

# Create Line
start = Point2D.Create(MM(p10x), MM(p10y))
end = Point2D.Create(MM(p11x), MM(p11y))
result = SketchLine.Create(start, end)
# EndBlock

# Create Line
start = Point2D.Create(MM(p11x), MM(p11y))
end = Point2D.Create(MM(p12x), MM(p12y))
result = SketchLine.Create(start, end)
# EndBlock

# Create Line
start = Point2D.Create(MM(p18x), MM(p18y))
end = Point2D.Create(MM(p19x), MM(p19y))
result = SketchLine.Create(start, end)

```

```

# EndBlock
# Create Line
start = Point2D.Create(MM(p19x), MM(p19y))
end = Point2D.Create(MM(p20x), MM(p20y))
result = SketchLine.Create(start, end)
# EndBlock
# Create Line
start = Point2D.Create(MM(p20x), MM(p20y))
end = Point2D.Create(MM(p21x), MM(p21y))
result = SketchLine.Create(start, end)
# EndBlock
# Create Line
start = Point2D.Create(MM(p21x), MM(p21y))
end = Point2D.Create(MM(p22x), MM(p22y))
result = SketchLine.Create(start, end)
# EndBlock
# Create Line
start = Point2D.Create(MM(p23x), MM(p23y))
end = Point2D.Create(MM(p24x), MM(p24y))
result = SketchLine.Create(start, end)
# EndBlock
# Create Line
start = Point2D.Create(MM(p24x), MM(p24y))
end = Point2D.Create(MM(p25x), MM(p25y))
result = SketchLine.Create(start, end)
# EndBlock
# Create Line
start = Point2D.Create(MM(p25x), MM(p25y))
end = Point2D.Create(MM(p26x), MM(p26y))
result = SketchLine.Create(start, end)
# EndBlock
# Create Line
start = Point2D.Create(MM(p26x), MM(p26y))
end = Point2D.Create(MM(p27x), MM(p27y))
result = SketchLine.Create(start, end)
# EndBlock
# Create Line
start = Point2D.Create(MM(p18x), MM(p18y))
end = Point2D.Create(MM(p23x), MM(p23y))
result = SketchLine.Create(start, end)
# EndBlock
# Create Line
start = Point2D.Create(MM(p19x), MM(p19y))
end = Point2D.Create(MM(p24x), MM(p24y))
result = SketchLine.Create(start, end)
# EndBlock
# Create Line
start = Point2D.Create(MM(p20x), MM(p20y))
end = Point2D.Create(MM(p25x), MM(p25y))
result = SketchLine.Create(start, end)
# EndBlock
# Create Line
start = Point2D.Create(MM(p21x), MM(p21y))
end = Point2D.Create(MM(p26x), MM(p26y))
result = SketchLine.Create(start, end)
# EndBlock
# Create Line
start = Point2D.Create(MM(p22x), MM(p22y))
end = Point2D.Create(MM(p27x), MM(p27y))
result = SketchLine.Create(start, end)
# EndBlock
# Create Line
start = Point2D.Create(MM(p2x), MM(p2y))
end = Point2D.Create(MM(p8x), MM(p8y))
result = SketchLine.Create(start, end)
# EndBlock

```

```

# Create Line
start = Point2D.Create(MM(p3x), MM(p3y))
end = Point2D.Create(MM(p9x), MM(p9y))
result = SketchLine.Create(start, end)
# EndBlock

# Solidify Sketch
mode = InteractionMode.Solid
result = ViewHelper.SetViewMode(mode,
None)
# EndBlock

# Revolve 10 Faces
# Record Failed
# EndBlock

```

Journal files

The journal files used to run the Ansys Fluent simulations are dependent on the model specifics. A sample journal file is provided below.

```

/file/read-case
/mnt/lustre/users/jquick/Ahmed/Validation_
analysis/11mil/ASG_2H_S077_11mil_paved.msh

define materials change-create air air yes
piecewise-linear 26 150 2.355 200 1.767
250 1.413 260 1.360 270 1.311 280 1.265
290 1.220 300 1.177 310 1.141 320 1.106
330 1.073 340 1.042 350 1.012 360 0.983
370 0.956 380 0.931 390 0.906 400 0.883
500 0.706 600 0.589 700 0.507 800 0.442
900 0.392 1000 0.354 1500 0.235 2000 0.176
yes piecewise-linear 26 150 1017 200 1009
250 1009 260 1009 270 1009 280 1008 290
1007 300 1005 310 1005 320 1006 330 1006
340 1007 350 1007 360 1007 370 1008 380
1008 390 1009 400 1009 500 1017 600 1038
700 1065 800 1089 900 1111 1000 1130 1500
1202 2000 1244 yes piecewise-linear 26 150
0.0158 200 0.0197 250 0.0235 260 0.0242
270 0.0249 280 0.0255 290 0.0261 300
0.0267 310 0.0274 320 0.0281 330 0.0287
340 0.0294 350 0.03 360 0.0306 370 0.0313
380 0.0319 390 0.0325 400 0.0331 500
0.0389 600 0.0447 700 0.0503 800 0.0559
900 0.0616 1000 0.0672 1500 0.0926 2000
0.1149 yes piecewise-linear 26 150 10.64e-
6 200 13.59e-6 250 16.14e-6 260 16.63e-6
270 17.12e-6 280 17.6e-6 290 18.02e-6 300
18.43e-6 310 18.87e-6 320 19.29e-6 330
19.71e-6 340 20.13e-6 350 20.54e-6 360
20.94e-6 370 21.34e-6 380 21.75e-6 390
22.12e-6 400 22.52e-6 500 26.33e-6 600
29.74e-6 700 33.03e-6 800 35.89e-6 900
38.65e-6 1000 41.52e-6 1500 53.82e-6 2000
64.77e-6 no no no

```

```

define/models/energy? yes no no no no
define/models/viscous transition-sst? yes

define/boundary-conditions velocity-inlet
inlet_ax no no yes yes no 2.59 no 0 no 293
no no yes no 1 5 10

define/boundary-conditions velocity-inlet
inlet_tan1 no no yes yes no 33.89 no 0 no
293 no no yes no 1 5 10

define/boundary-conditions velocity-inlet
inlet_tan2 no no yes yes no 33.89 no 0 no
293 no no yes no 1 5 10

define/boundary-conditions velocity-inlet
inlet_tan3 no no yes yes no 33.89 no 0 no
293 no no yes no 1 5 10

define/boundary-conditions pressure-outlet
outlet_52 yes no 0 no 293 no yes no no yes
no 1 5 10 yes no no no

define/boundary-conditions pressure-outlet
outlet_52ax yes no 0 no 293 no yes no no
yes no 1 5 10 yes no no no

define/boundary-conditions pressure-outlet
outlet_62 yes no 0 no 293 no yes no no yes
no 1 5 10 yes no no no

define/boundary-conditions pressure-outlet
outlet_72 yes no 0 no 293 no yes no no yes
no 1 5 10 yes no no no

define/boundary-conditions wall
wall_heatflux7 0 no 0 no no no 1120 no no
no no 0 no 0.5 no 1

define/boundary-conditions wall
wall_heatflux71 0 no 0 no no no 1120 no no
no no 0 no 0.5 no 1

define/boundary-conditions wall
wall_heatflux72 0 no 0 no no no 1120 no no
no no 0 no 0.5 no 1

solve/set p-v-coupling 24

solve/set/discretization-scheme pressure
14

solve/set/discretization-scheme k 1

solve/set/discretization-scheme omega 1

solve/set/discretization-scheme intermit 1

solve/set/discretization-scheme mom 1

solve/set/discretization-scheme retheta 1

solve/set/discretization-scheme
temperature 1

```

```

solve/monitors/residual check-convergence?
no no no no no no no no no no

solve/initialize hyb-initialization

define/custom-field-functions define "nu"
(1120*0.04)/((temperature-293)*0.02628)

/solve/report-definitions add report-nu-7
surface-areaavg average-over 1 field nu
per-surface? no surface-names
(wall_heatflux7) q

/solve/report-plots add nu-7 report-defs
report-nu-7 () print? yes q

solve report-files add nu-avg-7 report-
defs report-nu-7 () print? no file-name
"/mnt/lustre/users/jquick/Ahmed/Validation
_analysis/11mil/nu-avg-7" q

/solve/report-definitions add report-nu-71
surface-areaavg average-over 1 field nu
per-surface? no surface-names
(wall_heatflux71) q

/solve/report-plots add nu-71 report-defs
report-nu-71 () print? yes q

solve report-files add nu-avg-71 report-
defs report-nu-71 () print? no file-name
"/mnt/lustre/users/jquick/Ahmed/Validation
_analysis/11mil/nu-avg-71" q

/solve/report-definitions add report-nu-72
surface-areaavg average-over 1 field nu
per-surface? no surface-names
(wall_heatflux72) q

/solve/report-plots add nu-72 report-defs
report-nu-72 () print? yes q

solve report-files add nu-avg-72 report-
defs report-nu-72 () print? no file-name
"/mnt/lustre/users/jquick/Ahmed/Validation
_analysis/11mil/nu-avg-72" q

solve/iterate 1000

file/export/ascii nu-
ASG_S077_2H_11mil_paved_SST wall_heatflux7
wall_heatflux71 wall_heatflux72 () yes nu
() no

file/export/ascii v-out-
ASG_S077_2H_11mil_paved_SST internal_65 ()
yes axial-velocity tangential-velocity
radial-velocity () no

/surface/plane-point-n-normal/plane-x 0 0
0 1 0 0

file/export/ascii v-xplane-
ASG_S077_2H_11mil_paved_SST plane-x () yes

```

```

velocity-magnitude axial-velocity          analysis/11mil/ASG_S077_2H_11mil_paved_SST
tangential-velocity radial-velocity turb-   _iter%i.cas.gz
kinetic-energy () no                         exit y
/file/write-case-data
/mnt/lustre/users/jquick/Ahmed/Validation_

```

Job file

In order to run the job at the high-performance computing cluster a job file is required that can schedule the Ansys fluent run. A sample job file is provided below:

```

#!/bin/bash
#PBS -N ASG_S077_2H_11mil_paved_SST
#PBS -l select=4:ncpus=24:mpiprocs=24
#PBS -l aa_r_cfd=1
#PBS -l aa_r_hpc=80
#PBS -q normal
#PBS -P MECH0000
#PBS -l walltime=12:00:00
#PBS                                     -o
/mnt/lustre/users/jquick/Ahmed/Validation_analysis/11mil/fluent_ASG_S077_2H_11mil_paved_SST
.out
#PBS                                     -e
/mnt/lustre/users/jquick/Ahmed/Validation_analysis/11mil/fluent_ASG_S077_2H_11mil_paved_SST
.err
#PBS -m abe
#PBS -M email@tuks.co.za
##### Running commands
export LM_LICENSE_FILE=1055@chpclic1
export ANSYS_LMD_LICENSE_FILE=1055@chpclic1
export PATH=/apps/chpc/compmech/CFD/ansys_inc/v195/fluent/bin:$PATH
export FLUENT_ARCH=lnamd64
export PBS_JOBDIR=/mnt/lustre/users/jquick/Ahmed/Validation_analysis/11mil
cd $PBS_JOBDIR
nproc=`cat $PBS_NODEFILE | wc -l`
exe=fluent
$exe 3ddp -t$nproc -pinfiniband -ssh -cnf=$PBS_NODEFILE -gu <
/mnt/lustre/users/jquick/Ahmed/Validation_analysis/11mil/ASG_S077_2H_11mil_paved_SST.jou >
run_ASG_S077_2H_11mil_paved_SST.out

```

APPENDIX E: SOLAR RECEIVER OPTIMISATION

For the solar receiver optimization the geometry creation was automated with a SpaceClaim script file. The optimization surrogate model was used and implemented in Python and the parametric investigation was conducted statistically using Python Seaborn.

Material properties

The material properties for the Solar salt and carbon steel are presented below.

Solar salt

```
define materials change-create air msalt yes polynomial 2 2263.641 -0.636 yes
polynomial 2 1396.044 +0.172 yes constant 0.45 yes polynomial 4 0.07543937 -2.77e-
4 +3.49e-7 -1.47e-10 no no no no
```

Carbon steel

```
define materials change-create aluminum csteel yes constant 8030 yes constant 502.48
yes piecewise-linear 6 273 59 373 58 573 49 773 40 973 32 1273 28 no
```

Shuttlecock cone geometry Script

The SpaceClaim script used to automate the cone geometry generation for the optimization study is provided below.

```
# Python Script, API Version = V18
import math as m

# Delete Selection
selection = Selection.SelectAll()
result = Delete.Execute(selection)
# EndBlock

#diameter
d=50

#entry length
Ld=5
L=Ld*d

#height
Hd=0.5
H=Hd*d

#concavity
Rd=1.2
R=Rd*d

#shell thickness
ts=5

#center point of arcs
C=L+H-R

#division line 1 in degrees
adiv1=45

#division line 2 in degrees
adiv2=60

#outlet diffuser ratio
tf=2*H
p1x=0
p1y=0
p2x=L
p2y=p1y
p3x=L+0.1*H
p3y=p1y
p4x=L+0.9*H
p4y=p1y
p5x=L+H
```



```

p5y=p1y
p6x=p5x+ts
p6y=p1y
p7x=p1x
p7y=d/2
p8x=p2x
p8y=p7y
p9x=p3x
p9y=p8y
r1=(((p8x-C)**2)+(p8y**2))**0.5
#r1=(p2x-C)/m.cos(m.atan(p7y/(p2x-C)))
r2=((p9x-C)**2+p9y**2)**0.5
r3=p2x-C+0.9*H
r4=p2x-C+H
r5=p2x-C+H+ts
p10x=C+(r3)*m.cos(m.asin(p7y/(r3)))
p10y=p7y
p11x=C+(r4)*m.cos(m.asin(p7y/(r4)))
p11y=p7y
p12x=C+(r5)*m.cos(m.asin(p7y/(r5)))
p12y=p7y
p13x=C+(r1)*m.cos((m.radians(adiv1)))
p13y=(r1)*m.sin((m.radians(adiv1)))
p14x=C+(r2)*m.cos((m.radians(adiv1)))
p14y=(r2)*m.sin((m.radians(adiv1)))
p15x=C+(r3)*m.cos((m.radians(adiv1)))
p15y=(r3)*m.sin((m.radians(adiv1)))
p16x=C+(r4)*m.cos((m.radians(adiv1)))
p16y=(r4)*m.sin((m.radians(adiv1)))
p17x=C+(r5)*m.cos((m.radians(adiv1)))
p17y=(r5)*m.sin((m.radians(adiv1)))
p18x=C+(r1)*m.cos((m.radians(adiv2)))
p18y=(r1)*m.sin((m.radians(adiv2)))
p19x=C+(r2)*m.cos((m.radians(adiv2)))
p19y=(r2)*m.sin((m.radians(adiv2)))
p20x=C+(r3)*m.cos((m.radians(adiv2)))
p20y=(r3)*m.sin((m.radians(adiv2)))
p21x=C+(r4)*m.cos((m.radians(adiv2)))
p21y=(r4)*m.sin((m.radians(adiv2)))
p22x=C+(r5)*m.cos((m.radians(adiv2)))
p22y=(r5)*m.sin((m.radians(adiv2)))
p23x=p1x
if tf<=H:
    p23y=p18y+p18x*m.sin((m.radians(90-
adiv2)))+(tf/m.sin(m.radians(adiv2)))
else:
    p23y=p18y+p18x*m.sin((m.radians(90-
adiv2)))-(tf/m.sin(m.radians(adiv2)))
p26x=p1x
p26y=p21y+p21x*m.sin((m.radians(90-
adiv2)))
p25x=p1x
p25y=p26y-
((0.1*tf)/m.sin(m.radians(adiv2)))
p27x=p1x
p27y=p22y+p22x*m.sin((m.radians(90-
adiv2)))
p23y=p26y-(tf/m.sin(m.radians(adiv2)))
p24x=p1x
p24y=p23y+((0.1*tf)/m.sin(m.radians(adiv2)
))
# Set Sketch Plane
sectionPlane = Plane.PlaneXY
result =
ViewHelper.SetSketchPlane(sectionPlane,
None)
# EndBlock
# Create Sweep Arc
origin = Point2D.Create(MM(C), MM(p1y))
start = Point2D.Create(MM(p4x), MM(p4y))
end = Point2D.Create(MM(p10x), MM(p10y))
senseClockwise = False
result = SketchArc.CreateSweepArc(origin,
start, end, senseClockwise)
# EndBlock
# Create Sweep Arc
origin = Point2D.Create(MM(C), MM(p1y))
start = Point2D.Create(MM(p5x), MM(p5y))
end = Point2D.Create(MM(p11x), MM(p11y))
senseClockwise = False
result = SketchArc.CreateSweepArc(origin,
start, end, senseClockwise)
# EndBlock
# Create Sweep Arc
origin = Point2D.Create(MM(C), MM(p1y))
start = Point2D.Create(MM(p6x), MM(p6y))
end = Point2D.Create(MM(p12x), MM(p12y))

```

```

senseClockwise = False
result = SketchArc.CreateSweepArc(origin,
start, end, senseClockwise)
# EndBlock
# Create Sweep Arc
origin = Point2D.Create(MM(C), MM(p1y))
start = Point2D.Create(MM(p8x), MM(p8y))
end = Point2D.Create(MM(p13x), MM(p13y))
senseClockwise = False
result = SketchArc.CreateSweepArc(origin,
start, end, senseClockwise)
# EndBlock
# Create Sweep Arc
origin = Point2D.Create(MM(C), MM(p1y))
start = Point2D.Create(MM(p9x), MM(p9y))
end = Point2D.Create(MM(p14x), MM(p14y))
senseClockwise = False
result = SketchArc.CreateSweepArc(origin,
start, end, senseClockwise)
# EndBlock
# Create Sweep Arc
origin = Point2D.Create(MM(C), MM(p1y))
start = Point2D.Create(MM(p10x), MM(p10y))
end = Point2D.Create(MM(p15x), MM(p15y))
senseClockwise = False
result = SketchArc.CreateSweepArc(origin,
start, end, senseClockwise)
# EndBlock
# Create Sweep Arc
origin = Point2D.Create(MM(C), MM(p1y))
start = Point2D.Create(MM(p11x), MM(p11y))
end = Point2D.Create(MM(p16x), MM(p16y))
senseClockwise = False
result = SketchArc.CreateSweepArc(origin,
start, end, senseClockwise)
# EndBlock
# Create Sweep Arc
origin = Point2D.Create(MM(C), MM(p1y))
start = Point2D.Create(MM(p12x), MM(p12y))
end = Point2D.Create(MM(p17x), MM(p17y))
senseClockwise = False
result = SketchArc.CreateSweepArc(origin,
start, end, senseClockwise)
# EndBlock

```

```

# Create Sweep Arc
origin = Point2D.Create(MM(C), MM(p1y))
start = Point2D.Create(MM(p13x), MM(p13y))
end = Point2D.Create(MM(p18x), MM(p18y))
senseClockwise = False
result = SketchArc.CreateSweepArc(origin,
start, end, senseClockwise)
# EndBlock
# Create Sweep Arc
origin = Point2D.Create(MM(C), MM(p1y))
start = Point2D.Create(MM(p14x), MM(p14y))
end = Point2D.Create(MM(p19x), MM(p19y))
senseClockwise = False
result = SketchArc.CreateSweepArc(origin,
start, end, senseClockwise)
# EndBlock
# Create Sweep Arc
origin = Point2D.Create(MM(C), MM(p1y))
start = Point2D.Create(MM(p15x), MM(p15y))
end = Point2D.Create(MM(p20x), MM(p20y))
senseClockwise = False
result = SketchArc.CreateSweepArc(origin,
start, end, senseClockwise)
# EndBlock
# Create Sweep Arc
origin = Point2D.Create(MM(C), MM(p1y))
start = Point2D.Create(MM(p16x), MM(p16y))
end = Point2D.Create(MM(p21x), MM(p21y))
senseClockwise = False
result = SketchArc.CreateSweepArc(origin,
start, end, senseClockwise)
# EndBlock
# Create Sweep Arc
origin = Point2D.Create(MM(C), MM(p1y))
start = Point2D.Create(MM(p17x), MM(p17y))
end = Point2D.Create(MM(p22x), MM(p22y))
senseClockwise = False
result = SketchArc.CreateSweepArc(origin,
start, end, senseClockwise)
# EndBlock
# Create Line
start = Point2D.Create(MM(p1x), MM(p1y))
end = Point2D.Create(MM(p2x), MM(p2y))
result = SketchLine.Create(start, end)

```

```

# EndBlock
# Create Line
start = Point2D.Create(MM(p2x), MM(p2y))
end = Point2D.Create(MM(p3x), MM(p3y))
result = SketchLine.Create(start, end)
# EndBlock
# Create Line
start = Point2D.Create(MM(p3x), MM(p3y))
end = Point2D.Create(MM(p4x), MM(p4y))
result = SketchLine.Create(start, end)
# EndBlock
# Create Line
start = Point2D.Create(MM(p4x), MM(p4y))
end = Point2D.Create(MM(p5x), MM(p5y))
result = SketchLine.Create(start, end)
# EndBlock
# Create Line
start = Point2D.Create(MM(p5x), MM(p5y))
end = Point2D.Create(MM(p6x), MM(p6y))
result = SketchLine.Create(start, end)
# EndBlock
# Create Line
start = Point2D.Create(MM(p1x), MM(p1y))
end = Point2D.Create(MM(p7x), MM(p7y))
result = SketchLine.Create(start, end)
# EndBlock
# Create Line
start = Point2D.Create(MM(p7x), MM(p7y))
end = Point2D.Create(MM(p8x), MM(p8y))
result = SketchLine.Create(start, end)
# EndBlock
# Create Line
start = Point2D.Create(MM(p8x), MM(p8y))
end = Point2D.Create(MM(p9x), MM(p9y))
result = SketchLine.Create(start, end)
# EndBlock
# Create Line
start = Point2D.Create(MM(p9x), MM(p9y))
end = Point2D.Create(MM(p10x), MM(p10y))
result = SketchLine.Create(start, end)
# EndBlock
# Create Line
start = Point2D.Create(MM(p10x), MM(p10y))
end = Point2D.Create(MM(p11x), MM(p11y))

```

```

result = SketchLine.Create(start, end)
# EndBlock
# Create Line
start = Point2D.Create(MM(p11x), MM(p11y))
end = Point2D.Create(MM(p12x), MM(p12y))
result = SketchLine.Create(start, end)
# EndBlock
# Create Line
start = Point2D.Create(MM(p13x), MM(p13y))
end = Point2D.Create(MM(p14x), MM(p14y))
result = SketchLine.Create(start, end)
# EndBlock
# Create Line
start = Point2D.Create(MM(p14x), MM(p14y))
end = Point2D.Create(MM(p15x), MM(p15y))
result = SketchLine.Create(start, end)
# EndBlock
# Create Line
start = Point2D.Create(MM(p15x), MM(p15y))
end = Point2D.Create(MM(p16x), MM(p16y))
result = SketchLine.Create(start, end)
# EndBlock
# Create Line
start = Point2D.Create(MM(p16x), MM(p16y))
end = Point2D.Create(MM(p17x), MM(p17y))
result = SketchLine.Create(start, end)
# EndBlock
# Create Line
start = Point2D.Create(MM(p18x), MM(p18y))
end = Point2D.Create(MM(p19x), MM(p19y))
result = SketchLine.Create(start, end)
# EndBlock
# Create Line
start = Point2D.Create(MM(p19x), MM(p19y))
end = Point2D.Create(MM(p20x), MM(p20y))
result = SketchLine.Create(start, end)
# EndBlock
# Create Line
start = Point2D.Create(MM(p20x), MM(p20y))
end = Point2D.Create(MM(p21x), MM(p21y))
result = SketchLine.Create(start, end)
# EndBlock
# Create Line
start = Point2D.Create(MM(p21x), MM(p21y))

```

```

end = Point2D.Create(MM(p22x), MM(p22y))
result = SketchLine.Create(start, end)
# EndBlock
# Create Line
start = Point2D.Create(MM(p23x), MM(p23y))
end = Point2D.Create(MM(p24x), MM(p24y))
result = SketchLine.Create(start, end)
# EndBlock
# Create Line
start = Point2D.Create(MM(p24x), MM(p24y))
end = Point2D.Create(MM(p25x), MM(p25y))
result = SketchLine.Create(start, end)
# EndBlock
# Create Line
start = Point2D.Create(MM(p25x), MM(p25y))
end = Point2D.Create(MM(p26x), MM(p26y))
result = SketchLine.Create(start, end)
# EndBlock
# Create Line
start = Point2D.Create(MM(p26x), MM(p26y))
end = Point2D.Create(MM(p27x), MM(p27y))
result = SketchLine.Create(start, end)
# EndBlock
# Create Line
start = Point2D.Create(MM(p18x), MM(p18y))
end = Point2D.Create(MM(p23x), MM(p23y))
result = SketchLine.Create(start, end)
# EndBlock
# Create Line
start = Point2D.Create(MM(p19x), MM(p19y))
end = Point2D.Create(MM(p24x), MM(p24y))
result = SketchLine.Create(start, end)
# EndBlock
# Create Line
start = Point2D.Create(MM(p20x), MM(p20y))
end = Point2D.Create(MM(p25x), MM(p25y))
result = SketchLine.Create(start, end)
# EndBlock
# Create Line
start = Point2D.Create(MM(p21x), MM(p21y))
end = Point2D.Create(MM(p26x), MM(p26y))
result = SketchLine.Create(start, end)
# EndBlock
# Create Line

```

```

start = Point2D.Create(MM(p22x), MM(p22y))
end = Point2D.Create(MM(p27x), MM(p27y))
result = SketchLine.Create(start, end)
# EndBlock
# Create Line
start = Point2D.Create(MM(p2x), MM(p2y))
end = Point2D.Create(MM(p8x), MM(p8y))
result = SketchLine.Create(start, end)
# EndBlock
# Create Line
start = Point2D.Create(MM(p3x), MM(p3y))
end = Point2D.Create(MM(p9x), MM(p9y))
result = SketchLine.Create(start, end)
# EndBlock

# Solidify Sketch
mode = InteractionMode.Solid
result = ViewHelper.SetViewMode(mode,
None)
# EndBlock

# Create Named Selection Group
primarySelection =
Selection.Create(GetRootPart().Bodies[0].F
aces[5])
secondarySelection = Selection()
result =
NamedSelection.Create(primarySelection,
secondarySelection)
# EndBlock

# Rename Named Selection
result = NamedSelection.Rename("Group1",
"fluid1")
# EndBlock

# Create Named Selection Group
primarySelection =
Selection.Create(GetRootPart().Bodies[0].F
aces[4])
secondarySelection = Selection()

```

```

result = secondarySelection = Selection()
NamedSelection.Create(primarySelection,
secondarySelection)
# EndBlock

# Rename Named Selection
result = NamedSelection.Rename("Group1",
"fluid2")
# EndBlock

# Create Named Selection Group
primarySelection =
Selection.Create(GetRootPart().Bodies[0].F
aces[16])
secondarySelection = Selection()
result =
NamedSelection.Create(primarySelection,
secondarySelection)
# EndBlock

# Rename Named Selection
result = NamedSelection.Rename("Group1",
"fluid3")
# EndBlock

# Create Named Selection Group
primarySelection =
Selection.Create(GetRootPart().Bodies[0].F
aces[15])
secondarySelection = Selection()
result =
NamedSelection.Create(primarySelection,
secondarySelection)
# EndBlock

# Rename Named Selection
result = NamedSelection.Rename("Group1",
"fluid4")
# EndBlock

# Create Named Selection Group
primarySelection =
Selection.Create(GetRootPart().Bodies[0].F
aces[13])

secondarySelection = Selection()
result =
NamedSelection.Create(primarySelection,
secondarySelection)
# EndBlock

# Rename Named Selection
result = NamedSelection.Rename("Group1",
"fluid5")
# EndBlock

# Create Named Selection Group
primarySelection =
Selection.Create(GetRootPart().Bodies[0].F
aces[12])
secondarySelection = Selection()
result =
NamedSelection.Create(primarySelection,
secondarySelection)
# EndBlock

# Rename Named Selection
result = NamedSelection.Rename("Group1",
"fluid6")
# EndBlock

# Create Named Selection Group
primarySelection =
Selection.Create(GetRootPart().Bodies[0].F
aces[11])
secondarySelection = Selection()
result =
NamedSelection.Create(primarySelection,
secondarySelection)
# EndBlock

# Rename Named Selection
result = NamedSelection.Rename("Group1",
"fluid7")
# EndBlock

# Create Named Selection Group
primarySelection =
Selection.Create(GetRootPart().Bodies[0].F
aces[13])

```

```

primarySelection          =      # Create Named Selection Group
Selection.Create(GetRootPart().Bodies[0].Faces[9])
secondarySelection = Selection()
result                  =      primarySelection          =
NamedSelection.Create(primarySelection,      Selection.Create(GetRootPart().Bodies[0].Faces[3])
secondarySelection)                          secondarySelection = Selection()
# EndBlock                                    result                  =
                                              NamedSelection.Create(primarySelection,
                                              secondarySelection)
                                              # EndBlock

# Rename Named Selection
result = NamedSelection.Rename("Group1",    # Rename Named Selection
"fluid8")
# EndBlock                                  result = NamedSelection.Rename("Group1",
                                              "fluid11")
                                              # EndBlock

# Create Named Selection Group
primarySelection          =      # Create Named Selection Group
Selection.Create(GetRootPart().Bodies[0].Faces[8])
secondarySelection = Selection()
result                  =      primarySelection          =
NamedSelection.Create(primarySelection,      Selection.Create(GetRootPart().Bodies[0].Faces[2])
secondarySelection)                          secondarySelection = Selection()
# EndBlock                                    result                  =
                                              NamedSelection.Create(primarySelection,
                                              secondarySelection)
                                              # EndBlock

# Rename Named Selection
result = NamedSelection.Rename("Group1",    # Rename Named Selection
"fluid9")
# EndBlock                                  result = NamedSelection.Rename("Group1",
                                              "fluid12")
                                              # EndBlock

# Create Named Selection Group
primarySelection          =      # Create Named Selection Group
Selection.Create(GetRootPart().Bodies[0].Faces[7])
secondarySelection = Selection()
result                  =      primarySelection          =
NamedSelection.Create(primarySelection,      Selection.Create(GetRootPart().Bodies[0].Faces[1])
secondarySelection)                          secondarySelection = Selection()
# EndBlock                                    result                  =
                                              NamedSelection.Create(primarySelection,
                                              secondarySelection)
                                              # EndBlock

# Rename Named Selection
result = NamedSelection.Rename("Group1",    # Rename Named Selection
"fluid10")
# EndBlock                                  result = NamedSelection.Rename("Group1",
                                              "fluid13")
                                              # EndBlock

```

EE

```

# EndBlock

# Create Named Selection Group
primarySelection = Selection.Create(GetRootPart().Bodies[0].Faces[14])
secondarySelection = Selection()
result = NamedSelection.Create(primarySelection, secondarySelection)
# EndBlock

# Rename Named Selection
result = NamedSelection.Rename("Group1", "solid_shell1")
# EndBlock

# Create Named Selection Group
primarySelection = Selection.Create(GetRootPart().Bodies[0].Faces[10])
secondarySelection = Selection()
result = NamedSelection.Create(primarySelection, secondarySelection)
# EndBlock

# Rename Named Selection
result = NamedSelection.Rename("Group1", "solid_shell2")
# EndBlock

# Create Named Selection Group
primarySelection = Selection.Create(GetRootPart().Bodies[0].Faces[6])
secondarySelection = Selection()
result = NamedSelection.Create(primarySelection, secondarySelection)
# EndBlock

# Rename Named Selection
result = NamedSelection.Rename("Group1", "solid_shell3")

# EndBlock

# Create Named Selection Group
primarySelection = Selection.Create(GetRootPart().Bodies[0].Faces[0])
secondarySelection = Selection()
result = NamedSelection.Create(primarySelection, secondarySelection)
# EndBlock

# Rename Named Selection
result = NamedSelection.Rename("Group1", "solid_shell4")
# EndBlock

# Create Named Selection Group
primarySelection = Selection.Create(GetRootPart().Bodies[0].Edges[17])
secondarySelection = Selection()
result = NamedSelection.Create(primarySelection, secondarySelection)
# EndBlock

# Rename Named Selection
result = NamedSelection.Rename("Group1", "inlet")
# EndBlock

# Create Named Selection Group
primarySelection = Selection.Create(GetRootPart().Bodies[0].Edges[18])
secondarySelection = Selection()
result = NamedSelection.Create(primarySelection, secondarySelection)
# EndBlock

# Rename Named Selection

```

```

result = NamedSelection.Rename("Group1",
"axis_1")
# EndBlock

```

```

# Create Named Selection Group
primarySelection =
Selection.Create(GetRootPart().Bodies[0].E
dges[14])
secondarySelection = Selection()
result =
NamedSelection.Create(primarySelection,
secondarySelection)
# EndBlock

```

```

# Rename Named Selection
result = NamedSelection.Rename("Group1",
"axis_2")
# EndBlock

```

```

# Create Named Selection Group
primarySelection =
Selection.Create(GetRootPart().Bodies[0].E
dges[42])
secondarySelection = Selection()
result =
NamedSelection.Create(primarySelection,
secondarySelection)
# EndBlock

```

```

# Rename Named Selection
result = NamedSelection.Rename("Group1",
"axis_3")
# EndBlock

```

```

# Create Named Selection Group
primarySelection =
Selection.Create(GetRootPart().Bodies[0].E
dges[41])
secondarySelection = Selection()
result =
NamedSelection.Create(primarySelection,
secondarySelection)
# EndBlock

```

```

# Rename Named Selection
result = NamedSelection.Rename("Group1",
"axis_4")
# EndBlock

```

```

# Create Named Selection Group
primarySelection =
Selection.Create(GetRootPart().Bodies[0].E
dges[38])
secondarySelection = Selection()
result =
NamedSelection.Create(primarySelection,
secondarySelection)
# EndBlock

```

```

# Rename Named Selection
result = NamedSelection.Rename("Group1",
"axis_5")
# EndBlock

```

```

# Create Named Selection Group
primarySelection =
Selection.Create(GetRootPart().Bodies[0].E
dges[13])
secondarySelection = Selection()
result =
NamedSelection.Create(primarySelection,
secondarySelection)
# EndBlock

```

```

# Rename Named Selection
result = NamedSelection.Rename("Group1",
"internal_12")
# EndBlock

```

```

# Create Named Selection Group
primarySelection =
Selection.Create(GetRootPart().Bodies[0].E
dges[15])
secondarySelection = Selection()
result =
NamedSelection.Create(primarySelection,
secondarySelection)
# EndBlock

```



```

# Rename Named Selection
result = NamedSelection.Rename("Group1",
"internal_23")
# EndBlock

# Create Named Selection Group
primarySelection =
Selection.Create(GetRootPart().Bodies[0].E
dges[40])
secondarySelection = Selection()
result =
NamedSelection.Create(primarySelection,
secondarySelection)
# EndBlock

# Rename Named Selection
result = NamedSelection.Rename("Group1",
"internal_34")
# EndBlock

# Create Named Selection Group
primarySelection =
Selection.Create(GetRootPart().Bodies[0].E
dges[16])
secondarySelection = Selection()
result =
NamedSelection.Create(primarySelection,
secondarySelection)
# EndBlock

# Rename Named Selection
result = NamedSelection.Rename("Group1",
"internal_25")
# EndBlock

# Create Named Selection Group
primarySelection =
Selection.Create(GetRootPart().Bodies[0].E
dges[35])
secondarySelection = Selection()
result =
NamedSelection.Create(primarySelection,
secondarySelection)

# EndBlock

# Rename Named Selection
result = NamedSelection.Rename("Group1",
"internal_36")
# EndBlock

# Create Named Selection Group
primarySelection =
Selection.Create(GetRootPart().Bodies[0].E
dges[33])
secondarySelection = Selection()
result =
NamedSelection.Create(primarySelection,
secondarySelection)
# EndBlock

# Rename Named Selection
result = NamedSelection.Rename("Group1",
"internal_47")
# EndBlock

# Create Named Selection Group
primarySelection =
Selection.Create(GetRootPart().Bodies[0].E
dges[34])
secondarySelection = Selection()
result =
NamedSelection.Create(primarySelection,
secondarySelection)
# EndBlock

# Rename Named Selection
result = NamedSelection.Rename("Group1",
"internal_56")
# EndBlock

# Create Named Selection Group
primarySelection =
Selection.Create(GetRootPart().Bodies[0].E
dges[32])
secondarySelection = Selection()

```

```

result = secondarySelection = Selection()
NamedSelection.Create(primarySelection, result =
secondarySelection) NamedSelection.Create(primarySelection,
# EndBlock secondarySelection)
# EndBlock

# Rename Named Selection
result = NamedSelection.Rename("Group1", # Rename Named Selection
"internal_67") result = NamedSelection.Rename("Group1",
# EndBlock "internal_710")
# EndBlock

# Create Named Selection Group
primarySelection = # Create Named Selection Group
Selection.Create(GetRootPart().Bodies[0].E primarySelection =
dges[28]) Selection.Create(GetRootPart().Bodies[0].E
secondarySelection = Selection() dges[25])
result = secondarySelection = Selection()
NamedSelection.Create(primarySelection, result =
secondarySelection)
# EndBlock NamedSelection.Create(primarySelection,
secondarySelection)
# EndBlock

# Rename Named Selection
result = NamedSelection.Rename("Group1", # Rename Named Selection
"internal_58") result = NamedSelection.Rename("Group1",
# EndBlock "internal_89")
# EndBlock

# Create Named Selection Group
primarySelection = # Create Named Selection Group
Selection.Create(GetRootPart().Bodies[0].E primarySelection =
dges[26]) Selection.Create(GetRootPart().Bodies[0].E
secondarySelection = Selection() dges[23])
result = secondarySelection = Selection()
NamedSelection.Create(primarySelection, result =
secondarySelection)
# EndBlock NamedSelection.Create(primarySelection,
secondarySelection)
# EndBlock

# Rename Named Selection
result = NamedSelection.Rename("Group1", # Rename Named Selection
"internal_69") result = NamedSelection.Rename("Group1",
# EndBlock "internal_910")
# EndBlock

# Create Named Selection Group
primarySelection = # Create Named Selection Group
Selection.Create(GetRootPart().Bodies[0].E
dges[24])

```

```

primarySelection          =      # Create Named Selection Group
Selection.Create(GetRootPart().Bodies[0].Edges[11])
secondarySelection = Selection()
result                  =      primarySelection          =
NamedSelection.Create(primarySelection,      Selection.Create(GetRootPart().Bodies[0].Edges[7])
secondarySelection)                          secondarySelection = Selection()
# EndBlock                                  result                  =
                                             NamedSelection.Create(primarySelection,
secondarySelection)                          # EndBlock

# Rename Named Selection
result = NamedSelection.Rename("Group1",    # Rename Named Selection
"internal_811")
# EndBlock                                  result = NamedSelection.Rename("Group1",
                                             "internal_1112")
# EndBlock

# Create Named Selection Group
primarySelection          =      # Create Named Selection Group
Selection.Create(GetRootPart().Bodies[0].Edges[8])
secondarySelection = Selection()
result                  =      primarySelection          =
NamedSelection.Create(primarySelection,      Selection.Create(GetRootPart().Bodies[0].Edges[4])
secondarySelection)                          secondarySelection = Selection()
# EndBlock                                  result                  =
                                             NamedSelection.Create(primarySelection,
secondarySelection)                          # EndBlock

# Rename Named Selection
result = NamedSelection.Rename("Group1",    # Rename Named Selection
"internal_912")
# EndBlock                                  result = NamedSelection.Rename("Group1",
                                             "internal_1213")
# EndBlock

# Create Named Selection Group
primarySelection          =      # Create Named Selection Group
Selection.Create(GetRootPart().Bodies[0].Edges[5])
secondarySelection = Selection()
result                  =      primarySelection          =
NamedSelection.Create(primarySelection,      Selection.Create(GetRootPart().Bodies[0].Edges[19])
secondarySelection)                          secondarySelection = Selection()
# EndBlock                                  result                  =
                                             NamedSelection.Create(primarySelection,
secondarySelection)                          # EndBlock

# Rename Named Selection
result = NamedSelection.Rename("Group1",    # Rename Named Selection
"internal_1013")
# EndBlock                                  result = NamedSelection.Rename("Group1",
                                             "wall_pipe1")
# EndBlock

```

```

# Create Named Selection Group
primarySelection = Selection.Create(GetRootPart().Bodies[0].Edges[36])
secondarySelection = Selection()
result = NamedSelection.Create(primarySelection, secondarySelection)
# EndBlock

# Rename Named Selection
result = NamedSelection.Rename("Group1", "wall_pipe5")
# EndBlock

# Create Named Selection Group
primarySelection = Selection.Create(GetRootPart().Bodies[0].Edges[27])
secondarySelection = Selection()
result = NamedSelection.Create(primarySelection, secondarySelection)
# EndBlock

# Rename Named Selection
result = NamedSelection.Rename("Group1", "wall_pipe8")
# EndBlock

# Create Named Selection Group
primarySelection = Selection.Create(GetRootPart().Bodies[0].Edges[10])
secondarySelection = Selection()
result = NamedSelection.Create(primarySelection, secondarySelection)
# EndBlock

# Rename Named Selection
result = NamedSelection.Rename("Group1", "wall_pipe11")

# EndBlock

# Create Named Selection Group
primarySelection = Selection.Create(GetRootPart().Bodies[0].Edges[37])
secondarySelection = Selection()
result = NamedSelection.Create(primarySelection, secondarySelection)
# EndBlock

# Rename Named Selection
result = NamedSelection.Rename("Group1", "wall_shell131")
# EndBlock

# Create Named Selection Group
primarySelection = Selection.Create(GetRootPart().Bodies[0].Edges[29])
secondarySelection = Selection()
result = NamedSelection.Create(primarySelection, secondarySelection)
# EndBlock

# Rename Named Selection
result = NamedSelection.Rename("Group1", "wall_shell172")
# EndBlock

# Create Named Selection Group
primarySelection = Selection.Create(GetRootPart().Bodies[0].Edges[20])
secondarySelection = Selection()
result = NamedSelection.Create(primarySelection, secondarySelection)
# EndBlock

# Rename Named Selection

```

```

result = NamedSelection.Rename("Group1",
"wall_shell103")
# EndBlock

# Create Named Selection Group
primarySelection =
Selection.Create(GetRootPart().Bodies[0].E
dges[0])
secondarySelection = Selection()
result =
NamedSelection.Create(primarySelection,
secondarySelection)
# EndBlock

# Rename Named Selection
result = NamedSelection.Rename("Group1",
"wall_shell134")
# EndBlock

# Create Named Selection Group
primarySelection =
Selection.Create(GetRootPart().Bodies[0].E
dges[39])
secondarySelection = Selection()
result =
NamedSelection.Create(primarySelection,
secondarySelection)
# EndBlock

# Rename Named Selection
result = NamedSelection.Rename("Group1",
"wall_heatflux1")
# EndBlock

# Create Named Selection Group
primarySelection =
Selection.Create(GetRootPart().Bodies[0].E
dges[31])
secondarySelection = Selection()
result =
NamedSelection.Create(primarySelection,
secondarySelection)
# EndBlock

```

```

# Rename Named Selection
result = NamedSelection.Rename("Group1",
"wall_heatflux2")
# EndBlock

# Create Named Selection Group
primarySelection =
Selection.Create(GetRootPart().Bodies[0].E
dges[22])
secondarySelection = Selection()
result =
NamedSelection.Create(primarySelection,
secondarySelection)
# EndBlock

# Rename Named Selection
result = NamedSelection.Rename("Group1",
"wall_heatflux3")
# EndBlock

# Create Named Selection Group
primarySelection =
Selection.Create(GetRootPart().Bodies[0].E
dges[2])
secondarySelection = Selection()
result =
NamedSelection.Create(primarySelection,
secondarySelection)
# EndBlock

# Rename Named Selection
result = NamedSelection.Rename("Group1",
"wall_heatflux4")
# EndBlock

# Create Named Selection Group
primarySelection =
Selection.Create(GetRootPart().Bodies[0].E
dges[12])
secondarySelection = Selection()
result =
NamedSelection.Create(primarySelection,
secondarySelection)
# EndBlock

```

```

# Rename Named Selection
result = NamedSelection.Rename("Group1",
"outlet_11")
# EndBlock

# Create Named Selection Group
primarySelection =
Selection.Create(GetRootPart().Bodies[0].E
dges[9])
secondarySelection = Selection()
result =
NamedSelection.Create(primarySelection,
secondarySelection)
# EndBlock

# Rename Named Selection
result = NamedSelection.Rename("Group1",
"outlet_12")
# EndBlock

# Create Named Selection Group
primarySelection =
Selection.Create(GetRootPart().Bodies[0].E
dges[6])
secondarySelection = Selection()
result =
NamedSelection.Create(primarySelection,
secondarySelection)
# EndBlock

# Rename Named Selection
result = NamedSelection.Rename("Group1",
"outlet_13")
# EndBlock

# Create Named Selection Group
primarySelection =
Selection.Create(GetRootPart().Bodies[0].E
dges[3])
secondarySelection = Selection()
result =
NamedSelection.Create(primarySelection,
secondarySelection)

```

```

# EndBlock

# Rename Named Selection
result = NamedSelection.Rename("Group1",
"wall_shell4")
# EndBlock

# Create Named Selection Group
primarySelection =
Selection.Create(GetRootPart().Bodies[0].E
dges[30])
secondarySelection = Selection()
result =
NamedSelection.Create(primarySelection,
secondarySelection)
# EndBlock

# Rename Named Selection
result = NamedSelection.Rename("Group1",
"internal_s12")
# EndBlock

# Create Named Selection Group
primarySelection =
Selection.Create(GetRootPart().Bodies[0].E
dges[21])
secondarySelection = Selection()
result =
NamedSelection.Create(primarySelection,
secondarySelection)
# EndBlock

# Rename Named Selection
result = NamedSelection.Rename("Group1",
"internal_s23")
# EndBlock

# Create Named Selection Group
primarySelection =
Selection.Create(GetRootPart().Bodies[0].E
dges[1])
secondarySelection = Selection()

```

```

result = NamedSelection.Create(primarySelection,
secondarySelection)
# EndBlock
# Rename Named Selection
result = NamedSelection.Rename("Group1",
"internal_s34")
# EndBlock

```

Optimization

The optimization source code used for the python investigation is presented below.

```

import matplotlib.pyplot as plt
import numpy as np
from sklearn import datasets, linear_model
from sklearn.metrics import r2_score
from sklearn.decomposition import PCA
from sklearn.preprocessing import scale
#from sklearn import cross_validation
import pandas as pd
import scipy.optimize as opt
from mpl_toolkits.mplot3d import Axes3D
import random as rand
%matplotlib inline

data=pd.read_excel('2D_cone_opt_v1.xlsx')
# data.head()
data

y1=data.loc[:, 'P24 - nuavg-shell']
y2=data.loc[:, 'P19 - tavg-out (K)']
y3=data.loc[:, 'P17 - tmax-shell (K)']

x=data.iloc[:,1:10]
x.head()

ass_x_train=x[:-20]
ass_x_test=x[-20:]
ass_y1_train=y1[:-20]
ass_y1_test=y1[-20:]
ass_y2_train=y2[:-20]
ass_y2_test=y2[-20:]
ass_y3_train=y3[:-20]
ass_y3_test=y3[-20:]

data2=data.iloc[:, [1,2,3,4,5,6,7,8,9,10, -
5, -6, -11, -13]]

from sklearn import preprocessing
y1=data.loc[:, 'P24 - nuavg-shell']
y2=data.loc[:, 'P19 - tavg-out (K)']
y3=data.loc[:, 'P17 - tmax-shell (K)']
x=data.iloc[:,1:10]
ass_x_train=preprocessing.scale(x[:-20])
ass_x_test=preprocessing.scale(x[-20:])
ass_y1_train=preprocessing.scale(y1[:-20])
ass_y1_test=preprocessing.scale(y1[-20:])
ass_y2_train=preprocessing.scale(y2[:-20])
ass_y2_test=preprocessing.scale(y2[-20:])
ass_y3_train=preprocessing.scale(y3[:-20])
ass_y3_test=preprocessing.scale(y3[-20:])

#y1
print('The regression model for y1: Nu-
avg')
print('-----')
regr=linear_model.LinearRegression()
regr.fit(ass_x_train,ass_y1_train)
ass_y1_pred=regr.predict(ass_x_test)

# The mean squared error
print("Mean squared error: {}".format((1./
len(ass_y1_test)*(np.sum((ass_y1_test-
ass_y1_pred)**2))))
print('-----')
# Explained variance score: 1 is perfect p
rediction
print('Variance score: {}'.format(r2_score
(ass_y1_test, ass_y1_pred)))

# The coefficients of the linear regressio
n
print('-----')
print('Linear regression coefficients: \n'
, regr.coef_)

#y1

```

```

print('The regression model for y2: Tout-
avg')
print('-----')
regr=linear_model.LinearRegression()
regr.fit(ass_x_train,ass_y2_train)
ass_y2_pred=regr.predict(ass_x_test)

# The mean squared error
print("Mean squared error: {}".format((1./
len(ass_y2_test)*(np.sum((ass_y2_test-
ass_y2_pred)**2))))
print('-----')
# Explained variance score: 1 is perfect p
rediction
print('Variance score: {}'.format(r2_score
(ass_y2_test, ass_y2_pred)))

# The coefficients of the linear regressio
n
print('-----')
print('Linear regression coefficients: \n'
, regr.coef_)

print('The regression model for y3: Tshell
-max')
print('-----')
regr=linear_model.LinearRegression()
regr.fit(ass_x_train,ass_y3_train)
ass_y3_pred=regr.predict(ass_x_test)

# The mean squared error
print("Mean squared error: {}".format((1./
len(ass_y3_test)*(np.sum((ass_y3_test-
ass_y3_pred)**2))))
print('-----')
# Explained variance score: 1 is perfect p
rediction
print('Variance score: {}'.format(r2_score
(ass_y3_test, ass_y3_pred)))

# The coefficients of the linear regressio
n
print('-----')
print('Linear regression coefficients: \n'
, regr.coef_)

from scipy.interpolate import Rbf
#rbfi=Rbf()

x1=np.array(pd.to_numeric(x.iloc[:,0]))
x2=np.array(pd.to_numeric(x.iloc[:,1]))
x3=np.array(pd.to_numeric(x.iloc[:,2]))
x4=np.array(pd.to_numeric(x.iloc[:,3]))
x5=np.array(pd.to_numeric(x.iloc[:,4]))
x6=np.array(pd.to_numeric(x.iloc[:,5]))
x7=np.array(pd.to_numeric(x.iloc[:,6]))
x8=np.array(pd.to_numeric(x.iloc[:,7]))
x9=np.array(pd.to_numeric(x.iloc[:,8]))
y1=np.array(pd.to_numeric(data.loc[:, 'P24
- nuavg-shell']))
y2=np.array(pd.to_numeric(data.loc[:, 'P19
- tavg-out (K)']))
y3=np.array(pd.to_numeric(data.loc[:, 'P17
- tmax-shell (K)']))

n=101
x1=np.array(pd.to_numeric(x.iloc[:-n,0]))
x2=np.array(pd.to_numeric(x.iloc[:-n,1]))
x3=np.array(pd.to_numeric(x.iloc[:-n,2]))
x4=np.array(pd.to_numeric(x.iloc[:-n,3]))
x5=np.array(pd.to_numeric(x.iloc[:-n,4]))
x6=np.array(pd.to_numeric(x.iloc[:-n,5]))
x7=np.array(pd.to_numeric(x.iloc[:-n,6]))
x8=np.array(pd.to_numeric(x.iloc[:-n,7]))
x9=np.array(pd.to_numeric(x.iloc[:-n,8]))
y1=np.array(pd.to_numeric(data.iloc[::-
n,26]))
y2=np.array(pd.to_numeric(data.iloc[::-
n,21]))
y3=np.array(pd.to_numeric(data.iloc[::-
n,19]))

rbf1=Rbf(x1,x2,x3,x4,x5,x6,x7,x8,x9,y1)

def RBF1(x):
    return -
1*rbf1(x[0],x[1],x[2],x[3],x[4],x[5],x[6],
x[7],x[8])

# 50-d
def g1(x):
    return 50-x[0]

# d=10
def g2(x):
    return x[0]-10

```



```

# 10-ts
def g3(x):
    return 15-x[1]

# ts-1
def g4(x):
    return x[1]-5

def g5(x):
    return 1.5-x[2]

def g6(x):
    return x[2]-0.2

def g7(x):
    return 3-x[3]

def g8(x):
    return x[3]-1

def g9(x):
    return 10-x[4]

def g10(x):
    return x[4]-1

def g11(x):
    return 90-x[5]

def g12(x):
    return x[5]-25

def g13(x):
    return 2-x[6]

def g14(x):
    return x[6]-0.5

def g15(x):
    return 60000-x[7]

def g16(x):
    return x[7]-10000

def g17(x):
    return 1.5-x[8]

```

```

def g18(x):
    return x[8]-0

# cons={'type':'eq','fun':g1}
cons=[{'type':'ineq','fun':g1},{'type':'ineq','fun':g2},{'type':'ineq','fun':g3},{'type':'ineq','fun':g4},{'type':'ineq','fun':g5},{'type':'ineq','fun':g6},{'type':'ineq','fun':g7},{'type':'ineq','fun':g8},{'type':'ineq','fun':g9},{'type':'ineq','fun':g10},{'type':'ineq','fun':g11},{'type':'ineq','fun':g12},{'type':'ineq','fun':g13},{'type':'ineq','fun':g14},{'type':'ineq','fun':g15},{'type':'ineq','fun':g16},{'type':'ineq','fun':g17},{'type':'ineq','fun':g18}]

# result=opt.minimize(HS6,x0,method='SLSQP',constraints=cons)
# x0=np.array([1,1,1,1,1,1,1,1,1])
x0=np.array([rand.uniform(10,50),rand.uniform(5,15),rand.uniform(0.2,1),rand.uniform(1,3),rand.uniform(2,10),rand.uniform(25,90),rand.uniform(0.2,2),rand.uniform(10000,60000),rand.uniform(0,1.5)])
result3=opt.minimize(RBF1,x0,method='SLSQP',constraints=cons)
print('RBF BFGS',result3.x)
print('')
print(result3)

rbf2=Rbf(x1,x2,x3,x4,x5,x6,x7,x8,x9,y2)

def RBF2(x):
    return -
1*rbf2(x[0],x[1],x[2],x[3],x[4],x[5],x[6],x[7],x[8])

# 50-d
def g1(x):
    return 50-x[0]

# d-10
def g2(x):
    return x[0]-10

# 10-ts
def g3(x):
    return 15-x[1]

```

```

# ts-1
def g4(x):
    return x[1]-5

def g5(x):
    return 1.5-x[2]

def g6(x):
    return x[2]-0.2

def g7(x):
    return 3-x[3]

def g8(x):
    return x[3]-1

def g9(x):
    return 10-x[4]

def g10(x):
    return x[4]-1

def g11(x):
    return 90-x[5]

def g12(x):
    return x[5]-25

def g13(x):
    return 2-x[6]

def g14(x):
    return x[6]-0.5

def g15(x):
    return 60000-x[7]

def g16(x):
    return x[7]-10000

def g17(x):
    return 1.5-x[8]

def g18(x):
    return x[8]-0
# cons={'type':'eq','fun':g1}

```

```

cons=[{'type':'ineq','fun':g1},{'type':'ineq','fun':g2},{'type':'ineq','fun':g3},{'type':'ineq','fun':g4},{'type':'ineq','fun':g5},{'type':'ineq','fun':g6},{'type':'ineq','fun':g7},{'type':'ineq','fun':g8},{'type':'ineq','fun':g9},{'type':'ineq','fun':g10},{'type':'ineq','fun':g11},{'type':'ineq','fun':g12},{'type':'ineq','fun':g13},{'type':'ineq','fun':g14},{'type':'ineq','fun':g15},{'type':'ineq','fun':g16},{'type':'ineq','fun':g17},{'type':'ineq','fun':g18}]

```

```

# result=opt.minimize(HS6,x0,method='SLSQP',constraints=cons)
# x0=np.array([1,1,1,1,1,1,1,1,1])
x0=np.array([rand.uniform(10,50),rand.uniform(5,15),rand.uniform(0.2,1),rand.uniform(1,3),rand.uniform(2,10),rand.uniform(25,90),rand.uniform(0.2,2),rand.uniform(10000,60000),rand.uniform(0,1.5)])
result3=opt.minimize(RBF2,x0,method='COBYLA',constraints=cons)
print('RBF BFGS',result3.x)
print('')
print(result3)

```

```

rbf3=Rbf(x1,x2,x3,x4,x5,x6,x7,x8,x9,y3)

def RBF3(x):
    return 1*rbf3(x[0],x[1],x[2],x[3],x[4],x[5],x[6],x[7],x[8])

```

```

# 50-d
def g1(x):
    return 50-x[0]

```

```

# d-10
def g2(x):
    return x[0]-10

```

```

# 10-ts
def g3(x):
    return 15-x[1]

```

```

# ts-1
def g4(x):
    return x[1]-5

```

```

def g5(x):
    return 1.5-x[2]

def g6(x):
    return x[2]-0.2

def g7(x):
    return 3-x[3]

def g8(x):
    return x[3]-1

def g9(x):
    return 10-x[4]

def g10(x):
    return x[4]-1

def g11(x):
    return 90-x[5]

def g12(x):
    return x[5]-25

def g13(x):
    return 2-x[6]

def g14(x):
    return x[6]-0.5

def g15(x):
    return 60000-x[7]

def g16(x):
    return x[7]-10000

def g17(x):
    return 1.5-x[8]

def g18(x):
    return x[8]-0
# cons={'type':'eq','fun':g1}
cons=[{'type':'ineq','fun':g1},{'type':'ineq','fun':g2},{'type':'ineq','fun':g3},{'type':'ineq','fun':g4},{'type':'ineq','fun':g5},{'type':'ineq','fun':g6},{'type':'ineq','fun':g7},{'type':'ineq','fun':g8},{'type':'ineq','fun':g9},{'type':'ineq','fun':g10},{'type':'ineq','fun':g11},{'type':'ineq','fun':g12},{'type':'ineq','fun':g13},{'type':'ineq','fun':g14},{'type':'ineq','fun':g15},{'type':'ineq','fun':g16},{'type':'ineq','fun':g17},{'type':'ineq','fun':g18}]

# result=opt.minimize(HS6,x0,method='SLSQP',constraints=cons)
# x0=np.array([1,1,1,1,1,1,1,1,1])
#x0=np.array([0,0,0,0,0,0,0,0,0])
x0=np.array([rand.uniform(10,50),rand.uniform(5,15),rand.uniform(0.2,1),rand.uniform(1,3),rand.uniform(2,10),rand.uniform(25,90),rand.uniform(0.2,2),rand.uniform(10000,60000),rand.uniform(0,1.5)])
result3=opt.minimize(RBF3,x0,method='SLSQP',constraints=cons)
print('RBF BFGS',result3.x)
print('')
print(result3)

wgt=np.array([0.1,0.8,0.1])

y4=-1*wgt[0]*(y1/np.mean(y1))-wgt[1]*(y2/np.mean(y2))+wgt[2]*(y3/np.mean(y3))

rbf4=Rbf(x1,x2,x3,x4,x5,x6,x7,x8,x9,y4)

def RBF4(x):
    return 1*rbf4(x[0],x[1],x[2],x[3],x[4],x[5],x[6],x[7],x[8])

# 50-d
def g1(x):
    return 50-x[0]

# d=10
def g2(x):
    return x[0]-10

# 10-ts
def g3(x):
    return 15-x[1]

# ts=1

```

```

def g4(x):
    return x[1]-5

def g5(x):
    return 1.5-x[2]

def g6(x):
    return x[2]-0.2

def g7(x):
    return 3-x[3]

def g8(x):
    return x[3]-1.5

def g9(x):
    return 10-x[4]

def g10(x):
    return x[4]-1

def g11(x):
    return 90-x[5]

def g12(x):
    return x[5]-25

def g13(x):
    return 2-x[6]

def g14(x):
    return x[6]-0.5

def g15(x):
    return 60000-x[7]

def g16(x):
    return x[7]-10000

def g17(x):
    return 1.5-x[8]

def g18(x):
    return x[8]-0
# cons={'type':'eq','fun':g1}
cons=[{'type':'ineq','fun':g1},{ 'type':'ineq','fun':g2},{ 'type':'ineq','fun':g3},{ 'type':'ineq','fun':g4},{ 'type':'ineq','fun':g5},{ 'type':'ineq','fun':g6},{ 'type':'ineq','fun':g7},{ 'type':'ineq','fun':g8},{ 'type':'ineq','fun':g9},{ 'type':'ineq','fun':g10},{ 'type':'ineq','fun':g11},{ 'type':'ineq','fun':g12},{ 'type':'ineq','fun':g13},{ 'type':'ineq','fun':g14},{ 'type':'ineq','fun':g15},{ 'type':'ineq','fun':g16},{ 'type':'ineq','fun':g17},{ 'type':'ineq','fun':g18}]

# result=opt.minimize(HS6,x0,method='SLSQP',constraints=cons)
# x0=np.array([50,10,1,2,10,45,0.5,10000,1.2])
x0=np.array([0,0,0,0,0,0,0,0,0])
result3=opt.minimize(RBF4,x0,method='SLSQP',constraints=cons)
print('RBF BFGS',result3.x)
print('')
print(result3)

import random as rand
for i in range(100):
    x0=np.array([rand.uniform(10,50),rand.uniform(5,15),rand.uniform(0.2,1),rand.uniform(1,3),rand.uniform(2,10),rand.uniform(25,90),rand.uniform(0.2,2),rand.uniform(1000,60000),rand.uniform(0,1.5)])
    wgt=np.array([0.2,0.5,0.3])

    y4=-1*wgt[0]*(y1/np.mean(y1))-wgt[1]*(y2/np.mean(y2))+wgt[2]*(y3/np.mean(y3))

    rbf4=Rbf(x1,x2,x3,x4,x5,x6,x7,x8,x9,y4)

def RBF5(x):
    return 1*rbf4(x[0],x[1],x[2],x[3],x[4],x[5],x[6],x[7],x[8])

# 50-d
def g1(x):
    return 50-x[0]

# d-10
def g2(x):
    return x[0]-10

```

```

# 10-ts
def g3(x):
    return 15-x[1]

# ts-1
def g4(x):
    return x[1]-5

def g5(x):
    return 1.5-x[2]

def g6(x):
    return x[2]-0.2

def g7(x):
    return 3-x[3]

def g8(x):
    return x[3]-1.5

def g9(x):
    return 10-x[4]

def g10(x):
    return x[4]-1

def g11(x):
    return 90-x[5]

def g12(x):
    return x[5]-25

def g13(x):
    return 2-x[6]

def g14(x):
    return x[6]-0.5

def g15(x):
    return 60000-x[7]

def g16(x):
    return x[7]-10000

def g17(x):
    return 1.5-x[8]

def g18(x):
    return x[8]-0

# cons={'type':'eq','fun':g1}
cons=[{'type':'ineq','fun':g1},{'type':
:'ineq','fun':g2},{'type':'ineq','fun':g3}
,{'type':'ineq','fun':g4},{'type':'ineq','
fun':g5},{'type':'ineq','fun':g6},{'type':
'ineq','fun':g7},{'type':'ineq','fun':g8},
{'type':'ineq','fun':g9},{'type':'ineq','f
un':g10},{'type':'ineq','fun':g11},{'type'
:'ineq','fun':g12},{'type':'ineq','fun':g1
3},{'type':'ineq','fun':g14},{'type':'ineq
','fun':g15},{'type':'ineq','fun':g16},{'t
ype':'ineq','fun':g17},{'type':'ineq','fun
':g18}]

result3=opt.minimize(RBF5,x0,method='S
LSQP',constraints=cons)
print('RBF BFGS',result3.x)
print('')
print(result3.fun)
print('')
print('Havg: ',-
1*RBF1(result3.x),'Tout: ',-
1*RBF2(result3.x),'Tshell,max: ',RBF3(resu
lt3.x))
print('')

import random as rand
for i in range(20):
    x0=np.array([rand.uniform(10,50),rand.
uniform(5,15),rand.uniform(0.2,1),rand.uni
form(1,3),rand.uniform(2,10),rand.uniform(
25,90),rand.uniform(0.2,2),rand.uniform(10
000,60000),rand.uniform(0,1.5)])
    wgt=np.array([0.2,0.7,0.1])

    y4=-1*wgt[0]*(y1/np.mean(y1))-
wgt[1]*(y2/np.mean(y2))+wgt[2]*(y3/np.mean
(y3))

    rbf4=Rbf(x1,x2,x3,x4,x5,x6,x7,x8,x9,y4
)

def RBF5(x):
    return 1*rbf4(x[0],x[1],x[2],x[3],
x[4],x[5],x[6],x[7],x[8])

```

```

# 50-d
def g1(x):
    return 50-x[0]

# d-10
def g2(x):
    return x[0]-10

# 10-ts
def g3(x):
    return 15-x[1]

# ts-1
def g4(x):
    return x[1]-5

def g5(x):
    return 1.5-x[2]

def g6(x):
    return x[2]-0.2

def g7(x):
    return 3-x[3]

def g8(x):
    return x[3]-1.5

def g9(x):
    return 10-x[4]

def g10(x):
    return x[4]-1

def g11(x):
    return 90-x[5]

def g12(x):
    return x[5]-25

def g13(x):
    return 2-x[6]

def g14(x):
    return x[6]-0.5

def g15(x):
    return 60000-x[7]

def g16(x):
    return x[7]-10000

def g17(x):
    return 1.5-x[8]

def g18(x):
    return x[8]-0

# cons={'type':'eq','fun':g1}
cons=[{'type':'ineq','fun':g1},{'type':
:'ineq','fun':g2},{'type':'ineq','fun':g3}
,{'type':'ineq','fun':g4},{'type':'ineq','
fun':g5},{'type':'ineq','fun':g6},{'type':
'ineq','fun':g7},{'type':'ineq','fun':g8},
{'type':'ineq','fun':g9},{'type':'ineq','f
un':g10},{'type':'ineq','fun':g11},{'type'
:'ineq','fun':g12},{'type':'ineq','fun':g1
3},{'type':'ineq','fun':g14},{'type':'ineq
','fun':g15},{'type':'ineq','fun':g16},{'t
ype':'ineq','fun':g17},{'type':'ineq','fun
':g18}]

result3=opt.minimize(RBF5,x0,method='S
LSQP',constraints=cons)
print('RBF BFGS',result3.x)
print('')
print(result3.fun)
print('')
print('Havg: ',-
1*RBF1(result3.x),' Tout: ',-
1*RBF2(result3.x),' Tshell,max: ',RBF3(
result3.x))
print('')

d1=[]
L1=[]
H1=[]
R1=[]
ts1=[]
a1=[]
tf1=[]
r1=[]
s1=[]
y11=[]
y21=[]
y31=[]
import random as rand

```

```

for i in range(500):
    x0=np.array([rand.uniform(10,50),rand.
uniform(5,15),rand.uniform(0.2,1),rand.uni
form(1,3),rand.uniform(2,10),rand.uniform(
25,90),rand.uniform(0.2,2),rand.uniform(10
000,60000),rand.uniform(0,1.5)])
    wgt=np.array([0.2,0.5,0.3])

    y4=-1*wgt[0]*(y1/np.mean(y1))-
wgt[1]*(y2/np.mean(y2))+wgt[2]*(y3/np.mean
(y3))

    rbf4=Rbf(x1,x2,x3,x4,x5,x6,x7,x8,x9,y4
)

    def RBF5(x):
        return 1*rbf4(x[0],x[1],x[2],x[3],
x[4],x[5],x[6],x[7],x[8])

    # 50-d
    def g1(x):
        return 50-x[0]

    # d-10
    def g2(x):
        return x[0]-10

    # 10-ts
    def g3(x):
        return 15-x[1]

    # ts-1
    def g4(x):
        return x[1]-5

    def g5(x):
        return 1.5-x[2]

    def g6(x):
        return x[2]-0.2

    def g7(x):
        return 3-x[3]

    def g8(x):
        return x[3]-1.5

    def g9(x):
        return 10-x[4]

    def g10(x):
        return x[4]-1

    def g11(x):
        return 90-x[5]

    def g12(x):
        return x[5]-25

    def g13(x):
        return 2-x[6]

    def g14(x):
        return x[6]-0.5

    def g15(x):
        return 60000-x[7]

    def g16(x):
        return x[7]-10000

    def g17(x):
        return 1.5-x[8]

    def g18(x):
        return x[8]-0
        # cons={'type':'eq','fun':g1}
        cons=[{'type':'ineq','fun':g1},{'type'
:'ineq','fun':g2},{'type':'ineq','fun':g3}
,{ 'type':'ineq','fun':g4},{'type':'ineq','
fun':g5},{'type':'ineq','fun':g6},{'type':
'ineq','fun':g7},{'type':'ineq','fun':g8},
{'type':'ineq','fun':g9},{'type':'ineq','f
un':g10},{'type':'ineq','fun':g11},{'type'
:'ineq','fun':g12},{'type':'ineq','fun':g1
3},{'type':'ineq','fun':g14},{'type':'ineq
','fun':g15},{'type':'ineq','fun':g16},{t
ype':'ineq','fun':g17},{'type':'ineq','fun
':g18}]

        result3=opt.minimize(RBF5,x0,method='S
LSQP',constraints=cons)

        y1l.append(-1*RBF1(result3.x))
        y2l.append(-1*RBF2(result3.x))
        y3l.append(RBF3(result3.x))

```

```

d1.append(result3.x[0])
L1.append(result3.x[1])
H1.append(result3.x[2])
R1.append(result3.x[3])
ts1.append(result3.x[4])
a1.append(result3.x[5])
tf1.append(result3.x[6])
r1.append(result3.x[7])
s1.append(result3.x[8])
# print('RBF BFGS',result3.x)
# print('')
# print(result3.fun)
# print('')
# print('Havg: ',-
1*RBF1(result3.x),'Tout: ',-
1*RBF2(result3.x),'Tshell,max: ',RBF3(resu
lt3.x))
# print('')
zipped = list(zip(y2l,d1,L1,H1,R1,ts1,a1,t
fl,r1,s1))
zipped.sort(reverse=True)
# print('d1',min(d1),max(d1))
# print('L1',min(L1),max(L1))
# print('H1',min(H1),max(H1))
# print('R1',min(R1),max(R1))
# print('ts1',min(ts1),max(ts1))
# print('a1',min(a1),max(a1))

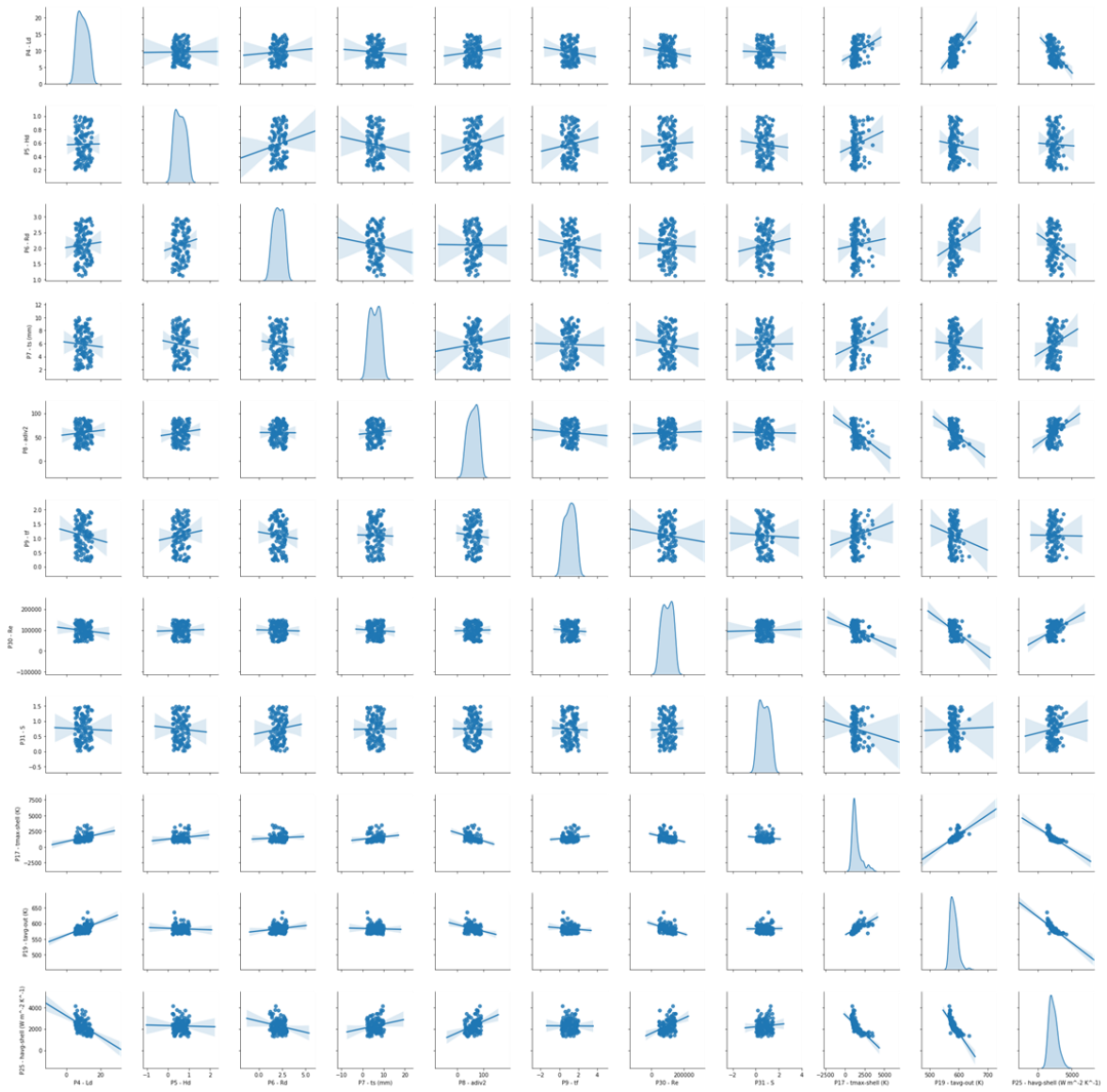
# print('tf1',min(tf1),max(tf1))
# print('r1',min(r1),max(r1))
# print('S1',min(s1),max(s1))
#print(zipped)
# print(zipped[0][0])
cnt=0
for i in range(len(zipped)):
    if cnt<=11 and zipped[i][0]<=874:
        print(zipped[i])
    else:
        continue
    cnt=cnt+1

x0=np.array([26.16,11.39,0.87,1.51,3.01,84
,0.5,18688,0.38])
x1=np.array([36.8,6.89,0.26,1.5,6.23,60.59
,1.13,19516,0.78])
x2=np.array([29.04,12.14,0.21,1.5,7.12,77.
9,0.2,15286,1.33])
print('Havg: ',-1*RBF1(x0),' Tout: ',-
1*RBF2(x0),' Tshell,max: ',RBF3(x0))
print('Havg: ',-1*RBF1(x1),' Tout: ',-
1*RBF2(x1),' Tshell,max: ',RBF3(x1))
print('Havg: ',-1*RBF1(x2),' Tout: ',-
1*RBF2(x2),' Tshell,max: ',RBF3(x2))

```

Pair plot of numerical parameters

The pair plot of the input and output parameters are presented below. The pair plot allows us to see the distribution of a single variable and the relationships between variables. This shows the trends between the input and output data.



APPENDIX F: HEAT SOURCE IMPLEMENTATION IN FLUENT

Modelling thermal characteristics within the ANSYS Fluent CFD environment is an established and well-known method of computational modelling and prediction. In some cases, as was done during this study, the optical modelling of the solar receiver model was done on another platform, which in this study's case was the MCRT software SolTrace. In this section, the author introduces an approach that uses ANSYS Fluent features for the integration of the optical and thermal modelling by mapping the optical flux as a volumetric heat source within ANSYS Fluent.

The process to implement a source variation-based profile as source term within ANSYS Fluent is as follows:

1. When the Fluent case is set up, activate one user-defined scalar (UDS-0) for all cell zones (fluent and solid), and one user-defined memory (UDM-0) location under the user-defined section.
2. Under the heading initialisation, patch the value zero to UDS-0 and UDM-0 after selecting all the available zones.
3. In file/interpolate, select the cell zones that represent the heat source zones. Read the *.ip file that provides the data of the flux that needs to be interpolated. If there are numerous interpolation files for different cell zones, select the cell zone with the intended interpolation file separately. This will interpolate the file to the UDS.
4. Interpret the user-defined function (UDF) by selecting the file under user-defined/functions/interpreted. When the UDF is selected, click Interpret. Following the explanation of the execution of the volumetric heat source implementation is the script of the UDF.
5. To copy the data from the UDS to the UDM, execute the command `uds_to_udm` in user-defined/execute on demand.
6. The UDS can now be switched off since the data is copied into the memory. This also saves computational memory during simulations.
7. The heat source can now be assigned to the corresponding cell zones by selecting the `udf solar_heat` as energy source term within the cell zone conditions of interest.

UDF script

```
#include "udf.h"
#include "sg.h"

/*=====*/
DEFINE_ON_DEMAND(copy_uds_to_udm)
{
Domain* d=Get_Domain(1);
Thread *t;
```

```

cell_t c;
thread_loop_c(t,d)
{
begin_c_loop(c,t)
{
C_UDMI(c,t,0)=C_UDSI(c,t,0);
}
end_c_loop (c,t)
}
return;
159
}
/*=====*/
DEFINE_SOURCE(solar_heat,c,t,dS,eqn)
{
real source;
dS[eqn]=0.0;
source=C_UDMI(c,t,0);
return source;
}
/*=====*/

```